Study of the Chinese loess and Siberian flood basalts: new global scale insights to the paleoclimate and geomagnetic field changes

by

Taslima Anwar

A thesis submitted in partial fulfillment of the requirements for the degree of

Doctor of Philosophy
in
Geophysics

Department of Physics
University of Alberta

Abstract

Paleomagnetism, in conjunction with other earth science methods, studies the behavior of the Earth's magnetic field, the drift of tectonic plate, climate and environmental changes. This thesis implements different applications of paleomagnetism to develop a technique to evaluate age for the Chinese red clay sequence, to reconstruct the regional climate and environment change in the Holocene recorded in the Chinese Loess, and to reveal absolute paleointensity variations for the gigantic magmatic events to fulfill the gaps in paleointensity data during the Permo-Triassic boundary and the late Devonian as the data for these periods are either contradictory or just absent.

A magnetostratigraphic age model for the Shilou red clay sequence on the eastern China is tested by cyclostratigraphy matching the magnetic susceptibility and grain size variations with the known orbital parameters of the Earth. This approach provides an age of 5.2 Ma for the Shilou profile instead of previously found age of 11 Ma with magnetostratigraphy alone. Wavelet analysis reveals the well-preserved 400 kyr and possible 100 kyr eccentricity cycles on the eastern Chinese Loess Plateau. Further, the paleomonsoon evolution during 2.58–5.2 Ma is reconstructed and divided into three intervals (2.58–3.6 Ma, 3.6–4.5 Ma, and 4.5–5.2 Ma). The use of cyclostratigraphy along with magnetostratigraphy proves to be an effective method of dating the red clay sequences, and it implies that many presently published age models for the red clay deposits based on magnetostratigraphy alone, perhaps, need to be re-evaluated.

A high-resolution petromagnetic analysis is conducted on the Holocene Chinese loess sequence. It reveals that three warm-humid intervals (~8.4–3.7 ka, ~2.4–1.2 ka, and ~0.81–0.48 ka) and

two cold-dry intervals (~3.7–2.4 ka and ~1.2–0.81 ka) occurred during the Holocene. A significant paleosol development from ~8.4 to 3.7 ka along with the higher values of proxy parameters indicates a generally strong warm-humid phase in the mid-Holocene which can be attributed as a Holocene optimum in the studied regions. A complete Holocene climate record is constructed and that correlates well with the other regional and global climate records. The study demonstrates that the Holocene climatic optimum took place at the same time interval all over the northern hemisphere.

A microwave paleointensity study for the Permo-Triassic boundary, considering both the northern extrusive and the southeastern intrusive parts of the Siberian trap basalt, is carried out for the first time. The accepted microwave paleointensity results from this study are combined with thermal Thellier results from previously published studies to obtain a grand mean paleomagnetic dipole moment for the Permo-Triassic boundary. The results suggest that multiple localities need to be considered to obtain an accurate paleomagnetic dipole moment for this time period. The grand mean paleointensity during the Permo-Triassic boundary is 19.5 ± 10.5 μT which corresponds to a mean virtual dipole moment of $3.2 \pm 1.5 \times 10^{22}$ Am^2. The study indicates that the magnetic field intensity during this period is significantly lower (by approximately 50%) than the present geomagnetic field intensity, implying that the Mesozoic dipole low might have begun at the Permo-Triassic boundary.

A microwave study, complemented by thermal Thellier one, for the late Devonian-aged volcanics and instrusives from the Viluy traps is performed. The Arai plots show a distinct two-slope concave-up shape, but pseudo-Thellier experiments support that it occurs due to a strong

overprint component rather than alteration or multi-domain effects. The site mean paleointensities, range from 4.6 μT to 16.5 μT which correspond to a virtual axial dipole moments of (0.81–2.97) $\times 10^{22}$ Am^2, suggest that the field was extremely weak during the late Devonian. It provides the evidence for the field being weak ~50 Ma before the onset of the superchron state, between ~310 and 265 Ma. Considering low dipole moment an indicator of high reversal frequency (as appears to be the case in the mid-Jurassic), this study demonstrates that rapid transitions between reversal hyperactivity and superchron states are a recurring feature in the paleomagnetic records, indicating the influence of mantle convection changing heat flow across the Core Mantle Boundary.

Preface

A version of Chapter 2 of this thesis has been published as Anwar, T., Kravchinsky, V.A., and Zhang, R., (2015), “Magneto- and cyclostratigraphy in the red clay sequence: new age model and paleoclimatic implication for the eastern Chinese Loess Plateau,” Journal of geophysical research: Solid Earth, 120(10), 6758-6770, doi:10.1002/2015JB012132. I, along with Kravchinsky, V.A., designed the research project. I did all the data analyses and wrote the manuscript. Kravchinsky, V.A. was the supervisory author and took the responsibility of editing the manuscript. Zhang, R. and Kravchinsky, V.A. provided the data. I gave an oral presentation on this project at the AGU Fall Meeting 2015.

A version of Chapter 3 will be submitted as Anwar, T., Kravchinsky, V.A., Zhang, R., Koukhar, L.P., Yang, L., Leping, Y. “Holocene climatic evolution at the Chinese Loess Plateau: implications of petromagnetic and grain size analyses.” I formulated the concept of the research project under the guidance and supervision of Kravchinsky, V.A. I was responsible for the all data analyses as well as writing of the manuscript. Kravchinsky, V.A. also contributed to the manuscript through editing. Kravchinsky, V.A., Zhang, R., Yang, L., and Leping, Y. went to the field to collect the samples. Zhang, R. and Koukhar, L.P. were responsible for the grain size and magnetic property measurements.

A version of Chapter 4 of this thesis has been published as Anwar, T., Hawkins L., Kravchinsky, V.A., Biggin, A.J., Pavlov, V.E., (2016), “Microwave paleointensities indicate a low paleomagnetic dipole moment at the Permo-Triassic boundary,” Physics of the Earth and Planetary Interiors, 260, 62-73, doi:10.1016/j.pepi.2016.09.007. I was responsible for conducting the experiment, data collection, data analysis, and the manuscript writing. Hawkins L. assisted in the data collection and manuscript composition. Kravchinsky, V.A. and Biggin, A.J. were the supervisory authors and were involved in concept formation and contributed to the editing of the manuscript. Pavlov, V.E. and Kravchinsky, V.A. provided the samples.

Chapter 5 of this thesis will be submitted as a part of the manuscript of Hawkins L., Anwar, T., Shcherbakova V., Biggin, A.J., Kravchinsky, V.A., Shatsillo A., Holt J., Pavlov, V.E., “Was the Earth's magnetic field weak in the Late Devonian?.” Under the guidance and supervision of Kravchinsky, V.A. and Biggin, A.J., I conducted the experiment, collected the data, and analyzed the data of my part. I presented the data at the AGU Fall Meeting 2014 and wrote a draft of the manuscript which includes only my data sets. The final version of the manuscript will combine the data of the University of Liverpool and University of Alberta.

Acknowledgments

This thesis is the result of time, efforts, supports, and guidance of some generous people. With sincere reverence, I would like to take the opportunity to thank these people without whom it would not be possible to complete the studies presented in this thesis.

I am eternally grateful to my supervisor Dr. Vadim A. Kravchisnky who has been a warm encouragement from the first day of our interaction. He has laid the foundation in me for the achievements throughout this process. He has refined my perceptions and thoughts through numerous discussions, guided me in difficult times, mentored me during my doubts and confusions, and supported me when I needed it most. He is an inspiration, and I am fortunate to have him as my supervisor.

I am indebted to my supervisory committee members Dr. Kim Chow and Dr. Mirko van der Baan who have been instrumental to enrich me for the last four years through their valuable critiques and recommendations. I also like to thank my examining committee members Dr. Alberto Reyes, Dr. Jeffrey Gu, and Dr. Guillaume St-Onge for their supports.

I would like to thank Dr. Ted Evans and Lei Wu of the paleomagnetic group at the University of Alberta for their efforts to refine my knowledge through critical conversations. I am grateful to Lioudmila P. Koukhar for her valuable supports in laboratory works at Paleomagnetism and Petromagnetism Laboratory, University of Alberta. I thank Elliot Hurst (Geomagnetism Laboratory, University of Liverpool) and Gerein Nathan (Scanning Electron Microscope Lab, University of Alberta) for their assistance during the laboratory measurements.

I would like to express my gratitude to Dr. Andrew J. Biggin for giving me the opportunity to work in the Geomagnetism Laboratory at University of Liverpool, for guiding and supporting me with patience. Thanks to Dr. Rui Zhang and Dr. Dunia Blanco for their sapient feedback time to time. I am also thankful to Louise Hawkins for her important support in paleointensity projects.

I am beholden to the Department of Physics, University of Alberta as it has uplifted my life profoundly by providing me various opportunities and facilities. I like to thank Sarah Derr and Dr. Richard Marchand for their help.

I love to convey my gratitude to my family, friends, and relatives who have inspired me to go extra miles. Last but definitely not the least, I am grateful to my parents for my lifetime as they have made me what I am today, and for believing in me that I can.

Table of Contents

Chapter 1

Introduction

Chapter 2

Magneto- and cyclostratigraphy in the red clay sequence: new age model and paleoclimatic implication for the Eastern Chinese Loess Plateau

Chapter 3

Holocene climatic evolution at the Chinese Loess Plateau: implications of petromagnetic and grain size analyses

Chapter 4

Microwave paleointensities indicate a low paleomagnetic dipole moment at the Permo-Triassic boundary

Chapter 5

Was the Earth's magnetic field weak in the Late Devonian?

Chapter 6

Conclusions

List of Tables

List of Figures

Chapter 1

Introduction

1.1 Rock Magnetism

Rock magnetism examines the magnetic properties of rocks, sediments, and soils to comprehend how these carriers capture and preserve the Earth's magnetic field. It can be applied to learn environmental magnetism, records of geomagnetic field variation and polarity reversals, sources of continental and oceanic magnetic anomalies, and paleomagnetic record of plate motion (Lowrie, 2007).

1.1.1 Magnetic Properties of Materials

Magnetism is arbitrated by a magnetic field which is generated by electric currents and magnetic moments of elementary particles. At the atomic level, the motions of electrons cause electric currents whereas the orbital and spin motions of electrons are responsible for magnetic moments (Butler, 1992). Shells, that are not complete and have unpaired spins, provide the net magnetic moments for an atom or ion. Motions of these spins and orbitals, along with electrons' interactions, produce magnetism in solids. Every material is influenced, to some extent, by an external magnetic field and can acquire an induced magnetization, which disappears in the absence of an external magnetic field (Tauxe, 2002). The relationship between the induced magnetization M in a material and the external field H is given by,

$$M = \chi \mathrm{H} \tag{1.1}$$

where χ is a proportionality factor which is known as magnetic susceptibility and depends on the properties of the object (e.g., chemical composition, crystal shape, atomic structure).

Certain materials can remain magnetized even in the absence of an external magnetic field, and hence, maintain a remanent magnetization (Butler, 1992). The reaction of a material to an applied magnetic field indicates the type of magnetization- induced or remanent; this nature of reaction defines the different types of magnetism of matters as all the matters are, somehow, magnetic. This magnetic behavior of matters or materials can be classified into three major groups- diamagnetism, paramagnetism, and ferromagnetism.

Diamagnetism

Diamagnetic materials do not exhibit magnetic moments as their atoms contain orbital shells with no unpaired electrons. In diamagnetic materials, a small induced magnetization is created through the orbital motion of electrons altered by the applied magnetic field in the opposite direction (Butler, 1992). This magnetization depends directly on the applied magnetic field and reduces to zero when the field is removed (Figure 1.1a). The magnetic susceptibility of these materials is weak, negative (Figure 1.1a), and independent of temperature.

Paramagnetism

Paramagnetic materials contain atoms with a net magnetic moment created from unpaired electrons in partially filled orbitals; however, there is no interaction between the adjacent magnetic moments of the electron. In paramagnetic materials, an induced magnetization is produced through the alignment of unpaired electrons with the applied magnetic field in the same direction (Butler, 1992). Such magnetization is linearly proportional to the applied magnetic field and becomes zero when the field is removed, similar to diamagnetic materials (Figure 1.1b). The susceptibility of paramagnetic materials is small, positive (Figure 1.1b), and varies inversely with temperature (known as Curie's law of paramagnetism).

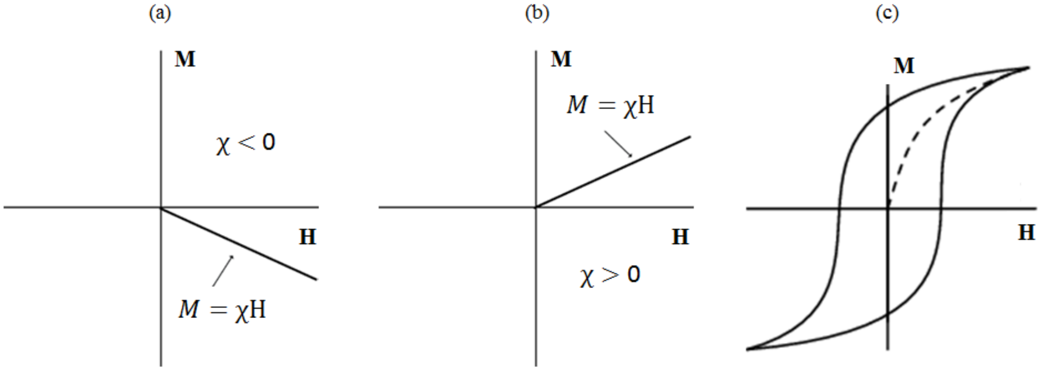

Figure 1.1. Variation of magnetization (M) versus applied magnetic field (H) for (a) diamagnetic material (b) paramagnetic material (c) ferromagnetic material. χ represents the magnetic susceptibility. The figure is modified from Butler (1992).

Ferromagnetism

Ferromagnetic materials have atoms with magnetic moments due to unpaired electrons, and unlike paramagnetic materials, there is a very strong interaction between the adjacent magnetic moments of the electron. The ferromagnetic materials can record the direction of an applied magnetic field, and that is a fundamental property of them (Lowrie, 2007). If the magnetizing field is removed, magnetization does not return to zero, but retains a memory of an applied field known as remanent or spontaneous magnetization. This characteristic is known as hysteresis and the path of the variation of magnetization as a function of an applied field is called a hysteresis loop (Figure 1.1c). Each ferromagnetic material possesses its unique temperature, the Curie temperature (~580˚C for magnetite and ~680˚C for hematite), above which ferromagnetic properties disappear entirely and the material becomes paramagnetic (Butler, 1992). For a given ferromagnetic material and temperature, the magnetization reaches a maximum value, at which the individual magnetic moments are aligned with the applied field, referred to as saturation magnetization (Ms). As temperature increases, saturation magnetization decreases and becomes zero at the Curie temperature.

The interaction of the electronic spins in a ferromagnetic material is produced by electronic exchange energy (quantum mechanical phenomenon) and results in a parallel or antiparallel alignment of spins (Tauxe, 2002). By considering different types of alignment of spins, three classes of ferromagnetism are distinguished – ferromagnetism, antiferromagnetism, and ferrimagnetism.

Ferromagnetic materials exhibit parallel alignment of spins (Figure 1.2a) as it happens in pure iron. When spins tend to align perfectly antiparallel to each other (equal in magnitude but opposite), there is no net magnetization, like ilmenite; antiferromagnetic materials exhibit such magnetization (Figure 1.2b). In some cases, the antiferromagnetic spins are not aligned precisely antiparallel; rather it is canted by a few degrees creating a weak net magnetic moment as it happens in hematite (Figure 1.2c). When the alignment of spins is antiparallel and the magnitudes of the moments in each direction are unequal, a resulting net moment is observed and ferrimagnetism is found in the material (Figure 1.2d). Ferrimagnetic materials (called ferrites) display all the properties of ferromagnetic behavior- large net magnetization, Curie temperatures, hysteresis, and remanence magnetization (Lowrie, 2007). The most important ferrimagnetic mineral is magnetite; but maghemite, pyrrhotite, and goethite are also significant contributors to the magnetic properties of rocks. Because of these natures or characteristics, ferromagnetic and ferrimagnetic materials are considered to be magnetic, whereas diamagnetic, paramagnetic, and antiferromagnetic materials are treated as nonmagnetic for their weak magnetic properties (Butler, 1992).

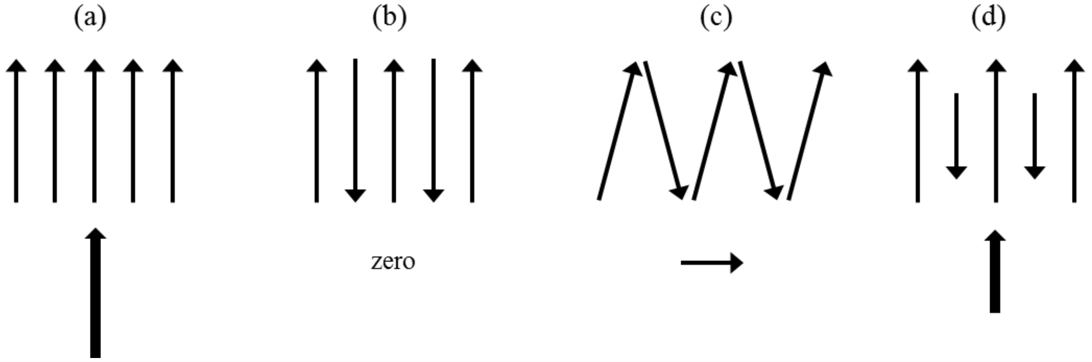

Figure 1.2. Schematic representations of spin alignment- (a) ferromagnetism (b) antiferromagnetism (c) spin-canted antiferromagnetism (d) ferrimagnetism. The resultant magnetic moment is indicated below the spin alignments. Modified from Tauxe et al. (2014).

1.1.2 Magnetic Properties of Rocks

A rock is a heterogeneous material as it contains a collection of ferromagnetic, paramagnetic and diamagnetic particles, and therefore, displays complex magnetization properties. The magnetic properties of a rock result from concentration of ferrimagnetic material. These magnetic properties depend on the type of ferrimagnetic mineral, its grain size, and the acquisition of remanent magnetization (Lowrie, 2007). As a consequence, the study of magnetic properties of rocks is the study of magnetic minerals, grain size, and remanent magnetization in those rocks.

Magnetic Minerals

Magnetic minerals are the iron-bearing minerals like iron oxides (such as magnetite, maghemite, and hematite), iron-oxyhydroxides (such as goethite and ferrihydrite), and some iron sulfides (such as greigite and pyrrhotite) that happen to be in traceable amounts in rock, soil, or sediment. In nature, iron–titanium oxides are the most dominant magnetic minerals which include two solid-solution series, titanomagnetite and titanohematite (Butler, 1992). One of the end members of the titanomagnetite solid-solution series is magnetite and the other end member is ulvöspinel. Hematite is one of the end members of the titanohematite solid-solution series and the other one is ilmenite. Rocks also consist of other magnetic minerals like goethite, pyrrhotite, and greigite. These ferrimagnetic minerals can be identified by its properties of Curie temperature, magnetic hysteresis measurements, utilization of magnetic properties as proxy parameters, optical or scanning electron microscopy, and so on (Lowrie, 2007).

Grain Size Indicators

The ferromagnetic properties of some materials, like metals and ferrites, differ considerably with grain size. Domains are zones within a grain that have a uniform magnetization direction. Magnetic domains are created due to the magnetic energy which is produced by the charge distribution at the surface of particles (Butler, 1992). The magnetic energy and grain volume are directly correlated. A magnetic grain can be composed of one or more magnetic domains. In the same magnetic mineral, smaller grains have a different number of magnetic domains compared to larger grains (Tauxe, 2002). Overall, four main domain structure types are found-superparamagnetic, single-domain, pseudo single-domain, and multi-domain.

The very finest grain, which cannot exhibit a stable domain configuration, is referred to as superparamagnetic (SP). It has a spin configuration that rapidly adapts to the new situation with a changing external field (Butler, 1992). In a single-domain (SD) state, the grain is sufficiently small, and the entire grain is uniformly magnetized (Figure 1.3a). SD grains are very stable and, thus, can be very efficient carriers of remanent magnetization or remanence (Butler, 1992). If the grain is large enough to contain a small number of domains, it then consists of a pseudo single-domain (PSD) (Figure 1.3b). PSD grains are also very stable and an important carrier of remanence (Tauxe, 2002). A large grain does not exhibit uniform magnetization as the magnetic energy, related to its magnetization, grows too large. It contains many domains which are separated by domain walls and is called multi-domain (MD) particle (Figure 1.3c). MD grains are less stable due to complicated spin structures (Lowrie, 2007). For these reasons, SD and PSD grains are usually preferred in paleomagnetic studies, while larger MD grains are avoided (Butler, 1992; Tauxe, 2002).

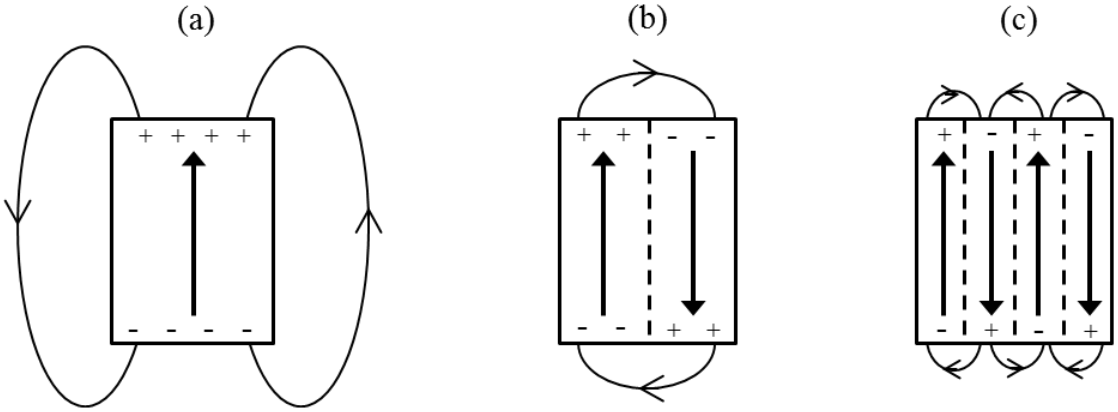

Figure 1.3. Different types of domain structures. (a) Single domain (Uniformly magnetized) (b) Two domains (oppositely magnetized) (c) Four domains (alternately magnetized). Modified from Lowrie (2007).

Remanent Magnetization in Rocks

Ferrimagnetic minerals, even in small concentration, can enable rocks to exhibit a remanent magnetization. Natural remanent magnetization (NRM) is the untreated remanence which is present in a rock sample collected from geological formations (Butler, 1992). NRM is usually composed of several components acquired through various ways at different times. A remanence acquired during the time of rock formation is called a primary NRM component, whereas a remanence acquired after the time of rock formation is referred to as a secondary NRM component (Lowrie, 2007). The geologically important types of remanence are the primary NRM component which is very stable and can preserve the magnetic signal during long geological epochs. The total NRM can be given as (Butler, 1992),

$$NRM = primary\ NRM + secondary\ NRM \tag{1.2}$$

Various natural processes enable particular rocks to acquire remanent magnetization. There are three basic forms of primary remanence-

(1) Thermoremanent magnetization (TRM): The most important type of remanent magnetization in igneous rocks, acquired during cooling from high temperature above the Curie temperature, is called TRM. Particles of these rocks are oriented into the direction of the applied field (geomagnetic field), and thermal remanence intensity is linearly related to the applied field intensity (Tauxe, 2002). This remanence, after the initial cooling during origination, remains constant over the time, and unaffected by the magnetic fields.

(2) Detrital remanent magnetization (DRM): The remanent magnetization, acquired by sedimentary rocks during or soon after deposition, is known as DRM. It is complicated since such rocks go through some, if not many, compound processes during their development. Detrital magnetic particles become aligned with the ambient magnetic field while settling

through still water (Lowrie, 2007). Post depositional processes including bioturbation, compaction, and diagenesis can affect this magnetization.

(3) Chemical remanent magnetization (CRM): The remanent magnetization, acquired during chemical changes that form ferromagnetic grains, is called CRM. It can occur through a chemical alteration of the preexisting magnetic minerals in a rock or authigenically formation of new minerals (Butler, 1992). CRM is typically observed in sedimentary rocks. CRM can be considered a secondary form of remanence when it is acquired long after deposition.

Chemical changes of rocks may cause secondary remanences during weathering, metamorphism, and laboratory experiments. The two basic forms of secondary NRM are-

(1) Isothermal remanent magnetism (IRM): Remanence, acquired from short-term interaction with strong magnetic field at ambient temperature, is referred to as IRM. Natural IRM can be resulting from exposure to nearby lightning strikes. In the laboratory, IRM is induced by known applied field larger than the coercivity at constant temperature (usually room temperature) (Butler, 1992).

(2) Viscous remanent magnetization (VRM): Remanence, acquired gradually during interaction or contact with a weak magnetic field, is known as VRM. This can arise in nature from long-term exposure to the geomagnetic field after rock formation (Lowrie, 2007).

1.2 Environmental Magnetism

Environmental magnetism examines and evaluates the magnetism of minerals focusing mainly on the impact of environmental factors. The formation, deposition, and post-depositional alterations of magnetic minerals are investigated through the rock and mineral magnetic techniques in a wide range of environmental processes (Evans and Heller, 2003).

1.2.1 Environmental Magnetic Parameters

The composition of magnetic elements in sediment or soil can be changed by the climatic conditions. The environmental setting can be revealed by analyzing the mineralogy, concentration, and grain size of the magnetic particles in natural samples (Thomson and Oldfield, 1986; Evans and Heller, 2003). Various studies or fields including paleoclimate, paleoceanography, and archeology consider the magnetic properties of minerals as imprints or proxies to investigate the variations in environment. Several magnetic parameters have already been identified in previous studies, and such parameters, used in this thesis, are described below.

Magnetic Susceptibility (χ)

Magnetic susceptibility can be presented as the magnetizability of a material (Thomson and Oldfield, 1986). The magnetizability indicates and, to some extent, explains the process of formation and transportation of iron-bearing minerals (Oldfield et al., 1999). It also gives us an idea about the nature and type of minerals. For this, in environmental studies, it is considered to be an effective parameter to examine a sample in a laboratory set-up or in the field. Moreover, it is an important factor for studying ferro- and ferrimagnetic minerals because of their high susceptibility. In fact, a high magnetic susceptibility corresponds to a greater concentration of magnetic minerals, such as magnetite (Thompson et al., 1980; Maher, 1986; Verosub and Roberts, 1995). It can give an idea about the grain size of the mineral as well (Thomson and Oldfield, 1986; Evans and Heller, 2003).

Frequency Dependence of Susceptibility (χ_{fd})

Frequency dependence of susceptibility χ_{fd} is a ratio, measured from the difference in susceptibility at two AC frequencies under low magnetic fields at room temperature. Magnetic susceptibility and operating frequency are inversely related and smaller grains, compared to larger ones, show profound change with increasing frequency near the SP/SD boundary (Thompson and Oldfield, 1986). This ratio can be applied to measure the impact of SP material to the signal, and it can reveal the ultrafine ferromagnetic minerals, particularly in the area of superparamagnetic grain size (Oldfield et al., 1999; Evans and Heller, 2003). It can be measured using the following relation,

$$\chi_{fd} = \frac{\chi_{lf} - \chi_{hf}}{\chi_{lf}} \times 100\% \tag{1.3}$$

Here, χ_{lf} is the low frequency susceptibility (measured at ~ 460 Hz), and χ_{hf} is the high frequency susceptibility (measured at ~ 4600 Hz), which are standard frequencies for the Bartington Magnetic Susceptibility Meter.

Anhysteretic Remanent Magnetization (ARM) and ARM Susceptibility

The remanent magnetization, produced while exposing a sample to a gradually decreasing alternating field with extant of the DC bias field, is called ARM. The bias field, usually 50-100 μT, decides the ARM value which is linearly related to the induced field at <100 μT (Oorschot, 2002). It is positively correlated with both the concentration of ferrimagnetic minerals and SD magnetic grain sizes (Oldfield, 1991; Verosub and Roberts, 1995). On the other hand, the ARM susceptibility (χ_{ARM}), the ARM intensity divided by the bias field value, evaluates and compares the various values of ARM acquired at distinct bias fields. It is also linearly related to the concentration of SD magnetic grains of ferrimagnetic minerals (Evans and Heller, 2003).

Saturation Isothermal Remanent Magnetization (SIRM)

The maximum isothermal remanent magnetization, acquired from an applied field, is known as SIRM. It is linearly related to the concentration of magnetic material and the amount of SD particles (Maher, 1986; Evans and Heller, 2003). Besides, the magnetic mineralogy also affects the SIRM showing a positive correlation between magnetization and SIRM (Thompson and Oldfield, 1986).

Ratio of Susceptibility and Remanence

The ratio of susceptibility and remanence helps to identify the variations of magnetic grain size in the samples. Here, in this thesis, typical ratios (χ_{ARM}/χ_{lf} and $\chi_{ARM}/SIRM$) are used for measuring magnetic grain size variation. These ratios, however, decrease with increasing grain size (Thompson and Oldfield, 1986; Maher, 1988; Evans and Heller, 2003).

1.2.2 Paleoclimatology

Paleoclimatology examines and evaluates the past climates of different geological parts and studies the natural phenomena to understand the variation of climates (Bradley, 1999). Imprints or proxies, archived in these phenomena, are the main source of studying paleoclimatology. For this, we can reconstruct the past climates and evaluate the reasons behind the climate change analyzing the paleoclimatic data (Bradley, 2015). If we comprehend the dynamics of past climates well, we can have a pragmatic foundation for understanding various aspects of the present climate and can be equipped to predict the future climate as well (Bradley and Eddy, 1991; Alverson et al., 1999; Bradley, 2008).

Climate Proxy

The dynamics of past climates are recorded through the imprints in the natural archives of biological, chemical, and geological evidences including marine and lacustrine sediments, glacial deposits, cave deposit, ice, loess-paleosols, tree growth and regional vegetation changes, and fossil remains of organisms (Bradley, 1999). Climate controls the Earth processes that produce such imprints or proxies. In fact, these are the outcomes of influence or impacts of climatic conditions. Climate conditions can influence the depositional character of proxies, on the other hand, proxies can reveal the chemical traces due to climate change. These imprints or proxies, can be used as indirect measurement or indicator of climate conditions and variations. In this thesis, magnetic susceptibility, sedimentary grain size, and rock-magnetic parameters are used as climate proxies in Chapter 2 and 3.

Terrestrial sediment records, such as cave deposits (speleothems) and loess deposits, provide paleoclimatic information through the studies of monsoon proxies. Differences in growth rate and composition of speleothems correspond to changes in climate conditions as the meteoric water cycle cause their formation. Oxygen and carbon isotope ratio, various types of recurrent laminae or bands, thickness of band, trace elements, and growth intervals of cave deposits are commonly used as paleoclimate proxies (e.g. Lauritzen and Lundberg, 1999; Frisia et al., 2003; Johnson et al., 2006; White, 2007) to reconstruct paleorainfall, paleotemperature, and/or paleovegetation. Magnetic susceptibility and other environmental magnetic parameters can also provide detailed record of the palaeoenvironmental conditions at the cave (Sroubek et al., 2001; 2007; Parés et al., 2010). The ratio and formation of oxygen isotope in cave calcite deposits are directly related to conditions like cave temperature and drip-water configuration, and therefore, depend indirectly on precipitation (e.g. Thompson et al., 1974; McDermott, 2004). Similarly, changes of stable isotope and trace elements in Chinese cave deposits act as the East Asian summer monsoon proxy as these record the fluctuations of precipitation during summer (Wang et al., 2001; Paulsen et al., 2003; Cheng et al., 2009; Johnson et al., 2006; Johnson, 2011).

Loess is the sediment of wind-swept materials mainly consisted of quartz, feldspars, micas, and calcium carbonate, with a small amount of clay (Pye, 1984; 1987). Particle size and magnetization of the loess-paleosol can also be used to reconstruct climate conditions like temperature and precipitation (Liu et al., 1985). In this thesis, Chinese loess deposits which present us with imprints or records of climate variation for a longer time-scale (10^3 – 10^6 years) have been studied. These loess deposits along with the climate proxies of loess that are widely used for paleoclimatic reconstruction are succinctly discussed later on.

Different proxies work in different ways depending on the spatial coverage, pertaining period, and ability to resolve events (e.g. Bradley, 1985). Based on these factors, proxies record relevant information of climate conditions and change to a various degrees: more or less. For this, it is important to consider the nature and ability of the proxy while studying paleoclimate. Also, it is critical to understand the continuity of the record (e.g. Bradley, 1985). However, proxies have different levels of inertia in responding to climate conditions and variations (e.g. Bryson & Wendland, 1967). Some respond immediately while some proxies do so after a period of time, sometimes, even after several centuries. There are proxies (e.g. ocean floor sediments) which provide information about climatic conditions and change for a longer period of time, but with a low frequency resolution. On the other hand, there are proxies (e.g. tree rings) that work well for a shorter period of time with a high frequency resolution. For all these differences in nature and ability of proxies to respond and record climatic conditions and change, a combination of multiple proxy indicators is used to study and reconstruct paleoclimate.

1.2.3 Chinese Loess Plateau

Loess deposits are commonly found in different parts of the world. Loess accumulates from mountains over the course of time on desert conditions. Across the Gobi desert in Asia, loess deposits build up in the north-central part of China creating the largest loess-covered area of the world, commonly known as the Chinese Loess Plateau. It covers an enormous area of approximately 500,000 km^2 up to the middle reaches of the Yellow River (Liu, 1985). During cold and dry conditions, the loess amassed due to the high dust fall and low vegetation, and on the other hand, it changed to accretionary soil (paleosols) due to weathering during warm and wet conditions through a process called pedogenesis. These two together, in alternating sequence, created an extensive record of paleoclimate on the continent (An et al., 1990; Ding et al., 1993).

The entire Chinese Loess Plateau, lithostratigraphically, can be distinguished, in wider perspective, into two geological constructions- the upper Quaternary loess-paleosol sequence and the lower Miocene–Pliocene red clay (Figure 1.4). The Quaternary sequence displays alternating layers of yellowish loess and reddish brown paleosol (Figure 1.4), exhibiting the interchanging nature of climate- cold and dry versus warm and wet (Kukla and An, 1989; Liu and Ding, 1998; An, 2000). It has a thickness, usually, between 150 and 300 m (Zhou et al., 1990; Heller et al., 1993). On the other hand, the red clay contains alternating layers of reddish wind-blown deposits and dark reddish carbonate rich paleosols (Figure 1.4), displaying analogous characteristics of the overlying loess-paleosol layers (Ding et al., 1998; 1999). Overall, it possesses a light to dark red color, having a thickness of several tens of meters (Sun et al., 1998). There has been evidence from the previous studies implying that the red clay corresponds to high-resolution climatic variation between relatively dry-cool and warm-humid periods (Sun et al., 1997; Guo et al., 2001; An et al., 2001; Liu et al., 2003).

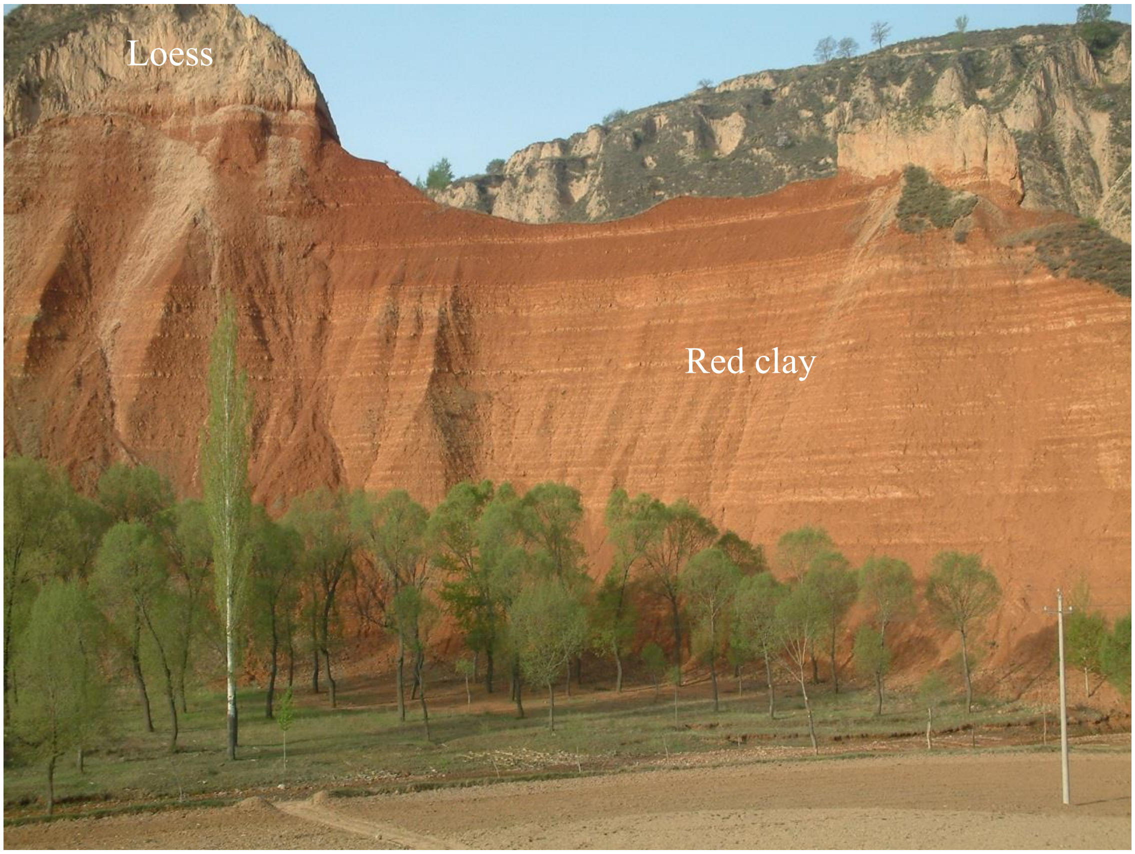

Figure 1.4. A loess-paleosol section at Shilou, Shanxi province, China (Anwar et al., 2015).

1.2.4 Climate Proxy for the Chinese Loess-Paleosol

The summer and winter monsoons, through their relative intensities, predominantly determined the climatic dynamics of the Chinese Loess Plateau, and to evaluate it, paleoclimatic studies happen to investigate proxies like magnetic properties and grain size of sediments. In fact, to study loess-paleosol, magnetic measurements play a critical role (Heller and Evans, 1995). Moreover, the amount of iron minerals in soil is directly related to the rate of pedogenesis (Le Borgne, 1955) which is influenced, and, to some extent, determined by the climatic conditions, implying that warmer and wetter climates correspond to stronger soils as well as higher magnetism (Heller and Evans, 1995). The magnetic particles usually originate in secondary formation of minerals, probably through biogenic processes. The magnetic enhancement can be caused by the in-situ formation of microcrystalline magnetite (Liu et al., 1994; Maher et al., 1994), or by a combination of both magnetite and maghemite (Maher, 1998) through chemical, biochemical or biogenic processes; these processes may be influenced considerably by rainfall and temperature. Though magnetic susceptibility (χ) was used as a climate proxy initially, recent studies have introduced other magnetic properties including low frequency susceptibility (χ_{lf}), frequency-dependent susceptibility (χ_{fd}), anhysteretic remanent magnetization susceptibility (χ_{ARM}), and saturation isothermal remanent magnetization (SIRM).

Magnetic susceptibility has been proved to be useful as a climate proxy (Kukla et al., 1988). It is commonly used in reconstructing terrestrial, marine, and lacustrine climatic conditions (e.g. Evans and Rutter, 1998; Evans and Heller, 2001, 2003; Maher and Thompson, 1992; Maher, 2011). Heller and Liu (1984) presented the first comprehensive study on changes in magnetic susceptibility of Chinese loess-paleosol sequences. This study indicated that maximum and minimum values of magnetic susceptibility correspond to warm and cold oxygen isotopic conditions respectively, captured in marine sediments. An et al. (1991) showed that such sequence can be considered a proxy to study variations in Asian monsoon as it is directly related to the changes in warm and humid summer monsoon in the East Asia. In fact, warmer and more humid climate conditions can alter non-magnetic iron-bearing silicate minerals to ferromagnetic finer grains with stronger magnetism (e.g. Zhou et al., 1990; Maher and Thompson, 1991; 1992). Such magnetic grains can be increased in amount or portion during summer monsoon through decreasing dust accumulation rate and stronger pedogenesis as precipitation causes frequent plant cover (e.g. An et al., 1990; 1991; Maher and Thompson, 1992). Therefore, magnetic susceptibility is an index to interpret the intensity of summer monsoons (An et al., 1991), indicating higher value for paleosols (warm and mild interglacial periods) compared to loess (cold and dry glacial periods) since the ultrafine grained magnetite and maghemite, formed during the pedogenesis, are the main carriers of the magnetic susceptibility signal (Maher and Tylor, 1988; Zhou et al., 1990). Furthermore, the magnetization intensity related parameters (χ_{lf}, χ_{fd}, χ_{ARM} and SIRM) exhibit high values in paleosols and low values in loess for the Chinese Loess Plateau, and indicate concentration as well as grain size changes of magnetic minerals (Evans and Heller, 2003).

Sedimentary grain size parameters including median grain size (An et al., 1991; Xiao et al., 1995; An, 2000; Ding et al., 2002), coarse fraction content (Porter and An, 1995; Zhang et al., 1999; Lu et al., 1999) and grain size ratio (Vandenberghe et al., 1997, 2004), are used extensively to reconstruct and depict paleoclimatic variations. Dust storms were common during the glacial periods and that caused a large amount of coarse-grained silts to be transformed into wind-blown sediments, whereas interglacial periods, when there was a paucity of such storms, resulted in finer-grained deposits on the Loess Plateau (Liu, 1985; Zhang et al., 1999; Prins et al., 2007). Though winter monsoon influences grain size compositions of loess and red clay deposits, such influence can be superseded by pedogenesis through changes in grain size distributions (e.g., Liu, 1985; Xiao et al., 1995; Sun et al., 2006a). For this, quartz grain size refers to the strength of winter monsoon, exhibiting the highest value for the cold and windy periods and transporting coarse-grained particles to a long distance from its origin (Porter and An, 1995; Xiao et al., 1995).

1.2.5 Causes of Paleoclimate Change

The variations in climates, reflected in the paleoclimatic records, can be attributed to the different forcing mechanisms- both internal and otherwise, playing roles at diverse frequencies for the different timescales. For a decade-to-century, usually, the factors including atmosphere-ocean interaction, solar variability, and human activity cause or influence the variations, whereas the nature of the Earth's orbit determines the climate in terms of hundreds-of-thousands to millions of years (Berger and Loutre, 1991; Bradley, 1999; Shindell et al., 2003). On the other hand, the tectonic motion, asteroid strikes, massive magmatic eruptions, the Earth's inner-dynamics are the critical determinants for the climate change beyond millions of years (Kutzbach, 1974; Bradley, 2015). However, various factors of different time-scales can collectively influence the climatic variations of different magnitude depending on the intensity and frequency of the factors while individual factor plays its role on the climate at a specific frequency (Bradley, 2015). There has been a doctrine that the Earth goes through a rhythmic or systematic climate change observed in or evident by the oxygen isotope of deep-marine sediments and polar ice cores, and the sporadic nature of the paleosols in the wind-swift loess in the central China (Evans and Heller, 2003). This fluctuating nature of climate is attributed, commonly, to the Earth's orbital cycles, known as Milankovitch cycles. The alternating sequences of the loess and paleosols layers are, indeed, considered to be the reflection of Milankovitch cycles (Hovan et al., 1989; Kukla et al., 1990; An et al., 1990; Xu and Liu, 1994; Lu et al., 2002).

1.2.6 Milankovitch Cycles

Milutin Milankovitch, a Serbian mathematician, explained the reasons behind the long-term climate cycles for the first time, explaining that the amount of solar radiation on the Earth, influenced by the gravitational forces of Sun, Moon, and the other celestial bodies, affects the climates periodically (Miliankovitch, 1930). There are three types of orbital changes– eccentricity, obliquity, and precession (Figure 1.5).

Eccentricity refers to the changes in the shape of the Earth's orbit from almost circular (with the lowest eccentricity of 0.005) to more elliptical (with the highest eccentricity of 0.058) over the time, taking around 100,000 or 400,000 years for the completion. The changes in the shape of the Earth's orbit occur because of its interaction with the gravitational fields of neighboring planets, mostly the large ones: Jupiter and Saturn (Hill, 1897; Laskar et al., 2004). The distance between the Earth and the Sun, perihelion (shortest distance) and aphelion (longest distance), changes with eccentricity, and therefore, the total amount of solar radiation received by the Earth at perihelion and aphelion differs the most (with more seasonality) while the orbit is more elliptical and varies the least (with less seasonality) in case of circular orbit (Berger, 1978; Laskar 1989).

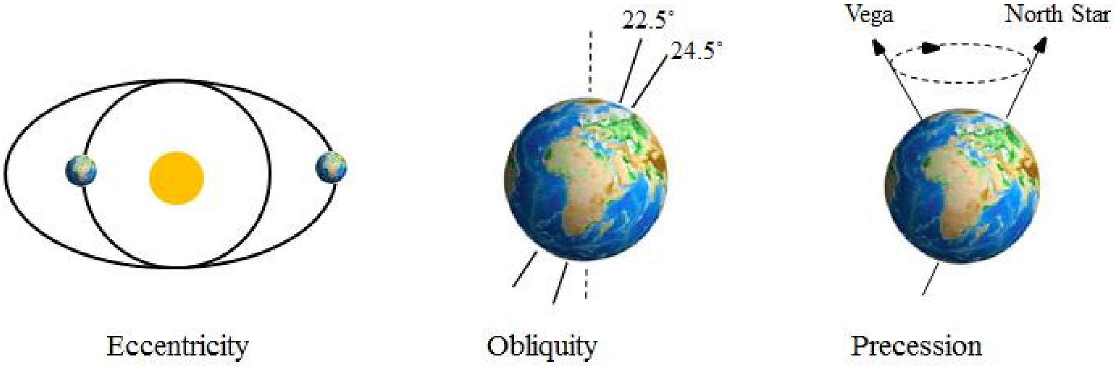

Figure 1.5. Schematic representations of Milankovitch Cycles.

Obliquity refers to the tilting position of the Earth on its axis, and it determines the amount of sunlight that reaches the hemispheres at any particular time. Now, the Earth inclines at 23.5°, whereas it differs from ~22° to 24.5° over a cycle of 41,000 years. Obliquity occurs due to the gravitational attraction between the Earth and all the other planetary bodies in the solar system (Berger et al., 1992; Berger and Loutre, 1991). This inclination is directly related to the extreme conditions between summer and winter seasons, and an increase in obliquity influences insolation in both higher and lower latitudes while increasing it for former and reducing it for latter ones (Berger, 1978; Laskar 1989).

Precession, the wobbling movement of the Earth on its axis, changes over a period of 19,000-23,000 years in the geological time. The tidal forces, exerted by the Sun and Moon on the Earth, cause the precession to change cyclically (Laskar et al., 1993). Moreover, precession and obliquity cycles are significantly affected by the Earth's rotational history and the Earth-Moon dynamics over time (Berger et al 1989, 1992; Berger and Loutre, 1994; Laskar et al., 2004). In the present day, the Earth comes closest to the Sun in January, in contrast, it stays farthest in July. This situation or position can be reversed by precession in around 11,000 years, resulting in more severe winters in the Northern Hemisphere.

Eccentricity, obliquity, and precession determine and influence the amount of sunlight reaching the Earth, and that, eventually, affects the global climate, which is now a widely accepted fact (Hinnov, 2013).

1.2.7 Cyclostratigraphy

Cyclostratigraphy is the study of astronomically induced climatic cycles as evidenced by the changes in sediments and sedimentary rocks. Hays et al. (1976) first explored the presence of orbital periodicities in a sedimentary sequence. Orbital forcing is critical for causing variations in climates, and for this, the periodicities concomitant of orbital variations are conspicuous signals in many paleoclimatic records (Berger et al., 1992). Again, the astronomic drivers affect the climate system in various ways, leaving traces in the proxy record, and through analysis of this record, we can examine the preserved orbital cycles (Figure 1.6). The time-series spectrum, portraying proxy as a function of time, can be used to characterize or explain variations in climate, and it can indicate the specific orbital periodicities where the variations are intense (Bradley, 2015). Overall, the application of cyclostratigraphy has been successfully conducted in the Chinese loess–paleosol sequences (Sun et al., 2006b) and in many other contexts.

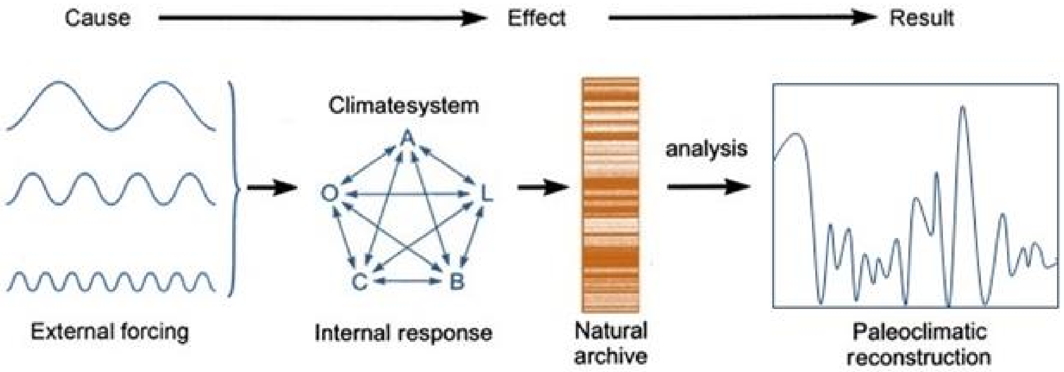

Figure 1.6. Schematic diagram illustrating the relationship between orbital forcing and the signal preserved in the sedimentary record. A: atmosphere; O: ocean (hydrosphere); C: cryosphere; B: biosphere; L: lithosphere. Modified from Bradley (2015).

1.3 Geomagnetism and Paleomagnetism

Geomagnetism studies the origin and nature of magnetic fields of the Earth and other planets of the solar system, whereas paleomagnetism studies the Earth's past geomagnetic field recorded in rocks and sediments. It is important to study and comprehend the Earth's ancient geomagnetic field as it helps understand the behavior and evolution of the Earth over time (Lowrie, 2007).

1.3.1 Geomagnetic Field

The majority of the geomagnetic field is generated by convection currents in the liquid outer core. The magnetic field of the Earth is a vector implying that it has both magnitude and direction (Butler, 1992). The magnetic vector can be described by the field strength (B) and direction (Figure 1.7). In paleomagnetism, the direction of the geomagnetic field vector is defined by two angles- declination (D) and inclination (I) (Lowrie, 2007). The declination is the horizontal angle between geographic and magnetic north, ranging clockwise from 0° to 360°. The inclination is the angle between the magnetic field direction and the horizontal one, ranging downward from -90° to +90°. The vertical component B_V and the horizontal component B_H of the geomagnetic field B are given by (Butler, 1992),

$$B_V = B \sin I\,; \qquad B_H = B \cos I \tag{1.4}$$

B_H can be, further, resolved into north and east components by,

$$B_N = B \cos I \cos D\,; \qquad B_E = B \cos I \sin D \tag{1.5}$$

The total intensity of the field is given by,

$$B = \sqrt{{B_N}^2 + {B_E}^2 + {B_V}^2} \tag{1.6}$$

There are many names for the Cartesian coordinates. In addition to the north, east and down (B_N, B_E, B_V), they could also be called X, Y, and Z. Therefore,

$$B = \sqrt{X^2 + Y^2 + Z^2}; \qquad D = \tan^{-1}\left(\frac{Y}{X}\right); \qquad I = \tan^{-1}\left(\frac{Z}{\sqrt{X^2 + Y^2}}\right) \tag{1.7}$$

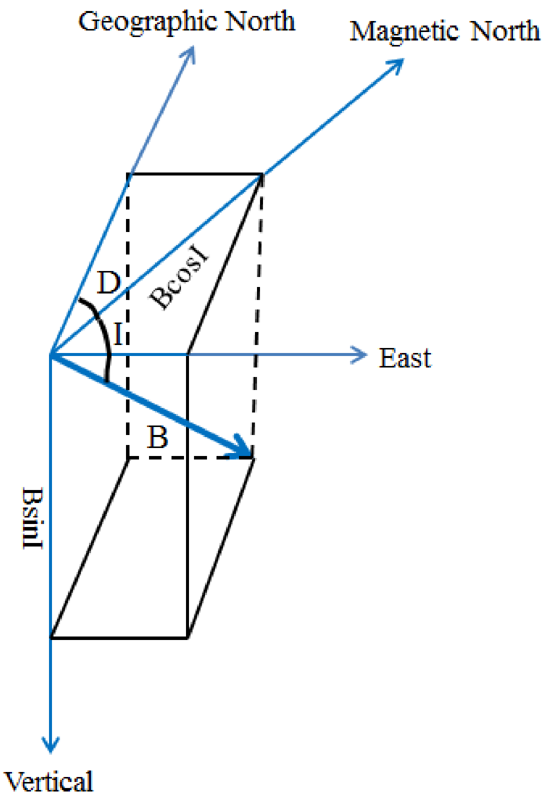

Figure 1.7. Illustration of the geomagnetic elements. The geomagnetic field can be described by the total field intensity (B), declination (D), and inclination (I). Modified from Lowrie (2007).

1.3.2 Geocentric Axial Dipole (GAD)

The geocentric axial dipole (GAD) model states that the time-averaged geomagnetic field corresponds to a single magnetic dipole that is aligned with the rotation axis at the center of the Earth (Hospers, 1954) (Figure 1.8). It is a fundamental assumption for many principles of paleomagnetism. Approximately 90% of the observed geomagnetic field can be described by a dipole (Butler, 1992). Currently, the axis of the geomagnetic dipole field is inclined at 11.5° relative to the rotational axis of the Earth. The current dipole moment of the geomagnetic field is 7.78×10^{22} Am^2 (Finlay et al., 2010).

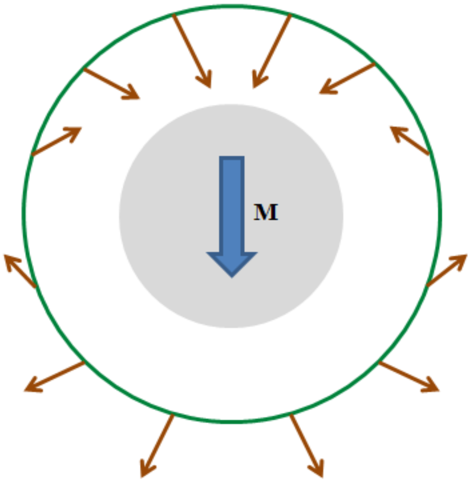

Figure 1.8. Geocentric axial dipole model. Magnetic dipole moment M is placed at the center of the Earth and aligned with the rotation axis. The magnetic field directions at the Earth's surface, produced by a geocentric axial dipole, are schematically shown. Modified from Butler (1992).

In the GAD model, the magnitude of the field can be determined by (Butler, 1992),

$$B_H = \frac{M\cos\lambda}{{r_e}^3}; \qquad B_V = \frac{2M\sin\lambda}{{r_e}^3} \tag{1.8}$$

$$B = \frac{M}{{r_e}^3}\sqrt{1 + 3sin^2\lambda} \tag{1.9}$$

where M is the dipole moment of the GAD, λ is the geographic latitude with a variation ranging from –90° to +90° (from the south geographic pole to the north geographic pole respectively), and r_e is the mean Earth radius.

Furthermore, the inclination of the field can be determined by,

$$\tan I = \left(\frac{B_V}{B_H}\right) = \left(\frac{2\sin\lambda}{\cos\lambda}\right) = 2\tan\lambda \tag{1.10}$$

Equation (1.10) is known as the dipole equation which is one of the most important relations in paleomagnetism (Lowrie, 2007).

1.3.3 Paleomagnetic Stability

The natural remanent magnetization (NRM), acquired at different times with different constituents during rock formation, does not change over time, as implied by paleomagnetism. It is much easier to alter the secondary NRM grains (magnetically softer) compared to the harder grains which possess the ancient remanent magnetization (Tauxe, 2002). Therefore, laboratory techniques need to be performed to remove the secondary NRM to keep the primary magnetization unaffected. Partial (alternating field and thermal) demagnetization experiments are applied to determine the directions of the magnetic components acquired by the rocks (Butler, 1992).

The components of the secondary magnetization exhibit low coercivities, and that is the ground for alternating field (AF) demagnetization (Lowrie, 2007). In AF demagnetization, a paleomagnetic specimen is exposed to an alternating magnetic field. The field fluctuates between equal and opposite peak values. AF demagnetization can eliminate a secondary NRM carried by the low coercive grains (less than the peak value of the field), and thus, isolate the primary NRM with coercivity higher than the peak field (Butler, 1992). In AF demagnetization, increasing magnetic field steps are used.

The components of the secondary magnetization possess lower blocking temperatures, and that is the ground for thermal demagnetization (Lowrie, 2007). In thermal demagnetization, a specimen is heated to a given temperature, and then, is allowed to cool to room temperature in zero magnetic field. It can eliminate the secondary NRM components that have lower blocking temperatures compared to given temperature (Butler, 1992). The heating and cooling cycles are repeated with progressively higher maximum temperatures.

The magnetization of a sample, after each heating or AF step, is evaluated through a magnetometer. The direction of magnetization changes progressively during the demagnetization unless the most stable component is revealed, and at this point, the direction, eventually, inclines towards a straight line to the origin (Figure 1.9). The stable component which remains is known as the characteristic remanent magnetization or ChRM. The results of demagnetization experiments are usually presented through a set of two projections of vectors plotted on the horizontal and vertical planes. These are referred to as Zijderveld diagrams (Zijderveld, 1967), also known as orthogonal projections or vector end-point diagrams (Figure 1.9). The mean direction of the magnetic vector for each specimen can be estimated from the orthogonal projection by using the principal component analysis (Kirschvink, 1980). Averaging and statistical analyses need to be carried out on the remanent magnetization vectors. For the measurement of the confidence intervals with respect to the mean direction calculation, Fisher's statistical test (Fisher, 1953) is applied. This test helps to calculate the dispersion of the points and the semi-angle cone of confidence around the observed mean (α_{95}), suggesting that the real mean of the direction lies in 95% probability within the cone (Buttler, 1992).

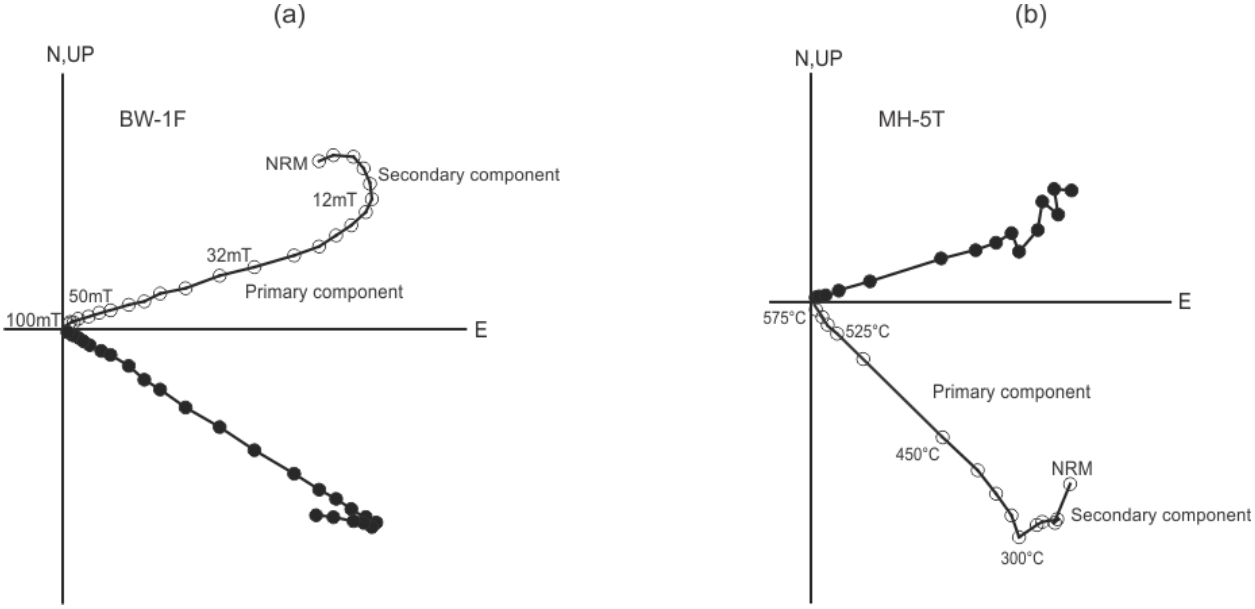

Figure 1.9. Representative vector end-point diagrams of stepwise (a) AF demagnetization and (b) thermal demagnetization of natural remanent magnetization for the African dyke basalts (unpublished report; Anwar and Kravchinsky). Open and solid circles represent vector endpoints projected onto the vertical and horizontal planes, respectively. NRM: natural remanent magnetization.

1.3.4 Paleointensity

The value of an ancient intensity of the geomagnetic field is called paleointensity. It is important to know the direction of field lines and information about its strength to study the variations of geomagnetic field over time. Paleointensity covers the study of mechanisms to magnetize rocks (thermal or detrital remanent magnetizations) and the techniques to replicate these mechanisms in a laboratory set up (Thellier and Thellier, 1959; Tauxe et al., 2014). In principle, the NRM of the rock (M_{NRM}) will be approximately linearly related to the low applied field, such as the geomagnetic field (Figure 1.10). This can be expressed as (Butler, 1992),

$$M_{NRM} = \vartheta B_{anc} \tag{1.11}$$

where B_{anc} is the intensity of ancient magnetic fields (paleointensity) and ϑ is a proportionality constant. The paleointensity experiment is designed to determine the proportionality constant ϑ (Tauxe, 2002). In the laboratory, the proportionality constant can be determined by giving the same sample a new remanent magnetization (M_{lab}) in a known magnetic field, B_{lab} (Figure 1.10) so that,

$$M_{lab} = \vartheta B_{lab} \tag{1.12}$$

The paleointensity can be obtained from the above equations (dividing equation 1.11 by equation 1.12), eliminating the proportionality constant ϑ and rearranging them to yield the following,

$$B_{anc} = \frac{M_{NRM}}{M_{lab}} B_{lab} \tag{1.13}$$

Equation (1.13) implies that paleointensity can be evaluated by multiplying the ratio of the two remanences with the known laboratory field. The entire experiment relies on the assumption that no change occurs in the proportionality constant (Butler, 1992). However, in practice, it is not easy to measure paleointensity since the ferromagnetic particles, bearing the natural remanence, may experience alterations; it may incur physical or chemical changes during the development of the laboratory remanence leaving an impact on the nature of the proportionality constant (Tauxe et al., 2008).

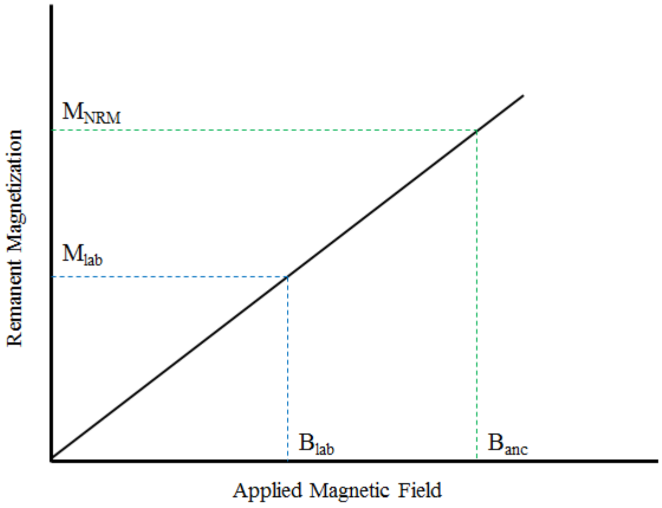

Figure 1.10. Schematic diagram for the principles of paleointensity estimation. Modified from Tauxe et al. (2014).

The principle of paleointensity experiment is to replace the natural remanence of the sample gradually with the partial thermal remanent magnetization (pTRM) developed in a known field. To perform the experiment, three assumptions are considered– Law of Independence, Law of Additivity, and the Law of Reciprocity (Tauxe, 2002).

- Law of Independence: "pTRMs acquired by cooling between any two temperature steps are independent of those acquired between any other two temperature steps."
- Law of Additivity: "The total TRM is the sum of all the independent pTRMs."
- Law of Reciprocity: "A magnetization, acquired by cooling from a given temperature is entirely replaced by reheating to the same temperature."

Many ways can be applied to replace the NRM increasingly with a pTRM in the laboratory. To extract paleointensity information from rocks carrying TRM, a step-wise heating to progressively higher temperatures is usually used. According to the original method proposed by Thellier

(1941), in the first step, the sample is heated to a specific temperature (T_1), and then, it is cooled to room temperature in the laboratory field B_{lab}. In the second step, the sample is again heated to that specific temperature, but cooled in the laboratory field $-B_{lab}$. Therefore, the remanence can be measured as follows,

$$M_1 = M_{NRM} + M_{pTRM} \tag{1.14}$$

$$M_2 = M_{NRM} - M_{pTRM} \tag{1.15}$$

The NRM remaining and the pTRM gained at each temperature step can be calculated from the above two equations. This procedure of heating steps is repeated to higher temperatures gradually until the Curie point is attained. Coe (1967) suggested modified protocols, to apply the first heating and cooling step in the zero field, and the second one in laboratory field (zero-field/ in-field, ZI). In contrast, Aitken et al. (1988) proposed to apply these steps in reverse ways- in the laboratory field, and in zero field respectively (in-field/zero-field, IZ).

In all experimental protocol (ZI and IZ), the NRM remaining is plotted against the pTRM acquired at each temperature step, known as Arai diagram (Nagata et al., 1963), to evaluate the ancient intensity. An example plot is shown in Figure 1.11. A lower temperature, for in-field cooling steps, is applied repeatedly to monitor alteration during the laboratory treatment (Thellier and Thellier, 1959). These repeated steps are known as pTRM checks (triangles in Figure 1.11). Moreover, various statistical parameters can be used to quantify the uncertainty and quality of the paleointensity estimate.

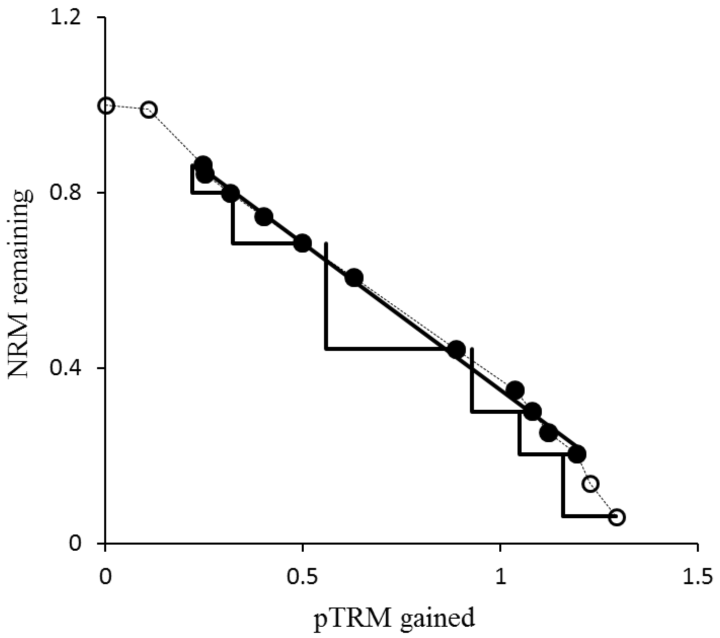

Figure 1.11. A typical representation of Arai plots for the samples from the Siberian traps (modified from Anwar et al., 2016). Triangles on the Arai plots represent pTRM checks and the solid straight lines marks the interval on which intensity was estimated.

In paleomagnetism, more is known about past directions compared to the past intensities of the geomagnetic field; because paleointensity experimental procedure is usually time consuming and exhibits a lower success rate of 10–20% (Valet, 2003). However, the past two decades have shown significant development through research works which have helped improve the selection of the samples and the success rate of determination (Buttler, 1992).

1.3.5 Virtual Dipole Moment

As geomagnetic intensity varies over the globe, paleointensity values can be expressed as an equivalent geocentric dipole moment which is called virtual dipole moment (VDM). This could produce the observed intensity at a specific (paleo) latitude, and is often convenient to compare geomagnetic intensity in different locations (Tauxe et al., 2014). VDM can be determined by,

$$VDM = \frac{4\pi r_e^3}{\mu_0} B_{anc}(1 + 3cos^2\theta_m)^{-1/2} \tag{1.16}$$

where r_e is the radius of the Earth, μ_0 is the permeability of free space ($4\pi\times10^{-7}$ N/A^2), B_{anc} is the paleointensity value, and θ_m is the magnetic (paleo) co-latitude. θ_m can be calculated from the observed inclination.

Sometimes site co-latitude is the only information known for a particular site, and thus, it provides a virtual axial dipole moment (VADM). It is the moment of an axial dipole aligned with the rotation axis that would yield the estimated paleointensity (Tauxe et al., 2014).

$$VADM = \frac{4\pi r_e^3}{\mu_0} B_{anc}(1 + 3cos^2\theta)^{-1/2} \tag{1.19}$$

θ is the geographic co-latitude at which B_{anc} is measured. Furthermore, the temporal and spatial averages of VDM and/or VADM are known as paleomagnetic dipole moments (PDMs).

1.3.6 Geomagnetic Polarity Reversals

Both the direction and strength of the Earth's magnetic field change with time. On a longer timescale, Earth's dipolar field reverses 180° relative to the present-day orientation, and this feature is known as geomagnetic polarity reversals (Opdyke and Channell, 1996; Butler, 1992). If the ancient magnetic field has the same orientation as the present dipole moment, it is termed the normal polarity; whereas the oppositely directed field is considered as reverse polarity. The interval between reversals can last for hundreds, thousands, or millions of years; however, the reversal pattern is not predictable (Lowrie, 2007). Approximately 780,000 years ago, the Earth's magnetic poles were simply opposite to that of today, and this polarity reversal is the most recent one. The average frequency, with which the Earth's magnetic field reverses its polarity, varied strongly in the past (Opdyke and Channell, 1996)– from perhaps as high as 12 reversals per million years at peak times (e.g. the mid-Jurassic) to no reversals for 30–40 million years during constant polarity superchrons (e.g. the mid-Cretaceous).

The history of magnetic field reversals is perceived to be widely known, but least comprehended, geophysical accounts on the Earth (Tauxe et al., 2008). Research indicates that no independent physical phenomenon is related to the Earth's magnetic field reversals. Several models are proposed by the researchers to describe reasons of the Earth's magnetic reversals. It has been investigated that geomagnetic reversal history could be related to many geological phenomena including changes in global heat flow, continental flood basalts, seafloor spreading, development of the oceanic plateau, variations in core-mantle boundary heat flow, mantle convection, and production of mantle plumes (Glatzmaier et al., 1999; Olson, 2003; Takahashi et al., 2005; Courtillot and Olson, 2007; Olson et al., 2013). Recent studies have suggested that reversals most likely reflect the changes in the core-mantle boundary (CMB) heat flow pattern and/or magnitude (Olson et al., 2010; Biggin et al., 2012; Biggin et al., 2015).

Magnitude of the CMB heat flow is a critical factor for regulating the core's thermal evolution which is a driving force of the geodynamo (Labrosse, 2007). The CMB, that separates the liquid iron-nickel outer core and the rocky silicate mantle, exhibits thermal and chemical heterogeneity which influences the heat flux to increase at the CMB. The chemical reaction, at the CMB, between (Mg,Fe)SiO_3 perovskite (in the mantle) and molten iron (in the core) produces oxide minerals, stishovite (SiO_2) and magnesium silicate perovskite ($MgSiO_3$), as well as metallic alloys, iron silicide (FeSi) and wüstite (FeO) (Knittle and Jeanloz, 1991); such reaction can change the core-mantle system considerably (Hirose and Lay, 2008). These oxide and metal introduce significant amount of oxygen and silicon into the core metal (liquid iron) while making it lighter; and on the other hand, iron gets depleted at the bottom of the mantle (Takafuji et al., 2005). Furthermore, just above the core-mantle boundary, perovskite goes through an exothermic phase change and transforms to post-perovskite due to a high pressure (Murakami et al., 2004; Oganov and Ono, 2004; Tsuchiya et al., 2004); this phase transition plays an important role in determining the heterogeneity at the CMB. Theoretical and experimental studies indicate that the density change is small (1.0–1.2%) whereas the Clapeyron slope (pressure/temperature slope) is large (7.5–11.5 MPa/K) for the perovskite to post-perovskite phase change with a transition temperature of 2,500 K and a pressure of 125 GPa (Murakami et al., 2004; Tsuchiya et al., 2004; Hirose, 2006; Lay et al., 2008). Nakagawa and Tackley (2004) suggested that this phase change plays an important role in destabilizing the CMB layer, increasing the CMB heat flow, rising mantle temperature, and growing the upwelling mantle plumes.

The geomagnetic field direction, sometimes, departs significantly and does not flip to a stable position at 180°. This phenomenon is known as geomagnetic excursion and lasts upto the first thousands of years (Butler, 1992). Such excursion is created by variations in the geomagnetic field driven by the flow of electrical currents in the outer core and its interaction with the mantle (Olson et al., 2013). Furthermore, geomagnetic field changes over periods of a year or more, known as geomagnetic secular variations. These indicate shorter-term changes in the Earth's outer core and are produced by dipolar as well as non-dipolar sources (McElhinny, 1973).

1.3.7 Geomagnetic Polarity Time Scale

Reversal is one of the most important features of the geomagnetic field in terms of chronological purposes. The geomagnetic polarity time scale (GPTS) is a list of dated polarity sequences (Figure 1.12). These polarity sequences are divided into long intervals of normal and reverse polarity, and these intervals are referred to as polarity chrons. The GPTS, a universal reference scale of polarity changes, is calibrated by radioisotopic methods and/or orbital tuning (Butler, 1992). The first GPTS in 0–5 Ma time interval was developed through the compilation of radiometric age and magnetic polarity determination of globally distributed igneous rocks (Cox et al., 1963). The continuous and reliable record of geomagnetic polarity can be found through the interpretation of marine magnetic anomalies (Vine and Matthews, 1963). By using such anomalies, Heirtzler et al. (1968) extended the GPTS to about 80 Ma. Since then, there have been adjustments to the temporal pattern of reversals, and thus, the GPTS has been refined gradually. For 160 Ma, reversals are very well documented from the marine magnetic anomalies (Cande and Kent, 1995; Gee and Kent, 2007), whereas, for older geological time scales, these are less reliably identified. An important application of the GPTS is its use as a dating tool for stratigraphic sequences since it provides stratigraphic markers for the correlations of geological sections (Langereis et al., 2010).

1.3.8 Magnetostratigraphy

To date an event (or a series of events) in the Earth's history occurring within a geological sequence is one of the most important applications of paleomagnetism. The pattern of polarity zones, registered in any sequence, provides a kind of geological fingerprint (Opdyke and Channell, 1996; Lowrie, 2007). The age of the rock succession can be derived through the correlation between an observed magnetic polarity pattern and the GPTS (Figure 1.12). This procedure is known as magnetic polarity stratigraphy or magnetostratigraphy. In Earth sciences, it constitutes a standard dating tool for a wide variety of sedimentary or volcanic sequences (Butler, 1992; Tauxe, 2002).

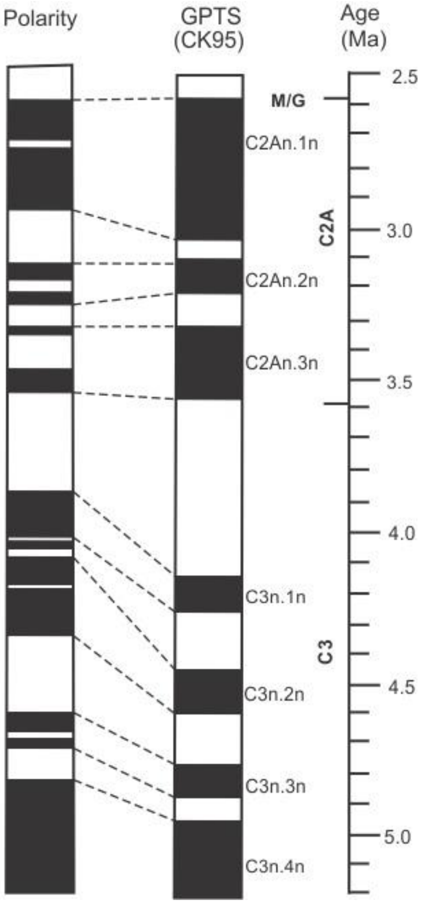

Figure 1.12. A typical representation of magnetostratigraphy (modified from Anwar et al., 2015). Correlation between magnetic polarity pattern of the Shilou red clay section and the geomagnetic polarity time scale (GPTS). CK95: Cande and Kent (1995); M/G: Matuyama-Gauss polarity boundary.

The robustness of a given correlation of an observed polarity sequence to the GPTS depends on several factors. For these reasons, some general principles are required to maintain the reliability of magnetostratigraphic studies (Opdyke and Channell, 1996; Tauxe et al., 2014):

(1) The primary component of the magnetization, which can be isolated by stepwise demagnetization, has to be identified to confirm that the studied materials are recorders of the geomagnetic field.

(2) Multiple samples per horizon are necessary to specify that the magnetization at a certain level can be reproducible.

(3) Sufficient stratigraphic coverage of sites is required to define the magnetic polarity zones.

(4) From the directional data, normal and reverse polarity needs to be clearly determined.

(5) The average direction has to be compared with the reference field and the expected direction.

(6) An independent approximate age constraints of the sequence is fundamental for the correlation of the magnetic polarity zonation with the GPTS.

(7) The pattern of the magnetic polarity zones needs to be matched with the sequence of polarity chrons of the GPTS. Few polarity zones may be ignored in the section or time scale.

1.4 Major Goals of the Thesis

The major goals of my thesis are as follows:

- The Chinese Loess Plateau contains red clay sequence which has continuous alternation of sedimentary cycles with recurrent paleoclimatic fluctuations from 2.58 Ma to Miocene. An accurate age model for the red clay record is necessary to investigate the paleoclimatic evolution through the analysis of climatic proxy records. The absence of abundant fossils and an inability of radiometric dating method have made magnetostratigraphy a leading method to build age model for the red clay. Magnetostratigraphy dating, based on visual correlation only, could potentially lead to an erroneous age model. Therefore, I have intended to check magnetostratigraphic age model for the red clay record on the eastern Chinese Loess Plateau with cyclostratigraphy as orbital parameters of the Earth are known. The hypothesis is that the presence of the Milankovitch cycles in the climate records can evaluate the correctness of the visual correlation between the magnetostratigraphic pattern and the GPTS. **The main objective of this first research is to demonstrate that only magnetostratigraphy and cyclostratigraphy together should be used to build an age model for red clays; and to reconstruct the paleoclimatic evolution during the red clay formation using climate proxy parameters.**

- The Holocene, during the last 11,700 years, encompasses the entire history of human civilization and exhibits fluctuations in climate. During this epoch, the Earth has experienced substantial variations in climate due to postglacial or interglacial regime, and also has developed most, if not all, of its present day landscapes and soils. To understand the present climate changes and to make the prediction of future climate changes, it is important to study the Holocene climatic variability as it is the closest analog for today's climate. I have concentrated on conducting magnetic proxy and grain size analyses on the Chinese loess-paleosol profiles to investigate these climatic variations. **The main objective of my second study is to reconstruct the regional climate and environment change in the Holocene, which is recorded in the Chinese Loess, and to investigate whether climate change differs from region to region.**

- The Siberian trap basalts are the largest igneous continental province on the Earth, covering an area of ~3.7×10^6 km^2 in the western part of the Siberian platform. These were emplaced during a relatively short period of time (~1 Ma) at the Permo-Triassic boundary (~250 Ma), the time when the largest mass extinction occurred. It is critical to study the characteristics of the magnetic field of the traps as it can reveal important information of the possible relationships between magnetic intensity variations during polarity reversals, which is an indicator of the outer earth core changes, and the largest mass extinction. Paleointensity studies at the Permo-Triassic boundary provide the opportunity to investigate the extension of the Mesozoic dipole low, during which, the dipole moment appeared to be about one-third of its present value (Prévot et al.,1990). There remains, however, a contradiction about the strength of the magnetic field at the Permo-Triassic boundary due to an insufficient amount of data. I investigated samples, which have been dated at ~250 Ma, of the Permo-Triassic trap basalts. **The main objective of this third research project is to clarify the geomagnetic field behavior and produce a grand mean paleomagnetic dipole moment for the Permo-Triassic boundary to investigate the duration and characteristics of the Mesozoic dipole low.**

- Dramatic changes in time-averaged geomagnetic field behavior have been observed in the Mesozoic Era. Specifically, a peak in reversal rate in the Jurassic (~170Ma) was associated with a weak geomagnetic field, while the field was apparently stronger during the Cretaceous Normal Superchron (121–84 Ma). To determine if there is a similar transition in geomagnetic field behavior during the Palaeozoic, preceding the Permo-Carboniferous Superchron (310–265 Ma), paleointensity data for the time preceding the superchron are required. However, limited data exist to describe geomagnetic field behavior in the late Devonian (~50 Myr before the superchron). To fill-up the gaps in paleointensity data at the late Devonian, I have focused on investigating samples, which have recently been Ar–Ar dated to 377–364 Ma, of late Devonian-aged volcanics and intrusives from the Viluy large igneous province in Siberia. Paleointensity studies at the late Devonian can provide insight to identify the recurring phenomenon in paleomagnetic behavior and the possible causes which could potentially influence this recurring feature. **The main objective of my fourth study is to fill-up the gaps in paleointensity data for the late Devonian and to investigate the prediction that the superchron state between ~310 and 265 Ma might have been preceded by a period when the field was weak and rapidly reversing.**

References

Aitken, M.J., Allsop, A.L., Bussel, G.D., Winter, M.B., 1988. Determination of the intensity of the Earth's magnetic field during archeological times: reliability of the Thellier technique. Reviews of Geophysics, 26, 3–12.

Alverson, K., Oldfield, F., Bradley, R.S. (Eds.), 1999. Past Global Changes and Their Significance for the Future. Elsevier, Amsterdam, 479.

An, Z.S., 2000. The history and variability of the East Asian paleomonsoon climate. Quat. Sci. Rev., 19, 171–187.

An, Z., Liu, T., Lu, Y., Porter, S.C., Kukla, G., Wu, X., Hua, Y., 1990. The long term paleomonsoon variation recorded by the loess paleosol sequence in central China. Quat. Int., 718, 91–95.

An, Z.S., Kukla, G.J., Porter, S.C., Xiao, J., 1991. Magnetic susceptibility evidence of monsoon variation on the Loess Plateau of central China during the last 130,000 years. Quat. Res., 36, 29–36.

An, Z.S., Kutzbach, J.E., Prell, W.L., Porter, S.C., 2001. Evolution of Asian monsoons and phased uplift of the Himalaya Tibetan plateau since Late Miocene times. Nature, 411, 62–66.

Anwar, T., Kravchinsky, V.A., and Zhang, R., 2015. Magneto- and cyclostratigraphy in the red clay sequence: New age model and paleoclimatic implication for the eastern Chinese Loess Plateau. Journal of Geophysical Research: Solid Earth, 120(10), 6758-6770.

Anwar, T., Hawkins L., Kravchinsky, V.A., Biggin, A.J., Pavlov, V.E., 2016. Microwave paleointensities indicate a low paleomagnetic dipole moment at the Permo-Triassic boundary. Physics of the Earth and Planetary Interiors, 260, 62–73.

Berger, A., 1978. Long-term variations of daily insolation and quaternary climatic changes. J. Atmos. Sci. 35, 2362–2367.

Berger, A., Loutre, M.F., 1991. Insolation values for the climate of the last 10 million years. Quat. Sci. Rev. 10, 297–318.

Berger, A., Loutre, M.F., 1994. Astronomical forcing through geologic time. In Orbital Forcing and Cyclic Sequences, ed. PL DeBoer, DG Smith, Spec. Publ. 19, Int. Ass. Sed., 15–24. Oxford: Blackwell Scientific.

Berger, A., Loutre, M.F., Dehant, V., 1989. Influence of the changing lunar orbit on the astronomical frequencies of pre-Quaternary insolation patterns. Paleoceanography 4(5): 555–64.

Berger, A., Loutre, M.F., Laskar, J., 1992. Stability of the astronomical frequencies over the Earth's history for paleoclimatic studies. Science, 255, 560–566.

Biggin, A.J., Steinberger, B., Aubert, J., Suttie, N., Holme, R., Torsvik, T.H., Van der Meer, D.G., Van Hinsbergen, D.J.J., 2012. Possible links between long term geomagnetic variations and whole-mantle convection processes. NatureGeosci., 8, 526–533.

Biggin, A.J., Piispa, E., Pesonen, L.J., Holme, R., Paterson, G.A., Veikkolainen, T., Tauxe, L., 2015. Palaeomagnetic field strength variations suggest Mesoproterozoic inner core nucleation. Nature 525, 245–248.

Bradley, R.S., 1985. Quaternary Palaeoclimatology: Methods of Palaeoclimatic Reconstruction. Unwin Hyman, London.

Bradley, R.S., 1999. Paleoclimatology, Reconstructing Climates of the Quaternary. Academic Press, San Diego, 610.

Bradley, R.S., 2008. Holocene perspectives on future climate change. In: Battarbee, R.W., Binney, H.A. (Eds.), Natural Climate Variability and Global Warming: A Holocene Perspective. Wiley-Blackwell, Chichester, 254–268.

Bradley, R.S., 2015. Paleoclimatology, Reconstructing Climates of the Quaternary (3rd edition). Elsevier/Academic Press, San Diego, 675.

Bradley, R.S., and Eddy, J.A., 1991. Records of past global changes. In: Bradley, R.S. (Ed.), Global Changes of the Past. University Corporation for Atmospheric Research, Boulder, 514.

Bryson, R.A. & Wendland, W.M., 1967. Tentative climate patterns for some late-glacial and post-glacial episodes in central North America. In: Life, land and water, Mayer-Oakes, W.J. (ed.). University of Manitoba Press, Winnipeg, 271–298.

Butler, R.F., 1992. Paleomagnetism: magnetic domains to geologic terranes. Blackwell Scientific Publications, Boston, MA, pp. 238.

Cande, S.C., and Kent, D.V., 1995. Revised calibration of the geomagnetic polarity timescale for the Late Cretaceous and Cenozoic. Journal of Geophysical Research: Solid Earth, 100, 6093–6095.

Cheng, H., Edwards, R.L., Broecker, W.S., Denton, G.H., Kong, X.G., Wang, Y.J., Zhang, R., Wang, X.F., 2009. Ice age terminations. Science, 326, 248–252.

Coe, R.S., 1967. Paleointensities of the Earth’s magnetic field determined from tertiary and quaternary rocks. Journal of Geophysical Research, 72, 3247–3262.

Courtillot, V., and Olson, P., 2007. Mantle plumes link magnetic superchrons to Phanerozoic mass depletion events: Earth and Planetary Science Letters, 260, 495–504.

Cox, A.V., Doell, R.R., and Dalrymple, G.B., 1963. Geomagnetic polarity epochs and Pleistocene geochronometry. Nature, 198, 1049–1051.

Ding, Z., Rutter, N.W., Liu, T.S., 1993. Pedostratigraphy of Chinese loess deposits and climatic cycles in the last 2.5 Ma. Catena, 20, 73–91.

Ding, Z.L., Sun, J.M., Liu, T.S., Zhu, R.X., Yang, S.L., Guo, B., 1998.Wind-blown origin of the Pliocene red clay formation in the central Loess Plateau, China. Earth and Planetary Science Letters, 161, 135–143.

Ding, Z.L., Xiong, S.F., Sun, J.M., Yang, S.L., Gu, Z.Y., Liu, T. S., 1999. Pedostratigraphy and paleomagnetism of a ∼7.0 Ma eolian loess–red clay sequence at Lingtai, Loess Plateau, north-central China and the implications for paleomonsoon evolution. Palaeogeography, Palaeoclimatology, Palaeoecology, 152, 49–66.

Ding, Z.L., Derbyshire, E., Yang, S.L., Yu, Z.W., Xiong, S.F., Liu, T.S., 2002. Stacked 2.6-Ma grain size record form the Chinese loess based on five sections and correlation with the deep-sea δ18Orecord. Paleoceanography, 17.

Evans, M.E. and Rutter, N.W., 1998. A magnetic investigation of a late Quaternary loess/palaeosol record in Siberia, Geophys. J. Int., 132, 128–132, 1998.

Evans, M.E., and Heller. F., 2001. Magnetism of loess/palaeosol sequences: recent developments, Earth-Sci. Rev., 54, 129–144.

Evans, M.E., and Heller, F., 2003. Environmental Magnetism: Principles and Applications of Enviromagnetics, Elsevier Science, Academic Press.

Fisher, R.A., 1953. Dispersion on a sphere. Proceedings of the Royal Society London, Series A, 217, 295–305.

Frisia, S., Borsato, A., Preto, N. and McDermott, F., 2003. Late Holocene annual growth in three Alpine stalagmites records the influence of solar activity and the North Atlantic Oscillation on winter climate. Earth and Planetary Science Letters, 216(3), 411–424.

Gee, J.S., and Kent, D.V., 2007. Source of oceanic magnetic anomalies and the geomagnetic polarity time scale. In Kone, M. (Eds.), Treatise on Geophysics. Amsterdam: Elsevier. Geomagnetism, Vol. 5, pp. 455–507.

Glatzmaier, G.A., Coe, R.S., Hongre, L., Roberts, P.H., 1999. The role of the Earth's mantle in controlling the frequency of geomagnetic reversals. Nature 401, 885–890.

Guo, Z.T., Peng, S.Z., Hao, Q.Z., Biscaye, P.E., Liu, T.S., 2001. Origin of the Miocene-Pliocene red earth formation at Xifeng in Northern China and implications for paleoenvironments. Palaeography, Palaeclimatology, Palaeoecology, 170, 11–26.

Hays, J.D., Imbrie, J. and Shackleton, N.J., 1976. Variations in the earth's orbit: pacemaker of the ice ages, Sciences, 194, 1121–1132.

Heirtzler, J.R., Dickson, G.O., Herron, E.M., Pitman, W.C.I., LePichon, X., 1968. Marine magnetic anomalies geomagnetic field reversals, and motions of the ocean floor and continents. J. Geophys. Res., 73, 2119–2136.

Heller, F., and Liu, T.S., 1984. Magnetism of Chinese loess deposits. Geophys. J. R. Astron. Soc., 77, 125–141.

Heller, F., and Evans, M.E., 1995. Loess magnetism. Rev. Geophys., 33, 211–240.

Heller, F., Shen, C.D., Beer, J., Liu, X.M., Liu, T.S., Bronger, A., Suter, M., Bonani, G., 1993. Quantitative estimates of pedogenic ferromagnetic mineral formation in Chinese loess and paleoclimatic implications. Earth Planet. Sci. Lett., 114, 385–390.

Hill, G., 1897. On the values of the eccentricities and longitudes of the perihelia of Jupiter and Saturn for distant epochs. Astron. J. 17(11), 81–87.

Hinnov, L.A., 2013. Cyclostratigraphy and its revolutionizing applications in the earth and planetary sciences. Geological Society of America Bulletin, 125, 11-12, pp.1703-1734.

Hirose, K., 2006. Postperovskite phase transition and its geophysical implications. Rev. Geophys. 44, 3001.

Hirose, K. and Lay, T., 2008. Discovery of post-perovskite and new views on the core-mantle boundary region. Elements, 4(3), 183-189.

Hospers, J., 1954. Rock magnetism and polar wandering, Nature, 173, 1183–1184.

Hovan, S.A., Rea, D.K., Pisias, N.G., Shackleton, N.J., 1989. A direct link between the China loess and marine d18O records: aeolian flux to the north Pacific. Nature, 340, 296–298.

Johnson, K.R., 2011. Long-distance relationship. Nature Geoscience, 4, 426–427.

Johnson, K.R., Hu, C., Belshaw, N.S. and Henderson, G.M., 2006. Seasonal trace-element and stable-isotope variations in a Chinese speleothem: The potential for high-resolution paleomonsoon reconstruction. Earth and Planetary Science Letters, 244(1), 394–407.

Kirschvink, J.L., 1980. The least-squares line and plane and the analysis of paleomagnetic data. Geophysical Journal of the Royal Astronomical Society, 62, 699–718.

Knittle, E., and Jeanloz, R., 1991. Earth's coremantle boundary: Results of experiments at high pressures and temperatures. Science 251: 1438-1443.

Kukla, G.J., and An, Z., 1989. Loess stratigraphy in central China. Palaeogeogr. Palaeoclimatol. Palaeoecol, 72, 203–225.

Kukla, G., Heller, F., Liu, X.M., 1988. Pleistocene climates in China dated by magnetic susceptibility. Geology, 16, 811–814.

Kukla, G., An, Z.S., Meliece, L., Gavin, G., Xiao, J.L., 1990. Magnetic susceptibility record of Chinese loess. Transactions of the Royal Society of Edinburgh: Earth Sciences, 81, 263–288.

Kutzbach, J.E., 1974. Fluctuations of climate-monitoring and modelling. World Meteorol. Organ. Bull. 23, 155–163.

Labrosse, S., 2007. Core-mantle Boundary, Heat flow across. In Encyclopedia of Geomagnetism and Paleomagnetism, Springer Netherlands, 127-130.

Langereis, C.G., Krijgsman, W., Muttoni, G., and Menning, M., 2010. Magnetostratigraphy concepts, definitions, and applications. Newsletters on Stratigraphy, 43(3), 207–233.

Laskar, J., 1989. A numerical experiment on the chaotic behavior of the solar system. Nature 338, 237–238.

Laskar, J., Joutel, F., Boudin, F., 1993. Orbital, precessional, and insolation quantities for the Earth from − 20 Myr to 10 Myr. Astron. Astrophys. 270, 522–533.

Laskar, J., Robutel, P., Joutel, F., Gastineau, M., Correia, A.C.M. and Levrard, B., 2004. A long-term numerical solution for the insolation quantities of the Earth. Astronomy & Astrophysics, 428(1), 261–285.

Lauritzen, S.E. and Lundberg, J., 1999. Speleothems and climate: a special issue of The Holocene. The Holocene, 9(6), 643–647.

Lay, T., Hernlund, J. and Buffett, B.A., 2008. Core–mantle boundary heat flow. Nature Geoscience, 1(1), 25–32.

Le Borgne, E., 1955. Abnormal magnetic susceptibility of the top soil. Ann. Geophys., 11, 399–419.

Liu, T.S., 1985. Loess and Environment. China Ocean Press, Beijing, 31–67.

Liu, T.S., Ding, Z.L., 1998. Chinese loess and the paleomonsoon. Annu. Rev. Earth Planet. Sci., 26, 111–145.

Liu, X., Rolph, T., Bloemendal, J., Shaw, J., Liu, T., 1994. Remanence characteristics of different magnetic grain size categories at Xifeng, central Chinese Loess Plateau. Quat. Res., 42, 162–165.

Liu, X.M., Rolph, T., An, Z.S., Hesse, P., 2003. Paleoclimatic significance of magnetic properties on the Red Clay underlying the loess and paleosols in China. Palaeogeography, Palaeoclimatology, Palaeoecology, 199, 153–166.

Lowrie, W., 2007. Fundamentals of geophysics. Cambridge university press.

Lu, H.Y., Huissteden, K.V., An, Z.S., Nugteren, G., Vandenberghe, J., 1999. East Asian winter monsoon changes on millennial time scale before the last glacial–interglacial cycle. J. Quat. Sci., 14, 101–111.

Lu, H.Y., Zhang, F., Liu, X.D., 2002. Patterns and frequencies of the East Asian winter monsoon variations during the past million years revealed by wavelet and spectral analyses. Global and Planetary Change, 35 (1–2), 67–74.

Maher, B.A., 1986. Characterization of soils by mineral magnetic measurements. Physics of Earth and Planetary Interiors, 42, 76–92.

Maher, B.A., 1988. Magnetic properties of some synthetic sub-micron magnetites. Geophysical Journal of Royal Astronomical Society, 94, 84–96.

Maher, B. A., 2011. The magnetic properties of Quaternary aeolian dusts and sediments, and their palaeoclimatic significance, Aeolian Research, 3, 87–144.

Maher, B.A., and Taylor, R.H., 1988. Formation of ultrafine-grained magnetite in soils. Nature, 336, 368–370.

Maher, B.A. and Thompson, R., 1991. Mineral magnetic record of the Chinese loess and paleosols. Geology, 19(1), 3–6.

Maher, B.A. and Thompson, R., 1992. Paleoclimatic significance of the mineral magnetic record of the Chinese loess and paleosols, Quaternary Res., 37, 155–170.

Maher, B.A., Thompson, R., Zhou, L.P., 1994. Spatial and temporal reconstructions of changes in the Asian paleomonsoon: a new mineral magnetic approach. Earth Planet. Sci. Lett., 44, 383–391.

McElhinny, M.W., 1973. Paleomagnetism and plate tectonics. Cambridge University Press, London. pp. 358.

McDermott, F., 2004. Palaeo-climate reconstruction from stable isotope variations in speleothems: a review. Quaternary Science Reviews, 23(7), 901–918.

Milankovitch, M., 1930. Mathematische klimalehre und astronomie theorie der klimaschwankungen. In: Ko¨ppen W and Geiger R (eds.) Handbuch der Klimatologie, vol. I(A), 1–176. Berlin: Gebru¨der Borntraeger.

Murakami, M., Hirose, K., Kawamura, K. Sato, N., Ohishi, Y., 2004. Post-perovskite phase transition in MgSiO3. Science, 304, 855–858.

Nagata, T., Arai, Y., Momose, K., 1963. Secular variation of the geomagnetic total force during the last 5000 years. Journal of Geophysical Research, 68, 5277–5281.

Nakagawa, T. and Tackley, P.J., 2004. Effects of a perovskite-post perovskite phase change near core-mantle boundary in compressible mantle convection. Geophysical Research Letters, 31(16).

Oganov, A. R. and Ono, S., 2004. Theoretical and experimental evidence for a post-perovskite phase of MgSiO3 in Earth's D" layer. Nature 430, 445–448.

Oldfield, F., 1991. Environmental magnetism- a personal perspective. Quaternary Science Reviews, 10, 73–85.

Oldfield, F., Walden, J. and Smith, J., 1999. Environmental magnetism: a practical guide. Quaternary Research Association, no. 6.

Olson, P., 2003. Thermal interaction of the core and mantle. In: Jones, C.A., Soward, A.M., Zhang, K. (Eds.), Earth's Core and Lower Mantle. Taylor and Francis, London and New York, 218.

Olson, P. L., Coe, R. S., Driscoll, P. E., Glatzmaier, G. A. & Roberts, P. H., 2010. Geodynamo reversal frequency and heterogeneous core-mantle boundary heat flow. Phys. Earth Planet. Inter. 180, 66–79.

Olson, P., Deguen, R., Hinnov, L. A., and Zhong, S., 2013. Controls on geomagnetic reversals and core evolution by mantle convection in the Phanerozoic. Physics of the Earth and Planetary Interiors, 214, 87–103.

Oorschot, I.H.M.V., 2002. Chemical distinction between lithogenic and pedogenic iron oxides in environmental magnetism: a search for the perfect solution. Universiteit Utrecht.

Opdyke, N.D., and Channell, 1996. Magnetic stratigraphy. Academic Press, San Diego, California. pp. 341.

Parés, J.M., PÉREZ-GONZÁLEZ, A., Arsuaga, J.L., Bermúdez de Castro, J.M., Carbonell, E. and Ortega, A.I., 2010. Characterizing the sedimentary history of cave deposits, using archaeomagnetism and rock magnetism, Atapuerca (Northern Spain). Archaeometry, 52(5), 882–898.

Paulsen, D.E., Li, H.C., and Ku, T.L., 2003. Climate variability in central China over the last 1270 years revealed by high-resolution stalagmite records. Quaternary Sci. Rev., 22, 691–701.

Porter, S.C., and An, Z., 1995. Correlation between climate events in the North Atlantic and China during the last glaciation. Nature, 375, 305–308.

Prévot, M., El_Messaoud Derder, M., McWilliams, M., Thompson, J., 1990. Intensity of the Earth's magnetic field: evidence for a mesozoic dipole low. Earth Planet. Sci. Lett., 97, 129–139.

Prins, M.A., Vriend, M., Nugteren, G., Vandenberghe, J., Lu, H.Y., Zheng, H.B., Ao, H., Dong, J.B., Weltje, G.J., 2007. Late Quaternary Aeolian dust input variability on the Chinese Loess Plateau: inferences from unmixing of loess grain-size records. Quat. Sci. Rev., 26, 230–242.

Pye, K., 1984. Loess. Prog. Phys. Geogr., 8, 176–217.

Pye, K., 1987. Aeolian Dust and Dust Deposits. Academic Press, London.

Shindell, D.T., Schmidt, G.A., Miller, R.L. and Mann, M.E., 2003. Volcanic and solar forcing of climate change during the preindustrial era. Journal of Climate, 16(24), 4094-4107.

Sroubek, P., Diehl, J.F., Kadlec, J. and Valoch, K., 2001. A Late Pleistocene palaeoclimate record based on mineral magnetic properties of the entrance facies sediments of Kulna Cave, Czech Republic. Geophysical Journal International, 147(2), 247–262.

Šroubek, P., Diehl, J.F. and Kadlec, J., 2007. Historical climatic record from flood sediments deposited in the interior of Spirálka Cave, Czech Republic. Palaeogeography, Palaeoclimatology, Palaeoecology, 251(3), 547–562.

Sun, D.H., Liu, T.S., Cheng, M.Y., An, Z., Shaw, J., 1997. Magnetostratigraphy and paleoclimate of Red Clay sequences from the Chinese Loess Plateau. Sci. China, Ser., D 40, 337–343.

Sun, D.H., An, Z.S., Shaw, J., Bloemendal, J., Sun, Y.B., 1998. Magnetostratigraphy and paleoclimatic significance of Late Tertiary aeolian sequences in the Chinese Loess Plateau. Geophysical Journal International, 134, 207–212.

Sun, Y., Lu, H. and An, Z., 2006a. Grain size of loess, palaeosol and Red Clay deposits on the Chinese Loess Plateau: Significance for understanding pedogenic alteration and palaeomonsoon evolution. Palaeogeography, Palaeoclimatology, Palaeoecology, 241(1), 129–138.

Sun, Y., Clemens, S.C., An, Z., and Yu, Z., 2006b. Astronomical timescale and palaeoclimatic implications of stacked 3.6-Myr monsoon records from the Chinese Loess Plateau. Quaternary Science Reviews, 25, 33–48.

Takafuji, N., Hirose, K., Mitome, M., Bando, Y., 2005. Solubilities of O and Si in liquid iron in equilibrium with (Mg,Fe)SiO3 perovskite and the light elements in the core. Geophysical Research Letters 32: L06313.

Takahashi, F., Matsushima, M., Honkura, Y., 2005. Simulations of a quasi-Taylor state geomagnetic field including polarity reversals on the Earth Simulator. Science 309, 459–461.

Tauxe, L., 2002. Paleomagnetism Principles and Practice. Kluwer Academic Publishers, The Netherlands, pp. 299.

Tauxe, L., Butler, R., Banerjee, S.K., van der Voo, R., 2008. Essentials of Rock and Paleomagnetism. University of California Press, USA, pp. 509.

Tauxe, L, Banerjee, S.K., Butler, R.F. and van der Voo, R., 2014. Essentials of Paleomagnetism, 2nd Web Edition, University of California Press, USA.

Thellier, E., 1941. Sur la vérification d'une method permattant de determiner l'intensité du champ terrestre dans le Passé. C.R. Hebd. Seances Acad. Sci., 212, 281–283.

Thellier, E., and Thellier, O., 1959. Sur l'intensité du champ magnétique terrestre dans le passé historique et géologique, Annales Geophysicae, 15, 285–376.

Thompson, P., Schwarcz, H.P., Ford, D.C., 1974. Continental Pleistocene climatic variations from speleothem age and isotopic data. Science, 184, 893–894.

Thompson, R., and Oldfield, F., 1986. Environmental Magnetism, Allen and Unwin, London.

Thompson, R., Bloemendal, J., Dearing, J. A., Oldfield, F., Rummery, T. A., Stober, J.C., and Turner, G. M., 1980. Environmental applications of Magnetic minerals. Science, 207, 481–485.

Tsuchiya, T., Tsuchiya, J., Umemoto, K. and Wentzcovitch, R.M., 2004. Phase transition in MgSiO3 perovskite in the Earth's lower mantle. Earth and Planetary Science Letters, 224(3), 241-248.

Valet, J.P., 2003. Time variations in geomagnetic intensity. Reviews of Geophysics, 44: 4-1, 4–44.

Vandenberghe, J., An, Z.S., Nugtern, G., Lu, H.Y., Huissteden, K.V., 1997. New absolute time scale for the Quaternary climate in the Chinese loess region by grain-size analysis. Geology, 25, 35–38.

Vandenberghe, J., Lu, H.Y., Sun, D.H., Huisseden, K.V., Konert, M., 2004. The late Miocene and Pliocene climate in East Asia as recorded by grain size and magnetic susceptibility of the Red Clay deposits (Chinese Loess Plateau). Palaeogeogr. Palaeoclimatol. Palaeoecol., 204, 239–255.

Verosub, K. L. and Roberts, A. P., 1995. Environmental magnetism: Past, present, and future. Jour. Geophys. Res., 100, 2175–2192.

Vine, F. J. and Matthews, D. H., 1963. Magnetic anomalies over oceanic ridges. Nature, 199, 947–949.

Wang, Y.J., Cheng, H., Edwards, R.L., An, Z.S., Wu, J.Y., Shen, C.C., Dorale, J.A., 2001. A high-resolution absolute-dated late Pleistocene monsoon record from Hulu Cave, China. Science, 294, 2345–2348.

White, W.B., 2007. Cave sediments and paleoclimate. Journal of Cave and Karst studies, 69(1), 76–93.

Xiao, J., Porter, S.C., An, Z., Kumai, H., Yoshikawa, S., 1995. Grain size of quartz as an indicator of winter monsoon strength on the loess plateau of central China during the last 130,000 yr. Quat. Res., 43, 22–29.

Xu, T.C., and Liu, T.S., 1994. Implication of the magnetic susceptibility curve fromthe Chinese loess profile at Xifeng. Quaternary Science Reviews, 12, 249–254.

Zijderveld, J.D.A., 1967. A.C. demagnetization of rocks, analysis of results. In: Methods in paleomagnetism, D.W. Collinson, K.M. Creer, and S.K. Runcorn, eds. Elsevier, Amsterdam, 254–286.

Zhang, X.Y., Arimoto, R., An, Z.S., 1999. Glacial and interglacial patterns for Asian dust transport. Quat. Sci. Rev., 18, 811–819.

Zhou, L.P., Oldfield, F., Wintle, A.G., Robinson, S.G., and Wang, J.T., 1990. Partly pedogenic origin of magnetic variations in Chinese loess. Nature, 346, 737–739.

Chapter 2[*]

Magneto- and cyclostratigraphy in the red clay sequence: new age model and paleoclimatic implication for the eastern Chinese Loess Plateau

2.1 Introduction

The Chinese Loess Plateau contains a loess-paleosol sequence underlain by red clay. As this red clay went through strong pedogenic processes and oxidation while depositing in a more humid and warmer climate compared to that of upper Quaternary loess and paleosol, it is more reddish in color. Both the red clay and loess-paleosol sequences show common magnetic mineralogy containing magnetite, maghemite, and hematite (Liu et al., 2003). The Quaternary loess-paleosol sequence in China is being extensively studied to determine paleoclimate variations (Lu, 1981; Kukla et al., 1990; An et al., 1990; Xu and Liu, 1994; Ding et al., 1994; Van Huissteden et al., 1997; Lu et al., 2002). The red clay sequence has been investigated to understand the earlier paleomonsoon evolution (Liu, 1985) and paleoclimatic history of the Pliocene and Miocene epochs (Liu et al., 2003). The absence of abundant fossils and inability of radiometric dating methods to date the red clay sequences made magnetostratigraphy a leading method to build age models (Vandenberghe et al., 2004; Sun et al., 2006; Nie et al., 2008; Sun et al., 2010). At the same time, magnetostratigraphy dating based on usually subjective correlation of the normal and reverse polarity intervals with the Geomagnetic Polarity Time Scale (GPTS) could potentially lead to erroneous age models. Testing magnetostratigraphy models in red clay sequences could be done using cyclostratigraphy as orbital parameters of the Earth (the 18–24 kyr precession, 40

---

[*] A version of this chapter has been published as: Anwar, T., Kravchinsky, V.A., and Zhang, R., 2015. Magneto-and cyclostratigraphy in the red clay sequence: new age model and paleoclimatic implication for the eastern Chinese Loess Plateau. Journal of Geophysical Research: Solid Earth, 120(10), 6758-6770.

kyr obliquity, and 95–125 kyr and 405 kyr eccentricity) are known accurately for the last 50 million years (Laskar et al., 2004, 2011). In our study we perform such testing on red clay and demonstrate that magnetostratigraphy alone could lead to dramatically different and possibly inadequate outcomes. We use cyclostratigraphy in order to establish the proper magnetostratigraphic age model for the red clay.

In order to perform cyclostratigraphy analysis we looked for the presence of Milankovitch periodicities recorded in the well-preserved red clay deposits at Shilou on the Loess Plateau in eastern China by analyzing the magnetic susceptibility and grain size data from Xu et al. (2009), which were reported but not processed. The red clay sequences on the eastern CLP are generally younger than 8.5 Ma (Song et al., 2007; Qiang et al., 2011), with the exception of the studied Shilou section.

Preserved orbital frequencies can be used to predict present and future climate variations in the global climate system. For example, magnetostratigraphy and rock magnetic cyclostratigraphy together have already been used in Eocene marine marls to establish chronostratigraphy (Kodama et al., 2010; Kodama and Hinnov, 2014). We used both the magnetic susceptibility and grain size as paleoclimate proxy parameters as suggested in Kukla et al. (1988), Liu (1985), Ding et al. (1994), Xiao et al. (1995), and others. The red clay shows gradual changes in light reddish color and pedogenic structures from lower to upper parts and variations in magnetic susceptibility (Sun et al., 1997). Xu et al. (2009) used a visual correlation between normal/reverse polarity intervals and the Geomagnetic Polarity Time Scale to conclude that this section is 11 million years old. Our spectral analyses of magnetic susceptibility and grain size records using the depth-age relationship from Xu et al. (2009) uncovered unreasonably large periodicities that did not correspond to Milankovitch cycles. An age model built on the basis of magnetostratigraphy alone might be incompatible to evaluate Milankovitch cycles recorded in the red clay deposit. The continuous sequence alternations of sedimentary cycles in the red clay are related to climate variations caused by Earth's orbital parameters. As the analysis of climatic variation depends mostly on the age of the red clay, we looked for a technique that would allow us to determine the precise age of the red clay. We used cyclostratigraphy to construct a new magnetostratigraphic age model assuming that Milankovitch cycles may be found through correction of the correlation between magnetic polarity patterns and the GPTS (Cande and Kent, 1995). Paleoclimatic evolution during the period of Shilou red clay deposits was also reanalyzed using magnetic susceptibility values and a grain size index. We further demonstrate that a combined technique of magnetostratigraphy and cyclostratigraphy could become a standard tool for evaluating the age from red clay sections where fossils are rare.

2.2 Geological Setting and Stratigraphy

The Shilou red clay profile is situated ~15 km northwest of Shilou County in Shanxi Province, China. It is located on the eastern edge of the Loess Plateau and bounded by the Lüliang Mountains in the east and the Yellow River in the west (Figure 2.1). The whole Shilou red clay sequence is about 72 m thick. The top 69.4 m is sampled, whereas the bottom 2–3 m is under water and has not been investigated (Xu et al., 2009). The Shilou red clay profile contains 2.8 m of Quaternary loess-paleosol sequence and 69.2 m of red clay. In general, the red clay is composed of reddish soils and calcareous nodules and displays stronger pedogenic weathering than the Quaternary loess-paleosol. The lower part of the red clay deposit is lighter in color than the upper part. Within the whole profile, 73 red clay and carbonate nodule couplets were identified in Xu et al. (2009). Normally, paleosol layers are accompanied by a carbonate nodule horizon in the red clay. In the Shilou sequence, some paleosol layers may not have carbonate nodules between them. Xu et al. (2009) observed that some carbonate nodules melded, making the section boundaries indistinguishable.

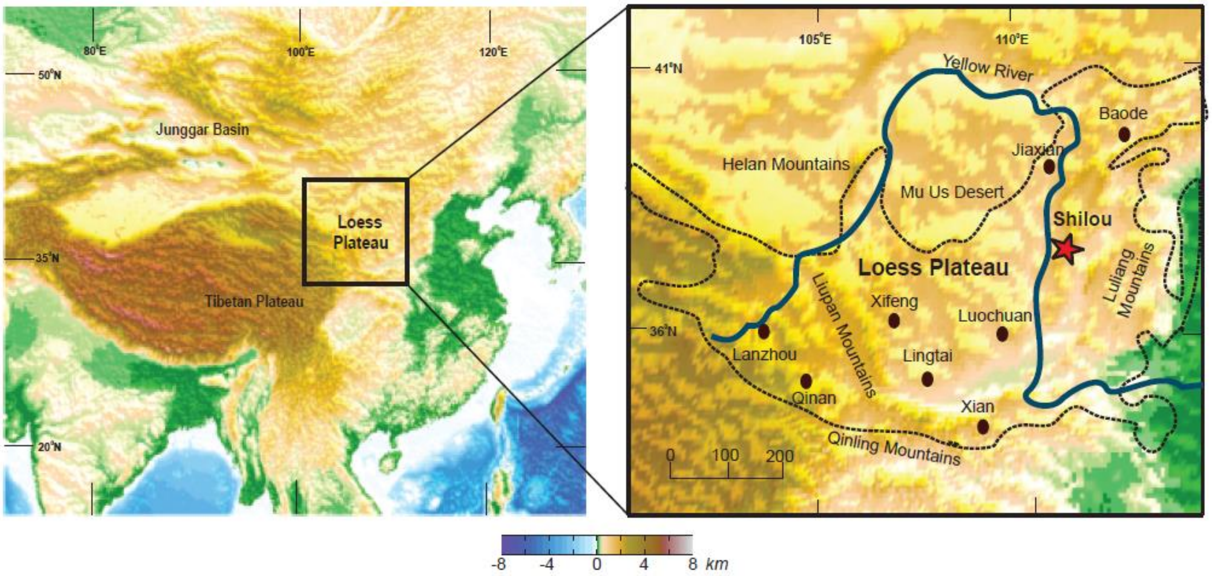

Figure 2.1. Geographic location of the Shilou red clay section in China. Dashed contour indicates the extent of the Chinese Loess Plateau.

Xu et al. (2009) originally defined the stratigraphic structure of this area in two units. Later, four stratigraphic parts were proposed for the whole section (Xu et al., 2012), and it was shown that the second and third parts had similar characteristics with weakly developed soil character. In our study, the Shilou red clay profile is divided into three units (Figure 2.2) according to lithological characteristics. Unit 1 (2.8 m to 28.5 m) of the Shilou red clay profile consists of dark reddish brown clay with carbonate nodule horizons and abundant Fe–Mn coatings. The color and soil structure of unit 1 indicate that it was subject to the strongest pedogenesis. Unit 2

(28.5 to 42.4 m) is light reddish brown with weakly developed soil and displays weaker pedogenesis than the overlying unit. Unit 3 (42.4 m to the bottom) is more reddish with stronger pedogenic features compared to unit 2 (Figure 2.2).

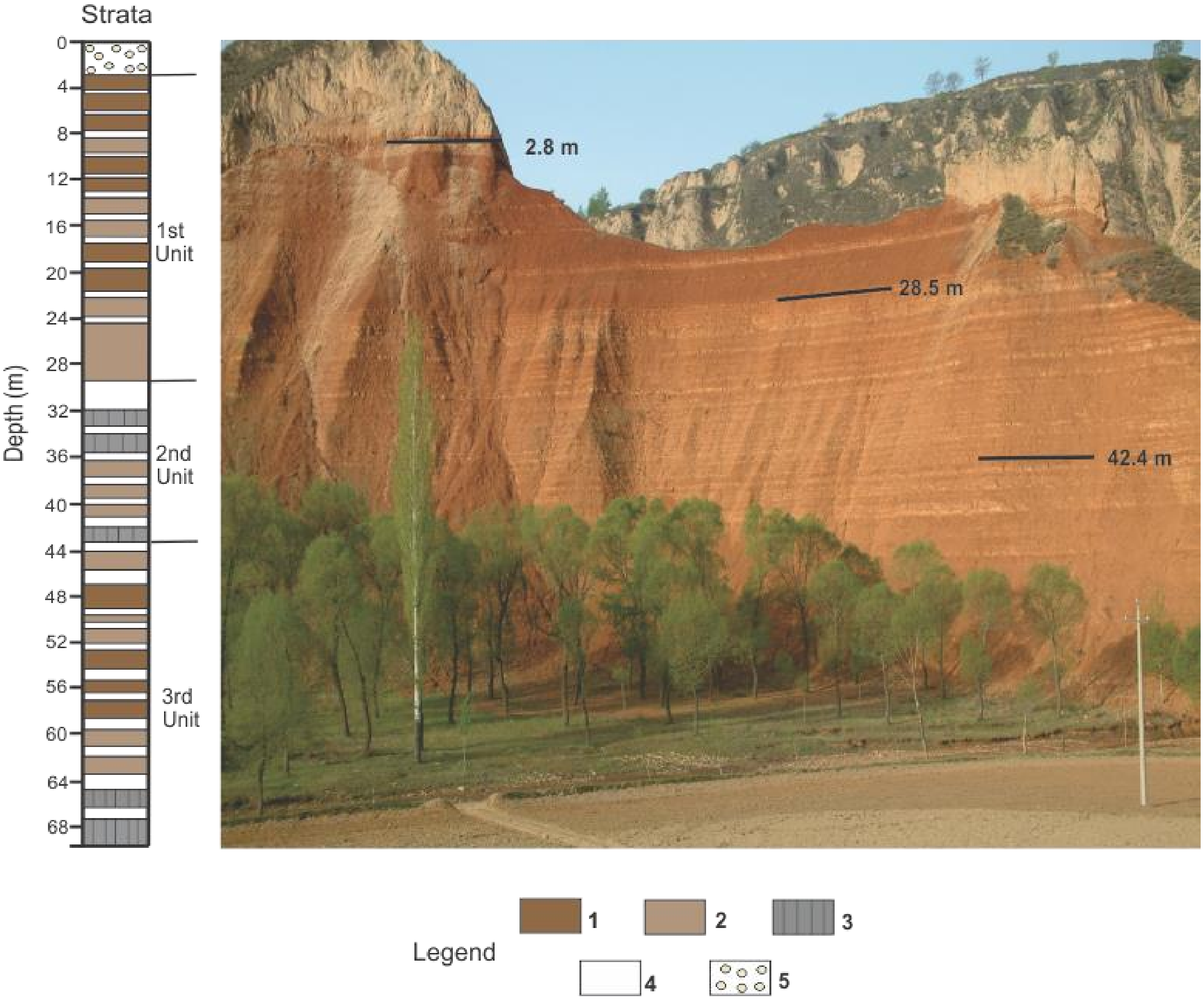

Figure 2.2. Stratigraphic feature (left) and field characteristics (right) denoting three different units of lithological record in the Shilou red clay deposit. Legend: 1—red clay with strong pedogenesis, 2—red clay with medial pedogenesis, 3—red clay with weak pedogenesis, 4—carbonatenodules, 5—loess. Photo courtesy of Yong Xu.

2.3 Methods

2.3.1 Sampling and Measurements

In our analysis we used a combination of the data from Xu et al. (2009) and our own data from the samples kindly provided by Y. Xu and L. Yue. Overall the paleomagnetic samples were taken at intervals of 20 cm. Oriented block hand samples were cut into 2×2×2 cm^3 cubic specimens. All the cubic specimens were demagnetized using a MMTD80 thermal demagnetizer and measured using a JR-6A spinner magnetometer in the State Key Laboratory of Continental Dynamic (Department of Geology, Northwest University, Xi'an, China). Both the demagnetizer and magnetometer are housed in a field free space (<300 nT) to avoid any viscous magnetization during laboratory procedure. A few (50) pilot samples were additionally measured in the paleomagnetic laboratory of University of Alberta (Canada) using 2 G cryogenic magnetometer and ASC furnace hosted in the permalloy room with the residual field <8 nT. Thermal demagnetization was applied using a 20–50°C increment from room temperature to 600°C or 680°C. Comparison of the sister sample results from both labs demonstrated strong agreement. Representative orthogonal vector diagrams for normal and reversed samples are shown in Figure 2.3. It is evident that all samples possess two magnetic components. The first was unblocked at low temperatures, generally ranging from room temperature to about 300°C. The direction of this component is consistent with the present-day field, and is thought to be a viscous overprint. After removal of the low-temperature component, the direction became stable and the vector decayed toward the origin on the orthogonal diagrams. The principal component direction was computed using least squares fitting technique (Kirschvink 1980) for selected demagnetization data points (minimum of three, but mostly five to eight).

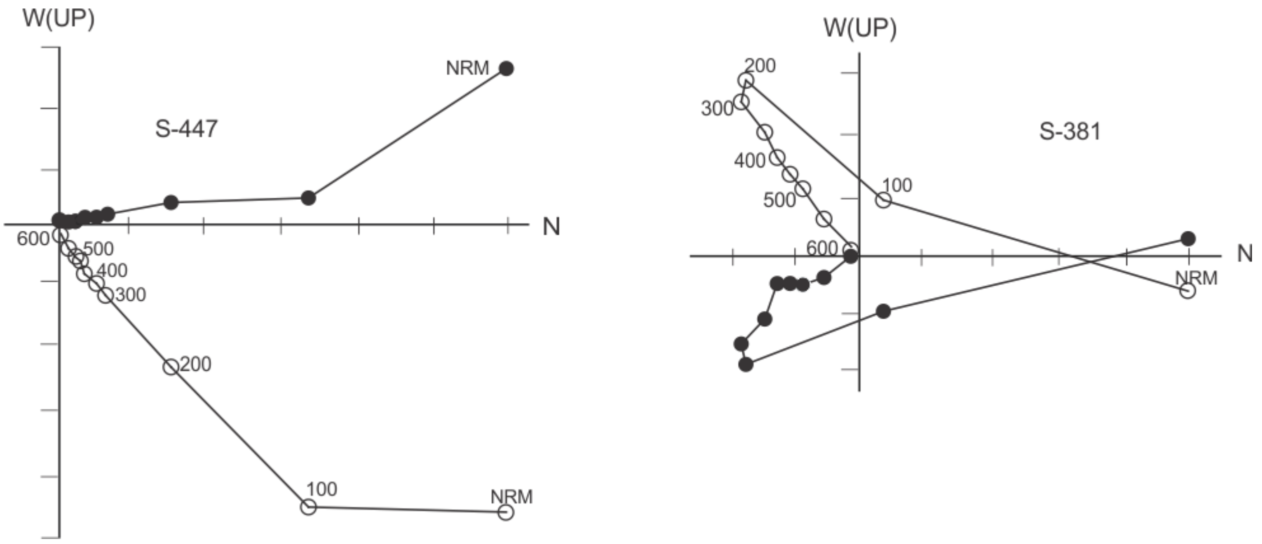

Figure 2.3. Orthogonal vector projections of stepwise thermal demagnetization of natural remanent magnetization for the typical normal and reversed samples. Demagnetization steps are in °C. The solid (open) symbols represent vector endpoints projected onto horizontal (vertical) plane. NRM is the natural remanent magnetization.

Powder samples were collected at intervals of 20 cm along the study section for both magnetic susceptibility and sedimentary grain size analyses. The magnetic susceptibility was measured by the susceptibility meter model-942, and the grain size was analyzed on a Mastersizer 2000 laser particle analyzer at Northwest University. The treatment procedure was identical to Xu et al. (2009, 2012). Before the measurements, the grain size samples were subjected to standard chemical pretreatment for red clays. Powder samples of 0.3–0.4 g were fully dissolved in 10 ml of 10% boiling hydrogen peroxide (H_2O_2) solution in a 200 ml beaker to remove the organic material components. The carbonates were also removed by boiling with 10 ml of 10% hydrochloric acid (HCl). To avoid drying of the solution, distilled water was added during the chemical treatment. Sample solution was then diluted with distilled water, and after standing overnight, the clear water was decanted from the sample. Dispersion of the components was done by adding 10 ml of 10% sodium hexametaphosphate [$(NaPO_3)_6$] solution and oscillating ultrasonically for about 10 min.

2.3.2 Magnetostratigraphy and Cyclostratigraphy

We reanalyzed both our data and data from Xu et al. (2009), and re-evaluated the magnetic polarity interpretation, applying changes in the previous polarity pattern (Figure 2.4). Some short polarity intervals based on only one sample could be an excursion and were removed from our new analysis. In the GPTS, this short event is not documented. A first-order magnetostratigraphic age model was obtained by correlating the new magnetic polarity results and the geomagnetic polarity time scale (Cande and Kent, 1995). The age of each sampling level for the red clay sequence was estimated by linear interpolation between correlation points of the magnetic polarity boundaries. Magnetic susceptibility and grain size parameters have been proven to be an excellent climate change recorder in the red clay sequences (Xu et al., 2012). Assuming that Milankovitch periodicities are recorded in the red clay record as shown by previous work (Vandenberghe et al., 2004; Sun et al., 2006; Nie et al., 2008; Sun et al., 2010), we tested our first-order magnetostratigraphic age model with cyclostratigraphy.

We performed cyclostratigraphy through spectral analysis of the magnetic susceptibility and grain size time series. If the spectral peaks of the magnetic susceptibility and grain size data sets did not correspond to any Milankovitch periodicities, new correlation between magnetic polarity patterns and the GPTS was made to find new age for the section. An age model based on only visual correlation could result in an inaccurate age model; therefore, we performed an iteration procedure (number of different correlations) for the data. The magnetostratigraphic age model was readjusted in the iterative manner by applying cyclostratigraphy (spectral analysis) for every correlation until the Milankovitch cycles appeared to be resolved in the best possible manner. Once the cycle was well resolved, the correlation of our polarity pattern with the GPTS was confirmed to obtain the final magnetostratigraphic age model. The sedimentation rate was evaluated from the depth-age relationship and checked for each correlation step as the sedimentation rate for red clay is lower than that of loess-paleosol (Sun et al., 1998a; Sun et al., 1998b; Ding et al., 1998; Ding et al., 2001). After trying several possible correlations, only one showed reasonable result for both the cases of Milankovitch cycles and sedimentation rate for the red clay section.

2.3.3 Spectral Analysis

Spectral analysis was performed by applying wavelet analysis to decompose the time series into time-frequency phase space simultaneously. For real-valued geophysical time series, wavelet analysis is more suitable than traditional spectrum analyses because it gives information about the amplitude and variation of amplitude of any periodic signal within the series (Weng and Lau, 1994). This technique is particularly useful for nonstationary time series which are dominated by periodicities that change in time (Torrence and Compo, 1998). Compared to classical Fourier analysis, the wavelet spectrum provides a direct visualization of the changing statistical properties in stochastic processes with time, a major advantage when studying climatic time series (Witt and Schumann, 2005). Besides, Debret et al. (2007) demonstrated the advantage of the wavelet analysis while detecting climatic periodicity. In this study, the modified Matlab code from Torrence and Compo (1998) was applied in order to perform wavelet analysis. The Morlet wavelet and background red noise (at 95% of confidence) were used for the wavelet transform described in Torrence and Compo (1998) and Debret et al. (2007).

2.4 Results and Discussion

2.4.1 A New Age Model for the Shilou Red Clay Sequence

The interface between classical loess and red clay is situated 2.8 m from the top of the plateau; previous studies considered this interface to be the Matuyama-Gauss polarity boundary (Sun et al., 1998b; Qiang et al., 2001; Zhu et al., 2008). In Figure 2.4, the 2.8 m to 27.3 m depth of red clay corresponds to the Gauss normal-polarity chron and the depth from 36.1 m to 69.5 m corresponds to four normal-polarity subchrons C3An.1n, C3An.2n, C3An.3n, and C3An.4n (known as the Gilbert reverse polarity chron). As we described in section 2.3.2, this correlation was executed in the iteration procedure manner until it is supported by cyclostratigraphy, rather than mere visual matching with a number of polarity events. The new total age for the whole Shilou profile, including the classical loess on the top, is 5.2 Ma (Figure 2.4) rather than 11 Ma (Xu et al., 2009). Xu et al. (2012) showed the existence at 46.6 m of a tooth of Meriones sp. which lived in the late Miocene; however, without further evidence, it is conceivable that the tooth was transported to the red clay deposit. In support of our new age model, the age of the upper, dark reddish brown clay part of the Shilou red clay section (unit 1, 2.8 m–28.5 m), named the Jingle Formation by Teilhard and Young (1930, 1931), is 2.58–3.66 million years old, which is similar to the age (2.5–3.4 Ma) of the Jingle Formation in the Hefeng section based on the presence of mammalian fossils (Chen, 1994; Flynn et al., 1997). The new age model is not consistent with the magnetostratigraphic age of the other red clay section in this region such as

Baode red clay section (Zhu et al., 2008). This infers that for the red clay sequences, the age models which were built by visual correlation only should likely be re-evaluated.

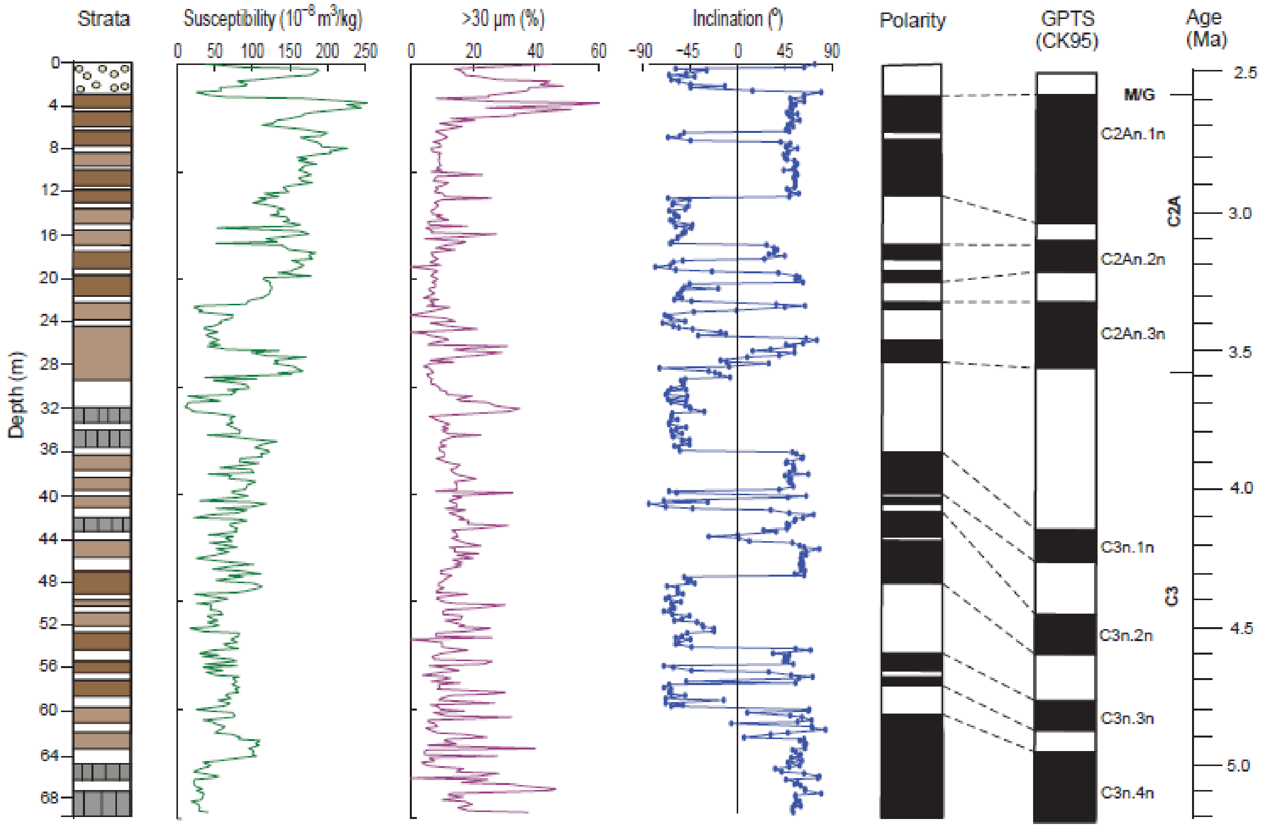

Figure 2.4. Lithostratigraphic characteristics, magnetic susceptibility, coarse fraction (>30 μm) content, inclination as a function of depth, and the new magnetic polarity interpretation of the Shilou red clay section, together with correlation to the standard magnetic polarity scale (Cande and Kent, 1995). The legend is the same as in Figure 2.2.

The age of each sampling level for the red clay sequence was estimated by linear interpolation between correlation points of the magnetic polarity boundaries. The changes in sedimentation rate were obtained from the depth-age relationship (Figure 2.5). The new age model yields an average sedimentation rate of approximately 2.54 cm/kyr versus ~0.8 cm/kyr for the Xu et al.

(2009, 2012) model. The sedimentation rate in the new age model varies from 1 to 4.5 cm/kyr (Figure 2.5), which is less variable than the sedimentation rate in the Xu et al., (2009, 2012) model and is consistent with the average dust depositional rate in other red clay sections located near Xifeng (Sun et al., 1998a), Lingtai (Sun et al., 1998b), Jiaxian (Ding et al., 1998), and Jingchuan (Ding et al., 2001). The fact that our new age model yields an average sedimentation rate comparable to other reported values supports our findings.

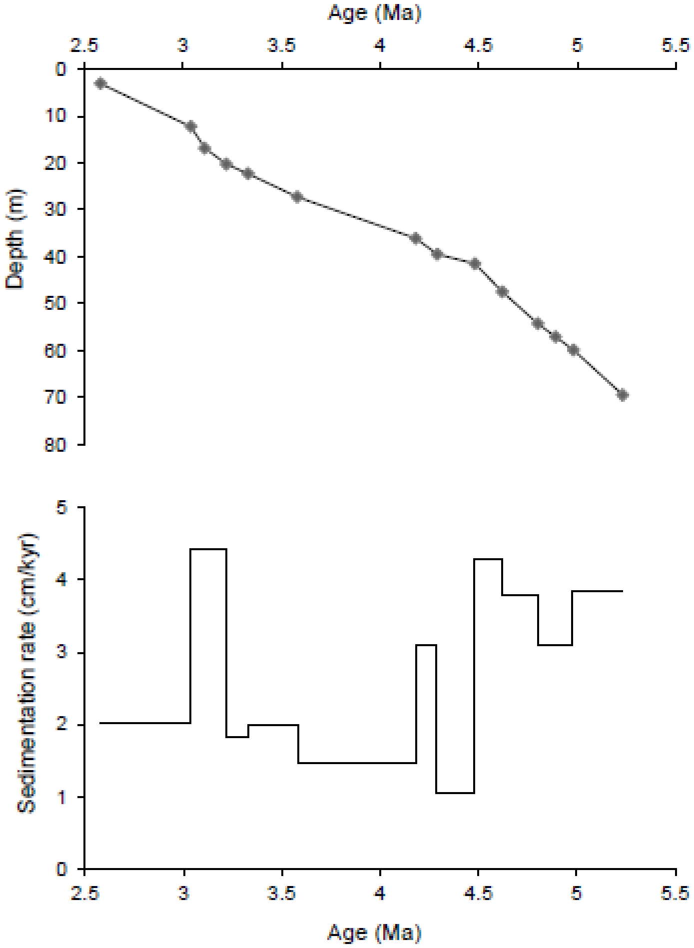

Figure 2.5. Depth-age relation and variation of the sedimentation rate of the Shilou red clay sequence based on magnetostratigraphic correlation.

2.4.2 Paleoclimatic Significance of Magnetic Susceptibility and Grain Size

Magnetic susceptibility and coarse fraction variations in the red clay were used to investigate paleoclimatic evolution. Magnetic mineral content in the Loess Plateau in China is connected to weathering and pedogenic processes. The fine-grained ferrimagnetic particles, such as magnetite and/or maghemite, produced during pedogenesis are the main carriers of the magnetic susceptibility signal (Maher and Thompson, 1991; Zhou et al., 1990; Deng et al., 2005). Since pedogenesis intensity is related to the summer monsoon, the magnetic susceptibility is regarded as a proxy for the summer monsoon (Kukla et al., 1990; An et al., 1991). The coarse fraction content in the loess-paleosol can be used as a proxy for the winter monsoon because it is strongly correlated to the strength of the wind during the winter monsoon (Lu et al., 1997; Lu and An, 1998) and is associated with the wet to dry climate changes in eastern Asia (Lu et al., 2004). The red clay contains the same magnetic minerals as the loess-paleosol sequence and shows a similar positive correlation between pedogenesis and magnetic susceptibility (Liu et al., 2003). Thus, the magnetic susceptibility and grain size of the red clay can be used as climate proxies similar to those of the loess-paleosol (Liu et al., 2003; Vandenberghe et al., 2004; Sun et al., 2010). Unlike the loess-paleosol, the magnetic susceptibility of the red clay increases from bottom to top. That is, the upper layers of red clay with higher clay content presented higher values of magnetic susceptibility than lower layers that were higher in silt content and brownish in color. In general, lower magnetic susceptibility and higher coarse grain size indicate winter monsoon intensification, whereas higher magnetic susceptibility and fine grain size suggest summer monsoon conditions.

The magnetic susceptibility and grain size data used in this study were obtained in coordination with the group from the Northwest University in Xi'an; a section from Xu et al. (2009) was re-evaluated. Magnetic susceptibility and grain size measurements are spaced at 20 cm sampling intervals. Xu et al. (2012) showed that the coarse fraction (>30 μm) content and median grain size of the section exhibited similar shape curves. Figure 2.4 shows the record of magnetic susceptibility and coarse fraction content (>30 μm) versus depth in the studied section. The magnetic susceptibility rises gradually from lower to upper parts of the section. The coarse fraction (>30 μm) content curve represents almost 10% of the whole Shilou red clay deposit (Figure 2.4). The time series of magnetic susceptibility and coarse fraction (>30 μm) content (Figure 2.6) was determined by assigning a time to each depth from the depth-age relationship (Figure 2.5). The time series of magnetic susceptibility and coarse fraction (>30 μm) content in the red clay section at Shilou corresponds to climatic variations from 2.58 to 5.2 Ma. Three stages of lithology comprising magnetic susceptibility and coarse fraction variation can be recognized during this period (Figure 2.6).

The first stage, 2.58–3.66 Ma, is characterized by an increase in magnetic susceptibility amplitude and a decrease in coarse fraction content, indicating a relative intensification of the summer monsoon in the upper part of the red clay section (Figure 2.6). It is theorized that the northern and eastern margins of the Tibetan Plateau began to rise about 3.6 Ma (Li, 1991; Liu et al., 1996; Li and Fang, 1999; An et al., 1999, 2001; Pan, 1999; Shi et al., 1999; Zheng et al., 2000; Song et al., 2001; Lu et al., 2001; Tang et al., 2003; Pan et al., 2004). The uplift in the Tibetan Plateau that began approximately 3.6 Ma might have caused abrupt ecological shifts by 3.7 Ma, strengthening the East Asian summer monsoon from that period onward (Li et al., 1997;

An et al., 2001; Guo et al., 2004; Wang et al., 2006). Simultaneous intensification of both summer and winter monsoons can be found about 2.6–3.6 Ma (An et al., 2001; Wan et al., 2006). Thus, independent paleoclimatic findings point to a reinforcement of the East Asian monsoon 2.5–3.6 Ma (Qiang et al., 2001; An et al., 2001; Wehausen and Brumsack, 2002; Tian et al., 2004a; Hess and Kuhnt, 2005), and the lithology evidence presented here supports this conclusion.

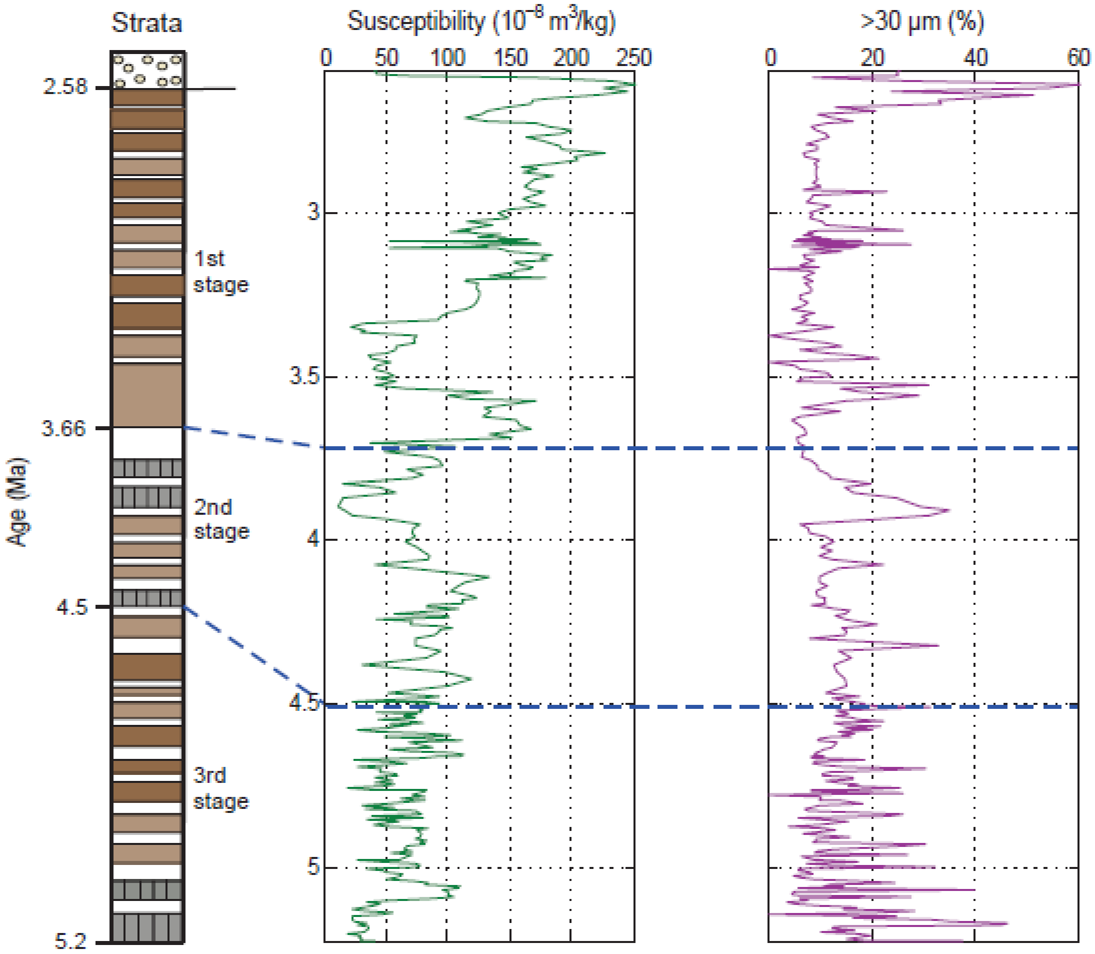

Figure 2.6. Stratigraphic characteristics and correlation of the time series of magnetic susceptibility and coarse fraction (>30 μm) content of the Shilou red clay section on eastern Chinese Loess Plateau during the interval of 2.58–5.2 Ma. Blue lines indicate that the climate evolution can be divided into three stages: 2.58–3.66 Ma, 3.66–4.5 Ma and 4.5–5.2 Ma. The legend is the same as in Figure 2.2.

In the second stage, 3.66–4.5 Ma, the magnetic susceptibility decreases and the coarse fraction content presents high peaks that reflect an intensification of the winter monsoon and aridification in Asia (Figure 2.6). A recent study reported prominent drying in the Loess Plateau in China from 3.7 to 4.5 Ma and proposed that high latitude cooling played a role in the regional climate change (Wang et al., 2006). A climate shift in 3.7 to 4.5 Ma was investigated in ice-rafting information from the North Atlantic (Jansen and Sjøholm, 1991) and the North Pacific (deMenocal, 1993). The closing of the Panamanian Isthmus at ~4.5 Ma and the Indonesia Seaway before 4 Ma might have initiated reform of global climate patterns (Janecek and Rea, 1983; Haug and Tiedemann, 1998; Driscoll and Haug, 1998; Rea et al., 1998) and, hence, accelerating global cooling and the subsequent growth of the ice sheets (Cane and Molnar, 2001).

In the third stage, 4.5 to 5.2 Ma, the susceptibility and coarse fraction content represent variations of remarkably high frequency and large amplitude (Figure 2.6). This behavior suggests that summer and winter monsoon cycles altered rapidly during this period. Atmospheric circulation and environmental changes in eastern Asia could be affected significantly by the uplift of the Tibetan Plateau (Ruddiman and Kutzbach, 1989; An et al., 2001; Guo et al., 2002, 2004; Wang et al., 2005). The climate shift at 4.5 Ma might have occurred due to the uplift of the Tibetan Plateau around that time (Zheng et al., 2000), and it plays an important role in the aridification of Asia (Wang et al., 2006). Research indicates a climate shift at this time for other sections of the Loess Plateau in China. Chemical weathering intensity declines in the Lingtai red clay section at 4.5 Ma (Guo et al., 1999), and the degree of pedogenesis decreases in the Xunyi red clay sequence at ~4.2 Ma (Xue and Zhao, 2003). Terrestrial snail fossil accumulations suggest that the climate became increasingly drier around 4.5 Ma (Pei et al., 2004). Again, the North Pacific dust flux, used as a proxy for the aridification of Asia, gradually increased from 4.5 Ma (Rea et al., 1998). Thus, all the above evidences support our data in three different time periods and their connection to climate changes.

2.4.3 Paleoclimatic Periodicities in Red Clay Sequence

Climatic history is recorded in cycles that can be explained by the Milankovitch theory of orbital forcing. Various sediment properties, such as grain sizes, coarse fraction content, and magnetic susceptibility, are influenced by orbital changes of the Earth, i.e., Milankovitch cycles (Imbrie et al., 1984; Shackleton et al., 1990; Kravchinsky et al., 2003; Laskar et al., 2004, 2011). Spectral analyses of the time series of magnetic susceptibility and coarse fraction (>30 μm) content were performed to evaluate climatic periodicities preserved in the red clay section of the Loess Plateau in China. Climatic proxies (magnetic susceptibility for the summer monsoon and coarse fraction content for the winter monsoon) exhibited variations in response to Earth's orbital forcing with time and space.

In Figure 2.7, wavelet power spectra from 2.58 to 5.2 Ma are shown for magnetic susceptibility and grain size. Coarse fraction content, a proxy for the winter monsoon and therefore less sensitive to pedogenesis, and magnetic susceptibility show consistent orbital evolution during this period. A 400 kyr cycle is visible with high power in the susceptibility and coarse fraction content spectrum between 2.58 and 4.5 Ma. A 100 kyr eccentricity band is noticeable during 3–4.5 Ma for magnetic susceptibility, whereas it is present from 3.5 to 4.5 Ma for coarse fraction content and oscillates significantly. A relatively lower amplitude 100 kyr band, which may be periodically shifted due to the frequency modulation by the 400 kyr cycle, is observable during 4.5–5.2 Ma (Figure 2.7). A possibility of such modulation is described in Rial (1999). The 100 kyr cycle is mostly found at 95 to 125 kyr according to the theoretical models of Laskar et al. (2004). Both magnetic susceptibility and coarse fraction show high amplitude at approximately 200 kyr which could be a harmonic to 95 and 125 kyr cycles. Strong 400 kyr and weak 100 kyr bands were reported for the Lingtai red clay section over the interval 2.6–3.4 Ma (Sun et al., 2006) and for the Chaona red clay section during 2–4 Ma (Nie et al., 2008). Therefore, we investigated three different orbital variation imprints in the climatic signals. Between 2.58 and 3.5 Ma, Earth's long eccentricity 400 kyr cycle is prominent in Figure 2.7. The strong 400 kyr eccentricity, in combination with the 100 kyr eccentricity cycle, is present in the interval 3.5–4.5 Ma. During 4.5–5.2 Ma, records have a weak 100 kyr variability that is shifted significantly (Figure 2.7). This study demonstrates that the frequency of climate cycles is correlated with paleomonsoon evolution as well as with lithological features.

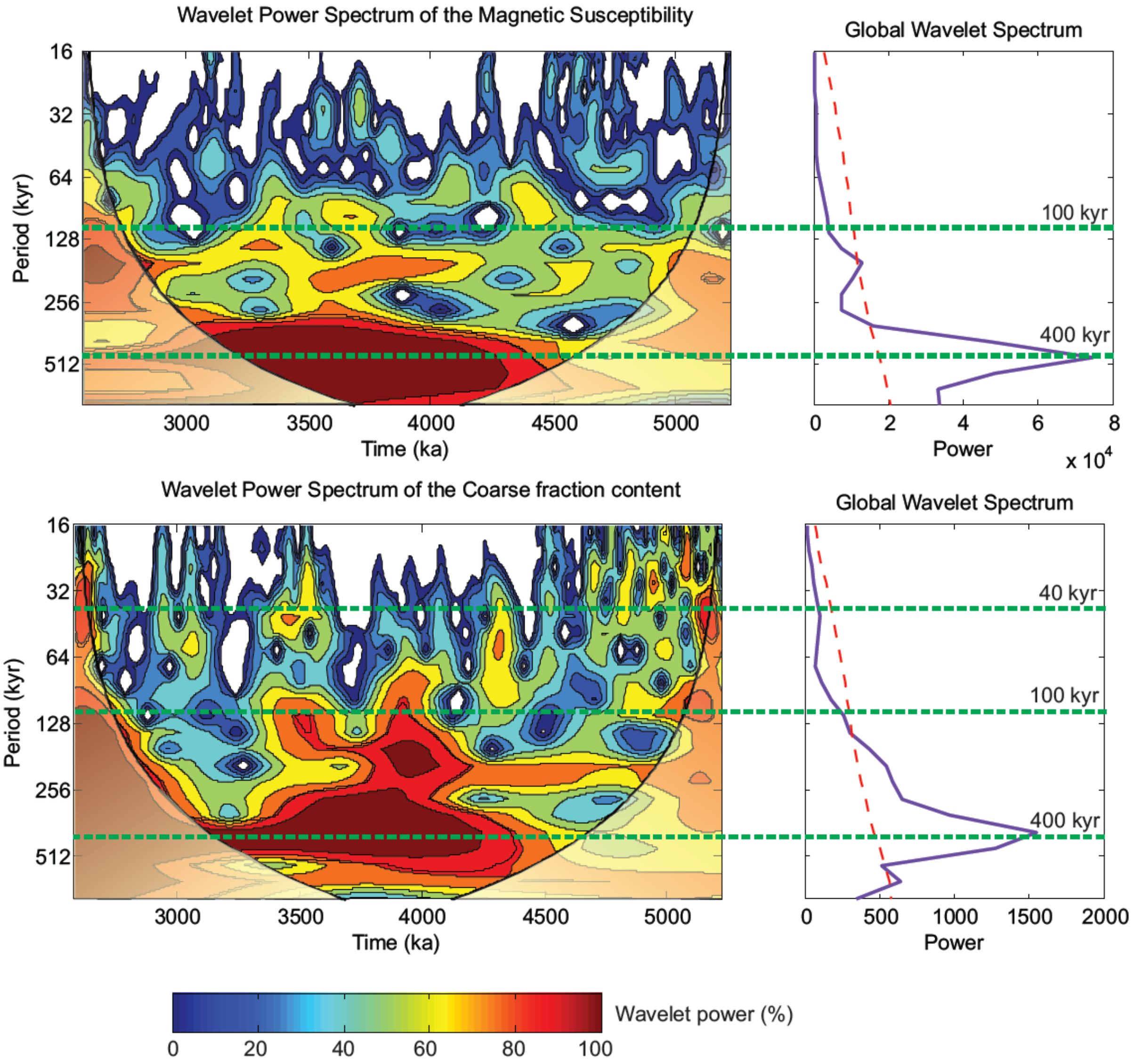

Figure 2.7. Wavelet analysis of the magnetic susceptibility (top) and coarse fraction (> 30 µm) content (bottom) between 2.58 and 5.2 Ma. The color bars correspond to wavelet power. The thick black line denotes a 5% significance level, the thin black contour shows the cone of influence, and green dashed lines represent known Milankovitch periodicities. A Fourier power spectrum is shown to the right. The red dashed line is the mean red noise spectrum (a lag of 0.45 for magnetic susceptibility and 0.5 for coarse fraction content).

In both the magnetic susceptibility and coarse fraction content series, force from Earth's 400 kyr orbital eccentricity cycle predominates because the eccentricity-related variance at 400 kyr is very strong during both summer and winter monsoons (Nie et al., 2008). Similar results were obtained from benthic oxygen isotope data for the same age (Clemens and Tiedemann, 1997; Kashiwaya et al., 2003). Magnetic susceptibility data suggest that intensified soil formation due to the severe penetration of pedogenesis creates a gradual but continual appearance of 400 kyr eccentricity cycles, whereas obliquity, precession, and 100 kyr eccentricity cycles are dampened during warmer periods (Nie et al., 2008). The Tibetan Plateau uplift could also have intensified the 400 kyr cycle in the paleoclimatic record (Nie et al., 2008). For most of the latitude, the 400 kyr cycle can be explained as an eccentricity modulated precession signal (Schwarzacher and Fischer, 1982; Clemens and Tiedemann, 1997; Hinnov, 2000; Weedon, 2003). From 3.5–4.5 Ma, our data show climatic variations with periods of 400 and 100 kyr eccentricity and winter monsoon intensification. During this period (3.5–4.5 Ma), aridification was intensified in Asia by the tectonic uplift in the northern and northeastern Tibetan Plateau. The 100 kyr cycle becomes strong only after 0.6 Ma and is negligible prior to 3.5 Ma according to planktonic oxygen isotope data ($\delta^{18}O$), whereas planktonic carbon isotope ($\delta^{13}C$) data suggest that the 100 kyr cycle is very weak during the last 5 million years (Tian et al., 2004b). Eccentricity cycles have possibly been prime pacemakers of climate evolution over the past several million years through the modulation of circulation patterns, carbonate production, and organic carbon burial processes (Shackleton, 1977; 2000; Holbourn et al., 2007). Our results also suggest that eccentricity was the main factor in climate evolution during 2.58–5.2 Ma.

Shorter cycles of 40 kyr (obliquity), and 24, 22, and 19 kyr (precession) are not present in the time series shown in Figure 2.7, possibly because of the relatively low time resolution of the paleosol unit in the paleoclimatic sequences (Lu et al., 2004). Just slightly below the red noise, there is a small peak in the 40 kyr range in the coarse fraction content spectrum, whereas there is no such peak in the magnetic susceptibility record (Figure 2.7). We cannot find high frequency precession cycles may be due to the spacing of our data points; the average time resolution of the samples is 8–10 kyr. Albeit the time series analysis can give precession when the sampling interval is at least twice per cycle, it is, indeed, only a bare minimum. Hence, it seems to be better to target possible precession cycles with three or four samples per cycle (Kodama and Hinnov, 2014). Besides, time series analysis of the astronomically tuned series is usually used to identify the shorter cycles (obliquity, precession). Here we performed cyclostratigraphy for untuned series to construct the new age model.

Our new age model enabled us to investigate Earth's orbital impact on changes in the Shilou red clay deposit during the Pliocene Epoch. Earth's orbital eccentricity varied in amplitude for both 100 kyr and 400 kyr cycles. The influence of eccentricity cycles on climatic evolution during the last several million years is not clearly understood (Clemens and Tiedemann, 1997; Muller and MacDonald, 1997; Rial, 1999; Elkibbi and Rial, 2001; Kashiwaya et al., 2003). It is remarkable that the 400 kyr eccentricity is well expressed, and 100 kyr eccentricity is preserved with slight shifts in the Shilou red clay section. The results imply that the addition of cyclostratigraphy to magnetostratigraphy analysis can change climate prediction model radically. This approach may contribute to a greater understanding of the eastern Asia monsoon system. It is possible that a large number of previously published red clay results based on magnetostratigraphy age model only should be verified using the cyclostratigraphy approach suggested in our paper.

2.5 Conclusions

(1) Constructed average sedimentation rate and spectral analyses result have enabled us to conclude that the red clay section at Shilou on the eastern Chinese Loess Plateau was formed 5.2 Ma instead of 11 Ma as calculated by Xu et al. (2009, 2012). We find the average sedimentation rate to be 2.54 cm/kyr, a value consistent with previous studies of red clay, and the spectral analyses show that Milankovitch periodicities are recorded in the studied section.

(2) Paleomonsoon evolution during 2.58–5.2 Ma was reconstructed and divided into three intervals (2.58–3.6 Ma, 3.6–4.5 Ma, and 4.5–5.2 Ma) using distinctive lithological features and amplitude as well as frequency variations of proxy indicators. The latest interval shows a relatively intensified summer monsoon, the middle interval indicates an intensification of the winter monsoon and aridification in Asia, and the earliest interval represents a rapid alteration of summer and winter monsoon cycles.

(3) The results indicate that a 400 kyr eccentricity cycle is well preserved, and the existence of a 100 kyr eccentricity in the red clay sequence on the Loess Plateau in eastern China suggests that eccentricity plays a vital role in Pliocene climate evolution. We suggest that the paleoclimatic response to the proxy variables and the orbital forcing was influenced by the accelerating uplift of the Tibetan Plateau.

(4) Our study demonstrates that cyclostratigraphy can greatly assist magnetostratigraphy in dating red clay sequences. This implies that many published age models for the red clay sequences should likely be re-assessed where possible. An evaluation of the monsoon system and climate change in eastern Asia might prominently benefit from our approach.

References

An, Z.S., Liu, T.S., Lou, Y.C., Porter, S.C., Kukla, G.J., Wu, X.H., Hua, Y.M., 1990. The long-term paleomonsoon variation recorded by the loess-paleosol sequence in central China. Quaternary International, 7(8), 91–95.

An, Z.S., Kukla, G., Porter S.C., Xiao, J.L., 1991. Magnetic susceptibility evidence of monsoon variation on the Loess Plateau of central China during the last 130,000 years. Quaternary Research, 36, 29–36.

An, Z.S., Wang, S.M., Wu, X.H., Chen, M.Y., Sun, D.H., Liu, X.M., Wang, F.B., Li, L., Sun, Y.B., Zhou, W.J., Zhou, J., Liu, X.D., Lu, H.Y., Zhang, Y.X., Dong, G.R., Qiang, X.K., 1999. Eolian evidence from the Chinese Loess Plateau: the onset of the Late Cenozoic Great Glaciation in the Northern Hemisphere and Qinghai–Xizang Plateau uplift forcing. Science in China, Ser. D, 42, 258–271.

An, Z.S., Kutzbach, J.E., Prell, W.L., Porter, S.C., 2001. Evolution of Asian monsoons and phased uplift of the Himalaya Tibetan plateau since Late Miocene times. Nature, 411, 62–66.

Cande, S.C., and Kent, D.V., 1995. Revised calibration of the geomagnetic polarity timescale for the Late Cretaceous and Cenozoic. Journal of Geophysical Research, 100, 6093–6095.

Cane, M.A., and Molnar, P., 2001. Closing of the Indonesian seaway as a precursor to east African aridification around 3–4 million years ago. Nature, 411, 157–162.

Chen, X.F., 1994. Stratigraphy and large mammals of the “Jinglean” stage, Shanxi, China [in Chinese with English abstract]. Quaternary Sciences, 4, 339–353.

Clemens, S.C., and Tiedemann, R., 1997, Eccentricity forcing of Pliocene–Early Pleistocene climate revealed in a marine oxygen-isotope record. Nature, 385, 801–804.

Debret, M., Bout-Roumazeilles, V., Grousset, F., Desmet, M., McManus, J.F., Massei, N., Sebag, D., Petit, J.-R., Copard, Y., Trentesaux, A., 2007. The origin of the 1500-year climate cycles in Holocene North-Atlantic records. Climate of the Past, 3, 569–575.

deMenocal, P., 1993. Wireline logging of the North Pacific transect. JOIDES Journal, 19, 29.

Deng C.L., Vidic N. J., Verosub K.L., Singer M.J., Liu Q.S., Shaw J., Zhu R.X., 2005. Mineral magnetic variation of the Jiaodao Chinese loess/paleosol sequence and its bearing on long-term climatic variability. Journal of Geophysical Research, 110, B03103.

Ding, Z.L., Yu, Z., Rutter, N.W., 1994. Towards an orbital time scale for Chinese loess deposits. Quaternary Science Reviews, 13, 39–70.

Ding, Z.L., Sun, J.M., Liu, T.S., Zhu, R.X., Yang, S.L., Guo, B., 1998. Wind-blown origin of the Pliocene red-clay formation in the central Loess Plateau, China. Earth and Planetary Science Letters, 161, 135–143.

Ding, Z.L., Xiong, S.F., Sun, J.M., Yang, S.L., Gu, Z.Y., Liu, T.S., 1999. Pedostratigraphy and paleomagnetism of a 7.0 Ma eolian loess– red clay sequence at Lingtai, Loess Plateau, north-central China and the implications for paleomonsoon evolution. Palaeogeography, Palaeoclimatology, Palaeoecology, 152, 49–66.

Ding, Z.L., Yang, S.L., Hou, S.S., 2001. Magnetostratigraphy and sedimentology of the Jingchuan red clay section and correlation of the Tertiary aeolian red clay sediments of the Chinese Loess Plateau. Journal of Geophysical Research, 106, 6399–6407.

Driscoll, N.W., and Haug, G.H., 1998. A short circuit in thermohaline circulation: A cause for Northern Hemisphere glaciation? Science, 282, 436–438.

Elkibbi, M., and Rial, J.A., 2001. An outsider's view of the ice ages. A review. Earth-Science Reviews, 55, 159–175.

Flynn, L., Wu, W.Y., Downs, W.R., 1997. Dating vertebrate microfaunas in the late Neogene record of Northern China. Palaeogeography, Palaeoclimatology, Palaeoecology, 133, 227–242.

Guo, Z.T., Peng, S.Z., Hao, Q.Z., Chen, X.H., Liu, D.S., 1999. Late Tertiary development of aridification in northwestern China: link with the arctic ice-sheet formation and Tibetan uplifts [in Chinese with English abstract]. Quaternary Sciences, 6, 556–567.

Guo, Z.T., Ruddiman, W.F., Hao, Q.Z., Wu, H.B., Qiao, Y.S., Zhu, R.X., Peng, S.Z., Wei, J.J., Yuan, B.Y., Liu, T.S., 2002. Onset of Asian desertification by 22 Myr ago inferred from loess deposits in China. Nature, 416, 159–163.

Guo, Z.T., Peng, S.Z., Hao, Q.Z., Biscaye, P.E., An, Z.S., Liu, T.S., 2004. Late Miocene–Pliocene development of Asian aridification as recorded in the Red-Earth Formation in the northern China. Global and Planetary Change, 41, 135–145.

Haug, G.H., and Tiedemann, R., 1998. Effect of the formation of the Isthmus of Panama on Atlantic Ocean thermohaline circulation. Nature, 393, 673–676.

Hess, S., and Kuhnt, W., 2005. Neogene and Quaternary paleoceanographic changes in the southern South China Sea (Site 1143): the benthic foraminiferal record. Marine Micropaleontology, 54, 63–87.

Hinnov, L.A., 2000. New perspectives on orbitally forced stratigraphy. Annual Review of Earth and Planetary Science, 28, 419-475.

Holbourn, A., Kuhnt, W., Schulz, M., Flores, J.A. and Andersen, N., 2007. Orbitally-paced climate evolution during the middle Miocene “Monterey” carbon-isotope excursion. Earth and Planetary Science Letters, 261(3), 534-550.

Imbrie, J., Hays, J.D., Martinson, D.B., Mcintyre, A., Mix, A.C., Morley, J.J., Pisias, N.G., Prell, W.L., and Shackleton, N.J., 1984. The orbital theory of Pleistocene climate: Support from a revised chronology of the marine δ18O record, in Milankovitch and Climate, edited by Berger, A., Imbrie, J., Kukla, G. and Saltzman, B., pp. 269–305, D. Riedel, Dordrecht, Netherlands.

Janecek, T.R., and Rea, D.K., 1983. Eolian deposition in the Northeast Pacific Ocean: Cenozoic history of atmospheric circulation. Geological Society of America Bulletin, 94, 730–738.

Jansen, E., and Sjøholm, J., 1991. Reconstruction of glaciation over the past 6 Myr from ice-borne deposits in the Norwegian Sea. Nature, 349, 600–603.

Kashiwaya, K., Ochiai, S., Sakai, H., and Kawai, T., 2003, Onset of current Milankovitch-type climatic oscillations in Lake Baikal sediments at around 4 Ma. Earth and Planetary Science Letters, 213, 185–195.

Kirschvink, J.L., 1980. The least-squares line and plane and the analysis of palaeomagnetic data. Geophys. J. R. Astr. Soc., 62, 699–718.

Kodama, K.P., and Hinnov, L.A., 2014. Front matter, in Rock Magnetic Cyclostratigraphy. New Anal. Methods Earth Environ. Sci. Ser., pp. 1–176, John Wiley, Oxford.

Kodama, K.P., Anastasio, D.J., Newton, M.L., Pares, J.M., Hinnov, L.A., 2010. High-resolution rock magnetic cyclostratigraphy in an Eocene flysch, Spanish Pyrenees. Geochemistry Geophysics Geosystems, 11, Q0AA07.

Kravchinsky, V.A., Krainov, M.A., Evans, M.E., Peck, J.A., King, J.W., Kuzmin, M.I., Sakai, H., Kawai, T. and Williams, D.F., 2003. Magnetic record of Lake Baikal sediments: chronological and paleoclimatic implication for the last 6.7 Myr. Palaeogeography, Palaeoclimatology, Palaeoecology, 195, 281–298.

Kukla, G., Heller, F., Liu, X.M., 1988. Pleistocene climates in China dated by magnetic susceptibility. Geology, 16, 811–814.

Kukla, G., An, Z.S., Meliece, L., Gavin, G., Xiao, J.L., 1990. Magnetic susceptibility record of Chinese loess. Transactions of the Royal Society of Edinburgh: Earth Sciences, 81, 263–288.

Laskar, J., Robutel, P., Joutel, F., Gastineau, M., Correia, A.C.M., Levrard B., 2004. A long term numerical solution for the insolation quantities of the Earth. Astronomy & Astrophysics, 428, 261–285.

Laskar, J., Fienga, A., Gastineau, M., Manche, H., 2011. La2010: a new orbital solution for the long term motion of the Earth. Astronomy and Astrophysics, 532, A89.

Li, J.J., 1991. The environmental-effects of the uplift of the Qinghai-Xizang Plateau. Quaternary Science Reviews, 10, 479–483.

Li, J.J., and Fang, X.M., 1999. Uplift of the Tibetan Plateau and environmental changes. Chinese Science Bulletin, 44, 2117–2124.

Li, J.J., Fang, X.M., Van, D.V., Zhu, J.J., Niocaill, C.M., Cao, J.X., Zhong, W., Chen, H.L., Wang, J., Wang, J.M., Zhang, Y.C., 1997. Late Cenozoic magnetostratigraphy (11–0 Ma) of the Dongshanding and Wangjiashan sections in the Longzhong Basin, western China. Geologie & Mijnbouw, 76, 121–134.

Liu, T.S., 1985. Loess and Environment. pp. 31–67, China Ocean Press, Beijing.

Liu, T.S., Ding, M.L., Derbyshire, E., 1996. Gravel deposits on the margins of the Qinghai–Xizang Plateau and their environmental significance. Palaeogeography, Palaeoclimatology, Palaeoecology, 120, 159–170.

Liu, X.M., Rolph, T., An, Z.S., Hesse, P., 2003. Paleoclimatic significance of magnetic properties on the Red Clay underlying the loess and paleosols in China. Palaeogeography, Palaeoclimatology, Palaeoecology, 199, 153–166.

Lu, H.Y., and An, Z.S., 1998. Palaeoclimatic significance of grain size of loess-paleosol sequence of Central China. Science in China, Ser. D, 41, 626–631.

Lu, H.Y., An, Z.S., Vandenberghe, J., Nugteren, G., 1997. Evidences for palaeoclimatic significance of grain size composite of loess deposit in Central Chinese Loess Plateau, in Proceedings of 30th International Geological Congress, edited by An, Z., vol. 21, pp. 5–10, VSP, The Netherlands.

Lu, H.Y., Zhang, F., Liu, X.D., 2002. Patterns and frequencies of the East Asian winter monsoon variations during the past million years revealed by wavelet and spectral analyses. Global and Planetary Change, 35, 67–74.

Lu, H.Y, Zhang, F., Liu, X., Duce, R.A., 2004. Periodicities of palaeoclimatic variations recorded by loess-paleosol sequences in China. Quaternary Sciences, 23, 1891-1900.

Lu, L.Q., Fang, X.M., Mason, J.A., Li, J.J., An, Z.S., 2001. The evolution of coupling of Asian winter monsoon and high latitude climate of Northern Hemisphere–Grain evidence from 8.1 Ma loess–red clay sequence on the Chinese central Loess Plateau. Science in China, Ser. D, 44, 185–191.

Lu, Y.C., 1981. Calcium carbonate content in Chinese loess deposit and the climatic cycles in the Pleistocene [in Chinese]. Geological Sciences, 2, 122–131.

Maher, B.A., and Thompson, R., 1991. Mineral magnetic record of the Chinese loess and paleosols. Geology, 19, 3–6.

Muller, R.A., and MacDonald, G., 1997. Spectrum of the 100 kyr glacial cycle: Orbital inclination, not eccentricity. Proceedings of the National Academy of Sciences of the U.S.A., 94, 8329–8334.

Nie, J., King, J., and Fang, X., 2008. Tibetan uplift intensified the 400 k.y. signal in paleoclimate records at 4 Ma. Geological Society of America Bulletin, 120, 1338–1344.

Pan, B.T., Gao, H.S., Li, B.Y., Li, J.J., 2004. Step-like landforms and uplift of the Qinghai–Xizang Plateau [in Chinese]. Quaternary Sciences, 24, 50–57.

Pan, Y.S., 1999. Formation and uplifting of the Qinghai–Tibet Plateau [in Chinese]. Earth Science Frontiers, 6, 153–163.

Pei, Y.P., Wu, N.Q., Li, F.J., 2004. Terrestrial mollusk evidence for the origin and sedimentary environment of the Late Tertiary red clay formation in the Loess Plateau, China. Chinese Science Bulletin, 49, 1072–1076.

Qiang, X.K., Li, Z.X., Powell, C.M., Zheng, H.B., 2001. Magnetostratigraphic record of the late Miocene onset of the East Asian monsoon, and Pliocene uplift of northern Tibet. Earth and Planetary Science Letters, 187, 83–93.

Qiang, X., An, Z., Song, Y., Chang, H., Sun, Y., Liu, W., Ao, H., Dong, J.B., Fu, C.F., Wu, F., Lu, F.Y., Cai, Y.J., Zhou, W.J., Cao, J.J., Xu, X.W., Ai, L., 2011. New eolian red clay sequence on the western Chinese Loess Plateau linked to onset of Asian desertification about 25 Ma ago. Science China Earth Sciences, 54 (1), 136–144.

Rea, D.K., Snoeckx, H., Joseph, L.H., 1998. Late Cenozoic eolian deposition in the North Pacific: Asian drying, Tibetan uplift, and cooling of the northern hemisphere. Paleoceanography, 13, 215–224.

Rial, J.A., 1999. Pacemaking the Ice Ages by frequency modulation of Earth's orbital eccentricity. Science, 285, 564–568.

Ruddiman, W.F., and Kutzbach, J.E., 1989. Forcing of late Cenozoic northern hemisphere climate by plateau uplift in southern Asia and the American West. Journal of Geophysical Research, 94, 18409–18427.

Schwarzacher, W., and Fischer, A.G., 1982. Lime-stone-shale bedding and perturbations in the earth's orbit. In Cyclic and Event Strat-ification, edited by G. Einsele, and A. Seilacher, pp. 72–95. Springer-Verlag, Berlin.

Shackleton, N.J., 1977. Carbon-13 in Uvigerina: tropical rainforest history and the equatorial Pacific carbonate dissolution cycles, in The Fate of Fossil Fuel CO2 in the Oceans, edited by Andersen, N.R., and Malahoff, A., pp. 401–427, Plenum Press, New York.

Shackleton, N.J., 2000. The 100,000-year ice-age cycle identified and found to lag temperature, carbon dioxide, and orbital eccentricity. Science, 289, 1897–1902.

Shackleton, N. J., Berger, A. Peltier, W. R., 1990. An alternative astronomical calibration of the Lower Pleistocene timescale based on ODP Site 677. Transactions of the Royal Society of Edinburgh Earth Sciences, 81, 251–261.

Shi, Y.F., Li, J.J., Li, B.Y., Yao, T.D., Wang, S.M., Li, S.J., Cui, Z.J., Wang, F.B., Pan, B.T., Fang, X.M., Zhang, Q.S., 1999. Uplift of the Qinghai-Xizang (Tibetan) Plateau and East Asian environmental change during late Cenozoic [in Chinese]. Acta Geographica Sinica, 54, 9–20.

Song, Y.G., Fang, X.M., Li, J.J., An, Z.S., Miao, X.D., 2001. The Late Cenozoic uplift of the Liupan Shan, China. Science in China, Ser. D, 44, 176–184.

Song, Y.G., Fang, X.M., Torii, M., Ishikawa, N., Li, J., An, Z., 2007. Late Neogene rock magnetic record of climatic variation from Chinese eolian sediments related to the uplift of the Tibetan Plateau. Journal of Asian Earth Sciences, 30, 324–332.

Sun, D.H., Liu, T.S., Cheng, M.Y., An, Z., Shaw, J., 1997. Magnetostratigraphy and paleoclimate of Red Clay sequences from the Chinese Loess Plateau. Sci. China, Ser. D, 40, 337-343.

Sun, D.H., An, Z.S., Shaw, J., Bloemendal, J., Sun, Y.B., 1998a. Magnetostratigraphy and paleoclimatic significance of Late Tertiary aeolian sequences in the Chinese Loess Plateau. Geophysical Journal International, 134, 207–212.

Sun, D.H., Shaw, J., An, Z.S., Chen, M.Y., Yue, L.P., 1998b. Magnetostratigraphy and paleoclimatic interpretation of a continuous 7.2 Ma late Cenozoic eolian sediments from the Chinese Loess Plateau. Geophysical Research Letters, 25, 85–88.

Sun, Y.B., Clemens, S.C., An, Z.S., Yu, Z.W., 2006. Astronomical timescale and palaeoclimatic implication of stacked 3.6-Myr monsoon records from the Chinese Loess Plateau. Quaternary Science Reviews, 25, 33–48.

Sun, Y.B., An, Z.S., Clemens, S.C., Bloemendal, J., Vandenberghe, J.F., 2010. Seven million years of wind and precipitation variability on the Chinese Loess Plateau. Earth and Planetary Science Letters, 297, 525–535.

Tang, M.C., Dong, W.J., Wang, N.L., 2003. The research on the uplift process of Tibetan Plateau [In Chinese]. Advance in Natural Science, 13, 331–336.

Teilhard, D.C., Young, C.C., 1930. Some correlations between the geology of China proper and geology of Mongolia. Bulletin of the Geological Society of China, 9, 119–125.

Teilhard, D.C., Young, C.C., 1931. Fossils mammals from the Late Cenozoic of Northern China. Palaeontologia Sinica, Ser. C, 9, 1–67.

Tian, J., Wang, P.X., Chen, X.R., 2004a. Development of the East Asian monsoon and Northern Hemisphere glaciation: oxygen isotope records from the South China Sea. Quaternary Science Reviews, 23, 2007–2016.

Tian, J., Wang, P., Cheng, X., 2004b. Responses of foraminiferal isotopic variations at ODP Site 1143 in the southern South China Sea to orbital forcing. Science in China, Ser. D, 47, 943–953.

Torrence, C., Compo, G.P., 1998. A practical guide to wavelet analysis. Bulletin of the American Meteorological Society, 79, 61–78.

Van Huissteden, J., Nugteren, G., Vandenberghe, J., An, Z.S., 1997. Spectral analysis of a grain size record of the loess deposits in Central China, in Proceedings of the 30th International Geology Congress edited by Zhang, et al., vol. 2, pp. 313–325, VSP The Netherlands.

Vandenberghe, J.F., Lu, H.Y., Sun, D.H., Van Huissteden, J., Konert, M., 2004. The late Miocene and Pliocene climate in East Asia as recorded by grain size and magnetic susceptibility of the Red Clay deposits (Chinese Loess Plateau). Palaeogeography, Palaeoclimatology, Palaeoecology, 204, 239–255.

Wan, S., Li, A., Clift, P.D. and Jiang, H., 2006. Development of the East Asian summer monsoon: Evidence from the sediment record in the South China Sea since 8.5 Ma. Palaeogeography, Palaeoclimatology, Palaeoecology, 241(1), 139-159.

Wang, L., Lu, H.Y., Wu, N.Q., Li, J., Pei, Y.P., Tong, G.B., Peng, S.Z., 2006. Palynological evidence for Late Miocene-Pliocene vegetation evolution recorded in the red clay sequence of the central Chinese Loess Plateau and implication for palaeoenvironmental change. Palaeogeography, Palaeoclimatology, Palaeoecology, 241, 118–128.

Wang, P., Clemens, S., Beaufort, L., Braconnot, P., Ganssen, G., Jian, Z., Kershaw, P., Sarnthein, M., 2005. Evolution and variability of the Asian monsoon system: state of the art and outstanding issues. Quaternary Science Reviews, 24, 595–629.

Weedon, G.P., 2003. Time-series Analysis and Cyclostratigraphy. P. 256, Cambridge University Press, Cambridge.

Wehausen, R., and Brumsack, H.J., 2002. Astronomical forcing of the East Asian monsoon mirrored by the composition of Pliocene South China Sea sediments. Earth and Planetary Science Letters, 201, 621–636.

Weng, H.Y., and Lau, K.M., 1994. Wavelets, period doubling, and timefrequency localization with application to organization of convection over the tropical western Pacific. Journal of Atmospheric Science, 51, 2523–2541.

Witt, A., and Schumann, A.Y., 2005. Holocene climate variability on millennial scales recorded in Greenland ice cores. Nonlinear Processes in Geophysics, 12, 345–352.

Xiao, J.L., Porter, S.C., An, Z.S., Kumai, H., Yoshikawa, S., 1995. Grain size of quartz as an indicator of winter monsoon strength on the Loess Plateau of central China during the last 130,000 yr. Quaternary Research, 43, 22–29.

Xu, T.C., and Liu, T.S., 1994. Implication of the magnetic susceptibility curve from the Chinese loess profile at Xifeng. Quaternary Science Reviews, 12, 249–254.

Xu, Y., Yue, L., Li, J., Sun, L., Sun, B., Zhang, J., Ma, J., Wang, J., 2009. An 11-Ma-old red clay sequence on the Eastern Chinese Loess Plateau. Palaeogeography, Palaeoclimatology, Palaeoecology, 284, 383-391.

Xu, Y., Yue, L., Li, J., Sun, L., Sun, B., Zhang, J., Ma, J., Wang, J., 2012. Red clay deposits on the Chinese Loess Plateau during 11.0–2.6 Ma and its implications for long-term evolution of East Asian monsoon. Environmental Earth Sciences, 66, 2021–2030.

Xue, X.X., and Zhao, J.B., 2003. Characteristic and significance of micromorphology of Neogene Red Clay of Xunyi Shanxi province [in Chinese with English abstract]. Acta Sedimentologica Sinica, 21, 448–481.

Zheng, H.B., Powell, C.M., An, Z.S., Zhou, J., Dong, G.R., 2000. Pliocene uplift of the northern Tibetan Plateau. Geology, 28, 715–718.

Zhou, L.P., Oldfield, F., Wintle, A.G., Robinson, S.G., and Wang, J.T., 1990. Partly pedogenic origin of magnetic variations in Chinese loess. Nature, 346, 737-739.

Zhu, Y.M., Zhou, L.P., Mo, D.W., Kaakinen, A., Zhang, Z.Q., Fortelius, M., 2008. A new magnetostratigraphic framework for late Neogene Hipparion Red Clay in the eastern Loess Plateau of China. Palaeogeography, Palaeoclimatology, Palaeoecology, 268, 47–57.

Chapter 3

Holocene climatic evolution at the Chinese Loess Plateau: implications of petromagnetic and grain size analyses

3.1 Introduction

Many paleoclimate studies have underlined the climate fluctuations in the Holocene interval in many places (Steig, 1999, Bianchi and McCave, 1999; Wurster and Patterson, 2001; Baker et al., 2001; McDermott et al., 2001 and others). Studies have explored six such fluctuations across the globe with an indication of polar cooling, tropical aridity, and significant atmospheric deviations (Mayewski et al., 2004). Although the development of the current human civilization has been nurtured by the Holocene climate, there is quite a limited knowledge on climate variability during this period. However, this limitation can be addressed through the approach of comprehensive paleoclimate data collecting from different locations of the globe, particularly from the climate sensitive ones. The arid and semi-arid China provides a highly sensitive and profound area for large-scale climatic variations (Thompson et al., 1989; Feng et al., 1993; D'Arrigo et al., 2000; Jacoby et al., 2000).

Scientists and researchers have been investigating the Holocene paleoclimates and paleoenvironments of the Chinese arid zone for quite a long time (Zhu et al., 1982; Liu, 1985; An et al., 2000; Xiao et al., 2004; Feng et al., 2006; Zhou et al., 2010 and others). For this, various records and archives including pollen and loess stratigraphy, variations in level of sea and lake, lacustrine sediments and ice cores with steady isotopes have been being studied and correlated to reconstruct the climatic variation in the Holocene. Particularly, pollen data, fossil fauna, paleosol, lake level, glacial remains, and archaeological data in China considered the mid Holocene (ca. 9.4–3.1 ka) to be the Holocene optimum (Shi et al., 1992; Li, 1996). In Inner Mongolia, strong monsoon fluctuations have been recorded as glacial advance and cessation of paleosol development (Zhou et al., 1991). Based on the analyses of various records of paleoclimatic imprints or proxies, He et al. (2004) suggested that the Holocene optimum occurred at ca. 6.5–5.5 ka in the eastern China. For each area in China, the Holocene climate had three distinct phases, and the middle Holocene optimum (8-5 ka) occurred in arid to semi-arid areas (Feng et al., 2006). Studying independent proxies including contemporary pollen data, Herzschuh (2006) explored that the event of the Holocene optimum with high precipitation happened in a different time period in the Indian monsoon and the East Asian monsoon region; it is the early Holocene and the mid-Holocene respectively for these regions. As there has been a discourse among the Quaternary scientists on the climatic variations in China in different intervals of the Holocene, it requires more clarification and better understanding of this climate change through the detailed records from various sources.

Selecting proper proxies and developing reliable chronologies is the key problem in reconstructing the variations in climate and environment during the Holocene. In arid and semi-arid regions, loess-paleosol sequences react to climatic variations, indicating that these areas are suitable for investigating the evolutions of paleoclimate and paleoenvironment (Rutter, 1992; Ding et al., 1993; Maher, 2011). These sequences can be instrumental to reconstruct climatic history of neighboring regions of the Loess Plateau through the last glacial cycle (e.g., Vandenberghe et al., 1997; Sun et al., 1999; Lu et al., 1999, 2000). It is clear that more complex Holocene loess-paleosol sequences exist, and these are attributable to fluctuations in the monsoonal climate (Zhou and An, 1994; Huang et al., 2000). The loess-paleosol records with reliable chronology are critical to understand the overall pattern of climate variations in the monsoonal China during the Holocene.

The analysis of petromagnetic properties of loess-paleosol deposits is instrumental for the interpretation of paleoclimatic conditions during the time of their accumulation. In this study, these properties, along with sedimentary grain size, are analyzed to investigate the Holocene climatic variations focusing on the loess-paleosols profiles from the region of the Guanzhong Basin and the Mu Us Desert lain in the East Asian monsoonal zone. The Guanzhong Basin is located at the southern edge of the Loess Plateau whereas the Mu Us Desert is situated at the northern part of the Plateau. Here, efforts have been made to reconstruct a regional climate and environmental changes in the Holocene recorded in the Chinese Loess; to explore the influence of temperature, precipitation, and wind strength on regional climate changes; to understand the responses of regional Holocene climate along the south-to-north eastern Chinese Loess Plateau; and to investigate whether the world and China exhibit common climate dynamics or climate change differs from region to region in the Holocene.

3.2 Study Area

In this study, five aeolian sections located in two different areas, the Yaozhou in the Guanzhong Basin and the Jinjie in the Mu Us Desert, were sampled (Figure 3.1). The Yaozhou (34°53′N, 108°58′E) is situated at the Guanzhong Basin, about 60-70 km east of Xi’an city (YZ in Figure 3.1). At middle zone of the Yellow River valley, the Guanzhong Basin is located while having the Loess Plateau to the north and the Qinling Mountains to the south (Figure 3.1). The land surface in the Guanzhong Basin has been quite settled because of less erosion, and eventually, it has made the aeolian dust deposits and soil surface well-preserved during the entire Holocene period (Huang et al., 2000). In the Guanzhong Basin, numerous Holocene loess-paleosol have been studied to examine changes in vegetation at the Yaoxian (Li et al., 2003), variations in climate at the Yaoxian (Zhao et al., 2007), and cultural effect at the Qingquicun (Huang et al., 2000). Analyzing the stratigraphy and the proxy data, such sequences can provide critical information regarding the fluctuations in climate, and also, they can explore major events occurred since 11 ka BP to date (Shi et al., 1992). The present mean annual temperature shows to be 13°C while mean rainfall is around 554 mm, and these are associated with a semi-humid climate that displays a significant seasonal variations in temperature and precipitation which becomes intense in summer. Three sections were investigated from this area: one at an outcrop (YZ1), the second one at 100 m further south (YZ2), and the third one at 300 m west (YZ3) from the first one. YZ2 is at the same pit of YZ1, whereas YZ3 is at a different pit. The sequence of 5 m YZ1, 3.3 m YZ2 and 4 m YZ3 are composed of three paleosol units of Holocene age (S_0S_1, S_0S_2 and S_0S_3), interbedded with two layers of loess (Figure 3.2-3.4). The stratigraphic unit was identified through the examination of colour, texture and structure of the sediment. However, the buried soils in these sections cannot be identified very well visually, and thus, the soil layers can be confirmed through the magnetic measurements.

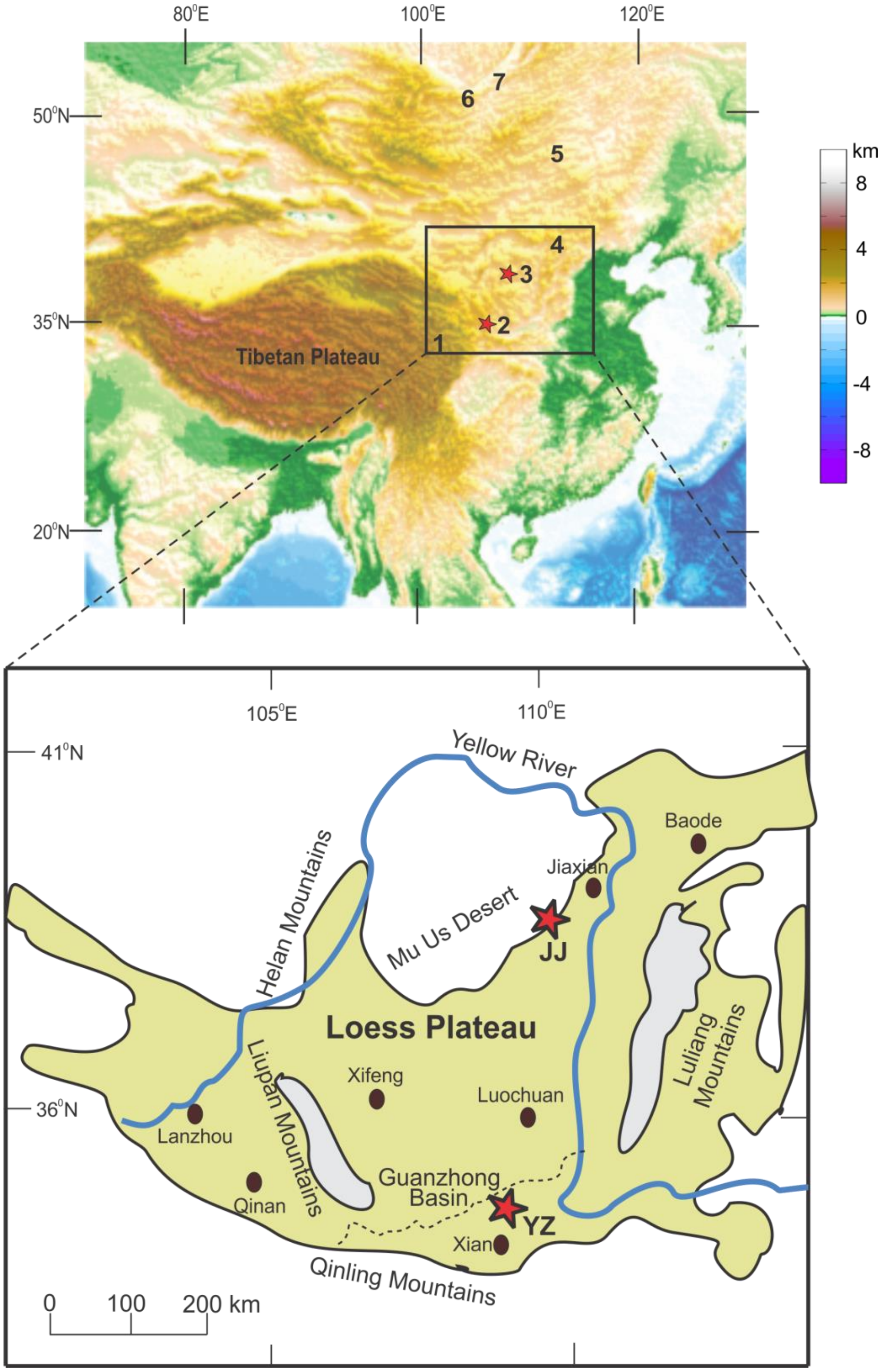

Figure 3.1. (top) Geographic location of the studied areas (red star) and the other sites discussed in the text: 1- Hongyuan peatland; 2- Yaozhou; 3- Jinjie; 4- Daihai Lake; 5- Hulun Lake; 6-Lake Baikal; 7- Burdukovo. (bottom) Geographic location of the Yaozhou (YZ) and Jinjie (JJ) studied areas in the Chinese Loess Plateau.

The Jinjie (38°44′N, 110°91′E) is located at the southeastern margin of the Mu Us Desert (JJ in Figure 3.1). The Mu Us Desert, being situated at the northern-central China and having sand dunes, belongs to the peripheral region of the East Asian monsoon. Currently, almost two-thirds of this desert are covered by these sand dunes (Sun, 2000). The ecosystem, in the semi-arid Mu Us Desert, exhibits high sensitivity towards climate change since external climatic forces can easily affect the vegetation, soil, and aeolian sand (Sun et al., 2006). The local mean annual temperature, currently, varies from 6.0° to 9.0°C, and it is 200-400 mm in case of the mean rainfall. 70% of the rainfall concentrates from July to September, with a warm and humid summer as well as autumn. In winter, it is cold and dry with the prevailing cold winds being northwesterly. Two sections from this area, JJ1 and JJ3 (along the road and about 1 km southeast from JJ1), were studied. The 7m deep JJ1 and 8m deep JJ3 aeolian sequences contain three distinctive dark brown sandy loam soil layers (S_0S_1, S_0S_2 and S_0S_3) separated by sand beds (Figure 3.5 and 3.6). The stratigraphic subdivision was made by the field observation of colour, texture, and structure of the sediment. For JJ3 section, there are mixture of sand and soils in between two soil layers. All of these sections are situated above the Malan loess (L1).

The Yaozhou and the Jinjie loess paleosol sequences are both dated using optically stimulated luminescence (OSL) dating technique (Zhao et al., 2007; Ma et al., 2011). In the Yaozhou, the boundary between the lowest paleosol (S_0S_3) and the Malan Loess was OSL dated 8.44 ± 0.59 ka (Zhao et al., 2007). At the Jinjie, the lowest paleosol (S_0S_3) was bracketed by two OSL dates– 7.07 ± 0.42 ka at the bottom and 3.91 ± 0.18 ka at the top (Ma et al., 2011). Ages of each soil section are assigned based on the OSL dating of Zhao et al. (2007) for the Yaozhou area and Ma et al. (2011) for the Jinjie area (Figure 3.2-3.6).

3.3 Methods

3.3.1 Sampling

A total of 573 non-oriented bulk samples were collected from the 5 sections (YZ1: 100, YZ2: 80, YZ3: 85, JJ1: 150 and JJ3: 158 samples) for petromagnetic analysis. Samples were taken continuously at 5 cm intervals (2.5 cm intervals only for the thin soils) from all sections. Sampling was started from the top that contains present day soil i.e. the cultivated layer.

3.3.2 Petromagnetic Analysis

A number of petromagnetic parameters such as low and high frequency magnetic susceptibility (MS), anhysteric remanent magnetization (ARM), saturation isothermal remanent magnetization (SIRM), and back field isothermal remanent magnetization (bIRM) were measured to identify variations in the concentration, grain size and mineralogy of magnetic material in the samples. This was conducted in the paleomagnetism and petromagnetism laboratory of the Physics Department at the University of Alberta. These parameters (low field mass specific magnetic susceptibility χ_{lf} and SIRM) and the ratios derived from them (frequency dependence of magnetic susceptibility FD and normalized to the steady field anhysteric remanent magnetization (χ_{ARM})) were used to interpret the paleoclimatic conditions during deposition of the studied loess-paleosol sections.

In the laboratory, 8 cm^3 plastic non-magnetic boxes were used to host the sediments for petromagnetic measurements. The low-frequency (0.43 kHz) and high-frequency (4.3 kHz) magnetic susceptibility of each sample were measured using a Bartington Instruments MS2B dual frequency meter. To reduce the level of considerably high noise from the Bartington instrument, special precaution was taken during measurements. Each sample was measured three times in different positions, and the average MS value was calculated for both low and high frequency measurements. All the values were checked before getting the average, and found consistent without high errors. Air measurements were taken in between two samples' measurement each time to monitor and eliminate the instrumental drift. The FD value was calculated for each sample using its averaged low and high frequency MS values. ARM was acquired in the samples subjecting to a peak AF field of 100 mT and a steady DC field of 0.1 mT by a 2G cryogenic magnetometer demagnetizer. This ARM was normalized to the steady field to yield χ_{ARM}. SIRM was acquired in the samples by subjecting them to a field of 0.6 T through a 2G IRM stand-along electromagnet. bIRM was induced to the samples by using a reversed field of 0.3 T and the acquired remanences were measured on the cryogenic magnetometer. Parameters (χ_{ARM}/χ_{lf} and $\chi_{ARM}/SIRM$) were also evaluated for each sample.

3.3.3 Grain Size Analysis

Grain size analysis was performed in order to determine relative wind strengths during loess deposition of the studied sections. Sedimentary grain size was measured on a Mastersizer 2000 laser particle analyzer at the Northwest University (Xian, China). The grain size samples were subjected to standard chemical pretreatment. To eliminate the organic material, samples of 0.3–0.4 g were fully dissolved in 10 ml of 10% boiling hydrogen peroxide (H_2O_2) solution in a 200 ml beaker. The carbonates were also removed by boiling with 10 ml of 10% hydrochloric acid (HCl). Distilled water was added during the chemical treatment to avoid drying of the solution. After standing overnight, the clear water was decanted from the sample. Through a combination of an addition of 10 ml of 10% sodium hexametaphosphate [$(NaPO_3)_6$] solution and an oscillation for around 10 minutes ultrasonically, dispersion was created for the components.

3.4 Results

3.4.1 Petromagnetic Parameters

The measured parameters of five sections (YZ1, YZ2, YZ3, JJ1, and JJ3) have been plotted against depth of the sections in Figure 3.2-3.11. Magnetic susceptibility has been widely used as a proxy indicator to investigate Quaternary climate change by loess-paleosol sequences on the Chinese Loess Plateau (Heller and Liu 1984; Balsam et al., 2004). The MS record demonstrates intensity variations of the pedogenesis, caused by precipitation changes related to summer monsoon climatic fluctuations (An et al., 1991; An and Xiao, 1990). χ_{lf} measures the magnetic response caused by magnetic remanences as well as non-remanent components present in the samples (Robinson, 1986; Thompson and Oldfield, 1986; Evans and Heller, 2003). χ_{lf} values (average 0.13×10^{-6} m^3kg^{-1}) for the Jinjie area (JJ1 and JJ3 sections) are relatively lower than that (average 1.05×10^{-6} m^3kg^{-1}) of the Yaozhou area (YZ1, YZ2 and YZ3 sections), suggesting that the latter area has higher concentration of magnetic particles. The loess and paleosol layers are all clearly identifiable in the χ_{lf} profiles from all sections (Figure 3.2-3.6). In this study, the susceptibility curves (χ_{lf}) of all the sections show that the soils have higher susceptibility compared to the loess/sand beds (Figure 3.2-3.6), indicating warm-wet climate conditions during the formation of these accretionary soils. On the other hand, lower χ_{lf} values in the loess/sand layers exhibit a cool-dry climate and intensified aeolian dust deposition as well as weak pedogenic processes during loess deposition. The upper layer of the soils (S_0S_1), formed thinner in a shorter period, shows weak χ_{lf} values almost as same as the values of adjacent aeolian loess/sands, whereas the lower layers of soils represent stronger signals for the sections YZ2, YZ3, JJ1, and JJ3 (Figure 3.3-3.6). For YZ1 section, S_0S_1 shows high peak with disturbance, probably due to the close proximity of S_0S_1 to the modern soil or the cultivated layer (Figure 3.2).

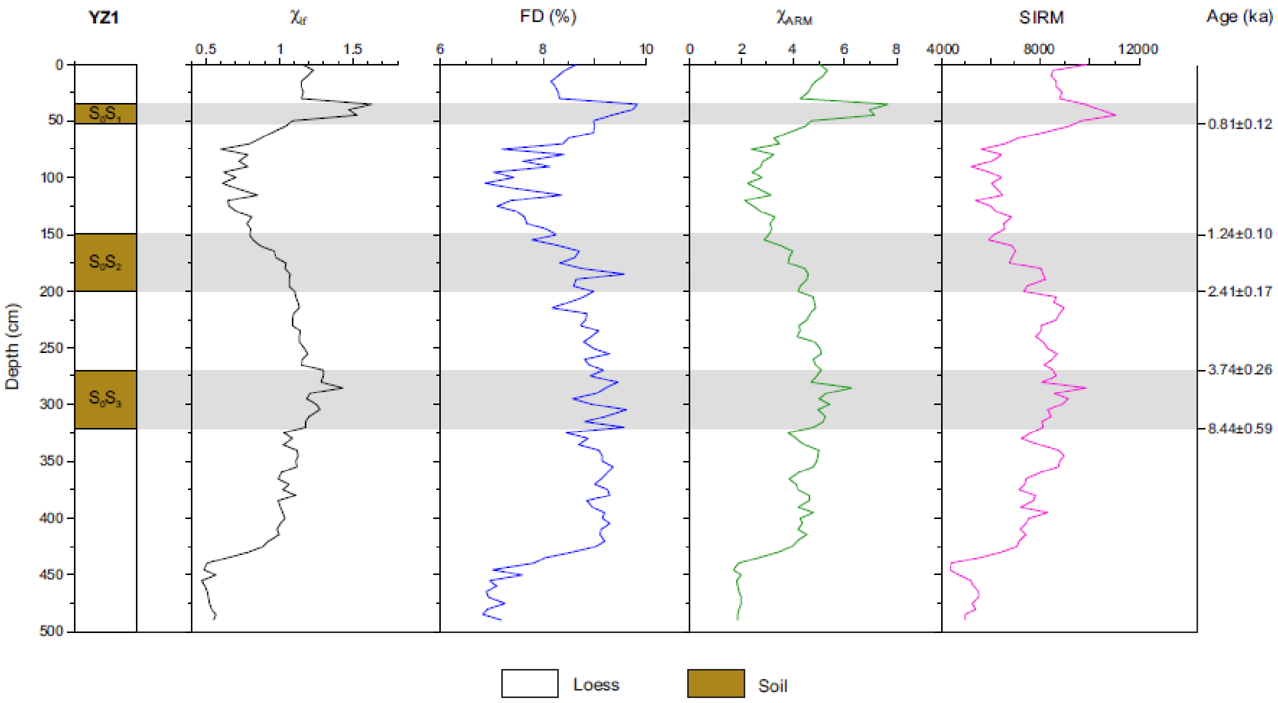

Figure 3.2. Stratigraphy and magnetic concentration parameters of the YZ1 section. χ_{lf} — low frequency magnetic susceptibility (10^{-6} m^3 kg^{-1}); FD (%) — frequency dependence parameter; χ_{ARM} — anhysteric remanent magnetization (10^{-6} m^3 kg^{-1}); and SIRM — saturation isothermal remanent magnetization (10^{-6} Am^2 kg^{-1}). Horizontal grey bars denote soil horizons, interpreted as relatively warm-wet intervals.

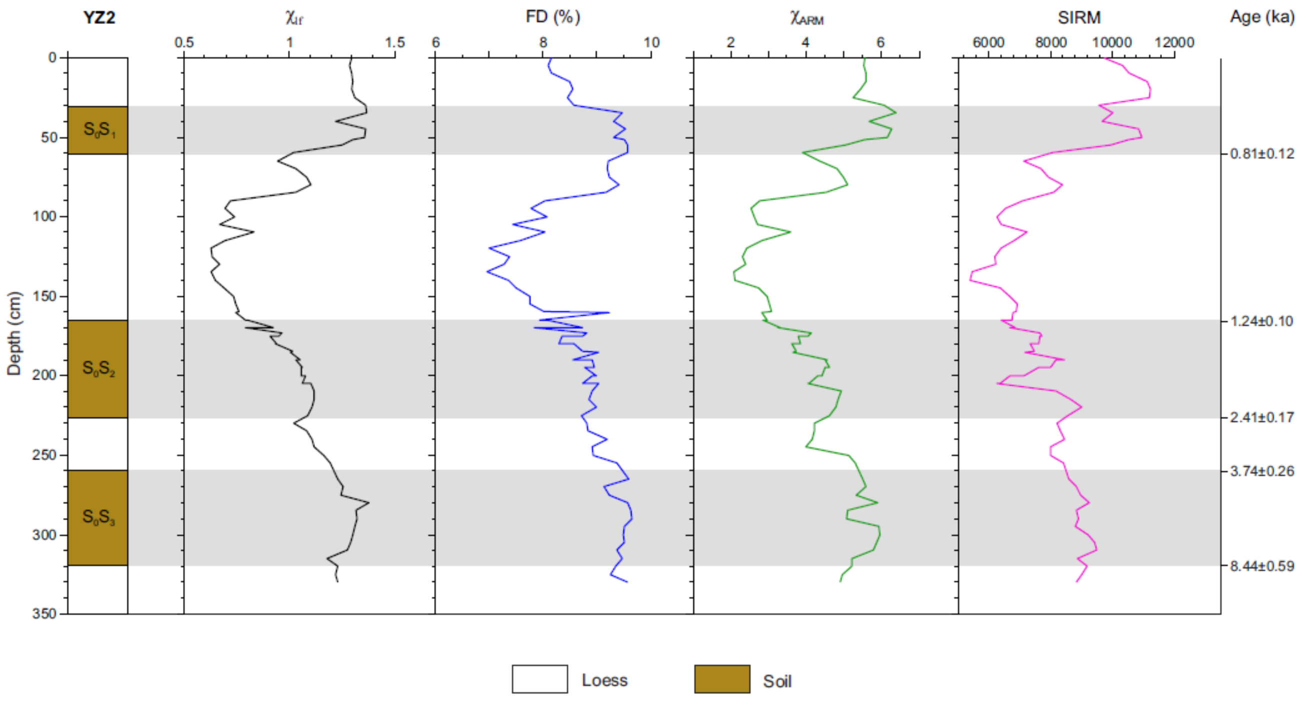

Figure 3.3. Stratigraphy and magnetic concentration parameters of the YZ2 section. Same abbreviations as in Figure 3.2.

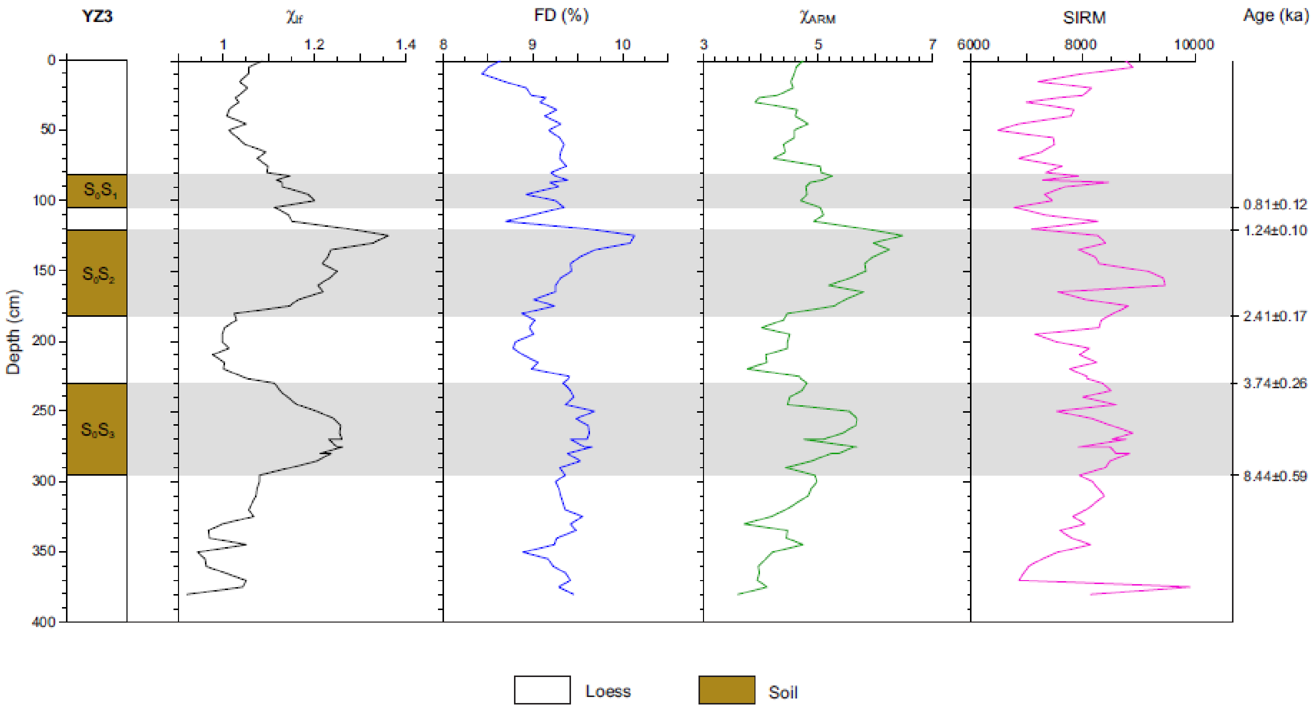

Figure 3.4. Stratigraphy and magnetic concentration parameters of the YZ3 section. Same abbreviations as in Figure 3.2.

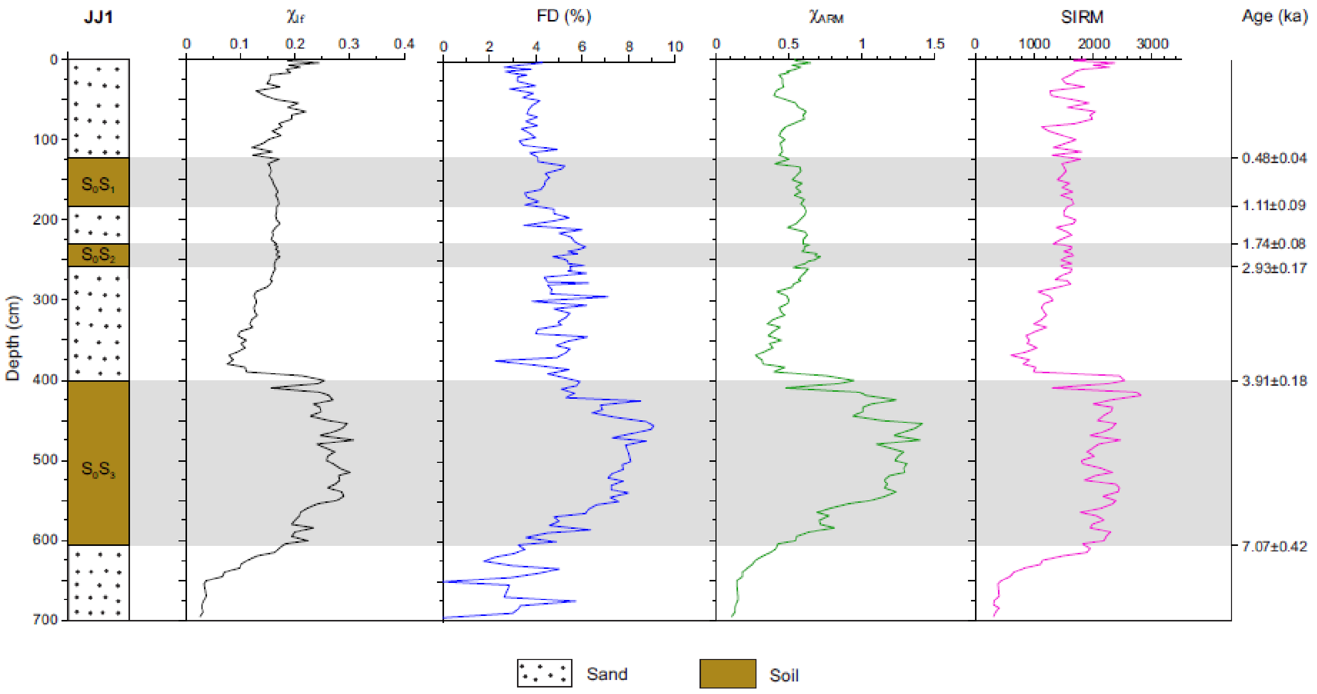

Figure 3.5. Stratigraphy and magnetic concentration parameters of the JJ1 section. Same abbreviations as in Figure 3.2.

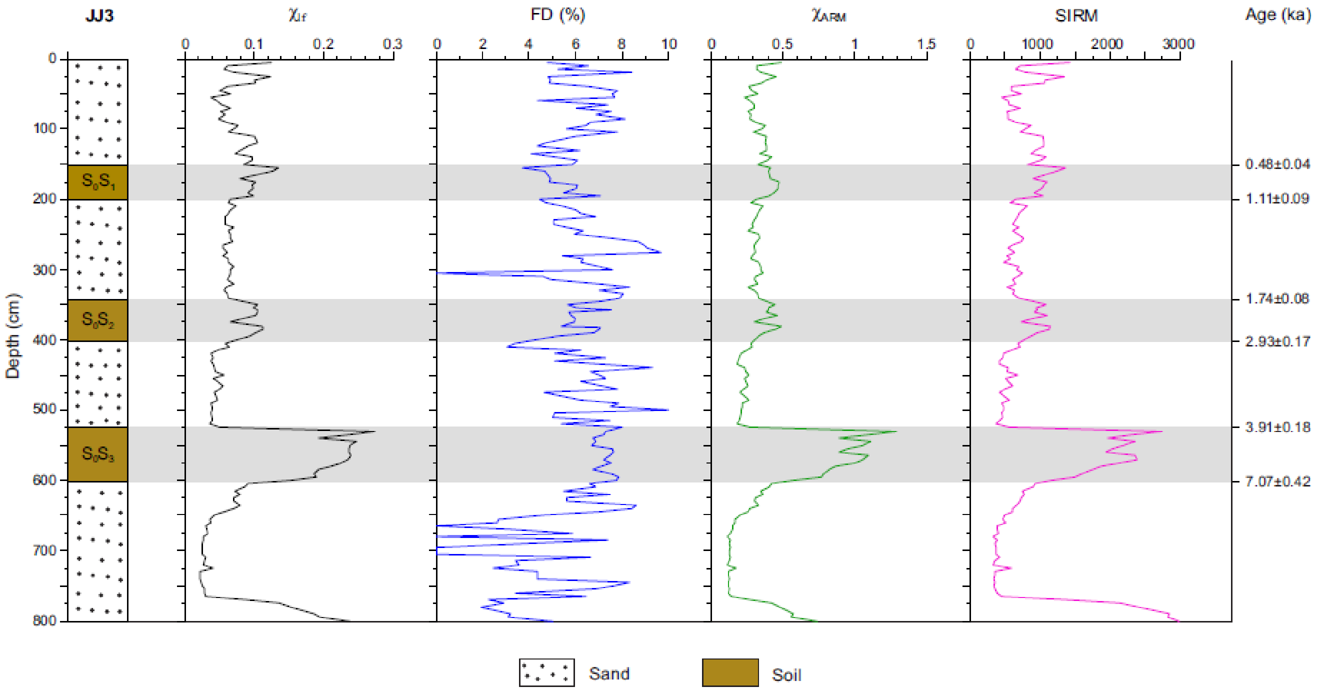

Figure 3.6. Stratigraphy and magnetic concentration parameters of the JJ3 section. Same abbreviations as in Figure 3.2.

The FD parameter appears to be higher in soil horizons compared to the loess as it is related to the distribution of ferromagnetic minerals, commonly superparamagnetic magnetite produced during soil formation (Thompson and Oldfield, 1986; Evans and Heller, 2003). All soil horizons exhibit higher FD values (ranging around 8-10%) compared to their respective parent loess horizons, and these are in agreement with the χ_{lf} values (Figure 3.2-3.5). These higher FD values of studied soil horizons confirm the continuous production of superparamagnetic particles during the pedogenesis in warmer interval. However, for the JJ3 section, the FD parameter does not show variations to corresponding sands and soils (Figure 3.6), probably due to the sandiness of the soils for this section.

χ_{ARM} and SIRM indicate variations in magnetic mineral concentration, and values get higher with increasing concentration of minerals having a high magnetization such as magnetite (Thompson and Oldfield, 1986; Yu and Oldfield, 1989; King and Channell, 1991; Evans and Heller, 2003). Figure 3.2-3.6 indicate that the paleosol horizons have higher χ_{ARM} and SIRM values compared to the loess/sand horizons. The higher χ_{ARM} and SIRM values represent higher concentration of magnetic particles within the soil layers, and indicate warmer-wetter conditions and active pedogenic processes during the time of soil formation. Whereas lower values, found in the loess/sand layers, indicate cooler-drier conditions and weak pedogenic intensity during the periods of intensified dust deposition. For all the sections, χ_{ARM} and SIRM curves indicate the presence of χ_{lf} and FD peaks, corresponding to the soil horizons (Figure 3.2-3.6).

3.4.2 Sedimentary Grain Size

The grain size variations of loess deposits have commonly been used to monitor past wind intensity changes (Pye and Zhou, 1989; Rea, 1994). Stronger winds are associated with more dust storms, coarser particle size and larger dust input to the Loess Plateau (Ding et al., 1994). The average median grain size values are larger for the Jinjie area (~220 μm) than the Yaozhou area (~13.9 μm), representing that the grain size records of the Holocene loess deposits decrease from north to south over the Chinese Loess Plateau. The grain size of the last glacial loess deposits also displays an overall southward decrease (Yang and Ding, 2004) as the loess was created primarily in the sandy Gobi deserts in northwestern China and was carried away by the near-surface northwesterly wind (Liu 1985; An et al., 1991). The median grain size of the studied sections does not demonstrate well the general characteristic of the smaller values for the soil horizons (Figure 3.7-3.11), indicating that the wind intensity did not vary much for these areas during the Holocene. Moreover, the median grain size of the loess and soil horizons of the Yaozhou area (YZ1, YZ2 and YZ3 sections) shows a little variability compared to the loess and soil layers of the Jinjie area (JJ1 and JJ3 sections), suggesting that the wind intensity fluctuation was higher in the north loess plateau (Jinjie area) in contrast with the south loess plateau (Yaozhou area).

The ratios χ_{ARM}/χ_{lf} and $\chi_{ARM}/SIRM$ indicate variations in magnetic grain size and the values decrease with increasing magnetic grain size (Thompson and Oldfield, 1986; King et al., 1982; Maher, 1988; Evans and Heller, 2003). For all the sections, magnetic grain size (χ_{ARM}/χ_{lf} and $\chi_{ARM}/SIRM$) varies in the same manner as the sedimentary grain size does (Figure 3.7-3.11).

Both the ratios reflect a little variability for loess and soil horizons indicating smaller relative changes in magnetic grain sizes.

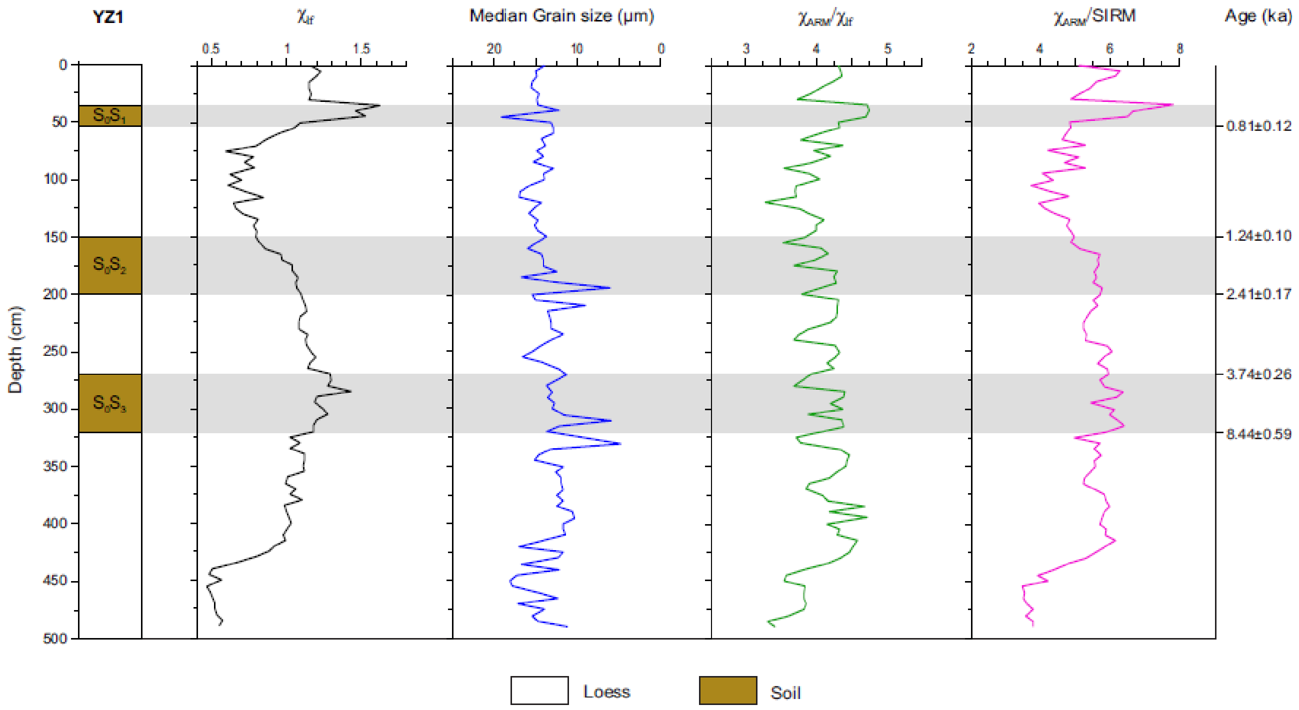

Figure 3.7. Stratigraphy and analytic data for the YZ1 section. χ_{lf} — low frequency magnetic susceptibility (10^{-6} m^3 kg^{-1}); MD — median sedimentary grain size (μm); χ_{ARM}/χ_{lf} — magnetic grain size parameter (unitless); and $\chi_{ARM}/SIRM$ — magnetic grain size parameter (10^{-4} mA^{-1}). Horizontal grey bars denote soil horizons, interpreted as relatively warm-wet intervals.

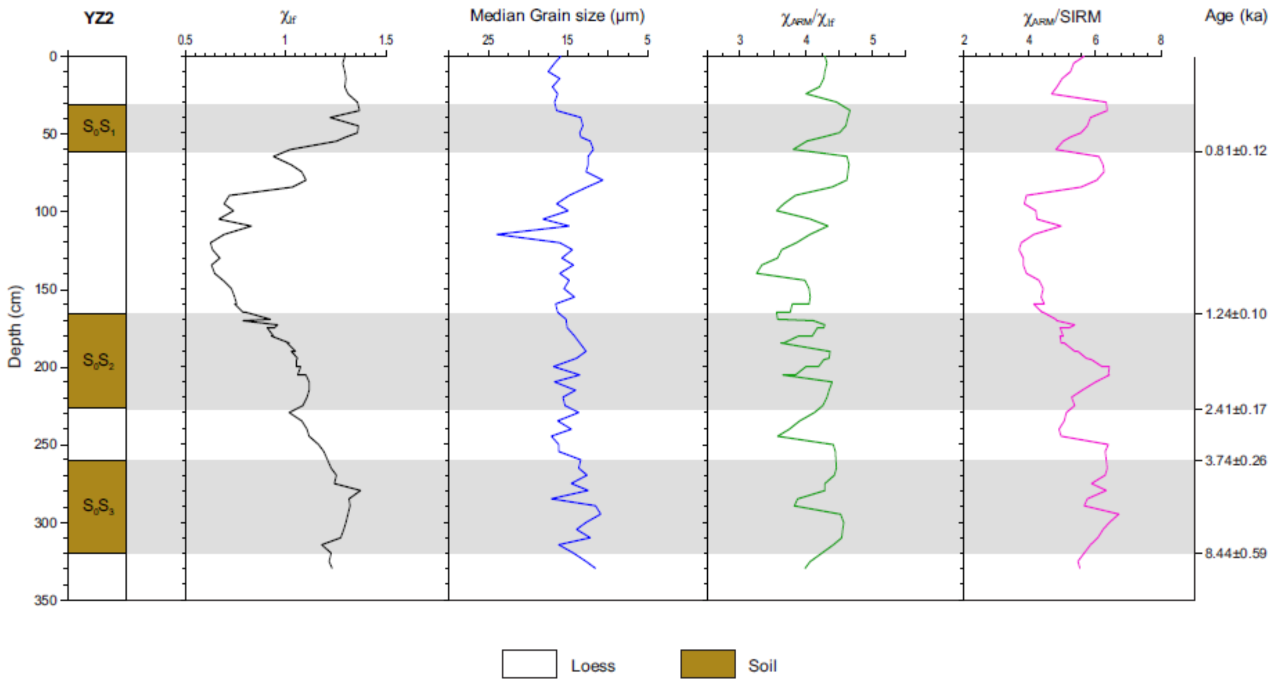

Figure 3.8. Stratigraphy and analytic data for the YZ2 section. Same abbreviations as in Figure 3.7.

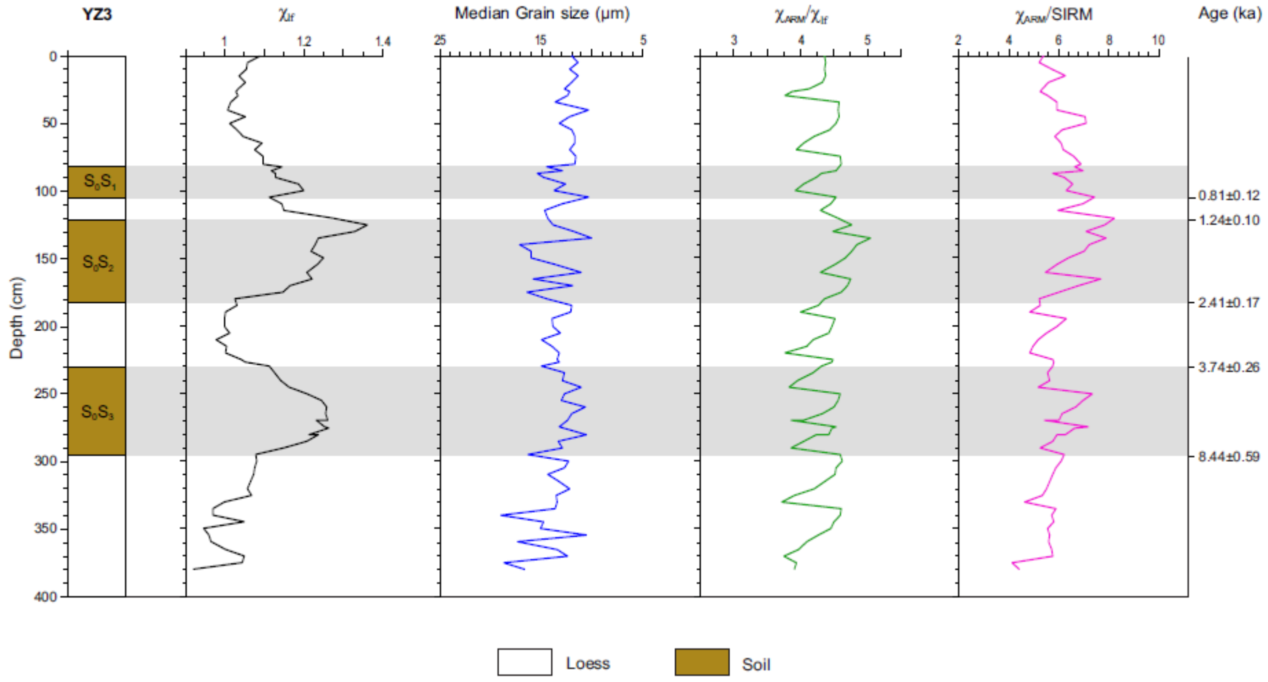

Figure 3.9. Stratigraphy and analytic data for the YZ3 section. Same abbreviations as in Figure 3.7.

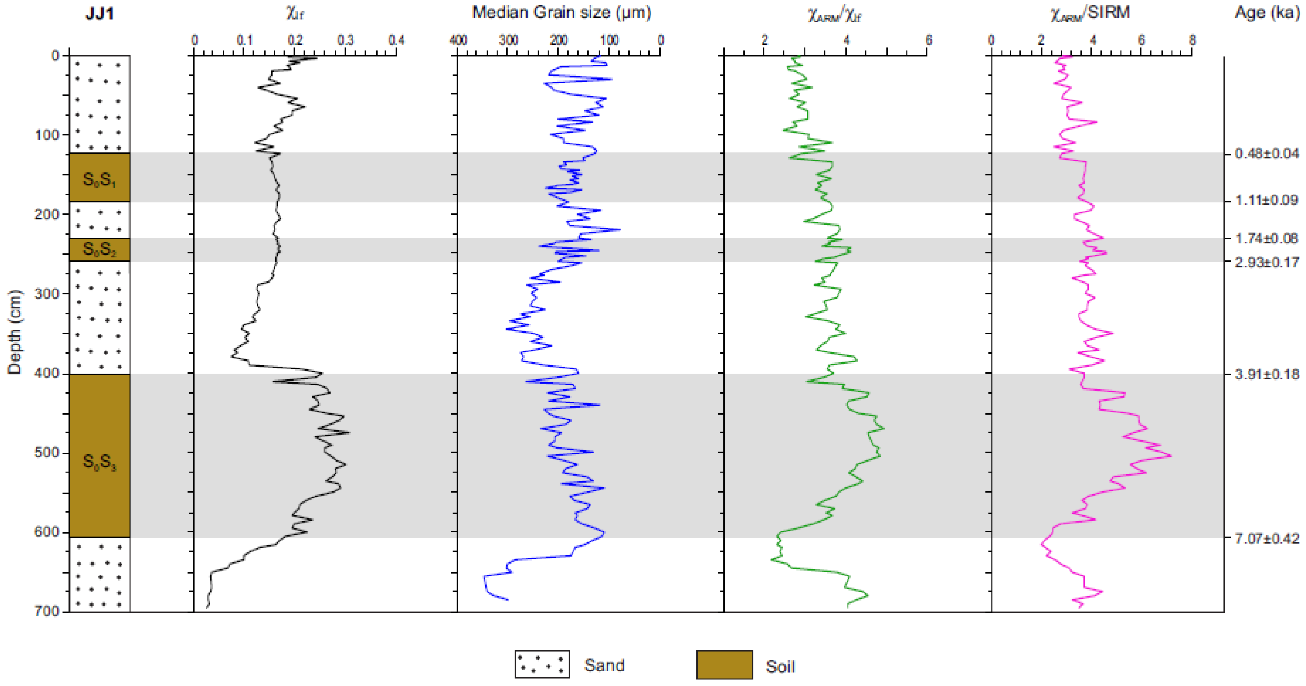

Figure 3.10. Stratigraphy and analytic data for the JJ1 section. Same abbreviations as in Figure 3.7.

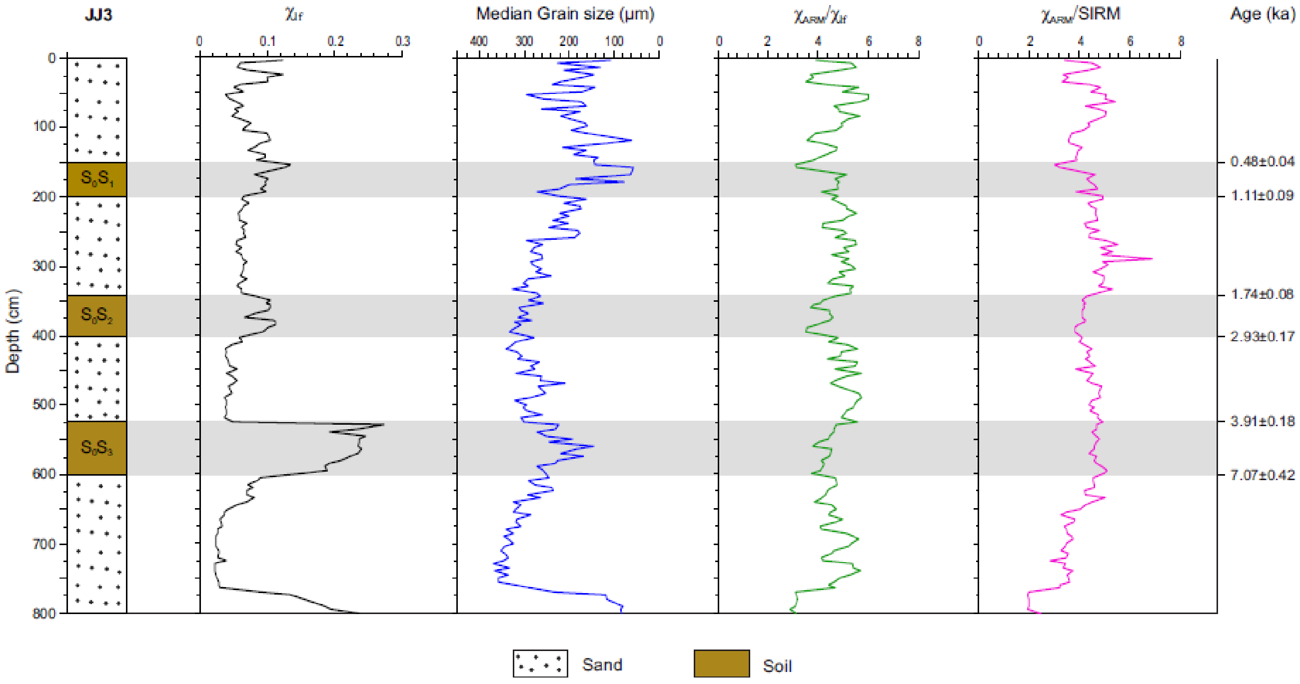

Figure 3.11. Stratigraphy and analytic data for the JJ3 section. Same abbreviations as in Figure 3.7.

3.5 Discussion

3.5.1 Variations in the Holocene Climate

Three soil layers (S_0S_1, S_0S_2 and S_0S_3) are identified for all the sections not only in the field but also in the laboratory by higher magnetic concentration parameters (χ_{lf}, χ_{ARM}, SIRM) and FD parameter. Therefore, χ_{lf}, FD, χ_{ARM} and SIRM are higher for soil and lower for loess/sand horizons, indicating warmer and colder assemblage respectively. The sedimentary and magnetic grain size variations do not correspond to the soil intervals entirely. Furthermore, the magnetic concentration parameters and FD parameter show a larger variation for the loess and soil layers compared to the sedimentary and magnetic grain sizes for these layers. It demonstrates that humidity fluctuation, which is related to the vegetation and soil formation, was stronger than the wind intensity variation for the studied sections during the Holocene.

Petromagnetic analysis of five loess sections in the Yaozhou and the Jinjie shows clear changes in regional climate, and provides paleoenvironmental information over the Holocene. Changes of parameters with soil formation in five studied sections, at the Yaozhou (Jinjie), suggests three distinct warm-humid time periods during the Holocene: the oldest warmer interval was between 8.4–3.7 ka (7.0–3.9 ka), the middle one occurred between 2.4–1.2 ka (2.9–1.7 ka), and the youngest started at 0.81 ka (1.1 ka) (Figure 3.2-3.6). Furthermore, based on the data, two cold-dry intervals associated with loess deposition can be considered at the Yaozhou (Jinjie): 3.7–2.4 ka (3.9–2.9 ka) and 1.2–0.81 ka (1.7–1.1 ka). However, at these areas, the onset and termination of warming-cooling intervals during the Holocene were almost similar with a slight difference. A subsequent warm-humid phase took place between ~8.4 ka and ~3.7 ka, indicated by the development of strong soil (S_0S_3) in all five sites. Combined with high values of all petromagnetic parameters in the studied regions (Figure 3.2-3.6), this period is attributed to the Holocene optimum, a warm period (generally warmer than today) in the middle of the Holocene. Soil S_0S_3 formation terminated around ~3.7 ka, suggesting a cold-arid period. This resulted in an active period for the loess/sand during ~3.7–2.4 ka. The soil S_0S_2 developed between ~2.4 and ~1.2 ka, and at that time, the values of the petromagnetic parameters indicate a warm-humid period in this region (Figure 3.2-3.6). The climate became colder and drier between ~1.2 and ~0.81 ka as the sand/loess was deposited, illustrated by low values of petromagnetic parameters. Soil S_0S_1 formed in the interval of ~0.81–0.48 ka (Figure 3.2-3.6), suggesting a warm-humid period.

3.5.2 Comparison of Regional Paleoclimatic Records

Changes in climate in the studied sections can be compared with the other reported paleoclimatic records from the neighboring monsoonal region of semi-arid China. In this study, we used tree pollen records from peatlands or lakes, located along the south-to-north regional transect on the eastern Loess Plateau, to make comparison with our results. In order to compare, low frequency magnetic susceptibility (χ_{lf}) of YZ3 section from the Yaozhou and JJ3 section from the Jinjie have been selected as reference curve since these identify soil intervals better than the others. The sites from south to north include the Hongyuan peatland (Zhou et al., 2010), the Yaozhou (YZ3), the Jinjie (JJ3), the Daihai Lake (Xiao et al., 2004), and the Hulun Lake (Wen et al., 2010) (Figure 3.12). Summer temperature and precipitation are two dominant climatic factors controlling soil formation as well as pollen assemblages (Shen et al., 2006). Thus, high magnetic parameters and high tree pollen should reflect warm-wet climates. Three warmer intervals of the studied region visually correlate well with the higher pollen data (Figure 3.12).

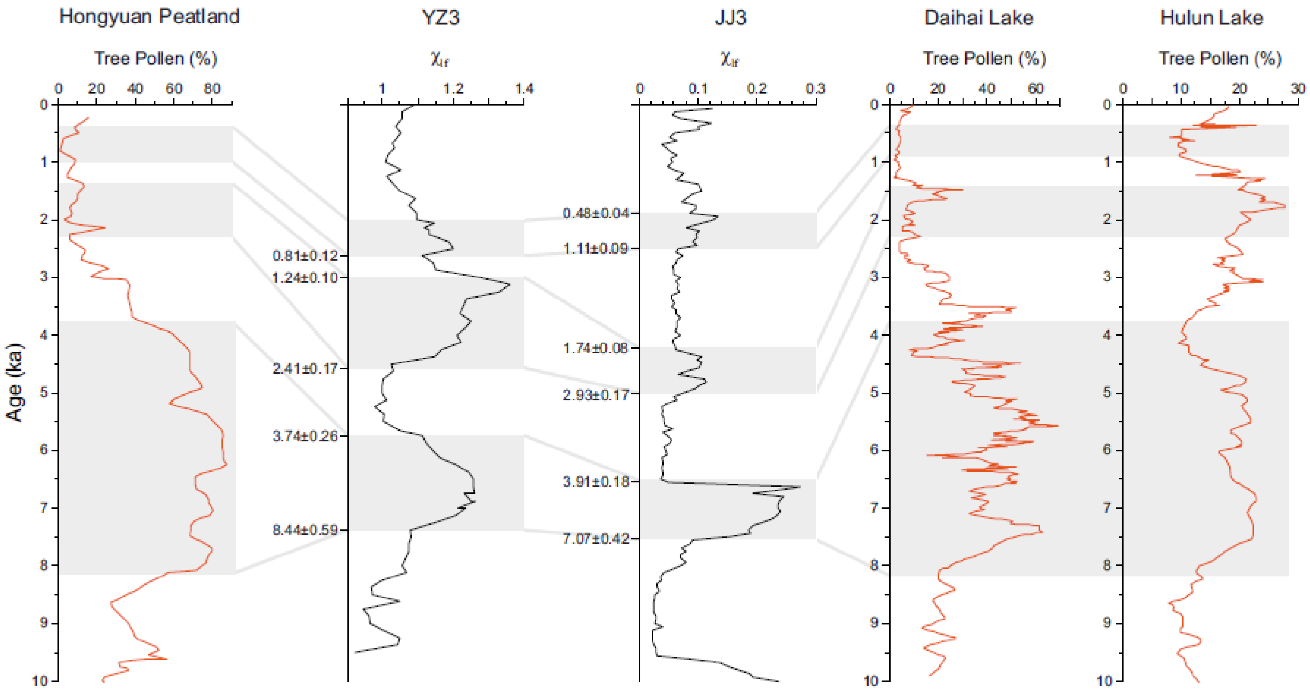

Figure 3.12. Comparison of Holocene paleoclimate records in China (from south to north): total tree pollen percentage at Hongyuan peatland (Zhou et al., 2010); χ_{lf} — low frequency magnetic susceptibility (10^{-6} m^3 kg^{-1}) for YZ3 section (this study); χ_{lf} (10^{-6} m^3 kg^{-1}) for JJ3 section (this study); total tree pollen percentage at Daihai Lake (Xiao et al., 2004); and total tree pollen percentage at Hulun Lake (Wen et al., 2010). Locations of these areas are shown in Figure 3.1. Grey horizontal bars represent the warm-wet climatic intervals based on the record of this study.

Pollen records from the Hongyuan peatland (Zhou et al., 2010), the Daihai Lake (Xiao et al., 2004), and the Hulun Lake (Wen et al., 2010) show peak tree pollen abundance in the mid-Holocene between ~8.4 and ~3.7 ka (Figure 3.12), suggesting a warmer-wetter climate. There is an agreement in the mid-Holocene maximum or climate optimum as documented at our studied sections and other sites (Figure 3.12). In the Lake Daihai which is situated at the northeast from the Mu Us Desert, high and stable lake level also occurred at ~8–3 ka (Sun et al., 2009). An ancient wetland existed continuously from ~7.8 to 4 ka at valleys, southeast of the Lanzhou, which is located further west from the Yaozhou (An et al., 2005). A humid mid-Holocene corresponds well with a more recent reconstruction of monsoonal precipitation through various imprints from the Chinese Loess Plateau (Lu et al., 2013). Zhao and Yu (2012) studied most of the sites of the temporary zone, located between forest and temperate steppe vegetation in the northeastern China, and confirmed the presence of the wettest climate occurred between ~8 and ~4 ka. The high level of the Lake Huangqihai during 8–4 ka (Shen, 2013), situated in the monsoonal region, indicates a strong East Asian summer monsoon happened in the mid-Holocene. In the Horqin dunefield, the greater density of vegetation coverage occurred between ~8 and ~3.2 ka, suggesting a warm and humid climate (Mu et al., 2016). In the studied sections, even though the termination of the warm-humid Holocene optimum slightly vary in different sections, this is possibly due to the age model imperfections and assumptions of the close to constant sedimentation rate, the inconsistencies of various of different dating methods or irregularity of the Holocene optimum (e.g., An et al., 2000; He et al., 2004).

From ~3.7 to ~2.4 ka, the decreasing susceptibility of the studied sections suggests a drying and cooling climate trend that correlates with the tree pollen data (Figure 3.12). The pollen sequence collected from the Taishizhuang peat site, located at the southeastern edge of the Mongolian Plateau, confirms a significant climatic variation taken place at around ~3.4 ka, and during that time, the tree component almost disappeared entirely (Jin and Liu, 2002; Tarasov et al., 2006). Both in the south-central and the southeastern Inner Mongolia region, a major cultural shift occurred at ~3.5 ka (Liu and Feng 2012). After ~3.7 ka, aeolian sand transportation took place more frequently and the East Asian summer monsoon strength decayed significantly, as perceived from the higher probability density values (Wang et al., 2014). A drying and cooling climatic shift also found in two cave speleothem sequences in the southern China from the Linhua Cave at ~3.3–3.0 ka (Cosford et al., 2008), and from the Heshang Cave at ~3.6–3.1 ka (Hu et al., 2008).

For the interval of ~2.4–1.2 ka, the magnetic climate data of this study coincides well with the tree pollen data of the Hongyuan peatland (Zhou et al., 2010), the Daihai Lake (Xiao et al., 2004), and the Hulun Lake (Wen et al., 2010) (Figure 3.12). This period can be confirmed by the moist grassland at the Guanzhong Basin (Li et al., 2003). Furthermore, in Figure 3.12, the correlation analysis of magnetic susceptibility and tree pollen data shows good agreement for the cold-dry interval of ~1.2–0.81 ka. Although the warmer interval of ~0.81–0.48 ka, recorded by the magnetic proxies in this study, does not correlate well with the tree pollen data of the Hongyuan peatland (Zhou et al., 2010) and the Hulun Lake (Wen et al., 2010), however, it shows a good agreement with the tree pollen data of the Daihai Lake (Xiao et al., 2004) (Figure 3.12). Our results are in broad agreement with pollen records, and demonstrate that same climatic variation occurred along the south-to-north eastern Chinese Loess Plateau during the Holocene.

3.5.3 Comparison of Global Paleoclimatic Records

Our results of Holocene climate changes in China can be compared with the global records. We compare our low frequency magnetic susceptibility (χ_{lf}) records of YZ3 and JJ3 sections with the Lake Baikal $\delta^{18}O$ values from diatom silica (Mackay et al., 2011), FD records of the Burdukovo loess section in Siberia (Kravchinsky et al., 2013), temperature variations in the northern hemisphere (McMichael, 2012), and Drift Ice Indices Stack from the North Atlantic (Bond et al., 2001) (Figure 3.13). Temperature variations in the northern hemisphere during the

Holocene have been reconstructed through the average of various published data (McMichael, 2012). The studied major episodes correspond visually to the other global records (Figure 3.13).

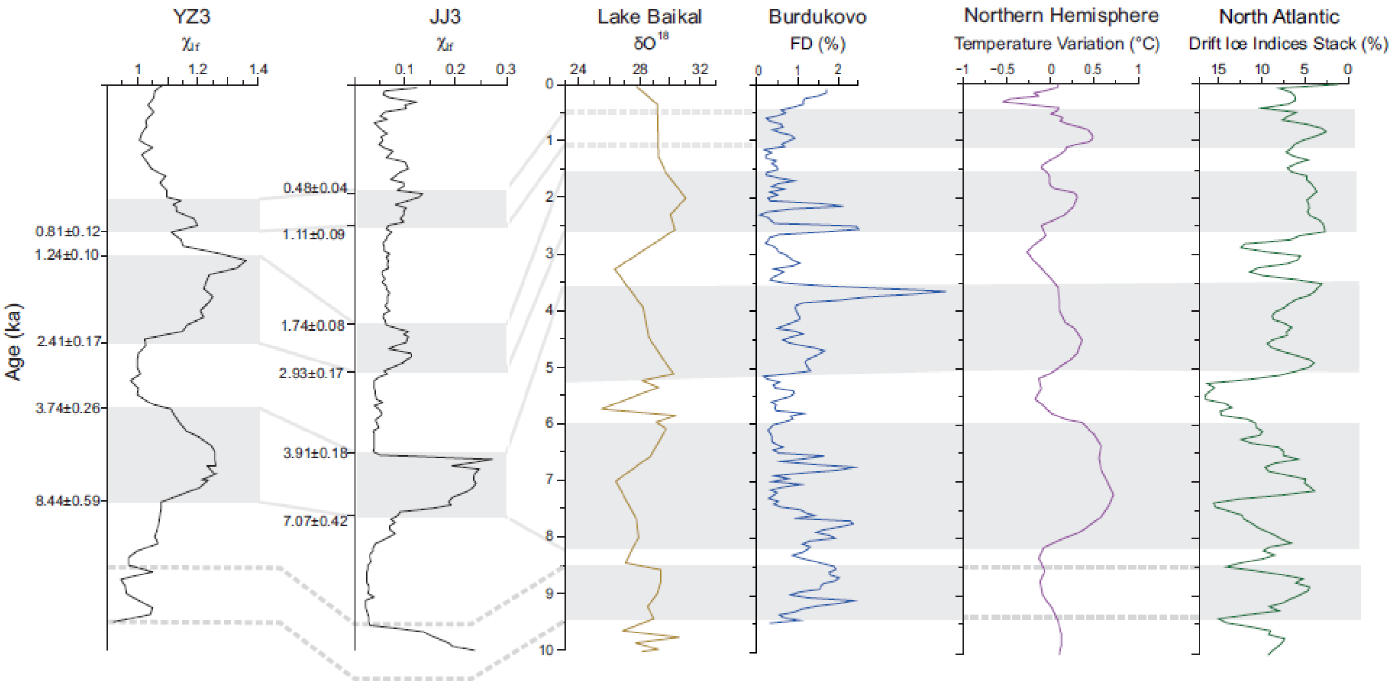

Figure 3.13. Regional and global correlations (from south to north): χ_{lf} — low frequency magnetic susceptibility (10^{-6} m^3 kg^{-1}) for YZ3 section (this study); χ_{lf} (10^{-6} m^3 kg^{-1}) for JJ3 section (this study); Lake Baikal δO^{18} profile linked to mass-balancing isotope measurements in per mil deviations from VSMOW (Vienna Standard Mean Ocean Water) (Mackay et al., 2011); frequency dependence (FD) parameter from loess section of Burdukovo in Siberia (Kravchinsky et al., 2013); temperature variations (°C) in the northern hemisphere (relative to mean temperature during 1960–1980) averaged from multiple published sources (McMichael, 2012); and Drift Ice Indices Stack from North Atlantic (Bond et al., 2001). See Figure 3.1 for the locations. Grey horizontal bars indicate the warm-wet climatic intervals based on the record of this study.

For ~8.4–3.7 ka, our data show high susceptibility and indicate warm-humid period for the whole interval. Whereas, $\delta^{18}O$ values of the Lake Baikal (Mackay et al., 2011), FD values of the Burdukovo loess section (Kravchinsky et al., 2013), temperature variations in the northern hemisphere (McMichael, 2012), and Drift Ice Indices Stack from the North Atlantic (Bond et al., 2001) show two peaks during that interval (Figure 3.13). The higher latitude section Burdukovo resolves short-term climate variations. The Lake Baikal record sampling resolution is quite low, but it also registers the cooling interval between ~5 and 6 ka very well. There exists no clear indication of such cooling interval in the Chinese loess, lacustrine, or other records. It may be due to the reason that the high latitudes are more sensitive to the millennial scale changes in the orbital parameters than the southern latitudes as demonstrated by the analysis in Loutre et al. (1992). Usoskin et al. (2007) suggested the probability of the effect of the orbital parameters of the Earth's climate being insignificant in clarifying the direct influence of solar variability on climate change. Beer et al. (2006) examined the probable feedback mechanisms for the amplification of the solar heating effect. Nevertheless, the whole interval of ~8.4–3.7 ka in China can be considered warm and humid period. The period between ~7 and 4.2 ka BP was demonstrated as high summer temperature in the mid and high latitude areas of the northern hemisphere (Klimenko et al., 1996; Alverson et al., 2003). Furthermore, an extensive paleosol, developed on the eastern belt of the Badain Jaran Desert, indicates a climate optimum in the mid Holocene (Yang et al., 2011). This humid episode between ~8.4 ka and ~3.7 ka is also found in the North Africa (Guo et al., 2000). Therefore, the interval of ~8.4–3.7 ka can be considered a globally registered Holocene optimum period.

A cool and dry climate from ~3.7 to ~ 2.4 ka caused the lowest χ_{lf} and well-preserved loess/sand in the studied area, also indicated by other global data (Figure 3.13). A cold and arid period from ~3.5 to ~2.5 ka in the northern hemisphere was determined by Mayewski et al. (2004), and this interval is almost the same arid period as found in this study. In the northern hemisphere, the 3.5–2.5 ka shows rapid climate change intervals including the North Atlantic ice-rafting events (Bond et al., 1997), and strengthened westerlies over the North Atlantic and Siberia (Meeker and Mayewski, 2002). The interval, at 3.5–2.5 ka, also presents a strong aridity in the regions like the East Africa, the Amazon Basin, Ecuador, and the Caribbean/Bermuda region (Haug et al., 2001). Wanner et al. (2011) reviewed that the global cooling event between ~3.3 and ~2.5 ka coincided with a considerably low solar activity forcing.

In Figure 3.13, warmer interval of ~2.4–1.2 ka and colder interval of ~1.2–0.81 ka in the studied area correlate well with the δ^{18}O values of the Lake Baikal (Mackay et al., 2011), FD values of the Burdukovo loess section (Kravchinsky et al., 2013), temperature variations in the northern hemisphere (McMichael, 2012), and Drift Ice Indices Stack from the North Atlantic (Bond et al., 2001). This event (~1.2 to 1.0 ka) corresponds to the maxima in the δ^{14}C and ^{10}Be records, indicating a weakening in solar output at this interval (Mayewski et al., 2004). At low latitudes, ~1.2–1.0 ka usually shows dry conditions in the tropical Africa and the monsoonal Pakistan (Gasse, 2000; 2001). During ~1.2 to 1.0 ka, atmospheric CO_2 surged moderately and caused variations in solar output resulting in drought in the Yucatan (Hodell et al., 1991, 2001). The other warmer interval of ~0.81–0.48 ka also corresponds to FD parameter in the Burdukovo (Kravchinsky et al., 2013), temperature variations in the northern hemisphere (McMichael, 2012), and Drift Ice Indices Stack from the North Atlantic (Bond et al., 2001). However, the resolution of the δ^{18}O data from the Holocene sediments of the Lake Baikal is not very high (Mackay et al., 2011), and does not allow to evaluate this interval in the Lake Baikal.

Our results demonstrate that changes in petromagnetic parameters of the loess-paleosol sequences in the studied area correlate closely with variations in climate documented separately, as explored by other proxies. Both regional and global record show similar pattern of climatic variations during the Holocene (Figures 3.12 and 3.13). Such correspondence demonstrates the global connections among the continental climate in Asia and the central Eurasia, temperature variations in the northern hemisphere, and the oceanic climate of the North Atlantic. Furthermore, the Holocene optimum period (~8.4 to 3.7 ka) in the studied regions, indicating a stronger warm-wet phase, appears to be a globally registered warming period.

3.6 Conclusions

(5) Petromagnetic and grain size analyses provide evidence for pedogenic alteration in the Holocene loess sequences of the Chinese Loess Plateau, affected by the climatic variation in temperature and precipitation but not by the climatic variation of wind intensity.

(6) Results indicate that subsequent warm-humid phase occurred in the studied regions during ~8.4–3.7 ka, ~2.4–1.2 ka, and ~0.81–0.48 ka, evidenced by the development of paleosols as well as high values of petromagnetic parameters in all sections.

(7) Results demonstrate that the Holocene climatic optimum period, in the studied regions, occurred between ~8.4 and ~3.7 ka.

(8) The Holocene climate record of the studied regions is consistent with the reported climate records from the tree pollen analysis along the south-to-north eastern Chinese Loess Plateau

at that time, suggesting that that same climatic variation occurred in the eastern monsoonal China.

(9) Our results correspond to the record of climate changes on regional and/or global scales, implying that similar climatic pattern of changes occurred in different regions of the world during the Holocene and the Holocene climatic optimum took place at the same time interval all over the northern hemisphere.

References

Alverson, K.D., Bradley, R.S., Pedersen, T.F., 2003. Paleoclimate, Global Change and the Future. Springer, New York.

An, Z.S., and Xiao, J.L., 1990. Study on the eolian dust flux over the Loess Plateau – an example. Chin. Sci. Bull., 35, 1627–1631.

An, Z.S., Kukla, G., Porter, S.C., Xiao, J.L., 1991. Late quaternary dust flow on the Chinese Loess Plateau. Catena, 18, 125–132.

An, Z.S., Porter, S.C., Kutzbach, J.E., Wu, X.H., Wang, S.M., Liu, X.D., Li, X.Q., Zhou, W.J., 2000. Asynchronous Holocene optimum of the East Asian monsoon. Quaternary Science Reviews, 19, 734–762.

An, C.B., Tang, L.Y., Barton, L., and Chen, F.H., 2005. Climate change and cultural response around 4000 cal yr B.P. in the western part of Chinese Loess Plateau. Quaternary Research, 63, 347–52.

Baker, P.A., Seltzer, G.O., Fritz, S.C., Dunbar, R.B., Grove, M.J., Tapia, P.M., Cross, S.L., Rowe, H.D., and Broda, J.P., 2001. The History of South American tropical precipitation for the past 25,000 years. Science, 291, 640–43.

Balsam, W., Ji, J.F., Chen, J., 2004. Climatic interpretation of the Luochuan and Lingtai loess sections, China, based on changing iron oxide mineralogy and magnetic susceptibility. Earth Planet. Sci. Lett., 223, 335–348.

Beer, J., Vonmoos, M., Muscheler, R., 2006. Solar variability over the past several millennia. Space Science Reviews, 125, 67–79.

Bianchi, G.G., and McCave, I.N., 1999. Holocene periodicity in north Atlantic climate and deep-ocean flow south of Iceland. Nature, 397, 515–17.

Bond, G., Showers, W., Cheseby, M., Lotti, R., Almasi, P., deMenocal, P., Priore, P., Cullen, H., Hajdas, I., Bonani, G., 1997. A pervasive millenial-scale cycle in North Atlantic Holocene and glacial climates. Science, 278, 1257– 1266.

Bond, G., Kromer, B., Beer, J., Muscheler, R., Evans, M.N., Showers, W., Hoffmann, S., Lotti-Bond, R., Hajdas, I., Bonani, G., 2001. Persistent solar influence on north Atlantic climate during the Holocene. Science, 294, 2130–2136.

Cosford, J., Qing, H., Eglington, B., Mattey, D., Yuan, D., Zhang, M., Cheng, H., 2008. East Asian monsoon variability since the Mid-Holocene recorded in a high-resolution, absolute-dated aragonite speleothem from eastern China. Earth and Planetary Science Letters, 275(3), 296–307.

D'Arrigo, R., Jacoby, G., Pederson, N., Frank, D., Buckley, B., Nachin, B., Mijiddorj, R. and Dugarjav, C., 2000. Mongolian tree-rings, temperature sensitivity and reconstructions of Northern Hemisphere temperature. The Holocene, 10(6), 669–672.

Ding, Z.L., Rutter, N.W., Liu, T., 1993. Pedostratigraphy of Chinese loess deposits and climatic cycles in the last 2.5 Ma. Catena, 20, 73–91.

Ding, Z. L., Z. W. Yu, N. W. Rutter, and T. S. Liu, 1994. Towards an orbital time scale for Chinese loess deposits, Quat. Sci. Rev., 13, 39–70.

Evans, M.E., and Heller, F., 2003. Environmental Magnetism: Principles and Applications of Enviromagnetics, Elsevier Science, Academic Press.

Feng, Z.D., Thompson, L.G., Mosley-Thompson, E., and Yao, T.D., 1993. Time-space model of climatic change in China during the past 10000 years. The Holocene, 3, 174–180.

Feng, Z.D., An, C.B., Wang, H.B., 2006. Holocene climatic and environmental changes in the arid and semi-arid areas of China: a review. The Holocene, 16, 119–130.

Gasse, F., 2000. Hydrological changes in the African tropics since the last glacial maximum. Quaternary Science Reviews, 19, 189–211.

Gasse, F., 2001. Hydrological changes in Africa. Science, 292, 2259–2260.

Guo, Z.T., Petit-Maire, N. and Kröpelin, S., 2000. Holocene nonorbital climatic events in present-day arid areas of northern Africa and China. Global and Planetary Change, 26, 97–103.

Haug, G.H., Hughen, K.A., Sigman, D.M., Peterson, L.C., Röhl, U., 2001. Southward migration of the intertropical Convergence zone through the olocene. Science, 293, 1304–1308.

He, Y., Theakstone, W.H., Zhang, Z.L., Zhang, D., Yao, T.D., Chen, T., Shen, Y.P., Pang, H.X., 2004. Asynchronous Holocene climatic change across China. Quaternary Research, 61, 52–61.

Heller, F., and Liu, T.S., 1984. Magnetism of Chinese loess deposits. Geophysical Journal of the Royal Astronomical Society, 77, 125–141.

Herzschuh, U., 2006. Palaeo-moisture evolution in monsoonal central Asia during the last 50,000 years. Quaternary Science Reviews, 25, 163–178.

Hodell, D.A., Curtis, J.H., Jones, G.A., Higuera-Gundy, A., Brenner, M., Binford, M.W., Dorsey, K.T., 1991. Reconstruction of Caribbean climate change over the past 10,500 years. Nature, 352, 790–793.

Hodell, D.A., Brenner, M., Curtis, J.H., Guilderson, T., 2001. Solar forcing of drought frequency in the Maya Lowlands. Science, 292, 1367–1370.

Hu, C., Henderson, G. M., Huang, J., Xie, S., Sun, Y., & Johnson, K. R., 2008. Quantification of Holocene Asian monsoon rainfall from spatially separated cave records. Earth and Planetary Science Letters, 266(3), 221–232.

Huang, C. C., Zhou, J., Pang, J., Han, Y., & Hou, C., 2000. A regional aridity phase and its possible cultural impact during the Holocene Megathermal in the Guanzhong Basin, China. The Holocene 10(1), 135–142.

Jacoby, G., D'Arrigo, R., Davaajamts, T.S., 2000. Mongolian tree-rings and 20th century warming. Science, 273, 771–773.

Jin, G.Y., and Liu, T.S., 2002. Mid-Holocene climate change in North China, and the effect on cultural development. Chinese Science Bulletin, 47, 408–413.

King, J.W., and Channell, J.E.T., 1991. Sedimentary magnetism, environmental magnetism, and magnetostratigraphy. Rev. Geophys., 358–370.

King, J.W., Banerjee, S.K., Marvin, J., Ozdemir O., 1982. A comparison of different magnetic methods for determining the relative grain size of magnetite in natural materials: some results from lake sediments, Earth Planet. Sci. Lett., 59, 404–419.

Klimenko, V.V., Klimanov, V.A., Fedorov, M.V., 1996. The history of the mean temperature of the Northern Hemisphere over the last 11,000 years. Trans. Russ. Acad. Sci., 4, 626–629.

Kravchinsky, V.A., Langereis, C.G., Walker, S.D., Dlusskiy, K.G. and White, D., 2013. Discovery of Holocene millennial climate cycles in the Asian continental interior: Has the sun been governing the continental climate?. Global and Planetary Change, 110, 386–396.

Loutre, M.F., Berger, A., Bretagnon, P. and Blanca, P.L., 1992. Astronomical frequencies for climate research at the decadal to century time scale. Climate Dynamics, 7(4), 181–194.

Li, J.J., 1996. Climatic change in arid areas of China and monsoon fluctuations during the past 10 kyears. Journal of Arid Environments, 32, 1–7.

Li, X.Q., Zhou, J., and Dodson, J., 2003. The vegetation characteristics of the 'Yuan' area at Yaoxian on the Loess Plateau in China over the last 12000 years. Review of Palaeobotany and Palynology, 124, 1–7.

Liu, T.S., 1985. Loess and Environment. Beijing: Science Press pp. 481.

Liu, F., and Feng, Z., 2012. A dramatic climatic transition at~ 4000 cal. yr BP and its cultural responses in Chinese cultural domains. The Holocene, 22(10), 1181–1197.

Lu, H.Y., VanHuissteden, K.O., An, Z.S., Nugteren, G., Vandenberghe, J., 1999. East Asia winter monsoon variations on a millennial time-scale before the last glacial– interglacial cycle. J. Quat. Sci., 14, 101–110.

Lu, H.Y., VanHuissteden, K.O., Zhou, J., Vandenberghe, J., Liu, X.D., An, Z.S., 2000. Variability of East Asian winter monsoon in Quaternary climatic extremes in North China. Quat. Res., 54, 321–327.

Lu, H.Y., Yi, S.W., Liu, Z.Y., Mason, J.A., Jiang, D.B., Cheng, J., Stevens, T., Xu, Z.W., Zhang, E.L., Jin, L.Y., Zhang, Z.H., Guo, Z.T., Wang, Y., Otto-Bliesner, B., 2013. Variation of East Asian monsoon precipitation during the past 21 ky and potential CO2 forcing. Geology, 41(9), 1023–1026.

Ma Ji., Yue L., Yang Li., Sun Lu, Xu, 2011. Southeastern margin of the Mu Us Desert Holocene sectional OSL's and paleoclimatic significance (in Chinese). Quaternary Research, 31 (1), 120–129.

Mackay, A.W., Swann, G.E.A., Brewer, T., Leng, M.J., Morley, D.W., Piotrowska, N., Rioual, P., White, D., 2011. A reassessment of late glacial-Holocene diatom oxygen isotope records from Lake Baikal using a mass balance approach. Journal of Quaternary Science, 26 (6), 627–634.

Maher, B.A., 1988. Magnetic properties of some synthetic submicron magnetite, Geophys. J., 94, 83–96.

Maher, B.A., 2011. The magnetic properties of Quaternary aeolian dust and sediments, and their palaeoclimatic significance. Aeolian Research, 3, 87–144.

Mayewski, P.A., Rohling, E.E., Stager, J.C., Karlén, W., Maasch, K.A., Meeker, L.D., Meyerson, E.A., Gasse, F., Kreveld, S.V., Holmgren, K., Lee-Thorp, J., Rosqvist, G., Rack, F., Staubwasser, M., Schneider, R.R. and Steig, E.J. 2004. Holocene climate variability. Quaternary Research, 62, 243–55.

McDermott, F., Mattey, D.P., and Hawkesworth, C., 2001. Centennial-scale Holocene climate variability revealed by a highresolution speleothem 5180 record from SW Ireland. Science, 294, 1328–31.

McMichael, A.J., 2012. Insights from past millennia into climatic impacts on human health and survival. Proceedings of the National Academy of Sciences, 109(13), 4730–4737.

Meeker, L.D., and Mayewski, P.A., 2002. A 1400-year high-resolution record of atmospheric circulation over the North Atlantic and Asia. Holocene, 12, 257–266.

Mu, Y., Qin, X., Zhang, L., Xu, B., 2016. Holocene climate change evidence from high-resolution loess/paleosol records and the linkage to fire–climate change–human activities in the Horqin dunefield in northern China. Journal of Asian Earth Sciences, 121, 1–8.

Pye, K., and Zhou, L.P., 1989. Late Pleistocene and Holocene aeolian dust deposition in North China and the Northwest Pacific Ocean. Palaeogeography, Palaeoclimatology, Palaeoecology, 73, 11–23.

Rea, D. K., 1994. The paleoclimatic record provided by eolian deposition in the deep sea: The geologic history of wind, Rev. Geophys., 32, 159–195.

Robinson, S.G., 1986. The late Pleistocene paleoclimatic record of North Atlantic deep-sea sediments revealed by mineral-magnetic measurements, Phys. Earth Planet. Inter., 42, 22–47.

Rutter, N.W., 1992. Chinese loess and global change. Quat. Sci. Rev., 11, 275– 281.

Shen, J., 2013. Spatiotemporal variations of Chinese lakes and their driving mechanisms since the Last Glacial Maximum: a review and synthesis of lacustrine sediment archives. Chinese Science Bulletin, 58 (1), 17–31.

Shen, C.M., Liu, K.-B., Tang, L.Y., Overpeck, J.T., 2006. Quantitative relationships between modern pollen rain and climate in the Tibetan Plateau. Review of Palaeobotany and Palynology, 140, 61–77.

Shi, Y.F., Kong, Z.C. and Wang, S.M., 1992. Climatic variations and the major events in the Holocene Megathermal in China (in Chinese). Science in China, 12, 300–308.

Steig, E.J., 1999. Mid-Holocene climate change. Science, 286, 1485–87.

Sun, J.M., 2000. Origin of eolian sand mobilization during the past 2300 years in the Mu Us Desert, China. Quaternary Research, 53, 73–88.

Sun, J.M., Ding, Z.L., Liu, T.S., Rokosh, D., Rutter, N.W., 1999. 580,000-year environmental reconstruction from aeolian deposits at the Mu Us desert margin, China. Quat. Sci. Rev., 18, 1351–1364.

Sun, J.M., Li, S. H., Han, P., Chen, Y., 2006. Holocene environmental changes in the central Inner Mongolia, based on single-aliquot-quartz optical dating and multi-proxy study of dune sands. Palaeogeography, Palaeoclimatology, Palaeoecology, 233, 51–62.

Sun, Q.L., Wang, S.M., Zhou, J., Shen, J., Cheng, P., Xie, X.P., Wu, F., 2009. Lake surface fluctuations since the late glaciation at Lake Daihai, North-central China: a direct indicator of hydrological process responses to East Asian monsoon climate. Quaternary International, 194, 45–54.

Tarasov, P., Jin, G.Y., and Wagner, M., 2006. Mid-Holocene environmental and human dynamics in Northeastern China reconstructed from pollen and archaeological data. Palaeogeography Palaeoclimatology Palaeoecology, 241, 284–300.

Thompson, R., and Oldfield, F., 1986. Environmental Magnetism, Allen and Unwin, London.

Thompson, L.G., Mosley-Thompson, E., Davis, M.E., Bolzan, J.F., Dai, J., Yao, T., Gundestrup, N., Wu, X., Klein, Z. and Xie, Z., 1989. Holocene-Late Pleistocene climatic ice core records from Qinghai-Tibetan Plateau. Science, 246, 474–477.

Usoskin, I.G., Solanki, S.K., Kovaltsov, G.A., 2007. Grand minima and maxima of solar activity: new observational constraints. Astronomy and Astrophysics, 471, 301–309.

Vandenberghe, J., An, Z.S., Nugteren, G., Lu, H.Y., VanHuissteden, K., 1997. New absolute time scale for the Quaternary climate in the Chinese loess region by grain-size analysis. Geology, 25, 35–38.

Wang, H., Chen, J., Zhang, X., & Chen, F., 2014. Palaeosol development in the Chinese Loess Plateau as an indicator of the strength of the East Asian summer monsoon: Evidence for a mid-Holocene maximum. Quaternary International, 334, 155–164.

Wanner, H., Solomina, O., Grosjean, M., Ritz, S. P., Jetel, M., 2011. Structure and origin of Holocene cold events. Quaternary Science Reviews, 30(21), 3109–3123.

Wen, R.L., Xiao, J.L., Chang, Z.G., Zhai, D.Y., Xu, Q.H., Li, Y.C., Itoh, S., 2010. Holocene precipitation and temperature variations in the East Asian monsoonal margin from pollen data from Hulun Lake in northeastern Inner Mongolia, China. Boreas, 39, 262–272.

Wurster, C.M., and Patterson, W.P., 2001. Late Holocene climate change for the eastern interior United States. evidence from highresolution 6180 value of marital otoliths. Palaeogeography Palaeoclimatology Palaeoecology, 170, 81–100.

Xiao, J.L., Xu, Q.H., Nakamura, T., Yang, X.L., Liang, W.D., Inouchi, Y., 2004. Holocene vegetation variation in the Daihai Lake region of north-central China: a direct indication of the Asian monsoon climatic history. Quaternary Science Reviews, 23, 1669–1679.

Yang, S. L., and Ding, Z. L., 2004. Comparison of particle size characteristics of the Tertiary 'red clay'and Pleistocene loess in the Chinese Loess Plateau: implications for origin and sources of the 'red clay'. Sedimentology, 51(1), 77–93.

Yang, X.P., Scuderi, L., Paillou, P., Liu, Z.T., Li, H.W., Ren, X.Z., 2011. Quaternary environmental changes in the drylands of China-a critical review. Quaternary Science Reviews, 30, 3219–3233.

Yu, L., and Oldfield, F., 1989. A multivariate mixing model for identifying sediment source from magnetic measurements, Quaternary Research, 32, 168–181.

Zhao, Y., and Yu, Z., 2012. Vegetation response to Holocene climate change in East Asian monsoon-margin region. Earth-Science Reviews, 113(1), 1–10.

Zhao, H., Chen, F. H., Li, S. H., Wintle, A. G., Fan, Y. X., Xia, D. S., 2007. A record of Holocene climate change in the Guanzhong Basin, China, based on optical dating of a loess-palaeosol sequence. The Holocene, 17(7), 1015–1022.

Zhou, W.J., and An, Z.S., 1994. Stratigraphic divisions of the Holocene loess in China. Radiocarbon, 36, 37–45.

Zhou, S.Z., Chen, F.H., and Pan, B.T., 1991. Environmental changes during the Holocene in the Western China on millennial timescale. The Holocene, 1, 151–56.

Zhou, W.J., Yu, S.Y., Georges, B., Kukla, G.J., Jull, A.J.T., Xian, F., Xiao, J.Y., Colman, S.M., Yu, H.G., Liu, Z., Kong, X.H., 2010. Postglacial changes in the Asian summer monsoon system: a pollen record from the eastern margin of the Tibetan Plateau. Boreas, 39, 528–539.

Zhu, Z.D., Liu, S., He, R.Z., 1982. Deserts evolution in the historic time, Physical Geography of China. Historic Geography, 6, 249–253.

Chapter 4[*]

Microwave paleointensities indicate a low paleomagnetic dipole moment at the Permo-Triassic boundary

4.1 Introduction

The behavior of Earth's magnetic field in the geological past is found to be inconsistent and poorly studied for some epochs. Interpreting the changes in the absolute paleointensity variations presents an opportunity to understand the evolution of Earth's magnetic field and to obtain new information about the geodynamo's behavior. It can inform us how the convection in the lowermost part of the Earth's mantle might be influencing the generation of the magnetic field in the underlying core (Valet et al., 2003; Tauxe & Yamazaki, 2007; Biggin et al., 2012). Reliable absolute geomagnetic field intensity data over geological time periods are required to solve geoscience problems such as the dynamics of Earth's core, the thermal interaction of the core-mantle boundary, the relationship between the mean paleointensity and the reversal frequency and the nucleation date of Earth's inner core (Glatzmaier et al., 1999; Tarduno et al., 2006; Christensen and Wicht, 2007; Biggin et al., 2012; Biggin et al., 2015). Although many studies have attempted to capture the detailed information about the variation in paleointensity, these are not sufficient enough to be reliable (see the absolute paleointensity PINT database; Biggin et al., 2010) due to the lack of proper materials and magnetomineralogical alterations during the experiments. Thus, it is important to get more reliable data about the history of Earth's magnetic

---

[*] A version of this chapter has been published as: Anwar, T., Hawkins L., Kravchinsky, V.A., Biggin, A.J., Pavlov, V.E., 2016. Microwave paleointensities indicate a low paleomagnetic dipole moment at the Permo-Triassic boundary. Physics of the Earth and Planetary Interiors, 260, 62-73.

field intensity to compare the behavior of geodynamo models with measured data on all accessible timescales.

Continental flood basalts (CFBs) are considered excellent objects for decoding the evolution of Earth's magnetic field since they are related to huge eruptions of lava flows during very short spans of volcanic activity. One of the largest CFBs is situated at and around the Siberian platform and was formed during the Permo-Triassic boundary (PTB) at approximately 250 Ma (Courtillot and Renne, 2003; Almukhamedov et al., 2004; Reichow et al., 2005, 2009, and references therein). This is a time interval when gigantic magma volumes erupted (Kuzmin et al., 2010), the largest mass extinction occurred, and dramatic climatic changes took place (Kravchinsky, 2012), and thus, this interval played a crucial role in Earth's geological history. This is also a period of particular interest concerning the characteristics of the dipolar field to investigate the extension of the Mesozoic dipole low (MDL), which is a time interval characterized by a dipole with a moment of approximately 30% of that of the present magnetic field (Prévot et al. 1990). The MDL hypothesis has also been supported by several other studies (Pick and Tauxe, 1993; Kosterov, 1998; Thomas and Biggin, 2003; Shcherbakova et al., 2011; 2012; Tauxe et al., 2013) although its duration is highly unclear.

Geomagnetic field directions are well known for the PTB, but paleointensity data are insufficient giving rise to a contradiction about the average dipole moment during this time period. Some studies from the northern part of the Siberian trap basalts (STB) have shown lower (approximately half) paleointensity values compared to the present day field and suggested that the MDL reached back to the PTB (Heunemann et al., 2004; Shcherbakova et al., 2005; 2013;

2015). By contrast, another study, conducted on the southeastern part of the STB, has indicated a possibility of higher absolute paleointensity values, almost equal to the present day field, and suggested that the MDL did not extend back to the PTB (Blanco et al., 2012). Previous studies used the conventional thermal Thellier-Thellier technique (Thellier and Thellier, 1959; Coe, 1967) to identify the ancient field intensity for the STB. However, the magnetic minerals in samples are sometimes chemically altered during thermal paleointensity experiments (Valet et al., 1996; Heller et al., 2002; Smirnov and Tarduno, 2003). Such studies were conducted on the sections of either the northern or the southeastern part of the formation. One argued source of discrepancy is that multi-domain behavior causing curvature of the Arai plots, with the lower paleointensity results coming from the high temperature components which are underestimates of the true paleointensity results. Another possibility is that this discrepancy is caused by secular variation and the geomagnetic field being recorded at slightly different times for the northern extrusive and southeastern intrusive localities, each being insufficiently large to provide a representative time average.

To derive whether Earth's magnetic field is weak or strong at that time period, further paleointensity measurements are required. Here, for the first time, this study presents the microwave paleointensity data of the PTB. The microwave paleointensity method (Walton et al., 1996; Hill and Shaw, 1999) minimizes the occurrence of magneto-mineralogical alteration which is the major problem associated with absolute paleointensity determination, resulting in a higher success rate compare to the conventional Thellier-Thellier method (Böhnel et al., 2003 and Biggin, 2010). Here, we intend to collate microwave Thellier-type paleointensity data of this study with the thermal Thellier-type paleointensity data of previous studies, and produce a grand mean paleomagnetic dipole moment for the PTB. This provides an opportunity to investigate the duration and characteristics of the MDL. Furthermore, QPI analyses (Biggin & Paterson, 2014; Biggin et al., 2015) performed on all the published data including this study for the Siberian Traps is presented. Moreover, this study covers a longer time interval involving both the extrusive and intrusive traps of the northern and the southeastern localities respectively, and thus, provides much wider geographical and spatial coverage.

4.2 Geological Settings

The STB of the Siberian platform represents the largest terrestrial continental igneous province. ^{40}Ar– ^{39}Ar radiometric dates indicate that Siberian trap volcanism was produced at the PTB (250 ± 1.6 Ma) (Renne et al., 1995; Reichow et al., 2002) and the geological evidence supports that these traps were deposited in a short time (0.9 ± 0.8 Ma) interval (Renne and Basu 1991) that did not exceed 2 Myr (Reichow et al., 2009). The enormous volcanic activity contributed the greatest mass extinction of flora and fauna in Earth’s history (Courtillot and Renne, 2003). The emplacement of the Siberian traps is coeval with a major environmental crisis (Erwin, 1994; Kravchinsky, 2012). These traps were built from one or more volcanic events involving the outpouring of large volumes of mainly basaltic magma. The volcanic sequence is about 6.5 km thick and the Permo-Triassic traps cover an area of approximately 3.7×10^6 km^2 with the original volume of almost 3.0×10^6 km^3 in the northern part of the Siberian platform and under the West Siberian sedimentary basin (Kravchinsky et al., 2002; Reichow et al., 2009; Kuzmin et al., 2010). The sills extend to the east and the southeast of the province with an approximate area of 1.5×10^6 km^2 (Zolotukhin and Al'mukhamedov, 1988). The magma source and emplacement mechanism of the traps can be described by numerous models. It is argued that the Siberian traps were linked to the rifting triggered by an upwelling mantle plume (Basu et al., 1998; Griffin et al., 1999; Courtillot et al., 1999; Kuzmin et al., 2010) rather than volcanism at an existing plate boundary (Almukhamedov et al., 1996; Courtillot et al., 1999; Saunders et al., 2005; Kuzmin et al., 2010). It has been further argued that melt intrusions could have produced the Siberian traps eruption (Elkins Tanton and Hager, 2000).

The Siberian traps contain mafic, ultramafic, and silicic rocks, both intrusive and extrusive. In this study, samples from both the northern extrusive (Maymecha-Kotuy region) and the southeastern intrusive (Sytikanskaya and Yubileinaya kimberlite pipes) part of the Permo-Triassic trap basalts on the Siberian platform were analyzed (Figure 4.1). Both these extrusive and intrusive localities are important to study as, together, these cover a longer time interval. Besides, these represent a huge territory providing a broad spatio-temporal representation of the PTB.

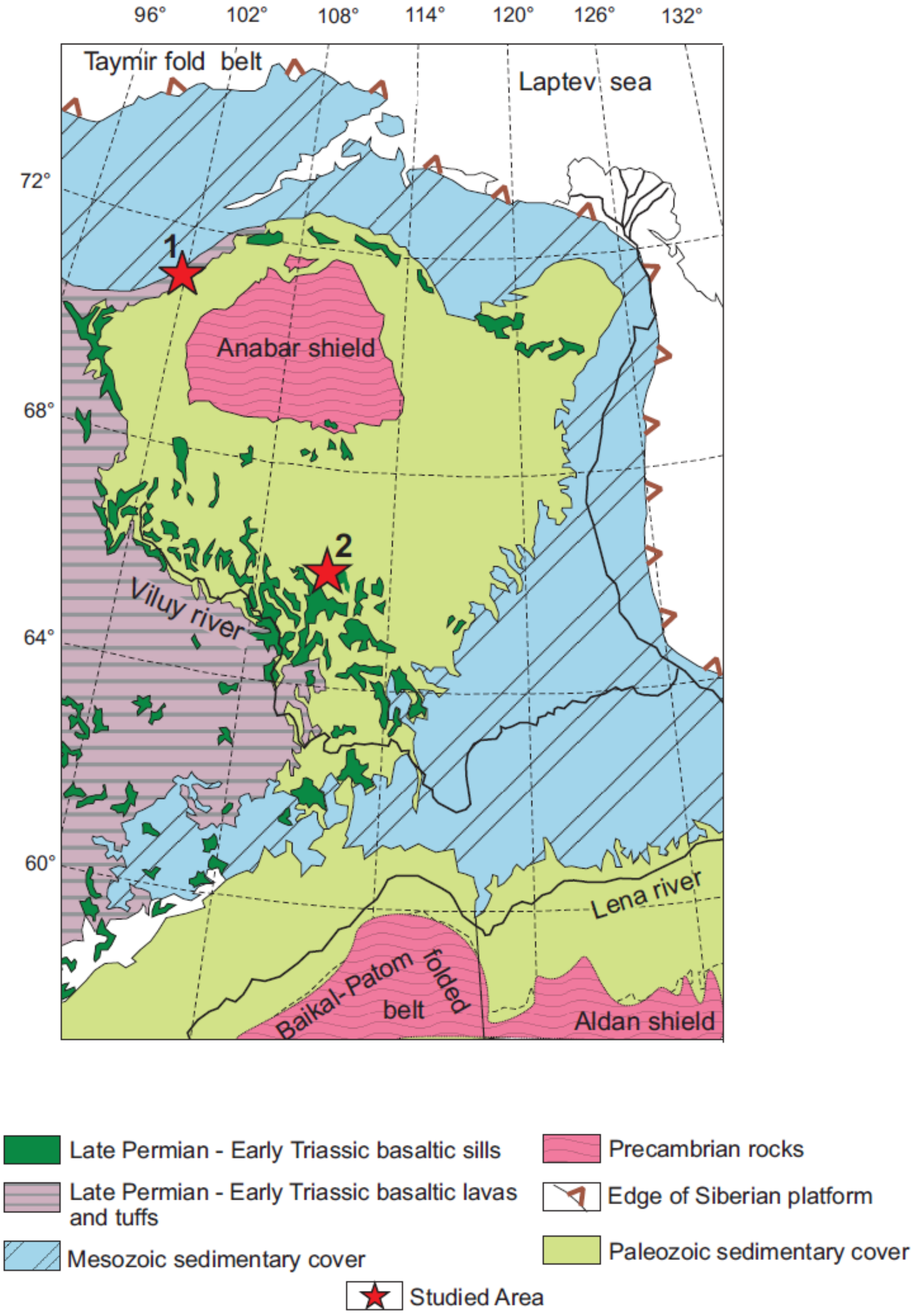

Figure 4.1. Geological map of the Siberian Traps and the geographic positions of the studied sections (after Courtillot et al., 2010). Red stars represent the study areas: 1 – Maymecha-Kotuy region, 2 – East Siberian intrusives (Sytikanskaya and Yubileinaya pipes).

The Maymecha-Kotuy region, comprising ~70,000 km^2, is situated in the northern part of the Siberian platform and in the western Anabar region (location 1 on Figure 4.1). The volcanic sequence is composed of the six formations, namely: Pravaboyar, Arydzhang, Onkuchak, Tyvankit, Delkan and Maymechin, overlying the Tunguss sedimentary series (Figure 4.2). The total thickness of this volcanic sequence is 4 km (Fedorenko and Czamanske, 1997). Both the Pravaboyar Formation located in the lower part of the Maymecha section and the Arydzhang Formation situated in the lower part of the Kotuy section are dated at 251.7 ± 0.4 Ma, while the Delkan Formation, representing upper part of the volcanic sequence of the Maymecha region, is dated at 251.1 ± 0.3 Ma by absolute U-Pb dating of the perovskite (Kamo et al., 2003). More recent studies indicate ages for these formations correspondingly to be 252.24 ± 0.12 and 251.90 ± 0.061 Ma (Burgess and Bowring, 2015). We have studied the samples from the Truba section (T) (71.55° N, 103.00° E) which comprises of the Onkuchak Formation along the Kotuy river valley (10 km downstream from the Kayak village) and from the Maymecha section (M) (70.82° N, 101.00° E) which corresponds to the Tyvankit and Delkan Formations in the Maymecha river (opposite to the mouth of the Kogotok stream). While the Onkuchak Formation is mainly composed of the tholeiitic basalts, the studied intervals of the Tyvankit and Delkan Formations are represented essentially by trachybasalts and high-Ti meta-nephelenitic lavas correspondingly (Kamo et al., 2003). The Truba section at Kotuy contains 42 basaltic flows and the total thickness of these strata is about 360 m. Samples of the 4 flows (flow 28, flow 29, flow 35, and flow 40) from the Truba section of the Onkuchak Formation have been measured (Figure 4.2). 17 directional groups (DG) and 13 individual directions (ID) were identified in the composite Kotuy section based on the analysis of the secular variations recorded in the lava flows, and the number of these DG and ID corresponds to the number of volcanic bursts and individual eruptions that formed the studied section (Pavlov et al., 2011; 2015). The division of the traps into separate lava flows was ambiguous for the Maymecha section; however, Shcherbakova et al. (2015) made an attempt to distinguish 42 lava flows and two intervals with undistinguishable flows (flows 1–34 are related to the Tyvankit Formation, and flows 35–42 are to the Delkan Formation) for this section. The total thickness of this section is about 380 m. Samples of the 3 flows (flow 23, flow 21, and flow 18) from the Maymecha section of the Tyvankit Formation have been measured. Paleomagnetic direction and magneto-mineralogical studies of these sections have already been published (Pavlov et al., 2011; Shcherbakova et al., 2013; 2015). Reversed polarity was identified for both the Truba section of the Onkuchak Formation (Fetisova et al., 2014; Pavlov et al., 2011), and the Maymecha section (Shcherbakova et al., 2015). Previous studies suggest that the main remanence carrier is titanomagnetite; for the Tyvankit Formation (Shcherbakova et al., 2015) and parts of the Onkuchak Formation (Shcherbakova et al., 2013), this is low titanium titanomagnetite with a Curie temperature close to pure magnetite, and for the rest of the Onkuchak Formation, the titanomagnetite is richer in titanium (Shcherbakova et al., 2013) with a depressed Curie temperature of 300–400°C. The grains that carry the remanent magnetization for the studied rocks are single-domain or small pseudo-single domain (Pavlov et al., 2011; Shcherbakova et al., 2013; 2015).

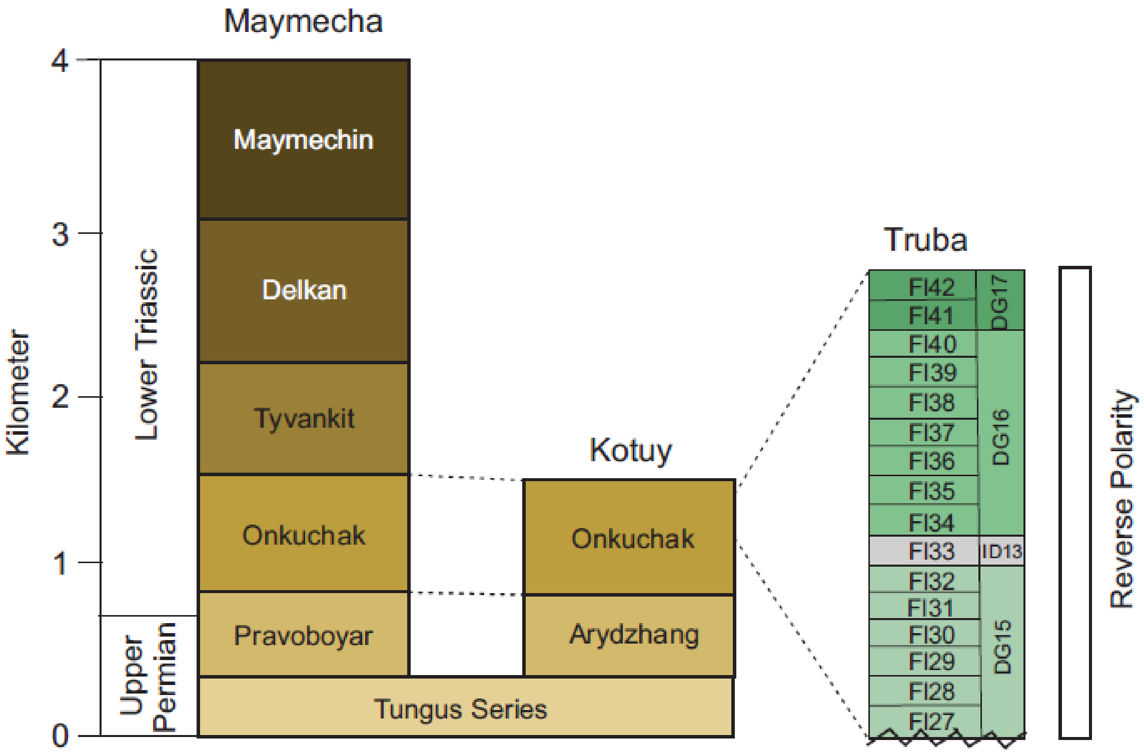

Figure 4.2. The stratigraphy and correlation of the volcanic sequences of Maymecha and Kotuy regions. Fl; flow, DG; directional groups (pulses), ID; individual directions (individual eruptions). (Correlation scheme after Pavlov et al., 2015).

A large part of the Siberian platform experienced only intrusive magmatism with extensive but relatively low-volume sills, which are hardly exposed on the surface and known mostly through drilling. For the southeastern part of the STB, 5-20 m thick intrusive (near surface intrusions) trap sills overlain in the area of Sytikanskaya (66.11˚ N, 111.80˚ E) and Yubileinaya (66.00˚ N, 111.70˚ E) kimberlite pipes have been studied (location 2 on Figure 4.1). This is one of the most eastern occurrences of Permo-Triassic flood basalts on the Siberian platform. The intrusive bodies are considered to be trap-related and coeval with the flood basalts but the ages of these are difficult to measure directly (Zolotukhin and Al'mukhamedov, 1988). Usually, the smaller sills extend from the main sill intrusion and comprise a few square kilometers. We have studied the samples from three sites (S1, S2, S3) of the Sytikanskaya and one site (Y1) of the Yubileinaya kimberlite pipe. Although the exact time relationship between the sills is hard to establish, the samples of different sites may be related to few phases of eruption that should provide some representation of geomagnetic secular variation. Paleomagnetic directions from these sills have already been reported and show a stable component of remanent magnetization with the presence of antipodal polarities- normal polarity for the Yubileinaya and reverse polarity for the Sytikanskaya section (Kravchinsky et al., 2002 and Blanco et al., 2012). The rock magnetic studies indicate that the primary remanence carriers are composed of a low titanium titanomagnetite or pure magnetite, containing single or pseudo-single domain particles (Kravchinsky et al., 2002; Blanco et al., 2012; Konstantinov et al., 2014).

4.3 Methodology

4.3.1 Scanning Electron Microscope

Scanning Electron Microscope (SEM) analysis was performed on the carbon coated polished thin sections using a Zeiss EVO LS15 EP-SEM instrument equipped with energy dispersive X-ray (EDX) spectroscopy to identify the morphological features and the chemical composition of the magnetic minerals in the samples. The SEM was operated at an acceleration voltage of 20 kV. The SEM results were obtained in the Scanning Electron Microscope Laboratory of the University of Alberta (Edmonton, Canada).

4.3.2 Microwave Paleointensity

In this study, absolute paleointensity has been investigated by using the internationally unique microwave paleointensity facility housed in the University of Liverpool's Geomagnetism Laboratory. For microwave paleointensity experiment, the high-frequency (14 GHz) microwaves are used instead of the conventional thermal energy to (de)magnetize the samples (Walton et al., 1996). The same experimental protocol can be used for both the microwave and thermal experiments (Hill and Shaw, 1999). In the thermal Thellier-Thellier method, phonons are responsible for the thermally induced alteration in samples. The microwave Thellier-Thellier technique minimizes the occurrence of magneto-mineralogical alteration by reducing the temperature that the bulk sample is heated to, and the duration of this heating (Hill & Shaw, 1999). This together with the fact that, unlike in batch heating experiments, measurement routines can be tailored to individual samples, tends to produce a higher success rate compared to the conventional Thellier-Thellier method (Böhnel et al., 2003; Biggin, 2010).

Microwave Thellier-type paleointensity experiments were performed using Liverpool's third generation system which incorporates three helium SQUID sensors, a triple-axis Helmholtz coil assembly surrounding the microwave resonant cavity, and vertical sample assembly with a vacuum holder. The samples were progressively demagnetized and remagnetized by the application of the high frequency (14 GHz) microwave radiation which was increased progressively in power and/or duration and the in-field/zero-field and zero-field/in-field (IZZI) protocol (Tauxe and Staudigel, 2004) was used for the paleointensity experiments. The experiment was usually continued until the NRM intensity was reduced to 10-20% of its original value. To test for sample alteration, partial thermoremanent magnetization (pTRM) checks (Coe, 1967 and Coe et al., 1978) were performed in all paleointensity experiments. Arai plots (Nagata et al., 1963) were used to analyze the results.

In total, 50 samples (23 samples from the northern localities and 27 samples from the southeastern localities) from 11 sites [T (flow 28), T (flow 29), T (flow 35), T (flow 40), M (flow 23), M (flow 21), M (flow 18), S1, S2, S3, and Y1] of 4 areas (Truba, Maymecha, Sytikanskaya, and Yubileinaya) of the Permo-Triassic trap basalts on the Siberian platform were subjected to microwave Thellier-type paleointensity measurements. In the previous study, rock magnetic and paleomagnetic directional analysis of these samples for both the northern localities (Pavlov et al., 2011 and Shcherbakova et al., 2013; 2015) and the southeastern localities (Kravchinsky et al., 2002 and Blanco et al., 2012) showed that the remanent magnetization represents stable primary magnetization components and these samples are suitable for paleointensity determination. Samples of small size, typically 5 mm in diameter and 3 to 6 mm in length, have been used for the microwave technique. The laboratory field intensity applied to the samples ranges between 7 and 50 μT. The applied field value was changed for additional verification of the results, and these indicated that the absolute paleointensity values were independent of these values. Furthermore, the laboratory field applied at an angle of at least 45° to the NRM to ensure that multidomain-like behavior would manifest as zig-zags in both the Arai plot and the Zijderveld plot as the latter can be invisible if the applied field is (anti-)parallel to the NRM (Yu & Tauxe, 2005).

4.3.3 Paleointensity Selection Criteria

There are a number of parameters to describe the behavior of experimental paleointensity data (e.g., Coe et al., 1978; Kirschvink, 1980; Selkin and Tauxe, 2000; Tauxe and Staudigel, 2004; Biggin et al., 2007, Paterson, 2011; Yu, 2012). The parameters used in this study to produce the reliable absolute paleointensity data were calculated according to the Standardized Paleointensity Definitions (Paterson et al., 2014). The threshold values listed in Table 4.1 have been applied for the selection here. This includes- the number of data points used to estimate the paleointensity (N), standard error of the slope over the slope of the best fitting line (β), fraction of the total NRM that is chosen from NRM-TRM plot to recover the paleointensity estimate (f), the gap factor representing the evenness of point spacing along the selected best-fit-line (g), the quality factor which is the combination of several parameters (q), the pTRM difference ratio (DRAT) which is the absolute discrepancy between a pTRM check and an original measurement of pTRM divided by the length of the best-fit-line, the sum of all DRATs over the range of temperatures used for the paleointensity measurement (CDRAT), the maximum angular deviation (MAD) of the data points on a vector diagram determined from a free-floating fit without the origin included and the angle between the anchored and free floating best-fit directions on a vector component diagram (α).

Table 4.1. Summary of the acceptance criteria for selecting paleointensity values of the individual samples.

Criterion	Threshold	Reference
Number of points (N)	≥4	
Scatter parameter (β)	≤0.1	Coe et al. 1978
Fraction of the NRM (f)	≥0.35	Coe et al. 1978
Quality factor (q)	≥2	Coe et al. 1978
Difference ratio (DRAT)	≤15%	Selkin and Tauxe, 2000
Maximum angle of deviation (MAD)	≤15°	Kirschvink 1980
Angular difference between anchored and floating PCA fit (α)	≤15°	Selkin and Tauxe, 2000

4.4 Results and Discussion

4.4.1 Scanning Electron Microscope

Six thin sections, one representing each site with accepted paleointensity results, were investigated using SEM analysis and compared to previously published petrographic and rock magnetic results. The magneto-mineralogy of the Truba section (flows 28 and 29) consists of titanomagnetite and ilmenite, as determined by Shcherbakova et al. (2013). The morphology of the magneto-mineral grains differs between the two flows, but both are consistent with rapidly cooling flows; T (flow 28) contains dendritic titanomagnetite and small needles of ilmenite (Figure 4.3a), while T (flow 29) is dominated by large (>100μm), skeletal titanomagnetite grains (Figure 4.3b). A few lamellae are present suggesting that the titanomagnetite might have begun high-temperature, solid-state exsolution into magnetite and ilmenite. However, fast cooling of the flow might have prevented any significant exsolution occurring, resulting in the titanium rich titanomagnetite, confirmed by EDX analysis (the Ti:Fe ratio is ~37%). These samples most likely correspond to the low Curie temperature titanomagnetite (Tc ~300–400°C). The EDX results also suggest that fractures in the large titanomagnetite grains of T (flow 29) experienced some secondary single-phase low-temperature oxidation but it is not clear whether this was sufficiently extensive to have had a substantial effect on the remanence. In comparison, the large (>100μm), subhedral titanomagnetite grains in the Maymecha section (site M) represent a long cooling history that may account for the greater number of lamellae from high-temperature, solid-phase exsolution than in the Truba section. The remainder of a small amount of high Ti titanomagnetite, that hadn't exsolved, is the probable cause of the small, non-reversible component in the Type A1 thermomagnetic curves from this section (Shcherbakova et al., 2015); however, all of the thermomagnetic curves gave a final Curie temperature close to that of magnetite.

For the Sytikanskaya kimberlite pipe (sites S1 and S3), EDX confirms that magnetite is present as a bimodal size distribution (Figure 4.3c); as large, subhedral grains (50–300μm long) and small magnetite grains (<10 μm), with neither containing any discernable titanium. The large grains also show that there is no fracturing to indicate the presence of secondary single-phase low-temperature oxidation. These grains are consistent with thermomagnetic curves for the Sytikanskaya pipe (Blanco et al., 2012), which are reversible and give a Curie temperature of ~560°C, approximately that of pure magnetite. Comparatively, SEM analysis of Yubileinaya kimberlite pipe (site Y1) contains dendritic titanomagnetite and needle-like ilmenite crystals (Figure 4.3d), similar to T (flow 28), although the proportion of titanomagnetite to ilmenite is much higher in the Yubileinaya sample. These results agree with the thermal dependent magnetic susceptibility curves that gave a Curie temperature of ~500°C indicating the presence of a higher Ti content (Blanco et al., 2012).

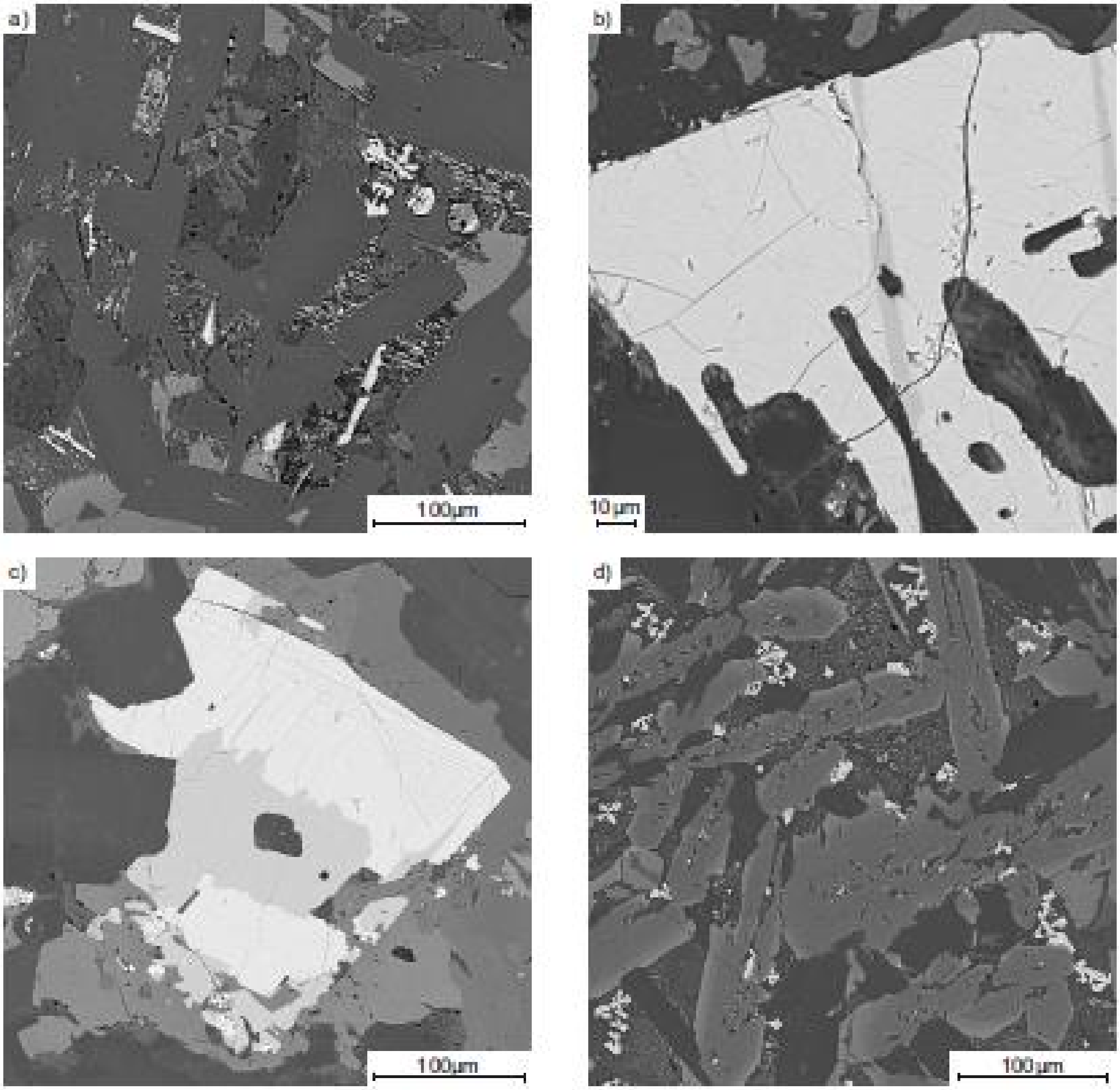

Figure 4.3. Representative magnetic mineralogy of the samples that passed palaeointensity section criteria; a) dendritic titanomagnetite and needles of ilmenite (sample 294; Truba, flow 28), b) skeletal titanomagnetite with ilmenite lamellae (sample 304; Truba, flow 29), c) subhedral magnetite grain (sample 15; Sytikanskaya pipe, site S1), and d) dendritic titanomagnetite (sample 1; Yubileinaya pipe, site Y1).

4.4.2 Microwave Paleointensity

Figure 4.4 presents examples of the accepted Arai plots along with the Zijderveld plots. Absolute microwave paleointensity results during the PTB with their associated quality factors are listed in Table 4.2. A total of 28 samples out of 50 samples from 7 sites of 4 areas satisfied the reliability criteria and were accepted. However, as only one sample from site M (flow 18) met the reliability criteria, this flow was not included in our result. No samples from site T (flow 35), T (flow 40) and S2 meet all the reliability criteria. The selected samples showed corresponding distinct directional components, positive pTRM checks and little or no zig-zagging of the Arai or Zijderveld plots (Figure 4.4), supporting that the samples were not influenced by lab-induced alteration or multi-domain behavior. In this study, the success rate for paleointensity determination is 56%.

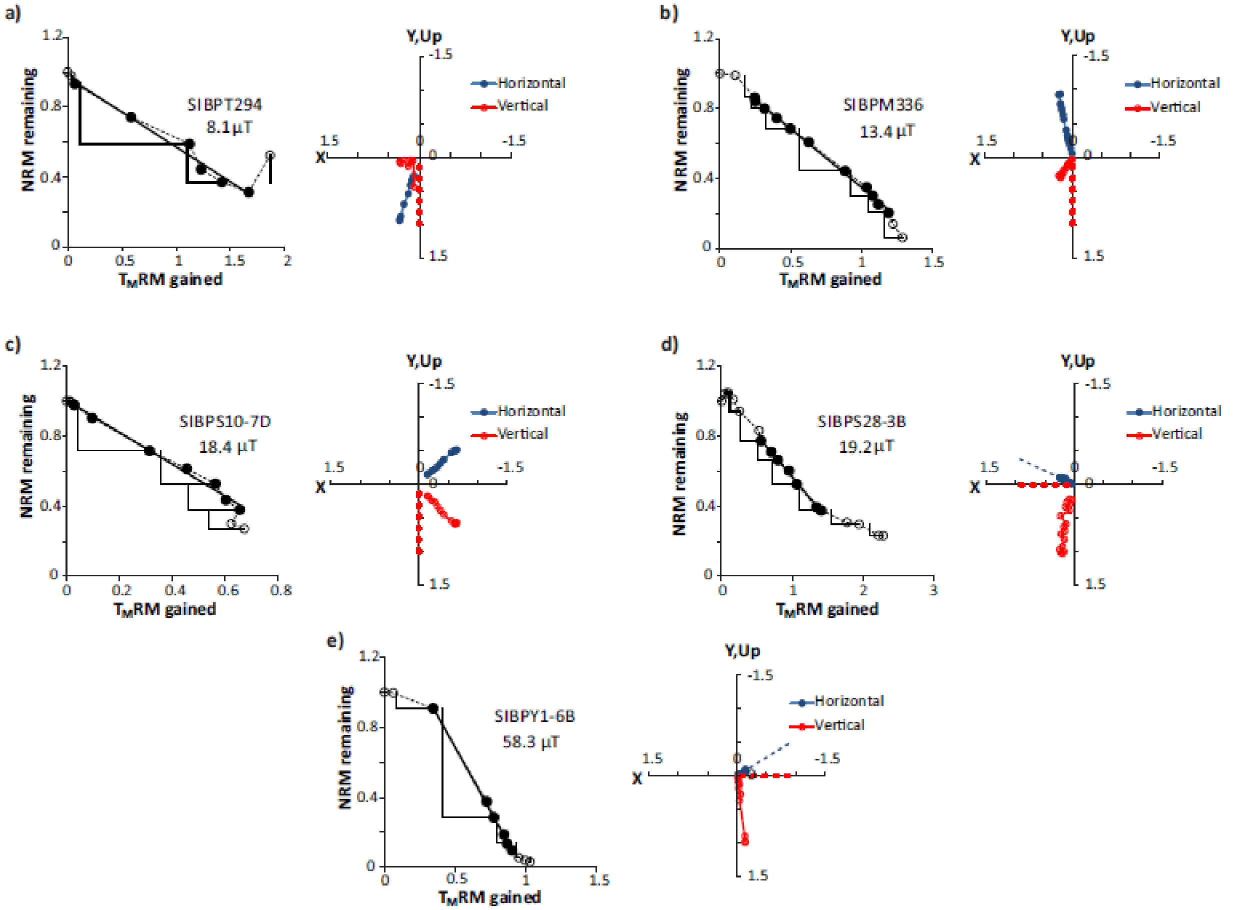

Figure 4.4. Examples of Arai and associated Zijderveld plots produced by microwave Thellier method. Triangles on the Arai plots represent pTRM checks and the solid straight lines marks the interval on which intensity was estimated. On the Zijderveld plots, red (blue) points represent the vertical (horizontal) component (all samples were unoriented). a) Truba (site T, flow 29) specimen, b) Maymecha (site M, flow 23) specimen, c) Sytikanskaya (site S1) specimen, d) Sytikanskaya (site S3) specimen, and e) Yubileinaya (site Y1) specimen.

Table 4.2. Microwave and previously published thermal Thellier paleointensity results during Permo-Triassic boundary. MW: Microwave paleointensity method, TT: Thellier-type paleointensity method and W: Wilson method (references: *[1] Scherbakova et al, 2013, *[2] Scherbakova et al, 2015 and *[3] Blanco et al., 2012). I/T: Integral (W.s)/Temperature (°C). Hlab: applied laboratory magnetic field. N: number of successive data points used for paleointensity calculations. β, f, g and q are the measure of linearity, fraction of the NRM, the gap factor and the quality factor respectively. DRAT: percentage of discrepancy in the pTRM check. CDRAT: cumulative DRAT. MAD: maximum angular deviation. k': curvature of the Arai plot. PI: paleointensity result. VDM: Virtual dipole moment with its associated standard deviation. Samples that are in grey represent previously published results that have been rejected from our site means as the results do not appear to be reliable (see text for details).

Site	Sample	Method	Low I/T	High I/T	Hlab (μT)	N	B	f	g	q	delCK	DRAT	CDRAT	Alpha	MAD	k'	PI (μT)	Site Mean (μT)	VDM ($x10^{22}$ Am^2)
Truba																			
T (flow 28)	SIBPT294	MW	4	9	20	6	0.079	0.408	0.763	6.3	2.2%	3.1%	2.0%	4.3	3.4	-0.14	8.1	7.9 ± 2.8	1.2 ± 0.4
	SIBPT294B	MW	6	18	10	13	0.045	0.369	0.856	6.4	4.8%	12.6%	12.0%	13	2.3	0.05	5.1		
	SIBPT294C	MW	3	10	7	7	0.033	0.609	0.664	13.3	6.5%	5.4%	8.8%	7.7	3.4	-0.14	10.6		
	294(1)*[1]	TT	200	350	20	7	-	0.42	0.82	2.7	-	-	-	-	-		20.4		
	294(jr6)*[1]	TT	200	390	20	10	-	0.68	0.88	5.6	-	-	-	-	-		21.3		
	294(1)*[1]	W															14.3		
T (flow 29)	SIBPT304	MW	3	11	30	8	0.064	0.672	0.757	9.1	0.5%	0.6%	-7.9%	1.5	1.5	0.27	13.7	9.4 ± 3.8	1.4 ± 0.6
	SIBPT307A	MW	4	12	15	9	0.021	0.593	0.865	29.6	12.2%	15.5%	32.4%	5.3	3		6.6		
	SIBPT307B	MW	4	10	10	7	0.101	0.36	0.799	3.8	1.5%	0.02%	-1.0%	6.2	1.9	0.49	7.9		
	308(1)*[1]	TT	200	270	20	3	-	0.28	0.5	1	-	-	-	-	-		18.9		
	308(2)*[1]	TT	160	270	20	7	-	0.33	0.83	4	-	-	-	-	-		23.9		
	308(1)*[1]	W															23.6		

Maymecha																			
M (flow 23)	SIBPM336	MW	7	17	20	11	0.018	0.645	0.859	29.8	4.5%	5.9%	9.9%	2.4	1.6	-0.13	13.4	11.0 ± 2.2	2.4 ± 0.5
	SIBPM336B	MW	9	17	20	9	0.036	0.584	0.85	13.5	5.2%	7.5%	-5.4%	5.5	6.1	-0.06	13.2		
	336*[2]	TT	500	620	20	13	-	0.58	0.89	35.2	-	-	-	-	-		10.8		
	336_jr6*[2]	TT	450	580	20	12	-	0.58	0.88	10.3	-	-	-	-	-		8.7		
	336*[2]	W															9		
M (flow 21)	SIBPM346	MW	7	12	30	6	0.044	0.589	0.762	10.9	7.8%	9.8%	4.7%	0.3	1.5	-0.08	23.8	25.2 ± 2.0	5.4 ± 0.4
	SIBPM346B	MW	7	14	20	8	0.033	0.747	0.829	18.1	10.2%	8.5%	6.0%	1.3	0.8	-0.04	26.6		
Mean (northern sites)																		13.4 ± 7.8	2.6 ± 1.9
Sytikanskaya																			
S1	S8-9a*[3]	TT	450	575	30	5	0.1	0.95	0.49	3.8	-	-	-	-	-		18.0	18.6 ± 2.8	3.2 ± 0.5
	SIBPS10-7B	MW	2	15	20	14	0.013	0.649	0.805	40.3	12.4%	14.5%	8.3%	7.6	2.6	-0.1	17.8		
	SIBPS10-7C	MW	5	10	20	6	0.102	0.604	0.591	4.2	11.1%	11.5%	8.5%	10.5	6	-0.37	17.5		
	SIBPS10-7D	MW	6	12	20	7	0.046	0.578	0.793	10	3.6%	4.6%	-6.3%	1.7	1.1	-0.18	18.4		
	S15-1bf*[3]	TT	200	450	40	9	0.07	0.384	0.796	4.2	-	-	-	-	-		40.1		
	SIBPS15-6	MW	1	7	40	7	0.054	0.508	0.645	6.8	1.9%	2.9%	5.4%	3.5	1.1	0.32	21.2		
	SIBPS15-6B	MW	3	11	20	9	0.058	0.382	0.793	5.5	4.3%	6.9%	9.0%	4.1	1.1	0.35	23.1		
	SIBPS15-6C	MW	8	16	20	9	0.027	0.52	0.83	19.5	7.5%	9.8%	23.9%	6.3	4.2	0	14.3		
S3	SIBPS27-5	MW	7	19	40	12	0.048	0.778	0.859	11.8	10.1%	13.7%	-6.7%	7.7	7.5	-0.34	20.2	16.0 ± 3.1	2.5 ± 0.5
	SIBPS27-5B	MW	8	11	20	4	0.083	0.375	0.625	3.3	4.3%	7.7%	11.7%	5.3	3.2	-0.47	15.2		
	S28-5b2*[3]	TT	350	575	25	7	0.07	0.86	0.77	9.1	-	-	-	-	-		27.98		
	SIBPS28-3B	MW	8	14	40	7	0.026	0.405	0.796	12	1.3%	2.9%	-5.7%	7.4	4.8	-0.05	19.2		
	SIBPS28-3C	MW	5	12	35	8	0.068	0.608	0.804	8.3	10.4%	13.5%	22.6%	8.3	4.4	0.19	15.3		
	SIBPS28-3D	MW	5	11	20	7	0.086	0.349	0.769	3.4	3.9%	8.4%	9.8%	0.8	1	0.45	13.9		
	SIBPS30-11	MW	5	12	30	8	0.047	0.745	0.807	13.6	13.2%	15.3%	13.6%	2.2	5.6	-0.09	12.3		
	S32-4b*[3]	TT	375	475	40	5	0.1	0.32	0.72	1.4	-	-	-	-	-		40.78		

	S32-4bf*³	TT	375	500	40	6	0.1	0.49	0.79	2	-	-	-	-	-		49.28		
Mean (Sytikanskaya)																		17.3 ± 2.5	2.9 ± 0.7
Yubileinaya																			
Y1	Y51-3b*³	TT	250	550	80	7	0.02	0.87	0.76	24.4	-	-	-	-	-		36.25		
	Y52-3a*³	TT	300	525	40	10	0.1	0.89	0.77	4.4	-	-	-	-	-		44.9		
	Y52-4a*³	TT	250	525	35	7	0.04	0.82	0.76	15.3	-	-	-	-	-		44.7		
	SIBPY1-6B	MW	2	7	40	6	0.017	0.788	0.522	18	6.4%	6.3%	9.4%	1.8	2.3	-0.08	58.3		
	SIBPY1-6C	MW	2	6	50	5	0.054	0.589	0.628	5.7	8.5%	12.0%	22.2%	6.1	4.5	0.2	51.4		
	SIBPY1-6D	MW	2	7	45	6	0.049	0.555	0.704	6.3	5.1%	7.3%	10.3%	6.1	4.4	-0.21	57.9		
	SIBPY4-2	MW	1	6	50	6	0.036	0.641	0.523	8.8	4.1%	5.2%	12.5%	8.1	7.7	-0.24	44.1	48.5 ± 7.3	6.4 ± 0.9
	SIBPY4-2B	MW	2	5	50	4	0.093	0.429	0.579	2.8	4.2%	6.9%	9.0%	4.6	5.1	-0.43	47.5		
	SIBPY4-2C	MW	2	7	50	6	0.05	0.552	0.706	6.8	5.8%	8.7%	14.7%	5	4.2	-0.23	47.9		
Grand mean																		19.5 ± 10.5	3.2 ±1.5

The accepted microwave paleointensity results from this study were combined with some of the thermal Thellier-type and and Wilson (Wilson, 1968) results from previously published studies (Table 4.2). For the Maymecha and Yubileinaya sites, the published thermal Thellier-type results are consistent with the new Microwave results. In contrast, there is a large degree of in-site dispersion when all of the results are combined for the Truba and Sytikanskaya sites, with site standard deviations of up to 55% of the site mean. Close analysis of the two accepted Truba flows reveals that the thermal paleointensity estimates are approximately double the value of the microwave results. One possible explanation for this discrepancy is that multidomain behavior was enhanced in one set of experiments over the other. In particular, we note that in the thermal Thellier experiments performed by Shcherbakov et al. (2013), no checks for MD behavior were performed and fraction (f) values from three out of the four estimates were less than 0.5. The use of the IZZI protocol in the microwave experiments and the resulting increased quality (q) values leads us to favour the new results over the old ones and thereby exclude the significantly higher thermal estimates from these two site means (Table 4.2; greyed out results). For the Sytikanskaya kimberlite pipe (sites S1 and S3), some of the thermal results are consistent with the microwave results while others are approximately twice as high. Blanco et al. (2012) divided the accepted thermal paleointensity results in two categories- ‘A’ and ‘B’; the ‘A’ category results met all the reliability criteria defined by Selkin and Tauxe, (2000) whereas the results fell into the ‘B’ category if one of the reliability criteria failed one of these but otherwise fell into the following limits: 10% < meanDEV < 25%, 20% < pTRM tail check < 25% and 30% < f < 60%. Since the ‘B’ category results are more prone to biasing from either laboratory induced alteration and/or MD effects, we exclude them from the site means for the Sytikanskaya (sites S1 and S3) and the Yubileinaya (site Y1) kimberlite pipe (Table 4.2; greyed out results).

The mean geomagnetic field intensity obtained from the four northern extrusive sites [T (flow 28), T (flow 29), M (flow 23), and M (flow 21)] is 13.4 ± 7.8 μT. This is slightly lower than the Sytikanskaya mean (17.3 ± 2.5 μT, sites S1 and S3) and substantially lower than the Yubileinaya (Y1) site mean (48.5 ± 7.3 μT). A similar regional discrepancy has been pointed out earlier by Blanco et al. (2012) and was suggested to be a consequence of bias from multidomain behavior in northern specimens (resulting from reductions of the paleointensity estimates made from at high temperatures portions of the Arai plots). The present study does not support this explanation as the discrepancy remains even within a result set that showed little evidence of zigzagging and generally lower curvature parameters (k' in Table 4.2; Paterson, 2011). Another possibile cause that we rule out is crustal magnetic anomalies as these are weak in the region considered (Abramova and Abramova, 2014).

Our preferred explanation is simply that the regional discrepancy reflects slightly different time intervals within the 0.1 to 2 Myr emplacement event. Pavlov et al. (2015) estimates that the formation of the Norilisk and Maymecha-Kotuy sections "did not exceed a time interval on the order of 10,000 years" based on secular variation analysis of the directions from the Truba section and the Norilisk section (directions from Heunemann et al., 2004). Therefore, in the context of rates of secular variation such as that seen in the last 2 Myr (Valet et al., 2005), it is perfectly feasible that the units from the northern, Sytikanskaya and Yubileinaya sites were emplaced during time periods perhaps a few tens or hundreds of kyr apart when the field was in a different intensity regime. Thus, it is reasonable to include multiple localities to obtain a more accurate geomagnetic mean for the PTB.

It is also worth noting that Pavlov et al. (2015) suggests that thick parts of the sequence towards the base of the Norilisk section: the upper part of the Ivakinskii Formation to the lower part of the Nadezhdinsky Formation, represent those of a transitional and/or excursional field. The published paleointensity results from these formations seem to be in agreement with this analysis as the VDM results are consistently lower than those form the same section in a distinct polarity zone (Figure 4.5). None of the samples from this transitional part of the section have been used for microwave analysis and we exclude these published results from our composite analysis outlined in the next section.

In this study, the calculated grand mean paleointensity during the PTB is 19.5 ± 10.5 μT which corresponds to a mean virtual dipole moment (VDM) of $3.2 \pm 1.5 \times 10^{22}$ Am^2. Results indicate, considering the northern and the southeastern localities collectively, that the average magnetic field intensity during these short intervals is significantly lower (approximately half) than the present geomagnetic field intensity.

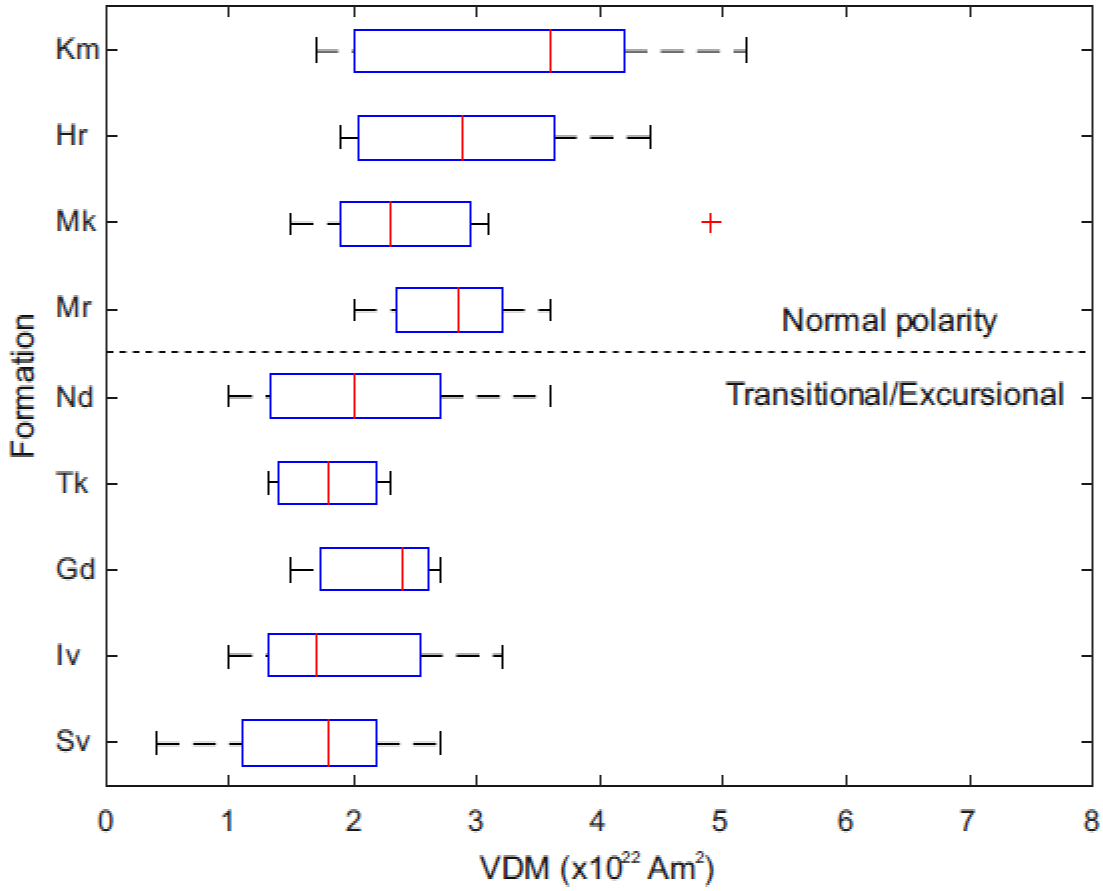

Figure 4.5. The virtual dipole moment (VDM) results for Norilisk section sites listed in the PINT databse by Formation. Km; Kumginsky Formation, Hr; Kharaelakhsky Formation, Mk; Mokulaevsky Formation, Mr; Morongovsky Formation, Nd; Nadezhdinsky Formation, Tk; Tuklonsky Formation, Gd; Gudchikhinsky Formation, Sv; Syverminskii Formation, Iv; Ivakinskii Formation. The Formations are listed in stratigraphic order (Km is the youngest, Iv the oldest) but the axis is not scaled to time as the ages of the individual formations are unknown. The sections is considered to represent on the order of 10,000 years based on geomagnetic secular variation (Pavlov et al., 2015), with a change from an excursional and transitional field to normal polarity during Nd.

4.4.3 Collation of Published Data and Q_{PI} (Quality of Paleointensity) Analysis

There are currently five published paleointensity studies for the Permo-Triassic Siberian traps listed in the PINT database (Biggin et al., 2010), that have not been superseded by another publication. All of the sites listed in these publications, along with the sites in this study and that of Shcherbakova et al., 2015 (which have also not yet been added to the database), have been collated and assessed. Each site mean VDM value was assigned a Q_{PI} value based on the number of criteria (Biggin and Paterson, 2014) that the estimate passed. Table A.1 in the Appendix A provides directions, intensities, and the complete breakdown of the estimation of Q_{PI} values for all the published studies and this one. The sites cover three regions- the two northern regions (Maymecha-Kotuy and Norilsk) which have distinct but correlatable stratigraphy, and the southeastern region which contains the sills from the areas around the kimberlite pipes Sytikanskaya, Yubileinaya and Aikhal. To test the robustness of the geomagnetic means from these regions, sites were filtered out based on their Q_{PI} values to see how the site mean changed as less reliable sites were removed (Table 4.3 and Figure 4.6).

Table 4.3. QPI (Quality of Paleointensity) summary for the Russian sites covering the Permo-Triassic boundary from the PINT database and this study.

Location	Qpi ≥ 2	Qpi ≥ 3	Qpi ≥ 4	Qpi ≥ 5	Qpi ≥ 6
Northern Localities					
Maymecha-Kotuy					
No. of sites	41	41	41	24	6
VDM (x10^{22} Am^2)	2.2 +0.2/-0.6	2.2 +0.2/-0.6	2.2 +0.2/-0.6	1.8 +0.6/-0.3	2.40 +0.7/-0.8
Norilisk					
No. of sites	52	49	33	0	0
VDM (x10^{22} Am^2)	3.1 ± 0.3	3.1 ± 0.3	2.8 +0.4/-0.6	-	-
Total Northern Localities					
No. of sites	93	90	74	24	6
VDM (x10^{22} Am^2)	2.5 +0.5/-0.2	2.5 +0.4/-0.2	2.3 +0.2/-0.1	1.8 +0.6/-0.3	2.4 +0.7/-0.8
Eastern Localities					
Aikhal, Sytikanskaya and Yubileinaya					
No. of sites	9	7	3	2	2
VDM (x10^{22} Am^2)	6.3 +0.2/-3.1	6.3 +0.1/-3.1	3.2	4.8	4.8
Siberian Traps Mean					
All sites					
No. of sites	102	97	77	26	8
VDM (x10^{22} Am^2)	2.8 ± 0.4	2.6 +0.4/-0.3	2.3 +0.3/-0.1	2.0 ± 0.5	2.6 +0.8/-0.7

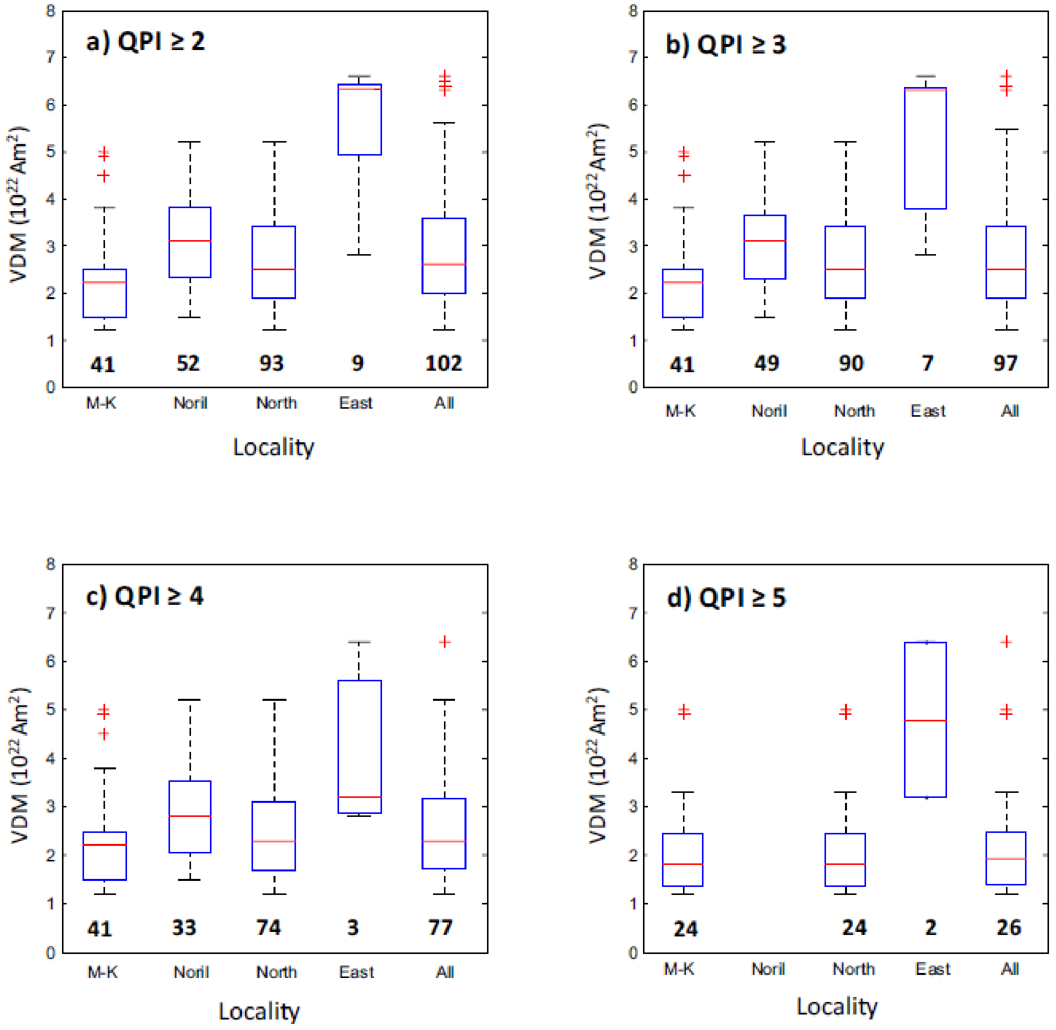

Figure 4.6. The virtual dipole moment (VDM) results from the PINT database and this study, by location, filtered for their Q_{PI} values. a) sites with Q_{PI} values ≥2, b) sites with Q_{PI} values ≥3, c) sites with Q_{PI} values ≥4 and d) sites with values Q_{PI} ≥5. M-K; Maymecha-Kotuy, Noril; Norilisk, North; Northern Localities of Maymecha-Kotuy and Norilisk, East; Eastern Localities of Aikhal, Sytikanskaya and Yubileinaya, and All; All of the PTB Siberia sites from the PINT database and this study. The number of sites represented by each boxplot is shown below the boxes.

For the northern localities, both of the regions have similar median paleointensities and show minimal variation with Q_{PI} filtering, as shown in Figure 4.6. For up to $Q_{PI} \geq 5$, the Norilsk section has a much greater range due to the larger number of sites associated with this locality.

There is a much greater variation in the median with Q_{PI} filtering for the southeastern localities because there are very few sites but the geomagnetic mean always remains significantly higher than the northern localities. In this study, results are considered to be reliable as we have studied almost an equal number of sites for each locality, and the Q_{PI} (Quality of Paleointensity) values are ≥ 4. The northern sites represent ~90% of the total sites studied indicating that the overall median is likely to be heavily biased by the potentially short-lived and extreme secular variation represented by the northern sites. Nevertheless, we point out that the simple average of the median northern and eastern regional results would still yield a dipole moment of only approximately half the present-day value.

4.4.4 Comparison to the Phanaerozoic record

Dipole moments based on different rock types for Permian to Cretaceous (300–65 Ma) are shown in Figure 4.7 to allow investigation of the extent of the MDL behavior. Here, the paleointensity data of previously published 55 different studies, archived in the 2015 version of the PINT database (http://earth.liv.ac.uk/pint/), and this study are analyzed. As geomagnetic field intensities vary across geographic locations, the VDM or VADM record is used for this analysis. It is obvious that there is a degree of variability of dipole moment between different materials, such as- volcanic rock, submarine basaltic glasses, plutonic rocks etc. Geomagnetic field strength recorded in submarine basaltic glasses, plutonic rocks and single silicate crystals is high relative to volcanic rocks and baked sedimentary rocks (Chang et al., 2013). The mean VDM/VADM of entire rock types for Permian (9.3×10^{22} Am^2) is higher than that of present day (8×10^{22} Am^2), whereas it is lower for the other three time intervals – PTB (2.7×10^{22} Am^2 for the PINT database and 3.2×10^{22} Am^2 for this study), Jurassic (3.3×10^{22} Am^2), and Cretaceous (6.7 ×

10^{22} Am^2) (Figure 4.7). The mean VDM/VADM has changed during the last 300 Ma indicating a period of low dipole moment during the Mesozoic, at least for the Jurassic (140–200 Ma), and, not withstanding a ~50 Myr gap in the record during the Triassic, now might extend to the PTB.

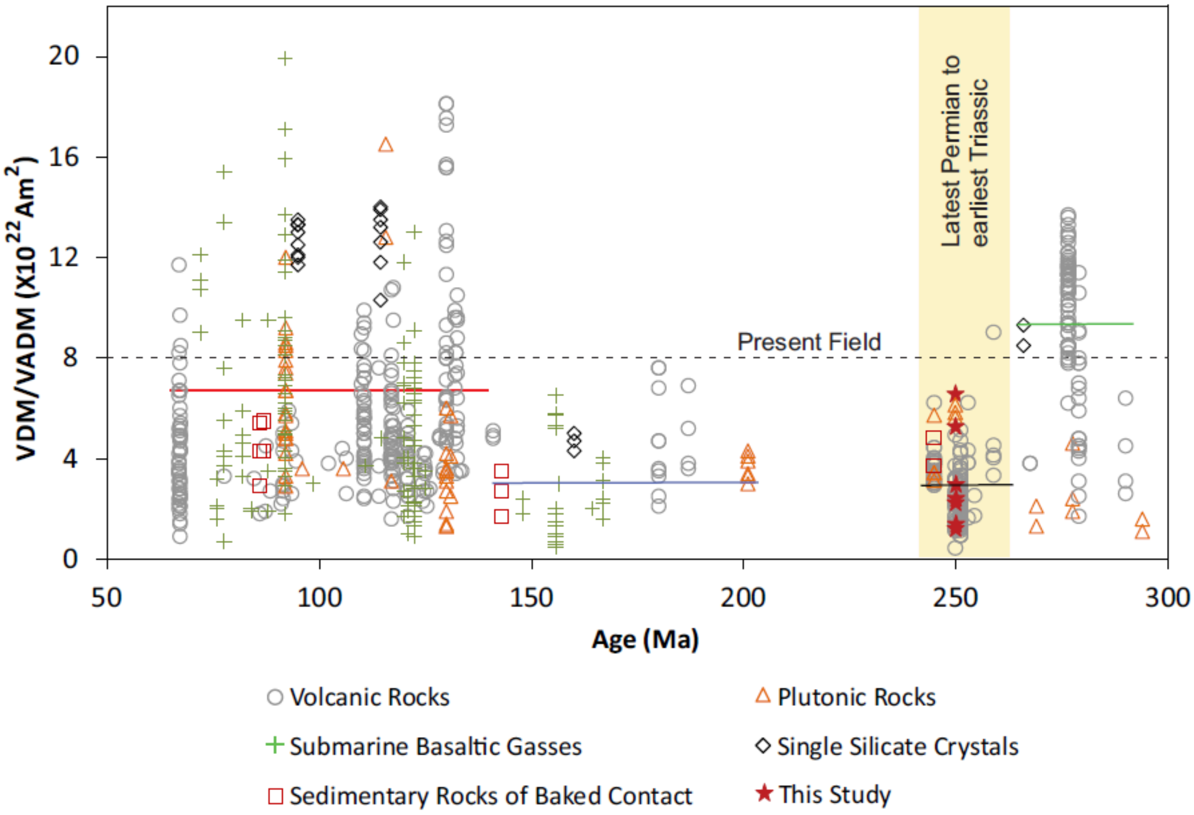

Figure 4.7. The virtual dipole moment (VDM) and virtual axial dipole moment (VADM) from Permian to Cretaceous (300–65 Ma), obtained from the PINT database and the data from this study. The dashed horizontal line represents the strength of the present geomagnetic dipole moment. Solid horizontal lines represent the average geomagnetic dipole moment for Permian (green), Permo-Triassic boundary (black), Jurassic (blue) and Cretaceous (red).

4.5 Conclusions

(1) Microwave paleointensity results for the PTB considering both the northern extrusive and the southeastern intrusive parts of the Siberian trap basalt are reported for the first time in this study.

(2) The results indicate that the average geomagnetic intensity for the different regions are distinctly different (being especially low – 13.4 ± 7.8 μT - in the northern extrusive localities and especially high – 48.5 ± 7.3 μT - in the single site from the Yubileinaya intrusives). This most likely reflects slightly different sampling of secular variation by the different suites of rocks. It demonstrates that it is important to consider multiple localities to evaluate the mean paleointensity for the PTB.

(3) In this study, the mean paleointensity recorded by the seven sites of the STB is 19.5 ± 10.5 μT which produces a grand mean virtual dipole moment (VDM) of $3.2 \pm 1.5 \times 10^{22}$ Am^2. This is higher than the mean paleointensity (2.7×10^{22} Am^2) from the PINT database, but this is due to a bias towards the number of sites in the northern regions, which is less of a problem in this study. These results are considered to be reliable and have Q_{PI} values ≥ 4.

(4) Results demonstrate that published northern localities show minimal variation with Q_{PI} filtering, whereas Eastern localities show much greater variation as there are very few studied sites. Therefore, further work is required to improve the number of sites in the eastern localities, and this will help to determine a more representative value for the strength of the field at the PTB.

(5) Results suggest that the magnetic field intensity during this period was significantly lower (approximately half) than the present geomagnetic field intensity, and, could indicate that the MDL began at the PTB. New paleointensity data from Triassic age rocks are urgently required to test this hypothesis.

References

Abramova, D.Y., and Abramova, L.M., 2014. Lithospheric magnetic anomalies in the territory of Siberia (from measurements by the CHAMP satellite). Russian Geology and Geophysics, 55(7), 854-863.

Almukhamedov, A.I., Medvedev, A.Ya., Mitchell, C., Zolotukhin, V.V., 1996. Flood basalts in the core of the Tunguska syneclinse: comparative geochemistry (in Russian). Russian Geol. Geophys. Novosibirsk, 37, 3–16.

Almukhamedov, A.I., Medvedev, A.Ya., Zolotukhin, V.V., 2004. Compositional evolution of the Permian–Triassic basalts of the Siberian Platform in time and space. Petrology, 2 (4), 339–353 (in Russian).

Basu, A.R., Hannigan, R.E., Jacobsen, S.B., 1998. Melting of the Siberian mantle plume. Geophys. Res. Lett., 25, 2209–2212.

Biggin, A.J., 2006. First-order symmetry of weak-field partial thermoremanence in multi-domain (MD) ferromagnetic grains: 2. Implications for Thellier-type palaeointensity determination. Earth Planet. Sci. Lett., 245 (1-2), 454-470.

Biggin, A.J., 2010. Are systematic differences between thermal and microwave Thellier-type palaeointensity estimates a consequence of multidomain bias in the thermal results? Phys. Earth Planet. Inter., 180, 16–40.

Biggin, A.J., and Paterson G.A., 2014. A new set of qualitative reliability criteria to aid inferences on palaeomagnetic dipole moment variations through geological time. Frontiers in Earth Science, 2, 24, 1-9.

Biggin, A.J., Perrin, M., Dekkers, M.J., 2007. A reliable absolute palaeointensity determination obtained from a non-ideal recorder. Earth Planet. Sci. Lett., 257, 545–563.

Biggin, A.J., McCormack, A., Roberts, A., 2010. Paleointensity database updated and upgraded. Eos Trans. AGU, 91(2), 15.

Biggin, A.J., Steinberger, B., Aubert, J., Suttie, N., Holme, R., Torsvik, T.H., Van der Meer, D.G., Van Hinsbergen, D.J.J., 2012. Possible links between long term geomagnetic variations and whole-mantle convection processes. NatureGeosci., 8, 526-533.

Biggin, A.J., Piispa, E, Pesonen, L.J., Holme, R., Paterson, G.A., Veikkolainen, T., Tauxe, L. 2015. Palaeomagnetic field strength variations suggest Mesoproterozoic inner core nucleation. Nature, 525, 245-248.

Blanco, D., Kravchinsky, V.A., Valet, J.P., Ali, A., Potter, D.K., 2012. Does the Permo-Triassic geomagnetic dipole low exist? Phys. Earth Planet. Inter., 204-205, 11–21.

Böhnel, H., Biggin, A.J., Walton, D., Shaw, J., Share, J.A., 2003. Microwave palaeointensities from a recent Mexican lava flow, baked sediments and reheated pottery. Earth Planet. Sci. Lett., 214 (1–2), 221–236.

Burgess, S.D., and Bowring, S.A., 2015. High-precision geochronology confirms voluminous magmatism before, during, and after Earth’s most severe extinction. Science advances, 1(7), e1500470.

Coe, R.S., 1967. Palaeointensities of the Earth’s magnetic field determined from tertiary and quaternary rocks. J. Geophys. Res., 72, 3247–3262.

Coe, R.S., Grommé, C.S., Mankinen, E.A., 1978. Geomagnetic paleointensities from radiocarbon dated lava flows on Hawaii and the question of the Pacific nondipole low. J. Geophys. Res., 83, 1740–1756.

Courtillot, V., and Renne, P.R., 2003. On the ages of flood basalt events. C.R. Geosci., 335, 113–140.

Courtillot, V., Jaupart, C., Manighetti, I., Tapponnier, P., Besse, J., 1999. On causal links between flood basalts and continental breakup. Earth Planet. Sci. Lett., 166, 177–195.

Courtillot, V., Kravchinsky, V.A., Quidelleur, X., Renne, P.R., Gladkochub, D.P., 2010. Preliminary dating of the Viluy traps (Eastern Siberia): Eruption at the time of Late Devonian extinction events? Earth Planet. Sci. Lett., 300, 239–245.

Chang, B., Kim, W., Doh, S.J., and Yu, Y., 2013. Paleointensity determination of Late Cretaceous basalts in northwest South Korea: implications for low and stable paleofield strength in the Late Cretaceous. Earth Planets Space, 65, 1501–1513.

Christensen, U.R., and Wicht, J., 2007. Numerical dynamo simulations. Treatise Geophys., 8, 245–282.

Elkins Tanton, L.T., and Hager, B.H., 2000. Melt intrusion as a trigger for lithospheric foundering and the eruption of the Siberian flood basalts. Geophys. Res. Lett., 27, 3937–3940.

Erwin, D.H., 1994. The Permo-Triassic extinction. Nature, 367, 231-236.

Fedorenko V., and Czamanske G., 1997. Results of New Field and Geochemical Studies of the Volcanic and Intrusive Rocks of the Maymecha-Kotuy Area, Siberian Flood-Basalt Province. International Geology Review, 39, 479-531.

Fetisova, A.M., Veselovskii, R.V., Latyshev, A.V., Rad'ko, V.A., Pavlov, V.E., 2014. Magnetic stratigraphy of the Permian-Triassic traps in the Kotui River valley (Siberian Platform): New paleomagnetic data. Stratigraphy and Geological Correlation, 22(4), 377-390.

Glatzmaier, G.A., Coe, R.S., Hongre, L., Roberts, P.H., 1999. The role of the Earth's mantle in controlling the frequency of geomagnetic reversals. Nature, 401, 885–890.

Griffin, W.L., Ryan, C.G., Kaminsky, F.V., O'Reilly, S.Y., Natapov, L.M., Win, T.T., Kinny, P.D., Ilupin, I.P., 1999. The Siberian lithosphere traverse, mantle terranes and the assembly of the Siberian Craton. Tectonophysics, 310, 1–35.

Heller, R., Merrill, R.T., McFadden, P.L., 2002. The variation of intensity of earth's magnetic field with time. Phys. Earth Planet. Inter., 131(3–4), 237–249.

Heunemann, C., Krasa, D., Soffel, H.C., Gurevitch, E., Bachtadse, V., 2004. Directions and intensities of the Earth's magnetic field during a reversal: results from the Permo-Triassic Siberian trap basalts, Russia. Earth Planet. Sci. Lett., 218, 197–213.

Hill, M.J., and Shaw, J., 1999. Palaeointensity results for historic lavas from Mt Etna using microwave demagnetization/remagnetization in amodified Thellier-type experiment. Geophys. J. Int., 139 (2), 583–590.

Kamo, S.L., Czamanske, G.K., Amelin, Y., Fedorenko, V.A., Davis, D.W., and Trofimov, V.R., 2003. Rapid Eruption of Siberian Flood_Volcanic Rocks and Evidence for Coincidence with the Permian–Triassic Boundary and Mass Extinction at 251 Ma. Earth Planet. Sci. Lett., 214, 75–91.

Kirschvink, J.L., 1980. The least-squares line and plane and the analysis of palaeomagnetic data. Geophys. J. R. Astron. Soc., 62(3), 699–718.

Konstantinov, K.M., Bazhenov, M.L., Fetisova, A.M., Khutorskoy, M.D., 2014. Paleomagnetism of trap intrusions, East Siberia: Implications to flood basalt emplacement and the Permo–Triassic crisis of biosphere. Earth Planet. Sci. Lett., 394, 242-253.

Kosterov, A.A., Perrin, M., Glen, J.M., and Coe, R.S., 1998. Paleointensity of the Earth's magnetic field in Early Cretaceous time: the Paraná Basalt, Brazil. J. Geophys. Res., 103, 9739–9753.

Kravchinsky, V.A., 2012. Paleozoic large igneous provinces of Northern Eurasia: Correlation with mass extinction events. Global and Planetary Change, 86-87, 31–36.

Kravchinsky, V.A., Konstantinov, K.M., Courtillot, V., Savrasov, J.I., Valet, J.P., Cherniy, S.D., Mishenin, S.G., Parasotka, S., 2002. Palaeomagnetism of the east Siberian traps and kimberlites: two new poles and palaeogeographic reconstruction at about 360 and 250 Ma. Geophys. J. Int., 148, 1–33.

Kuzmin, M.I., Yarmolyuk, V.V., Kravchinsky, V.A., 2010. Phanerozoic hot spot traces and paleogeographic reconstruction of the Siberian continent based on interaction with the African large low shear velocity province. Earth Sci. Rev., 102, 29–59.

Nagata, T., Arai, Y., Momose, K. 1963. Secular variation of the geomagnetic total force during the last 5000 years. J. Geophys. Res., 68, 5277–5281.

Paterson, G.A., 2011. A simple test for the presence of multidomain behavior during paleointensity experiments. J. Geophys. Res. (Solid Earth), 116, B10104.

Paterson, G.A., Tauxe, L., Biggin, A.J., Shaar, R., and Jonestrask, L.C., 2014. On improving the selection of paleointensity data. Geochem. Geophys. Geosyst., 15, 1180–1192.

Pavlov, V.E., Fluto, F., Veselovskii, R.V., Fetisova, A.M., and Latyshev, A.V., 2011. Secular Geomagnetic Variations and Volcanic Pulses in the Permian–Triassic Traps of the Norilsk and Maymecha–Kotui Provinces, Maymecha Izv. Phys. Solid Earth, 47(5), 402–417.

Pavlov, V.E, Fluteau, F., Veselovskiy, F., Fetisov, A., Latyshev, A., Elkins-Tanton, L.T., Sobolev, A., Krivolutskaya, N., 2015. Volcanic Pulses in the Siberian Traps as Inferred from Permo-Triassic Geomagnetic Secular Variations, In Volcanism and Global Environmental Change, Ed. A. Schmidt, K. Fristad, L. Elkins-Tanton, Cambridge University Press, United Kingdom, 63–78.

Pick, T. and Tauxe, L., 1993. Geomagnetic palaeointensities during the Cretaceous normal superchron measured using submarine basaltic glass. Nature, 366, pp. 238–242.

Prévot, M., El_Messaoud Derder, M., McWilliams, M., Thompson, J., 1990. Intensity of the Earth’s magnetic field: evidence for a mesozoic dipole low. Earth Planet. Sci. Lett., 97, 129–139.

Reichow, M.K., Saunders, A.D., White, R.V., Pringle, M.S., Mukhamedov, A.I., Medvedev, A.I., Kirda, N.P., 2002. Ar-40/ Ar-39 dates from the West Siberian Basin: Siberian flood basalt province doubled. Science, 296, 1846-1849.

Reichow, M.K., Saunders, A.D., White, R.V., Almukhamedov, A.I., Medvedev, A.Ya., 2005. Geochemistry and petrogenesis of basalts from the West Siberian Basin: an extension of Permo-Triassic Siberian Traps, Russia. Lithos, 79, 425–452.

Reichow, M.K., Pringle, M.S., Al’Mukhamedov, A.I., Allen, M.B., Andreichev, V.L., Buslov, M.M., Davies, C.E., Fedoseer, G.S., Fitton, J.G., Inger, S., Medvedev, A.Ya., Mitchell, C., Puchkov, V.N., Safonava, I.Yu., Scoot, R.A., Saunders, A.D., 2009. The timing and the extent of the eruption of the Siberian traps large igneous province. Implications for the end-Permian environmental crisis. Earth Planet. Sci. Lett., 227, 9–20.

Renne, P.R., and Basu, A.R., 1991. Rapid eruption of the Siberian Traps Flood Basalts at the Permo-Triassic boundary. Science, 253, 176-179.

Renne, P.R., Zhang, Z.C., Richards, M.A., Black, M.T., Basu, A.R., 1995. Synchrony and causal relations between Permian-Triassic boundary crises and Siberian flood volcanism. Science, 269, 1413-1416.

Saunders, A.D., Englend, R.W., Reichow, M.K., White, R.W., 2005. A mantle plume origin for the Siberian traps: uplift and extension in the West Siberian Basin, Russia. Lithos, 79, 407–424.

Selkin, P. A. and Tauxe, L., 2000. Long-term variations in palaeointensity. Philos. Trans. R. Soc. Lond. A, 358(1768), 1065–1088.

Shcherbakova, V.V., Shcherbakov, V.P., Vodovozov, V.V., Sycheva, N.K., 2005. Paleointensity at the Permian_Triassic boundary and in the late Permian. Izv. Acad. Sci. Phys. Solid Earth, 41 (11), 931–944.

Shcherbakova, V.V., Kovalenko, D.V., Shcherbakov, V.P., and Zhidkov, G.V., 2011. Paleointensity of the geomagnetic field in the Cretaceous (from Cretaceous rocks of Mongolia), Izv., Phys. Solid Earth, 47 (9), 775–791.

Shcherbakova, V.V., Bakhmutov, V.G., Shcherbakov, V.P., Zhidkov, G. V., Shpyra, V. V., 2012. Palaeointensity and palaeomagnetic study of Cretaceous and Palaeocene rocks from Western Antarctica. Geophys. J. Int., 189, 204–228.

Shcherbakova, V.V., Zhidkova, G.V., Latyshevb, A.V., Scherbakov V.P., 2013. Estimating the Variations in Paleointensity from the Siberian Traps of Maymecha–Kotui and Norilsk Regions. Izv. Phys. Solid Earth, 49(4), 488–504.

Shcherbakova, V. V., Zhidkov, G. V., Shcherbakov, V. P., Latyshev, A. V., Fetisova, A. M., 2015. Verifying the mesozoic dipole low hypothesis by the Siberian trap data. Izv. Phys. Solid Earth, 51 (3), 362–382.

Smirnov, A. V. and Tarduno, J. A., 2003. Magnetic hysteresis monitoring of Cretaceous submarine basaltic glass during Thellier paleointensity experiments: evidence for alteration and attendant low field bias, Earth Planet. Sci. Lett., 206(3–4), 571–585.

Tarduno, J.A., Cottrell, R.D., Smirnov, A.V., 2006. The paleomagnetism of single silicate crystals: recording geomagnetic field strength during mixed polarity intervals, superchrons, and inner core growth. Rev. Geohys., 44, RG1002. doi:10.1029/ 2005RG000189.

Tauxe, L., and Staudigel, H., 2004. Strength of the geomagnetic field in the Cretaceous Normal Superchron: new data from submarine basaltic glass of the Troodos Ophiolite. Geochem. Geophys. Geosyst., 5 (2) (Art. No. Q02H06).

Tauxe, L., and Yamazaki, T., 2007. Paleointensities, in: Kono, M. (Ed.), Geomagnetism. Elsevier, Amsterdam, pp. 510-563.

Tauxe, L., Gee, J. S., Steiner, M. B., & Staudigel, H., 2013. Paleointensity results from the Jurassic: New constraints from submarine basaltic glasses of ODP Site 801C. Geochemistry, Geophysics, Geosystems, 14(10), 4718-4733.

Thellier, E., and Thellier, O., 1959. Sur l'intensité du champ magnétique terrestre dans le passé historique et géologique. Annales Geophysicae, 15, 285–376.

Thomas, D.N. and Biggin, A.J., 2003. Does the Mesozoic dipole low really exist? EOS, Trans. Am. Geophys. Union, 84, (11), 97–104.

Valet, J.P., 2003. Time variations in geomagnetic intensity. Rev Geophys., 41, 1004, doi:1010.1029/2001RG000104.

Valet, J.P., Brassart, J., Le Meur, I., Soler, V., Quidelleur, X., Tric, E., Gillot, P.Y., 1996. Absolute paleointensity and magnetomineralogical changes. J. Geophys. Res., 101(B11), 25029–25044, doi:10.1029/96JB02115.

Valet, J.P., Meynadier, L., Guyodo, Y., 2005. Geomagnetic dipole strength and reversal rate over the past two million years. Nature, 435, 802-805.

Walton, D., Snape, S., Rolph, T.C., Shaw, J., Share, J., 1996. Application of ferromagnetic resonance heating to palaeointensity determinations. Physics of the Earth and Planetary Interiors, 94 (3–4), 183–186.

Wilson, R.L., 1961. The Thermal Demagnetization of Natural Magnetic Moments in Rocks. Geophys. J. R. Astron. Soc., 5, (1), 45–58.

Yu, Y., 2012. High-fidelity paleointensity determination from historic volcanoes in Japan, J. Geophys. Res. (Solid Earth), 117, B08101.

Yu, Y.J., and Tauxe, L., 2005. Testing the IZZI protocol of geomagnetic field intensity determination. Geochem Geophy Geosy., 6.

Zolotukhin, V.V., and Al'mukhamedov, A.I., 1988. Traps of the Siberian platform. In: Macdougall, J.D. (Ed.), Continental Flood Basalts. Kluwer, Dordrecht, Netherlands, 273–310.

Chapter 5

Was the Earth's magnetic field weak in the Late Devonian?

5.1 Introduction

The average frequency, with which the Earth's magnetic field has reversed its polarity, has varied strongly in the past – from perhaps as high as 12 reversals per million years at peak times (e.g. the mid-Jurassic) to no reversals for 30–40 million years during constant polarity superchrons (e.g. the mid-Cretaceous). These variations are likely indicating forcing by mantle convection processes and resulting changes in the core-mantle boundary heat flow pattern (Biggin et al., 2012). Long term fluctuations in the characteristics of the Earth's magnetic field are supposed to correspond to variations in the core convection (Courtillot and Besse, 1987). Geodynamo simulation ensures the impact of heat from the core, allowed by the mantle, over the strength and stability of the field through the influence on the convection's form and extent (Glatzmaier et al., 1999; Wicht and Olson, 2004). Out of the core, the temperature distribution in the lower mantle influences the heat flux. This implies the probability of relation in variations between the geomagnetic field and the mantle convection. The mantle controls the geodynamo through the regulation of the core-mantle boundary heat flow (Labrosse, 2002; Roberts et al., 2003), and changes in this heal flow cause an end to superchrons (Olson, 2003). Self-consistent numerical dynamo models indicate a positive correlation between the reversal frequency and the magnitude of core-mantle boundary heat flow, while this reversal frequency also shows a sensitivity towards the pattern of this heat flow (Glatzmaier et al., 1999; Kutzner and Christensen, 2002; Wicht and Olson, 2004; Takahashi et al., 2005).

The ~50 million years transition from the peak in reversal frequency in the Middle Jurassic (~170 Ma), associated with a weak geomagnetic field, to the stable and apparently strong field during the Cretaceous Normal Superchron (CNS; 121−84 Ma), represents a dramatic change in time-averaged geomagnetic field behaviour during the Mesozoic Era. To determine if similar variations can be seen during the Paleozoic, preceding the Permo-Carboniferous Superchron (PCRS; 310−265 Ma), paleointensity data for the time preceding the superchron are required. However, very few data exist to describe geomagnetic field behavior in the late Devonian (~50 Myr before the superchron) although a recent magnetostratigraphic study (Hansma et al., 2015) has suggested that reversal frequency was indeed high.

In this study, samples, which have recently been ^{40}Ar– ^{39}Ar dated to 377–364 Ma (Ricci et al., 2013), of late Devonian volcanics and intrusives from the Viluy large igneous province in Siberia, are investigated to establish the field strength. These units have already demonstrated reliable, paleomagnetic directions consistent with the retention of a primary remanence (Kravchinsky et al., 2002). Here, new paleointensity measurements from this suite of rocks have been presented to fill-up the gaps in paleointensity data at the late Devonian and to investigate the prediction that the superchron state between ~310 and 265 Ma should have been preceded by a period during which the field was weak and rapidly reversing.

5.2 Geological Setting

The Viluy traps are situated at the northeastern side of the Siberian platform (Figure 5.1). The Devonian period created the triple-junction rift system (Kuzmin et al., 2010) consisting of the Viluy rift, the western branch, and the Siberian platform forming two rifts (Zonenshain et al., 1991; Kiselev et al., 2006). The Viluy rift has a dimension of 800 km and 450 km in length and width respectively (Gaiduk, 1987; Kiselev et al., 2006). In and out sides of this rift, the Viluy volcanics are in extant ranging along the Lena-Markha-Viluy rivers, the rift margin faults, and on the inclination of the Aldan and Anabar shields (Kravchinsky et al., 2002). Out of the various intrusive rocks, the traps possess dykes, sills and layered basalt breccias; these rocks, along with the volcanic ones, cover a large volume of the Viluy rift with an area of more than 300×10^3 km^3 according to a present estimation (Kuzmin et al., 2010). The rift is surrounded by two large NE–SW dike belts which extend up to 700 km. A thickness of 6-8 km, substantial for sediment, covers the volcanic materials and sediments of different time periods including late Proterozoic, early Paleozoic, and Silurian. However, much, if not the whole, of these materials either decayed or got covered by the Siberian Traps and the Mesozoic sediments on the West and the East sides respectively. Intrusions, underneath of the sedimentary layer, extend to the edges of the paleorifts, with large normal faults. Presence of excessive amounts of lavas in the lower part of the Devonian traps indicates the multi-phase behavior of volcanism (Courtillot et al., 2010).

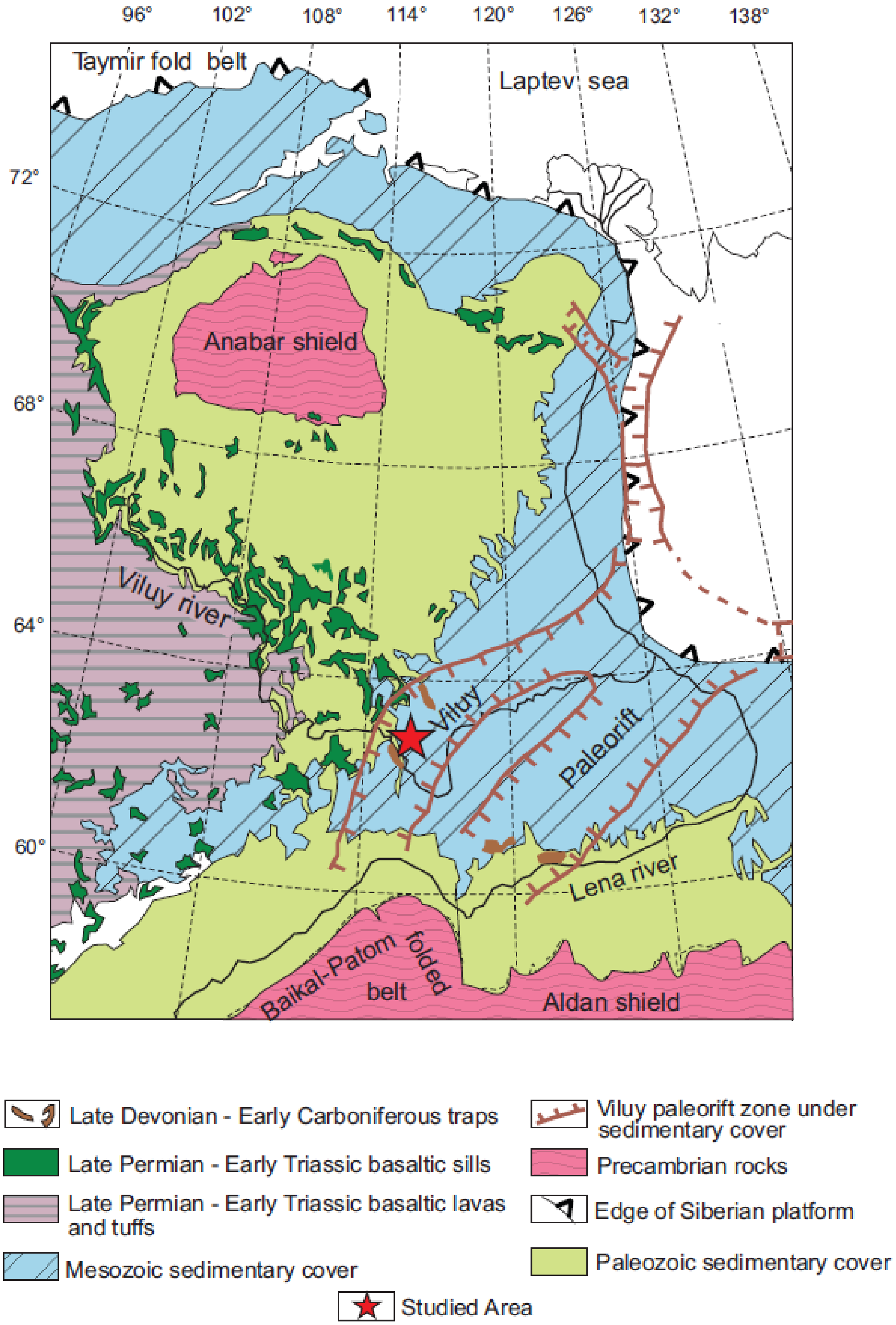

Figure 5.1. Geological map of the Siberian and Viluy traps in Siberia (after Courtillot et al., 2010). Red star represents the geographic positions of the study area: Viluy river Late Devonian traps (sills and dykes).

According to Masaitis et al. (1975), eruptions of these traps dated back to the late Devonian–early Carboniferous. Kravchinsky et al. (2002) suggested that the sedimentary depression system was filled in by volcanic and clastic rocks, having a major eruption occurring during the late Devonian–early Carboniferous. The major phase of Viluy traps magmatism might have happened in a shorter time interval around the Frasnian–Famennian boundary, correlating well with the mass extinction during this time (Kravchinsky et al., 2002). Kiselev et al. (2006) showed that the age of the Viluy traps magmatism is around 380–350 Ma. Courtillot et al. (2010) provided the first high-resolution absolute dating of samples using both K–Ar and ^{40}Ar– ^{39}Ar techniques, suggesting that the major stage of the magmatism might have been limited to the period of 370–360 Ma.. A recent study obtained 377–364 Ma through ^{40}Ar– ^{39}Ar ages for the samples from the Viluy rift (Ricci et al., 2013).

In this study, samples of volcanics and intrusives from the Viluy traps (63.50˚ N and 116.00˚ E), along the Viluy river in Siberia, were analyzed (Figure 5.1). Samples of the 14 sites (V1, V2, V3, V4, V5, V6, V7, V8, Vil4, Vil8, Vil13, Vil16, Vil18, and Vil20) from the Viluy traps, with various occurrences of trap sills (V1, V2, V3, V4, V5, V6) and dykes (V7, V8) as well as basites (Vil4, Vil8, Vil13, Vil16, Vil18, Vil20), were studied. Normal polarity was identified for the sites V1, V2, V4, V5, V8, Vil8, Vil13, Vil16, Vil18, and Vil20; whereas reverse polarity was identified for the sites V3, V6, V7, Vil4 (Kravchinsky et al., 2002 and V. Pavlov, personal communication). The rock magnetic studies indicate that the primary remanence carriers are composed of a low titanium titanomagnetite or pure magnetite, containing single or pseudo-single domain particles (Kravchinsky et al., 2002).

5.3 Methodology

5.3.1 Scanning Electron Microscope

To identify the morphological features and the chemical composition of the magnetic minerals in the samples, the Scanning Electron Microscope (SEM) analysis was performed on the carbon coated polished thin sections using a Zeiss EVO LS15 EP-SEM instrument equipped with energy dispersive X-ray (EDX) spectroscopy. The SEM is operated at an acceleration voltage of 20 kV. This analysis was performed and the results were obtained in the Scanning Electron Microscope Laboratory of the University of Alberta (Edmonton, Canada).

5.3.2 Paleointensity

Absolute paleointensity was investigated by using the internationally unique microwave paleointensity facility housed in the University of Liverpool's Geomagnetism Laboratory. This microwave technique has already been discussed in section 4.3.2. Microwave Thellier-type paleointensity experiments, using IZZI protocol (Tauxe and Staudigel, 2004), were performed on 60 samples from 14 sites of Viluy province. To test the sample alteration, partial thermoremanent magnetization (pTRM) checks (Coe, 1967 and Coe et al., 1978) was also carried out for all the samples. The laboratory field intensity, ranging from 5 to 20 μT, was applied to the samples. The laboratory field, with an angle of at least 45° to the NRM, was applied to ensure that multidomain-like behavior would manifest as zig-zags in the Arai plot (Biggin, 2006). In the previous study, rock magnetic and paleomagnetic direction analysis of these samples indicated that the remanent magnetization represents stable primary magnetization components (Kravchinsky et al., 2002), and thus, these samples are reliable for paleointensity measurements.

A modified version of the thermal Thellier–Thellier technique (Coe, 1967) was also carried out [on 16 samples from 6 sites] to be included with microwave paleointensity data. In this approach, the first heating step is followed by a cooling in zero magnetic field and the second heating step is followed by a cooling in a known magnetic field, imparting a partial thermoremanent magnetization (pTRM) to the specimen (ZI protocol). Partial thermoremanent magnetization (pTRM) checks (Thellier and Thellier, 1959) and tail checks (McClelland and Briden, 1996; Riisager and Riisager, 2001) were performed on the samples. The 1 cm^3 samples were heated in a shielded ASC thermal demagnetizer and were measured with 2G cryogenic magnetometers at the Laboratory of Paleomagnetism and Petromagnetism of the University of Alberta (Edmonton, Canada). The field, applied in the oven, ranged between 15 and 20 μT**.** Paleointensity selection criteria, discussed in section 4.3.3 and Table 4.1, were used to produce the reliable absolute paleointensity data for both the microwave and the thermal Thellier–Thellier techniques. Arai plots (Nagata et al., 1963) were used to analyze the absolute paleointensity results.

Furthermore, the non-heating Pseudo-Thellier method (Tauxe et al., 1995) was used to support the microwave paleointensity data. The Pseudo-Thellier method is usually used for relative paleointensity estimation. After natural remanent magnetization (NRM) destroyed in a series of alternating field (AF) demagnetization steps, step-wise acquisition of ARM was performed on each 1 cm^3 sample at the identical steps as AF demagnetization. ARM was imparted along the z direction in an AF decaying from 100 mT with a steady field of H (ranges between 5 and 40 μT) using a 2G cryogenic magnetometer demagnetizer in the paleomagnetism and petromagnetism laboratory at the University of Alberta. The vector difference sum was used to account for the overprint component not converging on the origin. The results are presented in the form of Arai plots (Nagata et al., 1963).

5.4 Results and Discussion

5.4.1 Scanning Electron Microscope

The SEM along with EDX analysis was performed on six thin sections, one representing each site with accepted paleointensity results. For site V5, samples are dominated by skeletal magnetite grains (Figure 5.2a) confirmed by EDX analysis (the Fe:O ratio is ~74%); but some patches of ilmenite are also present. Sites V6 and V7 contain dendritic titanomagnetite and small needles of ilmenite. For the large (>100μm) subhedral titanomagnetite grains in the samples from site V8 (Figure 5.2b), EDX analysis indicates the presence of intermediate Ti- titanomagnetite (the Ti:Fe ratio is ~31%). For site Vil13, EDX confirms that samples contain low Ti-titanomagnetite (the Ti:Fe ratio is ~7.5%) and small needle-like ilmenite crystals (Figure 5.2c). In comparison, the large (>100μm) skeletal titanomagnetite grains with a few ilmenite lamellae are present in the samples of site Vil20 (Figure 5.2d) resulting in the intermediate Ti-titanomagnetite, confirmed by EDX analysis (the Ti:Fe ratio is ~32%). The large grains also show that there is no fracturing to indicate the presence of secondary single-phase low-temperature oxidation. Overall, three distinct magneto-mineralogical types were revealed from the SEM technique; low Ti- and intermediate Ti- titanomagnetite and possible magnetite, with mineral type affecting the success rate of samples without resulting in significant variation in paleointensity results. The previous rock magnetic studies for these sites also indicate that the primary remanence carriers are composed of a low titanium titanomagnetite or pure magnetite, containing single or pseudo-single domain particles (Kravchinsky et al., 2002).

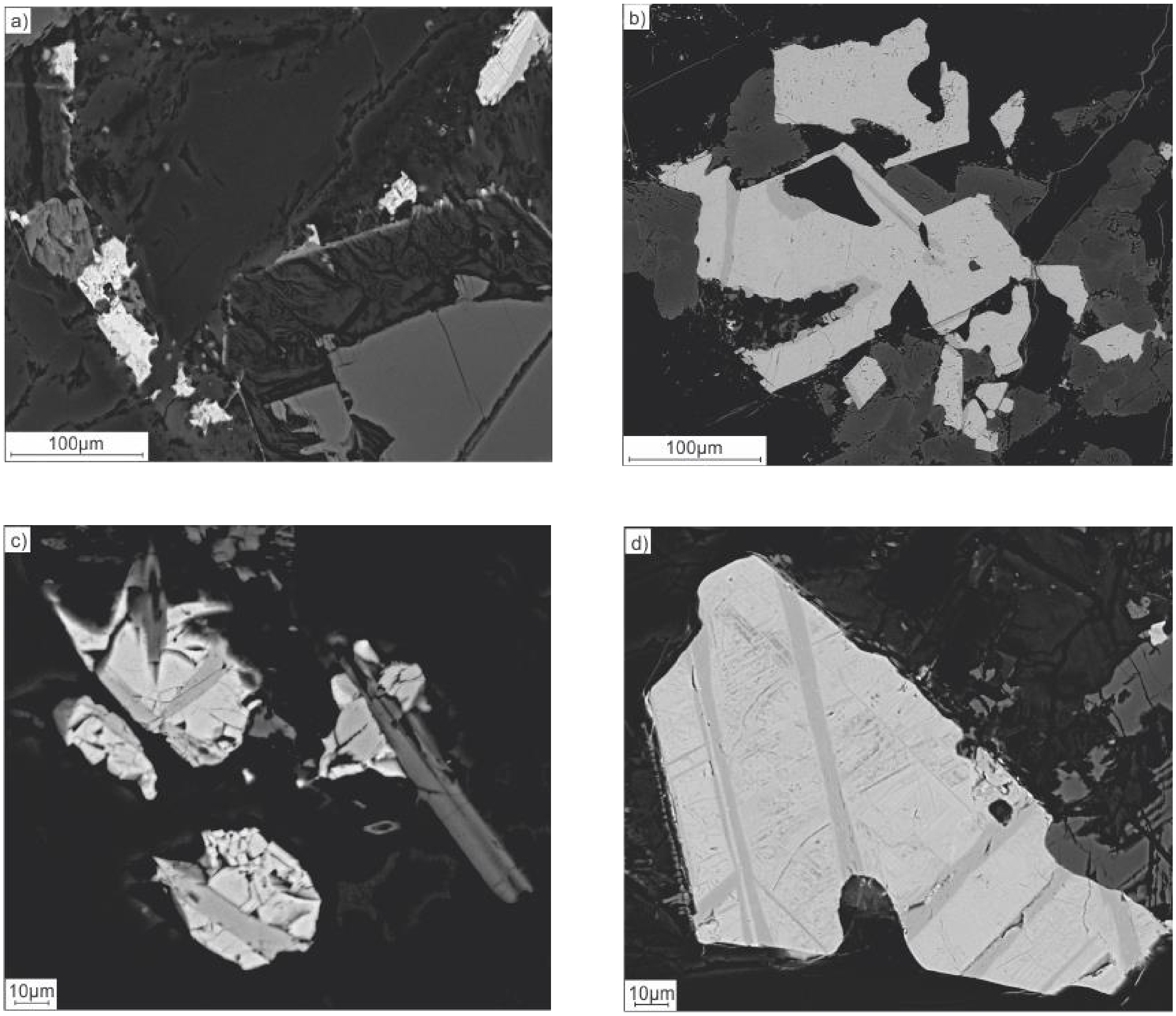

Figure 5.2. Representative scanning electron microscope images of polished samples. The magnetic mineralogy of the samples that passed palaeointensity section criteria; a) magnetite with patches of ilmenite (sample 92; site V5), b) skeletal titanomagnetite with ilmenite lamellae (sample 166; site V8), c) titanomagnetite and needles of ilmenite (sample 271; site Vil13), and d) skeletal titanomagnetite with ilmenite lamellae (sample 333; site Vil20).

5.4.2 Paleointensity

Absolute paleointensity results of the late Devonian samples with their quality factors are listed in Table 5.1. For microwave technique, 23 samples out of 60 samples from 6 sites (V5, V6, V7, V8, Vil13, and Vil20) have provided satisfactory (in terms of quality and statistics) paleointensity data. No samples from other 8 sites (V1, V2, V3, V4, Vil4, Vil8, Vil16, and Vil18) meet all the reliability criteria. In this study, the success rate for the microwave paleointensity determination is 38%. An example of the accepted Arai and associated Zijderveld plots are shown in Figure 5.3. Arai plots are strongly concave-up in shape but multiple lines of evidence support that this is caused by a strong component of magnetization, overprinting a weak primary magnetization rather than by lab-induced alteration or multi-domain behavior. The samples display corresponding distinct directional components, positive pTRM checks and little or no zig-zagging of the Arai plot. For thermal Thellier-Thellier technique, only 2 out of 16 samples from 2 sites (V5 and Vil20) have shown satisfactory paleointensity data. The success rate for this technique is low (12.5%) as the magnetic minerals in samples are, sometimes, altered chemically during the thermal paleointensity experiments (Valet et al., 1996; Heller et al., 2002; Smirnov and Tarduno, 2003). However, the overall sample behavior agrees well with the microwave results, showing a marginal directionally-offset overprint associated with the steep initial slope.

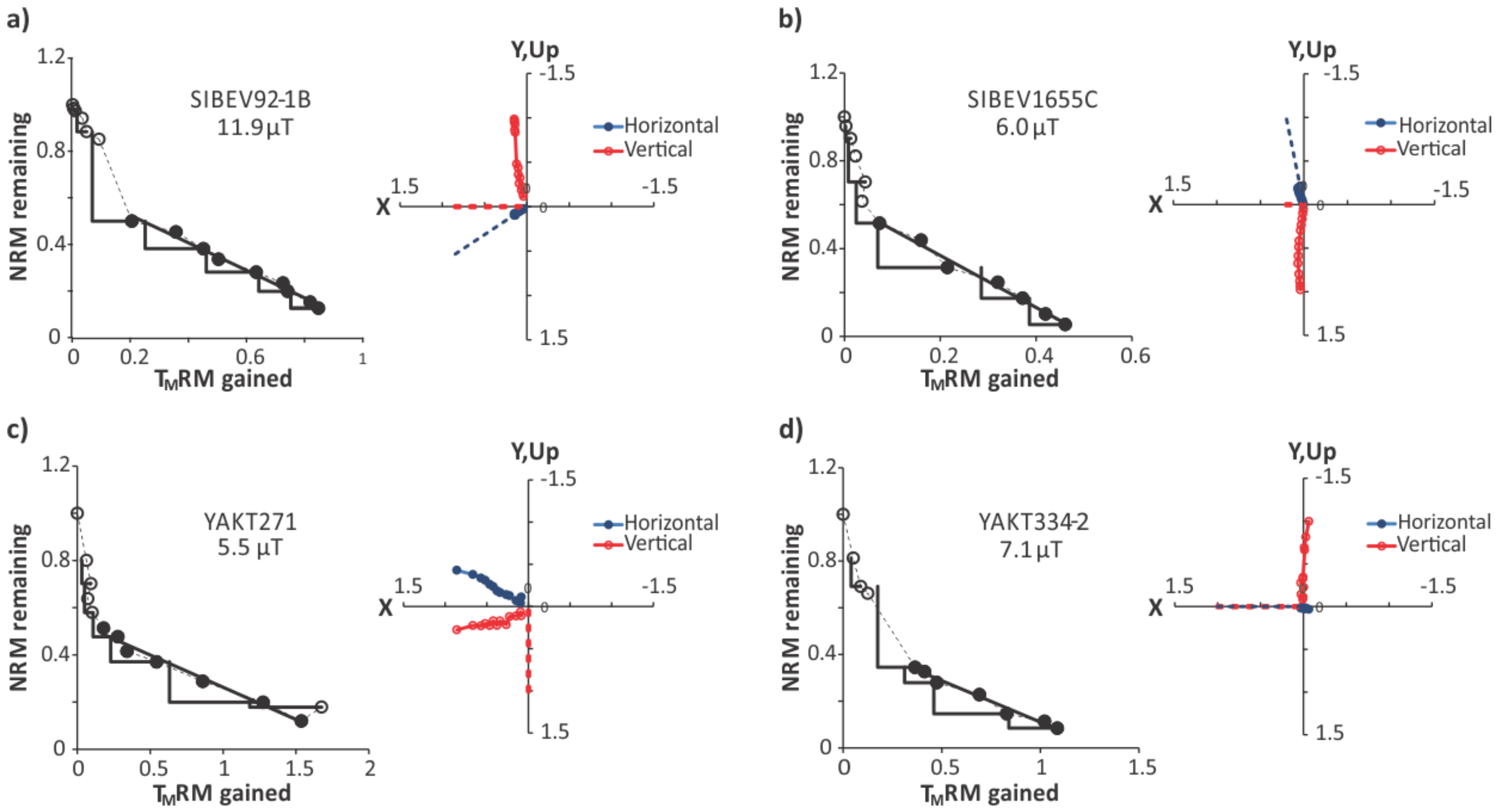

Figure 5.3. Examples of Arai and associated Zijderveld plots produced by the microwave Thellier method. Triangles on the Arai plots represent pTRM checks and the solid straight lines mark the interval on which intensity was estimated. On the Zijderveld plots, red (blue) points represent the vertical (horizontal) component (all samples were unoriented). Samples from a) site V5, b) site V8, c) site Vil13, and d) site Vil20.

Table 5.1. Absolute paleointensity results for the late Devonian. MW: Microwave paleointensity method and TT: thermal Thellier-type paleointensity method. I/T: Integral (W.s)/Temperature (℃). Hlab: applied laboratory magnetic field. N: number of successive data points used for paleointensity calculations. β, f, g and q are the measure of linearity, fraction of the NRM, the gap factor and the quality factor respectively. DRAT: percentage of discrepancy in the pTRM check. CDRAT: cumulative DRAT. MAD: maximum angular deviation. PI: paleointensity result. VADM: Virtual axial dipole moment with its associated standard deviation.

Site	Sample	Method	Low I/T	High I/T	Hlab (μT)	N	B	f	G	Q	delCK	DRAT	CDRAT	Alpha	MAD	PI (μT)	Site Mean (μT)	VADM ($\times 10^{22}$Am^2)
V5	SIBEV92-1B	MW	6	13	20	8	0.048	0.359	0.844	9.7	4.1%	6.5%	12.6%	3.5	2.1	11.6	8.5 ± 4.2	1.55 ± 0.76
	SIBEV92-1C	MW	6	11	15	6	0.060	0.261	0.782	5.3	2.2%	4.2%	-4.6%	13.2	7.2	11.0		
	SIBEV92-1D	MW	6	14	15	9	0.043	0.349	0.819	11.1	9.9%	13.9%	-1.2%	4.5	2.4	10.3		
	SIBEV99-2	MW	6	10	15	4	0.047	0.418	0.109	1.8	4.0%	4.5%	5.4%	3.3	5.6	7.9		
	V99	TT	250	500	15	6	0.061	0.258	0.570	6.1	4.4%	6.8%	-14.3%	3.2	3.7	1.5		
V6	SIBEV1102D	MW	6	14	5	8	0.095	0.415	0.770	6.6	0.0%	0.0%	0.0%	1.0	0.9	8.0	16.5 ± 10.2	2.97 ± 1.83
	SIBEV1144B	MW	0	8	5	6	0.071	0.745	0.742	7.7	11.6%	2.8%	-5.5%	5.3	2.4	27.7		
	SIBEV1144C	MW	1	4	5	9	0.049	0.632	0.503	3.6	0.0%	0.0%	0.0%	4.1	0.8	13.7		
V7	SIBEV1475B	MW	8	12	10	5	0.082	0.288	0.698	2.2	3.8%	12.8%	-13.8%	1.9	2.5	5.7	5.9 ± 0.3	1.07 ± 0.05
	SIBEV1503B	MW	0	13	5	5	0.063	0.567	0.552	6.7	0.7%	0.5%	-7.2%	0.5	1.1	6.2		
V8	SIBEV1543	MW	9	12	5	4	0.024	0.519	0.379	10.1	1.7%	2.0%	3.5%	6.8	3.5	4.3	5.9 ± 1.0	1.06 ± 0.18
	SIBEV165-5	MW	5	12	5	8	0.078	0.374	0.775	7.1	11.0%	10.4%	-0.2%	1.2	2.1	5.4		
	SIBEV1655B	MW	7	13	5	7	0.079	0.432	0.789	7.0	9.0%	7.5%	5.0%	1.6	1.7	6.9		
	SIBEV1655C	MW	6	12	5	7	0.053	0.461	0.824	11.8	14.0%	11.8%	8.8%	2.2	1.6	6.0		
	SIBEV1655D	MW	5	10	5	6	0.073	0.454	0.762	6.9	7.5%	7.2%	-8.9%	10.8	5.0	6.0		
	SIBEV1666C	MW	8	13	5	6	0.045	0.262	0.766	7.6	3.2%	4.2%	2.0%	6.3	2.5	6.9		

Vil13	YAKT271	MW	5	11	20	7	0.061	0.400	0.807	9.5	4.5%	6.1%	-2.1%	6.7	5.7	5.5	4.6 ± 1.1	0.81 ± 0.19
	YAKTVL274C	MW	6	11	5	6	0.062	0.504	0.701	7.9	3.8%	4.3%	-5.2%	4.3	5.4	3.9		
	YAKTVL276D	MW	2	8	5	6	0.092	0.571	0.741	7.2	6.3%	4.5%	-6.0%	13.6	10.6	6.0		
	YAKTVL276E	MW	5	9	5	5	0.077	0.333	0.738	4.9	3.8%	5.8%	2.3%	7.2	4.3	3.9		
	YAKT277-2	MW	5	8	20	4	0.022	0.351	0.624	14.7	0.7%	1.4%	-1.6%	10.8	4.1	5.0		
	YAKTVL279C	MW	5	9	5	5	0.068	0.294	0.683	7.0	5.8%	6.9%	-14.4%	7.0	6.4	3.2		
Vil20	Vil329a	TT	415	500	20	6	0.092	0.396	0.781	5.7	6.1%	8.0%	13.2%	4.3	4.0	10.4	8.8 ± 2.3	1.58 ± 0.41
	YAKT334-2	MW	5	11	20	7	0.062	0.285	0.804	7.2	6.7%	11.3%	2.4%	4.0	3.6	7.1		
Overall Mean																	8.4 ± 4.3	1.51 ± 0.78

Furthermore, 14 samples from 6 sites with accepted microwave paleointensity results were investigated using non-heating Pseudo-Thellier method to support microwave paleointensity data. As the samples show the ratio >>1 for slope1/slope2 (Figure 5.4), it supports the absolute microwave paleointensity data. The majority of the samples measured using this approach produced similarly concave-up pseudo-Arai plots (Figure 5.4), suggesting that the high coercivity component was acquired in a weaker field than the low coercivity component. Therefore, the results of non-heating pseudo-Thellier experiment support the existence of a strong component overprinting a much weaker one.

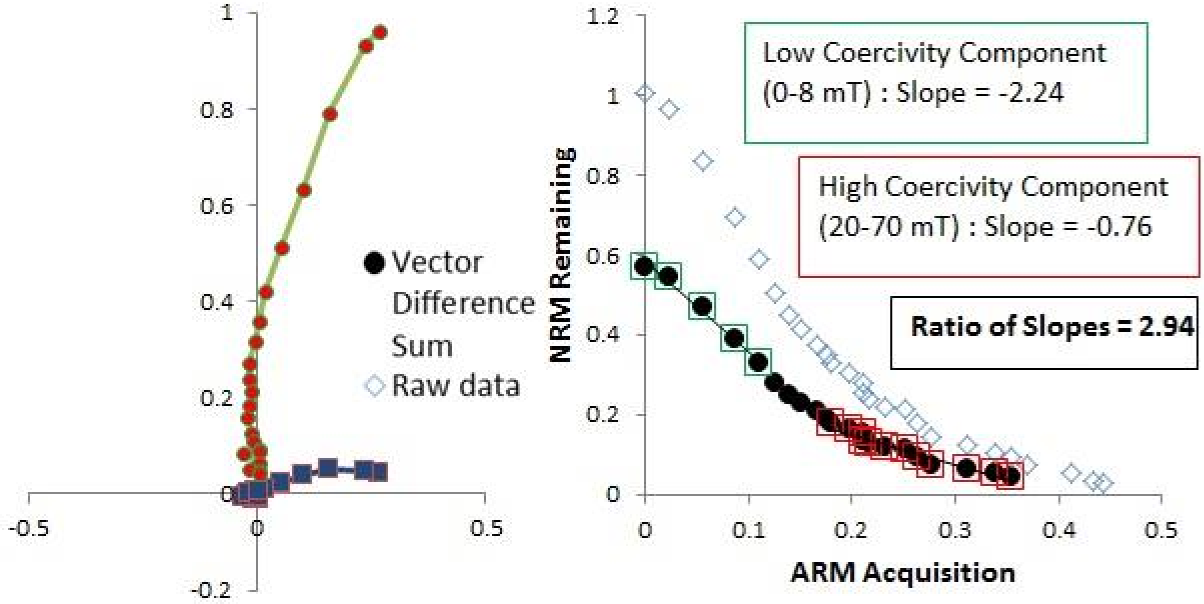

Figure 5.4. An example of a non-heating pseudo-Thellier experiment performed on sample V105-2B from site V5. The vector difference sum was used to account for the overprint component not converging on the origin.

Moreover, each accepted site was assigned a Q_{PI} (Quality of Paleointensity) value based on the number of criteria (Biggin and Paterson, 2014) that the site passed (Table 5.2). The paleointensity data of this study are considered to be reliable as Q_{PI} values are ≥ 5 for each site. Our study presents the site-mean paleointensities of 4.6−16.5 μT which corresponds to the virtual axial dipole moments (VADMs) of $0.81-2.97 \times 10^{22}$ Am^2. The paleointensity results from the six studied sites are fairly consistent with each other. The calculated mean paleointensity is 8.4 ± 4.3 μT which corresponds to a mean VADM of $1.51 \pm 0.78 \times 10^{22}$ Am^2, suggesting that the field was extremely weak during the late Devonian (Figure 5.5). Results indicate that the magnetic field intensity during late Devonian is significantly lower (< 30%) than the present geomagnetic field intensity. Furthermore, the paleointensity results for both the normal (V5, V8, Vil13, Vil20) and reverse (V6, V7) polarity sites are low, supporting our argument that the geomagnetic dipole low is a characteristic of the late Devonian. As the published data are old and small in number for this time period, it is difficult to determine whether there is a difference between field intensities corresponding to this study and previous studies. However, Smith (1968), Kono (1979), Didenko and Pechersky (1989), and Solodovnikov (1996) reported similar weak field values for the Devonian. Thus, the low field intensity in the Devonian period seems to be substantiated.

Similar to the transition from the Mid Jurassic to the CNS, this study would suggest that the field was weak ~50Ma before the onset of the PCRS (Figure 5.5). Although there are not enough existing data to identify reversal frequency in the late Devonian, a recent study (Hansma et al., 2015) indicates that reversals were really more frequent during that time. Therefore, based on the present knowledge, we can conclude that the geomagnetic field in the late Devonian times was weak and multipolar. Low dipole moment can be considered an indicator of high reversal frequency as appears to be the case in the mid-Jurassic and also in the late Devonian, demonstrating that these transitions between reversal hyperactivity and superchron states in geomagnetic field behavior are a recurring feature in the paleomagnetic record. We, therefore, have evidence of a recurring phenomenon in paleomagnetic behavior that most likely reflects a quasi-periodic process in the lower mantle producing changes in the pattern and/or magnitude of core-mantle heat flow.

Table 5.2. Breakdown of criteria fulfillment and Q_{PI} (Quality of Paleointensity) values determined for each accepted studied site.

Site	AGE	STAT	TRM	ALT	MD	A C N	TECH	LITH	Q_{PI}
V5	1	0	1	1	0	1	1	0	5
V6	1	0	1	1	1	1	0	0	5
V7	1	0	1	1	1	1	0	0	5
V8	1	1	1	1	1	1	0	0	6
Vil13	1	0	1	1	1	1	0	0	5
Vil20	1	0	1	1	1	1	1	0	6

"AGE: A reliable age and palaeomagnetic behavior consistent with paleointensity derived from a primary component of remanence, STAT: A minimum of 5 individual sample estimates per unit with low dispersion (true SD/mean ≤25%), TRM: Reasonable independent (e.g., microscopic) evidence that the component of remanence in the bulk of samples is likely a thermoremanent magnetization (TRM), ALT: Reasonable evidence (e.g., pTRM checks or rock mag) that the final estimate was not significantly biased by alteration occurring during the experiment, MD: Reasonable evidence (e.g., high f or pTRM tail checks) that the final estimate was not significantly biased by multidomain behavior during the experiment, ACN: Reasonable evidence that the final estimate was not significantly biased by anisotropy of TRM, cooling rate effects, and non-linear TRM effects, TECH: Estimate is an average of results from more than one palaeointensity technique, LITH: Estimate is an average of results from more than one lithology or from samples from the same lithology showing significantly different unblocking behavior" (Biggin and Paterson, 2014). Here, '1' indicates that the given criterion has been met, while '0' indicates failure to do so.

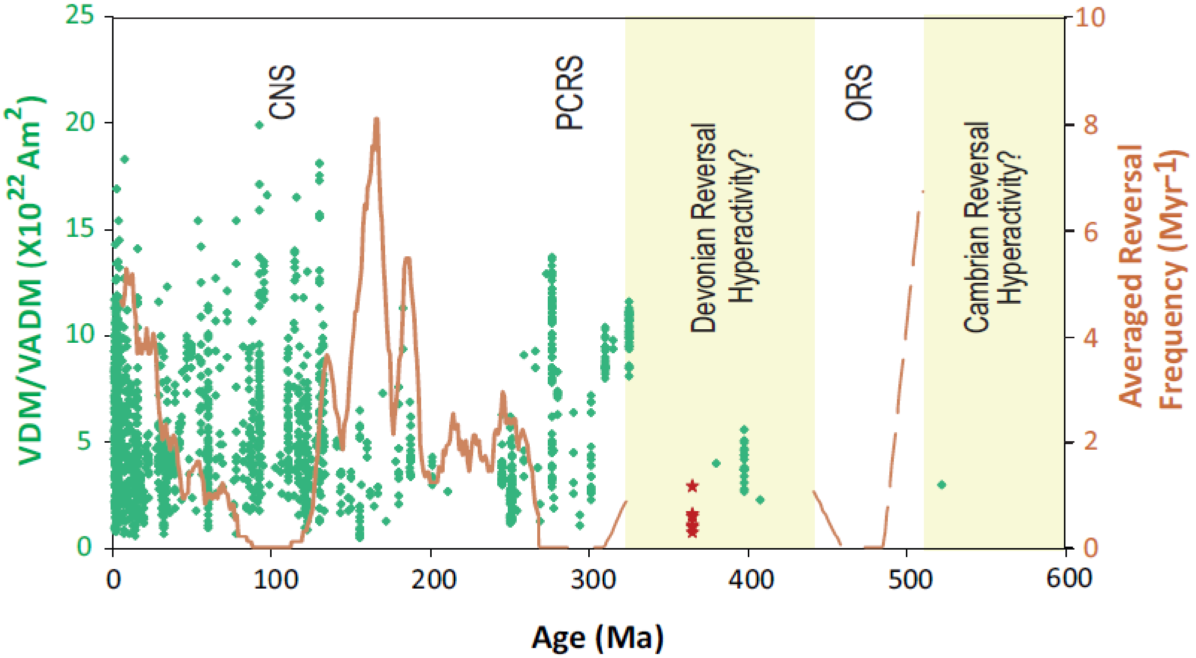

Figure 5.5. Records of virtual (axial) dipole moment [V(A)DM] from the PINT database (green points) and the data from this study (red star) alongside geomagnetic polarity reversal frequency from the marine magnetic anomaly record (Cande and Kent, 1995; Tominaga and Sager 2010) and magnetostratigraphic studies (Ogg, 2004). Shaded area indicates insufficient data. ORS: Ordovician Reversed Superchron; PCRS: Permo-Carboniferous Reversed Superchron; CNS: Cretaceous Normal Superchron.

5.5 Conclusions

Paleointensity study of the Late Devonian provides new paleointensity results and information about the behavior of the geodynamo during a largely unstudied time period. Results indicate that the Late Devonian was a time of extremely weak magnetic field intensity varied from 4.6–16.5 µT which corresponds to virtual axial dipole moments (VADMs) of (0.81–2.97) ×10^{22} Am^2. Results are considered to be reliable as the Q_{PI} (Quality of Paleointensity) values are ≥ 5.

It provides the evidence that the superchron state, between ~310 and 265 Ma, is preceded by a very weak field in the late Devonian (~50 Ma before the superchron). If low dipole moment can be considered an indicator of high reversal frequency (as appears to be the case in the mid-Jurassic), these results support the idea that rapid transitions between reversal hyperactivity and superchron states are a recurring feature in the paleomagnetic record. These apparently periodic (~180 million years) transitions in geomagnetic field behavior may indicate the influence of mantle convection changing heat flow across the core-mantle boundary.

References

Biggin, A.J., 2006. First-order symmetry of weak-field partial thermoremanence in multi-domain (MD) ferromagnetic grains: 2. Implications for Thellier-type palaeointensity determination. Earth Planet. Sci. Lett., 245 (1-2), 454–470.

Biggin, A.J. and Paterson G.A., 2014. A new set of qualitative reliability criteria to aid inferences on palaeomagnetic dipole moment variations through geological time. Frontiers in Earth Science, 2, 24, 1–9.

Biggin, A.J., Steinberger, B., Aubert, J., Suttie, N., Holme, R., Torsvik, T.H., Van der Meer, D.G., Van Hinsbergen, D.J.J., 2012. Possible links between long term geomagnetic variations and whole-mantle convection processes. NatureGeosci., 8, 526–533.

Cande, S.C., and Kent, D.V., 1995. Revised calibration of the geomagnetic polarity timescale for the Late Cretaceous and Cenozoic. J. Geophys. Res.-Sol. Ea., 100, 6093–6095.

Coe, R.S., 1967. Palaeointensities of the Earth's magnetic field determined from tertiary and quaternary rocks. Journal of Geophysical Research-Solid Earth, 72, 3247–3262.

Coe, R.S., Grommé, C.S., Mankinen, E.A., 1978. Geomagnetic paleointensities from radiocarbon dated lava flows on Hawaii and the question of the Pacific nondipole low. J. Geophys. Res., 83, 1740–1756.

Courtillot, V., and Besse, J., 1987. Magnetic field reversals, polar wander, and core–mantle coupling. Science, 237, 1140–1147.

Courtillot, V., Kravchinsky, V.A., Quidelleur, X., Renne, P.R., Gladkochub, D.P., 2010. Preliminary dating of the Viluy traps (Eastern Siberia): eruption at the time of Late Devonian extinction events? Earth and Planetary Science Letters, 300, 239–245.

Didenko, A.N. and Pechersky, D.M., 1989. Direction and intensity of the geomagnetic field in the Middle Devonian and Lower Ordovician: southern Mugodjary ophiolites (Urals). Physics of the earth and planetary interiors, 58(4), 289–306.

Gaiduk, V.V., 1987. Viluy middle Paleozoic rift system. Geotectonics, 3, 66–76.

Glatzmaier, G.A., Coe, R.S., Hongre, L., Roberts, P.H., 1999. The role of the Earth's mantle in controlling the frequency of geomagnetic reversals. Nature, 401, 885–890.

Hansma, J., Tohver, E., Yan, M., Trinajstic, K., Roelofs, B., Peek, S., Slotznick, S.P., Kirschvink, J., Playton, T., Haines, P., Hocking, R., 2015. Late Devonian carbonate magnetostratigraphy from the Oscar and Horse Spring Ranges, Lennard Shelf, Canning Basin, Western Australia. Earth and Planetary Science Letters, 409, 232–242.

Heller, R., Merrill, R.T., McFadden, P.L., 2002. The variation of intensity of earth’s magnetic field with time. Phys. Earth Planet. Inter., 131(3–4), 237–249.

Kiselev, A., Yarmolyuk, V., Egorov, K., Chernyshov, R., Nikiforov, A., 2006. Middle Paleozoic basic magmatism of the northwestern Vilyui Rift: composition, sources, and geodynamics. Petrology, 14, 588–608.

Kono, M., 1979. Palaeomagnetism and palaeointensity studies of Scottish Devonian volcanic rocks. Geophysical Journal International, 56(2), 385–396.

Kravchinsky, V.A., Konstantinov, K.M., Courtillot, V., Savrasov, J.I., Valet, J.P., Cherniy, S.D., Mishenin, S.G., Parasotka, B.S., 2002. Palaeomagnetism of East Siberian traps and kimberlites: two new poles and palaeogeographic reconstructions at about 360 and 250 Ma. Geophys. J. Int., 148, 1–33.

Kutzner, C., Christensen, U., 2002. From stable dipolar to reversing numerical dynamos. Phys. Earth Planet. Inter., 121, 29–45.

Kuzmin, M.I., Yarmolyuk, V.V., Kravchinsky, V.A., 2010. Phanerozoic hot spot traces and paleogeographic reconstructions of the Siberian continent based on interaction with the African large low shear velocity province. Earth-Science Reviews, 102, 29–59.

Labrosse, S., 2002. Hotspots, mantle plumes and core heat loss. Earth Planet Sci. Lett., 199, 147–156.

McClelland, E., and Briden, J.C., 1996. An improved methodology for Thellier-type paleointensity determination in igneous rocks and its usefulness for verifying primary thermoremanence. J. Geophys. Res., 101, 21995–22013.

Masaitis, V.L., Mikhailov, M.V., Selivanovskaya, T.V., 1975. Volcanism and Tectonics of Patom-Vylyu Middle Paleozoic Aulacogen. Nedra, Moscow, 184.

Nagata, T., Arai, Y., Momose, K. 1963. Secular variation of the geomagnetic total force during the last 5000 years. J. Geophys. Res., 68, 5277–5281.

Ogg, J.G., 2004. In A Geological Time Scale 2004. Gradstein, F.M., Ogg, J.G., and Smith, A.G., (Eds.), Cambridge Univ. Press, 307–339.

Olson, P., 2003. Thermal interaction of the core and mantle. In: Jones, C.A., Soward, A.M., Zhang, K. (Eds.), Earth's Core and Lower Mantle. Taylor and Francis, London and New York, 218.

Ricci, J., Quidelleur, X., Pavlov, V., Orlov, S., Shatsillo, A., Courtillot, V., 2013. New 40Ar/39Ar and K–Ar ages of the Viluy traps (Eastern Siberia): Further evidence for a relationship with the Frasnian–Famennian mass extinction. Palaeogeog.Palaeoclim.Palaeoecol., 386, 531–540.

Riisager, P., and Riisager, J., 2001. Detecting multidomain magnetic grains in Thellier palaeointensity experiments. Phys. Earth Planet. Int., 125, 111–117.

Roberts, P.H., Jones, C.A., Calderwood, A., 2003. Energy fluxes and Ohmic dissipation in the Earth's core. In: Jones, C.A., Soward, A.M., Zhang, K. (Eds.), Earth's Core and Lower Mantle. Taylor and Francis, London and New York, 218.

Smirnov, A.V. and Tarduno, J.A., 2003. Magnetic hysteresis monitoring of Cretaceous submarine basaltic glass during Thellier paleointensity experiments: evidence for alteration and attendant low field bias, Earth Planet. Sci. Lett., 206(3–4), 571–585.

Smith, P.J., 1968. Estimates of the Devonian geomagnetic intensity in Scotland. US Geol. Surv. 575-D, 164–168.

Solodovnikov, G.M., 1996. Geomagnetic Intensity in the Early-Middle Devonian. Izvestiya Physics of the Solid Earth, 32(7), 615–621.

Takahashi, F., Matsushima, M., Honkura, Y., 2005. Simulations of a quasi-Taylor state geomagnetic field including polarity reversals on the Earth Simulator. Science, 309, 459–461.

Tauxe, L., Staudigel, H., 2004. Strength of the geomagnetic field in the Cretaceous Normal Superchron: new data from submarine basaltic glass of the Troodos Ophiolite. Geochemistry Geophysics Geosystems, 5 (Art. No. Q02H06).

Tauxe, L., Pick, T., Kok, Y., 1995. Relative paleointensity in sediments: a pseudo-Thellier approach. Geophys. Res. Lett., 22, 2885–2888.

Tominaga, M., and Sager, W.W., 2010. Revised Pacific M-anomaly geomagnetic polarity timescale. Geophys. J. Int., 182, 203–232.

Valet, J.P., Brassart, J., Le Meur, I., Soler, V., Quidelleur, X., Tric, E., Gillot, P.Y., 1996. Absolute paleointensity and magnetomineralogical changes. J. Geophys. Res., 101(B11), 25029–25044, doi:10.1029/96JB02115.

Wicht, J., and Olson, P., 2004. A detailed study of the polarity reversal mechanism in a numerical dynamo model. Geochem. Geophys. Geosys., 5.

Zonenshain, L.P., Kuzmin, M.I., Natapov, L.M., 1991. Geology of the USSR: a Platetectonic Synthesis. American geophysical Union, Washington,s 442.

Chapter 6

Conclusions

6.1 Conclusions

This thesis presents different applications of paleomagnetism to implement a new technique to evaluate age for the Chinese red clay sequence; to investigate the regional climate and environment change in the Holocene recorded in the Chinese Loess; to produce a grand mean paleomagnetic dipole moment for the Permo-Triassic boundary; and to obtain intensity of the dipolar field during the late Devonian. All the results, acquired through various paleomagnetic applications, reveal critical understanding of the Earth's climate and evolution. The studies, indeed, fulfill the objectives of this thesis through the findings which are summarized in the following main points.

The first study, where the magnetostratigraphic age model is tested using cyclostratigraphy, confirms that the red clay section at Shilou on the eastern Chinese Loess Plateau was formed 5.2 Ma. The well preserved 400 kyr eccentricity and the existence of 100 kyr eccentricity in the red clay sequence imply that eccentricity plays a vital role in Pliocene climate evolution. Paleomonsoon evolution during 2.58–5.2 Ma was reconstructed and divided into three intervals (2.58–3.6 Ma, 3.6–4.5 Ma, and 4.5–5.2 Ma). The latest interval shows a relatively intensified summer monsoon, the middle interval indicates an intensification of the winter monsoon and aridification in Asia, and the earliest interval represents a rapid alteration of summer and winter monsoon cycles. Overall, this study indicates that cyclostratigraphy can assist magnetostratigraphy in dating red clay sequences more accurately.

The second study investigates the Holocene Chinese loess sequence through petromagnetic and grain size analyses and confirms that subsequent warm-humid phase occurred there during ~8.4–3.7 ka, ~2.4–1.2 ka, and ~0.81–0.48 ka associated with the soil formation and relatively high values of petromagnetic parameters. The results also suggest that the Holocene optimum period occurred between ~8.4 and ~3.7 ka, while the summer monsoon influenced the region quite strongly. Findings also indicate that the Holocene climate record of the studied regions is consistent with the reported climate records from the tree pollen analysis along the south-to-north eastern Chinese Loess Plateau at that time. It implies that the same climatic variation occurred in the eastern monsoonal China. Overall, the results respond to the rapid changes found in records from elsewhere in the world, indicating that these relate to the changes in global climate.

The third research in this thesis explores the microwave paleointensity of the Permo-Triassic trap basalts for the first time. The results indicate that the average geomagnetic intensity for the northern and the southeastern Siberian traps are significantly different, most likely reflects slightly different sampling of secular variation by the distinct suites of rocks. It demonstrates that it is important to consider multiple localities to evaluate the mean paleointensity for the Permo-Triassic boundary (PTB). After combining the microwave paleointensity data of this study with thermal Thellier paleointensity data of previous studies, the study reveals the grand mean paleointensity at the PTB as 19.5 ± 10.5 μT, which corresponds to a grand mean virtual dipole moment (VDM) of $3.2 \pm 1.5 \times 10^{22}$ Am^2. These are considered to be reliable as QPI (Quality of Paleointensity) values ≥ 4. The research suggests that the magnetic field intensity during this period was significantly lower (approximately half) than the present geomagnetic field intensity, implying that the Mesozoic dipole low might have begun at the PTB.

The forth study explores the behavior of the geodynamo during a largely unstudied time period, the late Devonian. The results confirm that the late Devonian was a time of extremely weak magnetic field intensity, varied from 4.6 μT to 16.5 μT, corresponding to virtual axial dipole moments (VADMs) of (0.81-2.97) $\times 10^{22}$ Am^2. This research reveals that the Permo-Carboniferous superchron state was preceded by a very weak field in the late Devonian (~50 Ma before the superchron). Considering low dipole moment to be an indicator of high reversal frequency (as appears to be the case in the mid-Jurassic), this study concludes that rapid transitions between reversal hyperactivity and superchron states are a recurring feature in the palaeomagnetic record. These apparently periodic (~180 million years) transitions in geomagnetic field behavior may indicate the influence of mantle convection changing heat flow across the core-mantle boundary.

6.2 Future Work

The works presented in this thesis shed more light on the understanding of the evolution of paleoclimate and geomagnetic field changes. This thesis also offers challenges and opportunities for further studies. These consist of, but are not limited to, the following potential future researches:

- The first study in this thesis demonstrates a steady long-term improvement in the approach to the problem of red clay dating. It could be applied more often for the way out of subjective correlation. However, this new dating approach requires well-preserved climate proxy records to resolve Milankovitch cycles. It is fundamental to measure proxy record for re-evaluating presently published magnetostratigraphic age models for the red clay deposits. Furthermore, it would be instrumental to apply this new approach for small sampling interval for resolving the shorter cycles (obliquity and precession) as it helps investigate the monsoonal climatic evolution.

- The second research in this thesis illustrates the Holocene climatic optimum period in Asia and its correlation with regional as well as global records. However, it would be advantageous to investigate whether the Holocene climate in China is only sensitive to the large warming and cooling events or if it is also (in)sensitive to the millennial scale climate changes as predicted by theory. Additionally, there still remains the opportunity to identify the possible sources of climate variability and climate cyclicity in Asia during the Holocene through the time series analysis of the studied paleoclimatic proxy records.

- The third research in this thesis demonstrates the geomagnetic field behavior for the Permo-Triassic boundary. It presents a grand mean paleomagnetic dipole moment for the PTB that helps identify the possible extension of the Mesozoic dipole low to the PTB. However, further study of the geomagnetic field behavior for the Triassic is required to substantiate this hypothesis of extension. Furthermore, the relationships between magnetic intensity variations during polarity reversals and the largest mass extinction can be investigated using the grand mean paleomagnetic dipole moment from this research. It can potentially provide a fundamental insight of the dynamics for the geodynamo processes operating on the Earth's core and mantle convection.

- The fourth research in this thesis portrays the nature of intensity of the Earth’s magnetic field during the late Devonian. Though there is a global lack of suitable sections to estimate the reversal frequency, it is necessary to extend the magnetostratigraphic analysis to support the prediction of the reversals frequency being high for this time period as explained by a single study. Furthermore, it would be interesting to test the hypothesis that an episode of true polar wander caused the strength of the Earth's magnetic field to increase dramatically between approximately 370 and 310 million years ago.

Bibliography

Abramova, D.Y., and Abramova, L.M., 2014. Lithospheric magnetic anomalies in the territory of Siberia (from measurements by the CHAMP satellite). Russian Geology and Geophysics, 55(7), 854-863.

Aitken, M.J., Allsop, A.L., Bussel, G.D., Winter, M.B., 1988. Determination of the intensity of the Earth's magnetic field during archeological times: reliability of the Thellier technique. Reviews of Geophysics, 26, 3–12.

Almukhamedov, A.I., Medvedev, A.Ya., Mitchell, C., Zolotukhin, V.V., 1996. Flood basalts in the core of the Tunguska syneclinse: comparative geochemistry (in Russian). Russian Geol. Geophys. Novosibirsk, 37, 3–16.

Almukhamedov, A.I., Medvedev, A.Ya., Zolotukhin, V.V., 2004. Compositional evolution of the Permian–Triassic basalts of the Siberian Platform in time and space. Petrology, 2 (4), 339–353 (in Russian).

Alverson, K., Oldfield, F., Bradley, R.S. (Eds.), 1999. Past Global Changes and Their Significance for the Future. Elsevier, Amsterdam, 479.

Alverson, K.D., Bradley, R.S., Pedersen, T.F., 2003. Paleoclimate, Global Change and the Future. Springer, New York.

An, Z.S., 2000. The history and variability of the East Asian paleomonsoon climate. Quat. Sci. Rev., 19, 171–187.

An, Z.S., and Xiao, J.L., 1990. Study on the eolian dust flux over the Loess Plateau – an example. Chin. Sci. Bull., 35, 1627–1631.

An, Z.S., Liu, T.S., Lou, Y.C., Porter, S.C., Kukla, G.J., Wu, X.H., Hua, Y.M., 1990. The long-term paleomonsoon variation recorded by the loess-paleosol sequence in central China. Quaternary International, 7(8), 91–95.

An, Z.S., Kukla, G., Porter S.C., Xiao, J.L., 1991. Magnetic susceptibility evidence of monsoon variation on the Loess Plateau of central China during the last 130,000 years. Quaternary Research, 36, 29–36.

An, Z.S., Kukla, G., Porter, S.C., Xiao, J.L., 1991. Late quaternary dust flow on the Chinese Loess Plateau. Catena, 18, 125–132.

An, Z.S., Wang, S.M., Wu, X.H., Chen, M.Y., Sun, D.H., Liu, X.M., Wang, F.B., Li, L., Sun, Y.B., Zhou, W.J., Zhou, J., Liu, X.D., Lu, H.Y., Zhang, Y.X., Dong, G.R., Qiang, X.K., 1999. Eolian evidence from the Chinese Loess Plateau: the onset of the Late Cenozoic Great Glaciation in the Northern Hemisphere and Qinghai–Xizang Plateau uplift forcing. Science in China, Ser. D, 42, 258–271.

An, Z.S., Porter, S.C., Kutzbach, J.E., Wu, X.H., Wang, S.M., Liu, X.D., Li, X.Q., Zhou, W.J., 2000. Asynchronous Holocene optimum of the East Asian monsoon. Quaternary Science Reviews, 19, 734–762.

An, Z.S., Kutzbach, J.E., Prell, W.L., Porter, S.C., 2001. Evolution of Asian monsoons and phased uplift of the Himalaya Tibetan plateau since Late Miocene times. Nature, 411, 62–66.

An, C.B., Tang, L.Y., Barton, L., and Chen, F.H., 2005. Climate change and cultural response around 4000 cal yr B.P. in the western part of Chinese Loess Plateau. Quaternary Research, 63, 347–52.

Anwar, T., Kravchinsky, V.A., and Zhang, R., 2015. Magneto- and cyclostratigraphy in the red clay sequence: New age model and paleoclimatic implication for the eastern Chinese Loess Plateau. Journal of Geophysical Research: Solid Earth, 120(10), 6758–6770.

Anwar, T., Hawkins L., Kravchinsky, V.A., Biggin, A.J., Pavlov, V.E., 2016. Microwave paleointensities indicate a low paleomagnetic dipole moment at the Permo-Triassic boundary. Physics of the Earth and Planetary Interiors, 260, 62–73.

Baker, P.A., Seltzer, G.O., Fritz, S.C., Dunbar, R.B., Grove, M.J., Tapia, P.M., Cross, S.L., Rowe, H.D., and Broda, J.P., 2001. The History of South American tropical precipitation for the past 25,000 years. Science, 291, 640–43.

Balsam, W., Ji, J.F., Chen, J., 2004. Climatic interpretation of the Luochuan and Lingtai loess sections, China, based on changing iron oxide mineralogy and magnetic susceptibility. Earth Planet. Sci. Lett., 223, 335–348.

Basu, A.R., Hannigan, R.E., Jacobsen, S.B., 1998. Melting of the Siberian mantle plume. Geophys. Res. Lett., 25, 2209–2212.

Beer, J., Vonmoos, M., Muscheler, R., 2006. Solar variability over the past several millennia. Space Science Reviews, 125, 67–79.

Berger, A., 1978. Long-term variations of daily insolation and quaternary climatic changes. J. Atmos. Sci. 35, 2362–2367.

Berger, A., and Loutre, M.F., 1991. Insolation values for the climate of the last 10 million years. Quat. Sci. Rev. 10, 297–318.

Berger, A., and Loutre, M.F., 1994. Astronomical forcing through geologic time. In Orbital Forcing and Cyclic Sequences, ed. PL DeBoer, DG Smith, Spec. Publ. 19, Int. Ass. Sed., pp. 15–24. Oxford: Blackwell Scientific.

Berger, A., Loutre, M.F., Dehant, V., 1989. Influence of the changing lunar orbit on the astronomical frequencies of pre-Quaternary insolation patterns. Paleoceanography 4(5): 555–64.

Berger, A., Loutre, M.F., Laskar, J., 1992. Stability of the astronomical frequencies over the Earth's history for paleoclimatic studies. Science, 255, 560–566.

Bianchi, G.G., and McCave, I.N., 1999. Holocene periodicity in north Atlantic climate and deep-ocean flow south of Iceland. Nature, 397, 515–17.

Biggin, A.J., 2006. First-order symmetry of weak-field partial thermoremanence in multi-domain (MD) ferromagnetic grains: 2. Implications for Thellier-type palaeointensity determination. Earth Planet. Sci. Lett., 245 (1-2), 454-470.

Biggin, A.J., 2010. Are systematic differences between thermal and microwave Thellier-type palaeointensity estimates a consequence of multidomain bias in the thermal results? Phys. Earth Planet. Inter., 180, 16–40.

Biggin, A.J., and Paterson G.A., 2014. A new set of qualitative reliability criteria to aid inferences on palaeomagnetic dipole moment variations through geological time. Frontiers in Earth Science, 2, 24, 1-9.

Biggin, A.J., Perrin, M., Dekkers, M.J., 2007. A reliable absolute palaeointensity determination obtained from a non-ideal recorder. Earth Planet. Sci. Lett., 257, 545–563.

Biggin, A.J., McCormack, A., Roberts, A., 2010. Paleointensity database updated and upgraded. Eos Trans. AGU, 91(2), 15.

Biggin, A.J., Steinberger, B., Aubert, J., Suttie, N., Holme, R., Torsvik, T.H., Van der Meer, D.G., Van Hinsbergen, D.J.J., 2012. Possible links between long term geomagnetic variations and whole-mantle convection processes. NatureGeosci., 8, 526–533.

Biggin, A.J., Piispa, E, Pesonen, L.J., Holme, R., Paterson, G.A., Veikkolainen, T., Tauxe, L. 2015. Palaeomagnetic field strength variations suggest Mesoproterozoic inner core nucleation. Nature, 525, 245-248.

Blanco, D., Kravchinsky, V.A., Valet, J.P., Ali, A., Potter, D.K., 2012. Does the Permo-Triassic geomagnetic dipole low exist? Phys. Earth Planet. Inter., 204-205, 11–21.

Böhnel, H., Biggin, A.J., Walton, D., Shaw, J., Share, J.A., 2003. Microwave palaeointensities from a recent Mexican lava flow, baked sediments and reheated pottery. Earth Planet. Sci. Lett., 214 (1–2), 221–236.

Bond, G., Showers, W., Cheseby, M., Lotti, R., Almasi, P., deMenocal, P., Priore, P., Cullen, H., Hajdas, I., Bonani, G., 1997. A pervasive millenial-scale cycle in North Atlantic Holocene and glacial climates. Science, 278, 1257– 1266.

Bond, G., Kromer, B., Beer, J., Muscheler, R., Evans, M.N., Showers, W., Hoffmann, S., Lotti-Bond, R., Hajdas, I., Bonani, G., 2001. Persistent solar influence on north Atlantic climate during the Holocene. Science, 294, 2130–2136.

Bradley, R.S., 1985. Quaternary Palaeoclimatology: Methods of Palaeoclimatic Reconstruction. Unwin Hyman, London.

Bradley, R.S., 1999. Paleoclimatology, Reconstructing Climates of the Quaternary. Academic Press, San Diego, 610.

Bradley, R.S., 2008. Holocene perspectives on future climate change. In: Battarbee, R.W., Binney, H.A. (Eds.), Natural Climate Variability and Global Warming: A Holocene Perspective. Wiley-Blackwell, Chichester, 254–268.

Bradley, R.S., 2015. Paleoclimatology, Reconstructing Climates of the Quaternary (3rd edition). Elsevier/Academic Press, San Diego, 675.

Bradley, R.S., and Eddy, J.A., 1991. Records of past global changes. In: Bradley, R.S. (Ed.), Global Changes of the Past. University Corporation for Atmospheric Research, Boulder, 514.

Bryson, R.A., and Wendland, W.M., 1967. Tentative climate patterns for some late-glacial and post-glacial episodes in central North America. In: Life, land and water, Mayer-Oakes, W.J. (ed.). University of Manitoba Press, Winnipeg, pp. 271-298.

Burgess, S.D., and Bowring, S.A., 2015. High-precision geochronology confirms voluminous magmatism before, during, and after Earth's most severe extinction. Science advances, 1(7), e1500470.

Butler, R.F., 1992. Paleomagnetism: magnetic domains to geologic terranes. Blackwell Scientific Publications, Boston, MA, 238.

Cande, S.C., and Kent, D.V., 1995. Revised calibration of the geomagnetic polarity timescale for the Late Cretaceous and Cenozoic. Journal of Geophysical Research: Solid Earth, 100, 6093–6095.

Cane, M.A., and Molnar, P., 2001. Closing of the Indonesian seaway as a precursor to east African aridification around 3–4 million years ago. Nature, 411, 157–162.

Chang, B., Kim, W., Doh, S.J., and Yu, Y., 2013. Paleointensity determination of Late Cretaceous basalts in northwest South Korea: implications for low and stable paleofield strength in the Late Cretaceous. Earth Planets Space, 65, 1501–1513.

Chen, X.F., 1994. Stratigraphy and large mammals of the "Jinglean" stage, Shanxi, China [in Chinese with English abstract]. Quaternary Sciences, 4, 339–353.

Cheng, H., Edwards, R.L., Broecker, W.S., Denton, G.H., Kong, X.G., Wang, Y.J., Zhang, R., Wang, X.F., 2009. Ice age terminations. Science, 326, 248–252.

Christensen, U.R., and Wicht, J., 2007. Numerical dynamo simulations. Treatise Geophys., 8, 245–282.

Clemens, S.C., and Tiedemann, R., 1997, Eccentricity forcing of Pliocene–Early Pleistocene climate revealed in a marine oxygen-isotope record. Nature, 385, 801–804.

Coe, R.S., 1967. Palaeointensities of the Earth's magnetic field determined from tertiary and quaternary rocks. Journal of Geophysical Research-Solid Earth, 72, 3247–3262.

Coe, R.S., Grommé, C.S., Mankinen, E.A., 1978. Geomagnetic paleointensities from radiocarbon dated lava flows on Hawaii and the question of the Pacific nondipole low. J. Geophys. Res., 83, 1740–1756.

Cosford, J., Qing, H., Eglington, B., Mattey, D., Yuan, D., Zhang, M., & Cheng, H., 2008. East Asian monsoon variability since the Mid-Holocene recorded in a high-resolution, absolute-dated aragonite speleothem from eastern China. Earth and Planetary Science Letters, 275(3), 296–307.

Courtillot, V., and Besse, J., 1987. Magnetic field reversals, polar wander, and core–mantle coupling. Science, 237, 1140–1147.

Courtillot, V., and Renne, P.R., 2003. On the ages of flood basalt events. C.R. Geosci., 335, 113–140.

Courtillot, V., and Olson, P., 2007. Mantle plumes link magnetic superchrons to Phanerozoic mass depletion events: Earth and Planetary Science Letters, 260, 495–504.

Courtillot, V., Jaupart, C., Manighetti, I., Tapponnier, P., Besse, J., 1999. On causal links between flood basalts and continental breakup. Earth Planet. Sci. Lett., 166, 177–195.

Courtillot, V., Kravchinsky, V.A., Quidelleur, X., Renne, P.R., Gladkochub, D.P., 2010. Preliminary dating of the Viluy traps (Eastern Siberia): Eruption at the time of Late Devonian extinction events? Earth Planet. Sci. Lett., 300, 239–245.

Courtillot, V., Kravchinsky, V.A., Quidelleur, X., Renne, P.R., Gladkochub, D.P., 2010. Preliminary dating of the Viluy traps (Eastern Siberia): eruption at the time of Late Devonian extinction events? Earth and Planetary Science Letters, 300, 239–245.

Cox, A. V., Doell, R.R., & Dalrymple, G.B., 1963. Geomagnetic polarity epochs and Pleistocene geochronometry. Nature, 198, 1049–1051.

D'Arrigo, R., Jacoby, G., Pederson, N., Frank, D., Buckley, B., Nachin, B., Mijiddorj, R. and Dugarjav, C., 2000. Mongolian tree-rings, temperature sensitivity and reconstructions of Northern Hemisphere temperature. The Holocene, 10(6), 669–672.

Debret, M., Bout-Roumazeilles, V., Grousset, F., Desmet, M., McManus, J.F., Massei, N., Sebag, D., Petit, J.-R., Copard, Y., Trentesaux, A., 2007. The origin of the 1500-year climate cycles in Holocene North-Atlantic records. Climate of the Past, 3, 569–575.

Deng C.L., Vidic N.J., Verosub K.L., Singer M.J., Liu Q.S., Shaw J., Zhu R.X., 2005. Mineral magnetic variation of the Jiaodao Chinese loess/paleosol sequence and its bearing on long-term climatic variability. Journal of Geophysical Research, 110, B03103.

deMenocal, P., 1993. Wireline logging of the North Pacific transect. JOIDES Journal, 19, 29.

Didenko, A.N. and Pechersky, D.M., 1989. Direction and intensity of the geomagnetic field in the Middle Devonian and Lower Ordovician: southern Mugodjary ophiolites (Urals). Physics of the earth and planetary interiors, 58(4), 289–306.

Ding, Z.L., Rutter, N.W., Liu, T.S., 1993. Pedostratigraphy of Chinese loess deposits and climatic cycles in the last 2.5 Ma. Catena, 20, 73–91.

Ding, Z.L., Yu, Z., Rutter, N.W., 1994. Towards an orbital time scale for Chinese loess deposits. Quaternary Science Reviews, 13, 39–70.

Ding, Z.L., Sun, J.M., Liu, T.S., Zhu, R.X., Yang, S.L., Guo, B., 1998. Wind-blown origin of the Pliocene red clay formation in the central Loess Plateau, China. Earth and Planetary Science Letters, 161, 135–143.

Ding, Z.L., Xiong, S.F., Sun, J.M., Yang, S.L., Gu, Z.Y., Liu, T. S., 1999. Pedostratigraphy and paleomagnetism of a ∼7.0 Ma eolian loess–red clay sequence at Lingtai, Loess Plateau, north-central China and the implications for paleomonsoon evolution. Palaeogeography, Palaeoclimatology, Palaeoecology, 152, 49–66.

Ding, Z.L., Yang, S.L., Hou, S.S., 2001. Magnetostratigraphy and sedimentology of the Jingchuan red clay section and correlation of the Tertiary aeolian red clay sediments of the Chinese Loess Plateau. Journal of Geophysical Research, 106, 6399–6407.

Ding, Z.L., Derbyshire, E., Yang, S.L., Yu, Z.W., Xiong, S.F., Liu, T.S., 2002. Stacked 2.6-Ma grain size record form the Chinese loess based on five sections and correlation with the deep-sea δ18Orecord. Paleoceanography, 17.

Driscoll, N.W., and Haug, G.H., 1998. A short circuit in thermohaline circulation: A cause for Northern Hemisphere glaciation? Science, 282, 436–438.

Elkibbi, M., and Rial, J.A., 2001. An outsider's view of the ice ages. A review. Earth-Science Reviews, 55, 159–175.

Elkins Tanton, L.T., and Hager, B.H., 2000. Melt intrusion as a trigger for lithospheric foundering and the eruption of the Siberian flood basalts. Geophys. Res. Lett., 27, 3937–3940.

Erwin, D.H., 1994. The Permo-Triassic extinction. Nature, 367, 231-236.

Evans, M.E. and Rutter, N.W., 1998. A magnetic investigation of a late Quaternary loess/palaeosol record in Siberia, Geophys. J. Int., 132, 128–132, 1998.

Evans, M.E., and Heller. F., 2001. Magnetism of loess/palaeosol sequences: recent developments, Earth-Sci. Rev., 54, 129–144.

Evans, M.E., and Heller, F., 2003. Environmental Magnetism: Principles and Applications of Enviromagnetics. Elsevier Science, Academic Press.

Fedorenko V., and Czamanske G., 1997. Results of New Field and Geochemical Studies of the Volcanic and Intrusive Rocks of the Maymecha-Kotuy Area, Siberian Flood-Basalt Province. International Geology Review, 39, 479-531.

Feng, Z.D., Thompson, L.G., Mosley-Thompson, E., and Yao, T.D., 1993. Time-space model of climatic change in China during the past 10000 years. The Holocene, 3, 174–180.

Feng, Z.D., An, C.B., Wang, H.B., 2006. Holocene climatic and environmental changes in the arid and semi-arid areas of China: a review. The Holocene, 16, 119–130.

Fetisova, A.M., Veselovskii, R.V., Latyshev, A.V., Rad'ko, V.A., Pavlov, V.E., 2014. Magnetic stratigraphy of the Permian-Triassic traps in the Kotui River valley (Siberian Platform): New paleomagnetic data. Stratigraphy and Geological Correlation, 22(4), 377-390.

Fisher, R.A., 1953. Dispersion on a sphere. Proceedings of the Royal Society London, Series A, 217, 295–305.

Flynn, L., Wu, W.Y., Downs, W.R., 1997. Dating vertebrate microfaunas in the late Neogene record of Northern China. Palaeogeography, Palaeoclimatology, Palaeoecology, 133, 227–242.

Frisia, S., Borsato, A., Preto, N. and McDermott, F., 2003. Late Holocene annual growth in three Alpine stalagmites records the influence of solar activity and the North Atlantic Oscillation on winter climate. Earth and Planetary Science Letters, 216(3), 411–424.

Gaiduk, V.V., 1987. Viluy middle Paleozoic rift system. Geotectonics, 3, 66–76.

Gasse, F., 2000. Hydrological changes in the African tropics since the last glacial maximum. Quaternary Science Reviews, 19, 189–211.

Gasse, F., 2001. Hydrological changes in Africa. Science, 292, 2259–2260.

Gee, J.S., and Kent, D.V., 2007. Source of oceanic magnetic anomalies and the geomagnetic polarity time scale. In Kone, M. (Eds.), Treatise on Geophysics. Amsterdam: Elsevier. Geomagnetism, Vol. 5, pp. 455–507.

Glatzmaier, G.A., Coe, R.S., Hongre, L., Roberts, P.H., 1999. The role of the Earth's mantle in controlling the frequency of geomagnetic reversals. Nature, 401, 885–890.

Griffin, W.L., Ryan, C.G., Kaminsky, F.V., O'Reilly, S.Y., Natapov, L.M., Win, T.T., Kinny, P.D., Ilupin, I.P., 1999. The Siberian lithosphere traverse, mantle terranes and the assembly of the Siberian Craton. Tectonophysics, 310, 1–35.

Guo, Z.T., Peng, S.Z., Hao, Q.Z., Chen, X.H., Liu, D.S., 1999. Late Tertiary development of aridification in northwestern China: link with the arctic ice-sheet formation and Tibetan uplifts [in Chinese with English abstract]. Quaternary Sciences, 6, 556–567.

Guo, Z.T., Petit-Maire, N., Kröpelin, S., 2000. Holocene nonorbital climatic events in present-day arid areas of northern Africa and China. Global and Planetary Change, 26, 97–103.

Guo, Z.T., Peng, S.Z., Hao, Q.Z., Biscaye, P.E., Liu, T.S., 2001. Origin of the Miocene-Pliocene red earth formation at Xifeng in Northern China and implications for paleoenvironments. Palaeography, Palaeclimatology, Palaeoecology, 170, 11–26.

Guo, Z.T., Ruddiman, W.F., Hao, Q.Z., Wu, H.B., Qiao, Y.S., Zhu, R.X., Peng, S.Z., Wei, J.J., Yuan, B.Y., Liu, T.S., 2002. Onset of Asian desertification by 22 Myr ago inferred from loess deposits in China. Nature, 416, 159–163.

Guo, Z.T., Peng, S.Z., Hao, Q.Z., Biscaye, P.E., An, Z.S., Liu, T.S., 2004. Late Miocene–Pliocene development of Asian aridification as recorded in the Red-Earth Formation in the northern China. Global and Planetary Change, 41, 135–145.

Hansma, J., Tohver, E., Yan, M., Trinajstic, K., Roelofs, B., Peek, S., Slotznick, S.P., Kirschvink, J., Playton, T., Haines, P., Hocking, R., 2015. Late Devonian carbonate magnetostratigraphy from the Oscar and Horse Spring Ranges, Lennard Shelf, Canning Basin, Western Australia. Earth and Planetary Science Letters, 409, 232–242.

Haug, G.H., and Tiedemann, R., 1998. Effect of the formation of the Isthmus of Panama on Atlantic Ocean thermohaline circulation. Nature, 393, 673–676.

Haug, G.H., Hughen, K.A., Sigman, D.M., Peterson, L.C., Röhl, U., 2001. Southward migration of the intertropical Convergence zone through the olocene. Science, 293, 1304–1308.

Hays, J.D., Imbrie, J. and Shackleton, N.J., 1976. Variations in the earth's orbit: pacemaker of the ice ages, Sciences, 194, 1121–1132.

He, Y., Theakstone, W.H., Zhang, Z.L., Zhang, D., Yao, T.D., Chen, T., Shen, Y.P., Pang, H.X., 2004. Asynchronous Holocene climatic change across China. Quaternary Research, 61, 52–61.

Heirtzler, J.R., Dickson, G.O., Herron, E.M., Pitman, W.C.I., LePichon, X., 1968. Marine magnetic anomalies geomagnetic field reversals, and motions of the ocean floor and continents. J. Geophys. Res., 73, 2119–2136.

Heller, F., and Liu, T.S., 1984. Magnetism of Chinese loess deposits. Geophysical Journal of the Royal Astronomical Society, 77, 125–141.

Heller, F., and Evans, M.E., 1995. Loess magnetism. Rev. Geophys., 33, 211–240.

Heller, F., Shen, C.D., Beer, J., Liu, X.M., Liu, T.S., Bronger, A., Suter, M., Bonani, G., 1993. Quantitative estimates of pedogenic ferromagnetic mineral formation in Chinese loess and paleoclimatic implications. Earth Planet. Sci. Lett., 114, 385–390.

Heller, R., Merrill, R.T., McFadden, P.L., 2002. The variation of intensity of earth's magnetic field with time. Phys. Earth Planet. Inter., 131(3–4), 237–249.

Herzschuh, U., 2006. Palaeo-moisture evolution in monsoonal central Asia during the last 50,000 years. Quaternary Science Reviews, 25, 163–178.

Hess, S., and Kuhnt, W., 2005. Neogene and Quaternary paleoceanographic changes in the southern South China Sea (Site 1143): the benthic foraminiferal record. Marine Micropaleontology, 54, 63–87.

Heunemann, C., Krasa, D., Soffel, H.C., Gurevitch, E., Bachtadse, V., 2004. Directions and intensities of the Earth's magnetic field during a reversal: results from the Permo-Triassic Siberian trap basalts, Russia. Earth Planet. Sci. Lett., 218, 197–213.

Hill, G., 1897. On the values of the eccentricities and longitudes of the perihelia of Jupiter and Saturn for distant epochs. Astron. J. 17(11), 81–87.

Hill, M.J., and Shaw, J., 1999. Palaeointensity results for historic lavas from Mt Etna using microwave demagnetization/remagnetization in amodified Thellier-type experiment. Geophys. J. Int., 139 (2), 583–590.

Hinnov, L.A., 2000. New perspectives on orbitally forced stratigraphy. Annual Review of Earth and Planetary Science, 28, 419-475.

Hinnov, L.A., 2013. Cyclostratigraphy and its revolutionizing applications in the earth and planetary sciences. Geological Society of America Bulletin, 125, 11-12, pp.1703-1734.

Hirose, K., 2006. Postperovskite phase transition and its geophysical implications. Rev. Geophys. 44, 3001.

Hirose, K. and Lay, T., 2008. Discovery of post-perovskite and new views on the core-mantle boundary region. Elements, 4(3), 183-189.

Hodell, D.A., Curtis, J.H., Jones, G.A., Higuera-Gundy, A., Brenner, M., Binford, M.W., Dorsey, K.T., 1991. Reconstruction of Caribbean climate change over the past 10,500 years. Nature, 352, 790–793.

Hodell, D.A., Brenner, M., Curtis, J.H., Guilderson, T., 2001. Solar forcing of drought frequency in the Maya Lowlands. Science, 292, 1367–1370.

Holbourn, A., Kuhnt, W., Schulz, M., Flores, J.A. and Andersen, N., 2007. Orbitally-paced climate evolution during the middle Miocene “Monterey” carbon-isotope excursion. Earth and Planetary Science Letters, 261(3), 534-550.

Hospers, J., 1954. Rock magnetism and polar wandering, Nature, 173, 1183–1184.

Hovan, S.A., Rea, D.K., Pisias, N.G., Shackleton, N.J., 1989. A direct link between the China loess and marine d18O records: aeolian flux to the north Pacific. Nature, 340, 296–298.

Hu, C., Henderson, G.M., Huang, J., Xie, S., Sun, Y., & Johnson, K.R., 2008. Quantification of Holocene Asian monsoon rainfall from spatially separated cave records. Earth and Planetary Science Letters, 266(3), 221–232.

Huang, C.C., Zhou, J., Pang, J., Han, Y., & Hou, C., 2000. A regional aridity phase and its possible cultural impact during the Holocene Megathermal in the Guanzhong Basin, China. The Holocene 10(1), 135–142.

Imbrie, J., Hays, J.D., Martinson, D.B., Mcintyre, A., Mix, A. C., Morley, J.J., Pisias, N.G., Prell, W .L., and Shackleton, N.J., 1984. The orbital theory of Pleistocene climate: Support from a revised chronology of the marine δ18O record, in Milankovitch and Climate, edited by Berger, A., Imbrie, J., Kukla, G. and Saltzman, B., pp. 269–305, D. Riedel, Dordrecht, Netherlands.

Jacoby, G., D'Arrigo, R., Davaajamts, T.S., 2000. Mongolian tree-rings and 20th century warming. Science, 273, 771–773.

Janecek, T.R., and Rea, D.K., 1983. Eolian deposition in the Northeast Pacific Ocean: Cenozoic history of atmospheric circulation. Geological Society of America Bulletin, 94, 730–738.

Jansen, E., and Sjøholm, J., 1991. Reconstruction of glaciation over the past 6 Myr from ice-borne deposits in the Norwegian Sea. Nature, 349, 600–603.

Jin, G.Y., and Liu, T.S., 2002. Mid-Holocene climate change in North China, and the effect on cultural development. Chinese Science Bulletin, 47, 408–413.

Johnson, K.R., 2011. Long-distance relationship. Nature Geoscience, 4, 426–427.

Johnson, K.R., Hu, C., Belshaw, N.S. and Henderson, G.M., 2006. Seasonal trace-element and stable-isotope variations in a Chinese speleothem: The potential for high-resolution paleomonsoon reconstruction. Earth and Planetary Science Letters, 244(1), 394–407.

Kamo, S.L., Czamanske, G.K., Amelin, Y., Fedorenko, V.A., Davis, D.W., and Trofimov, V.R., 2003. Rapid Eruption of Siberian Flood_Volcanic Rocks and Evidence for Coincidence with the Permian–Triassic Boundary and Mass Extinction at 251 Ma. Earth Planet. Sci. Lett., 214, 75–91.

Kashiwaya, K., Ochiai, S., Sakai, H., and Kawai, T., 2003, Onset of current Milankovitch-type climatic oscillations in Lake Baikal sediments at around 4 Ma. Earth and Planetary Science Letters, 213, 185–195.

King, J.W., and Channell, J.E.T., 1991. Sedimentary magnetism, environmental magnetism, and magnetostratigraphy. Rev. Geophys., 358–370.

King, J.W., Banerjee, S.K., Marvin, J., Ozdemir O., 1982. A comparison of different magnetic methods for determining the relative grain size of magnetite in natural materials: some results from lake sediments, Earth Planet. Sci. Lett., 59, 404–419.

Kirschvink, J.L., 1980. The least-squares line and plane and the analysis of paleomagnetic data. Geophysical Journal of the Royal Astronomical Society, 62, 699–718.

Kiselev, A., Yarmolyuk, V., Egorov, K., Chernyshov, R., Nikiforov, A., 2006. Middle Paleozoic basic magmatism of the northwestern Vilyui Rift: composition, sources, and geodynamics. Petrology, 14, 588–608.

Klimenko, V.V., Klimanov, V.A., Fedorov, M.V., 1996. The history of the mean temperature of the Northern Hemisphere over the last 11,000 years. Trans. Russ. Acad. Sci., 4, 626–629.

Knittle, E., and Jeanloz, R., 1991. Earth's coremantle boundary: Results of experiments at high pressures and temperatures. Science 251: 1438-1443.

Kodama, K.P., and Hinnov, L.A., 2014. Front matter, in Rock Magnetic Cyclostratigraphy. New Anal. Methods Earth Environ. Sci. Ser., pp. 1–176, John Wiley, Oxford.

Kodama, K.P., Anastasio, D.J., Newton, M.L., Pares, J.M., Hinnov, L.A., 2010. High-resolution rock magnetic cyclostratigraphy in an Eocene flysch, Spanish Pyrenees. Geochemistry Geophysics Geosystems, 11, Q0AA07.

Kono, M., 1979. Palaeomagnetism and palaeointensity studies of Scottish Devonian volcanic rocks. Geophysical Journal International, 56(2), 385–396.

Konstantinov, K.M., Bazhenov, M.L., Fetisova, A.M., Khutorskoy, M.D., 2014. Paleomagnetism of trap intrusions, East Siberia: Implications to flood basalt emplacement and the Permo–Triassic crisis of biosphere. Earth Planet. Sci. Lett., 394, 242-253.

Kosterov, A.A., Perrin, M., Glen, J.M., and Coe, R.S., 1998. Paleointensity of the Earth's magnetic field in Early Cretaceous time: the Paraná Basalt, Brazil. J. Geophys. Res., 103, 9739–9753.

Kravchinsky, V.A., 2012. Paleozoic large igneous provinces of Northern Eurasia: Correlation with mass extinction events. Global and Planetary Change, 86-87, 31–36.

Kravchinsky, V.A., Konstantinov, K.M., Courtillot, V., Savrasov, J.I., Valet, J.P., Cherniy, S.D., Mishenin, S.G., Parasotka, S., 2002. Palaeomagnetism of the East Siberian traps and kimberlites: two new poles and palaeogeographic reconstruction at about 360 and 250 Ma. Geophys. J. Int., 148, 1–33.

Kravchinsky, V.A., Krainov, M.A., Evans, M.E., Peck, J.A., King, J.W., Kuzmin, M.I., Sakai, H., Kawai, T. and Williams, D.F., 2003. Magnetic record of Lake Baikal sediments: chronological and paleoclimatic implication for the last 6.7 Myr. Palaeogeography, Palaeoclimatology, Palaeoecology, 195, 281–298.

Kravchinsky, V.A., Langereis, C.G., Walker, S.D., Dlusskiy, K.G. and White, D., 2013. Discovery of Holocene millennial climate cycles in the Asian continental interior: Has the sun been governing the continental climate?. Global and Planetary Change, 110, 386–396.

Kukla, G.J., and An, Z., 1989. Loess stratigraphy in central China. Palaeogeogr. Palaeoclimatol. Palaeoecol, 72, 203–225.

Kukla, G., Heller, F., Liu, X.M., 1988. Pleistocene climates in China dated by magnetic susceptibility. Geology, 16, 811–814.

Kukla, G., An, Z.S., Meliece, L., Gavin, G., Xiao, J.L., 1990. Magnetic susceptibility record of Chinese loess. Transactions of the Royal Society of Edinburgh: Earth Sciences, 81, 263–288.

Kutzbach, J.E., 1974. Fluctuations of climate-monitoring and modelling. World Meteorol. Organ. Bull. 23, 155–163.

Kutzner, C., Christensen, U., 2002. From stable dipolar to reversing numerical dynamos. Phys. Earth Planet. Inter., 121, 29–45.

Kuzmin, M.I., Yarmolyuk, V.V., Kravchinsky, V.A., 2010. Phanerozoic hot spot traces and paleogeographic reconstructions of the Siberian continent based on interaction with the African large low shear velocity province. Earth-Science Reviews, 102, 29–59.

Labrosse, S., 2002. Hotspots, mantle plumes and core heat loss. Earth Planet Sci. Lett., 199, 147–156.

Labrosse, S., 2007. Core-mantle Boundary, Heat flow across. In Encyclopedia of Geomagnetism and Paleomagnetism, Springer Netherlands, 127-130.

Langereis, C.G., Krijgsman, W., Muttoni, G., and Menning, M., 2010. Magnetostratigraphy concepts, definitions, and applications. Newsletters on Stratigraphy, 43(3), 207–233.

Laskar, J., 1989. A numerical experiment on the chaotic behavior of the solar system. Nature 338, 237–238.

Laskar, J., Joutel, F., Boudin, F., 1993. Orbital, precessional, and insolation quantities for the Earth from − 20 Myr to 10 Myr. Astron. Astrophys. 270, 522-533.

Laskar, J., Robutel, P., Joutel, F., Gastineau, M., Correia, A.C.M. and Levrard, B., 2004. A long-term numerical solution for the insolation quantities of the Earth. Astronomy & Astrophysics, 428(1), 261-285.

Laskar, J., Fienga, A., Gastineau, M., Manche, H., 2011. La2010: a new orbital solution for the long term motion of the Earth. Astronomy and Astrophysics, 532, A89.

Lauritzen, S.E. and Lundberg, J., 1999. Speleothems and climate: a special issue of The Holocene. The Holocene, 9(6), 643–647.

Lay, T., Hernlund, J. and Buffett, B.A., 2008. Core–mantle boundary heat flow. Nature Geoscience, 1(1), 25-32.

Le Borgne, E., 1955. Abnormal magnetic susceptibility of the top soil. Ann. Geophys., 11, 399–419.

Li, J.J., 1991. The environmental-effects of the uplift of the Qinghai-Xizang Plateau. Quaternary Science Reviews, 10, 479–483.

Li, J.J., 1996. Climatic change in arid areas of China and monsoon fluctuations during the past 10 kyears. Journal of Arid Environments, 32, 1–7.

Li, J.J., and Fang, X.M., 1999. Uplift of the Tibetan Plateau and environmental changes. Chinese Science Bulletin, 44, 2117–2124.

Li, J.J., Fang, X.M., Van, D.V., Zhu, J.J., Niocaill, C.M., Cao, J.X., Zhong, W., Chen, H.L., Wang, J., Wang, J.M., Zhang, Y.C., 1997. Late Cenozoic magnetostratigraphy (11–0 Ma) of the Dongshanding and Wangjiashan sections in the Longzhong Basin, western China. Geologie & Mijnbouw, 76, 121–134.

Li, X.Q., Zhou, J., and Dodson, J., 2003. The vegetation characteristics of the 'Yuan' area at Yaoxian on the Loess Plateau in China over the last 12000 years. Review of Palaeobotany and Palynology, 124, 1–7.

Liu, F., and Feng, Z., 2012. A dramatic climatic transition at~ 4000 cal. yr BP and its cultural responses in Chinese cultural domains. The Holocene, 22(10), 1181–1197.

Liu, T.S., 1985. Loess and Environment. China Ocean Press, Beijing, 31–67.

Liu, T.S., and Ding, Z.L., 1998. Chinese loess and the paleomonsoon. Annu. Rev. Earth Planet. Sci., 26, 111–145.

Liu, T.S., Ding, M.L., Derbyshire, E., 1996. Gravel deposits on the margins of the Qinghai–Xizang Plateau and their environmental significance. Palaeogeography, Palaeoclimatology, Palaeoecology, 120, 159–170.

Liu, X.M., Rolph, T., Bloemendal, J., Shaw, J., Liu, T., 1994. Remanence characteristics of different magnetic grain size categories at Xifeng, central Chinese Loess Plateau. Quat. Res., 42, 162–165.

Liu, X.M., Rolph, T., An, Z.S., Hesse, P., 2003. Paleoclimatic significance of magnetic properties on the Red Clay underlying the loess and paleosols in China. Palaeogeography, Palaeoclimatology, Palaeoecology, 199, 153–166.

Loutre, M.F., Berger, A., Bretagnon, P. and Blanca, P.L., 1992. Astronomical frequencies for climate research at the decadal to century time scale. Climate Dynamics, 7(4), 181–194.

Lowrie, W., 2007. Fundamentals of geophysics. Cambridge university press.

Lu, H.Y., and An, Z.S., 1998. Palaeoclimatic significance of grain size of loess-paleosol sequence of Central China. Science in China, Ser. D, 41, 626–631.

Lu, H.Y., An, Z.S., Vandenberghe, J., Nugteren, G., 1997. Evidences for palaeoclimatic significance of grain size composite of loess deposit in Central Chinese Loess Plateau, in Proceedings of 30th International Geological Congress, edited by An, Z., vol. 21, pp. 5–10, VSP, The Netherlands.

Lu, H.Y., VanHuissteden, K.O., An, Z.S., Nugteren, G., Vandenberghe, J., 1999. East Asia winter monsoon variations on a millennial time-scale before the last glacial– interglacial cycle. J. Quat. Sci., 14, 101–110.

Lu, H.Y., VanHuissteden, K.O., Zhou, J., Vandenberghe, J., Liu, X.D., An, Z.S., 2000. Variability of East Asian winter monsoon in Quaternary climatic extremes in North China. Quat. Res., 54, 321–327.

Lu, H.Y., Zhang, F., Liu, X.D., 2002. Patterns and frequencies of the East Asian winter monsoon variations during the past million years revealed by wavelet and spectral analyses. Global and Planetary Change, 35 (1–2), 67–74.

Lu, H.Y, Zhang, F., Liu, X., Duce, R.A., 2004. Periodicities of palaeoclimatic variations recorded by loess-paleosol sequences in China. Quaternary Sciences, 23, 1891-1900.

Lu, H.Y., Yi, S.W., Liu, Z.Y., Mason, J.A., Jiang, D.B., Cheng, J., Stevens, T., Xu, Z.W., Zhang, E.L., Jin, L.Y., Zhang, Z.H., Guo, Z.T., Wang, Y., Otto-Bliesner, B., 2013. Variation of East

Asian monsoon precipitation during the past 21 ky and potential CO2 forcing. Geology, 41(9), 1023–1026.

Lu, L.Q., Fang, X.M., Mason, J.A., Li, J.J., An, Z.S., 2001. The evolution of coupling of Asian winter monsoon and high latitude climate of Northern Hemisphere–Grain evidence from 8.1 Ma loess–red clay sequence on the Chinese central Loess Plateau. Science in China, Ser. D, 44, 185–191.

Lu, Y.C., 1981. Calcium carbonate content in Chinese loess deposit and the climatic cycles in the Pleistocene [in Chinese]. Geological Sciences, 2, 122–131.

Ma Ji., Yue L., Yang Li., Sun Lu, Xu, 2011. Southeastern margin of the Mu Us Desert Holocene sectional OSL's and paleoclimatic significance (in Chinese). Quaternary Research, 31 (1), 120–129.

Mackay, A.W., Swann, G.E.A., Brewer, T., Leng, M.J., Morley, D.W., Piotrowska, N., Rioual, P., White, D., 2011. A reassessment of late glacial-Holocene diatom oxygen isotope records from Lake Baikal using a mass balance approach. Journal of Quaternary Science, 26 (6), 627–634.

Maher, B.A., 1986. Characterization of soils by mineral magnetic measurements. Physics of Earth and Planetary Interiors, 42, 76–92.

Maher, B.A., 1988. Magnetic properties of some synthetic sub-micron magnetites. Geophysical Journal of Royal Astronomical Society, 94, 84–96.

Maher, B.A., 2011. The magnetic properties of Quaternary aeolian dust and sediments, and their palaeoclimatic significance. Aeolian Research, 3, 87–144.

Maher, B.A., and Taylor, R.H., 1988. Formation of ultrafine-grained magnetite in soils. Nature, Maher, B.A., and Thompson, R., 1991. Mineral magnetic record of the Chinese loess and paleosols. Geology, 19, 3–6.

Maher, B.A. and Thompson, R., 1992. Paleoclimatic significance of the mineral magnetic record of the Chinese loess and paleosols, Quaternary Res., 37, 155–170.

Maher, B.A., Thompson, R., Zhou, L.P., 1994. Spatial and temporal reconstructions of changes in the Asian paleomonsoon: a new mineral magnetic approach. Earth Planet. Sci. Lett., 44, 383–391.

Masaitis, V.L., Mikhailov, M.V., Selivanovskaya, T.V., 1975. Volcanism and Tectonics of Patom-Vylyu Middle Paleozoic Aulacogen. Nedra, Moscow, 184.

Mayewski, P.A., Rohling, E.E., Stager, J.C., Karlén, W., Maasch, K.A., Meeker, L.D., Meyerson, E.A., Gasse, F., Kreveld, S.V., Holmgren, K., Lee-Thorp, J., Rosqvist, G., Rack, F., Staubwasser, M., Schneider, R.R. and Steig, E.J. 2004. Holocene climate variability. Quaternary Research, 62, 243–55.

McClelland, E., and Briden, J.C., 1996. An improved methodology for Thellier-type paleointensity determination in igneous rocks and its usefulness for verifying primary thermoremanence. J. Geophys. Res., 101, 21995–22013.

McDermott, F., 2004. Palaeo-climate reconstruction from stable isotope variations in speleothems: a review. Quaternary Science Reviews, 23(7), 901–918.

McDermott, F., Mattey, D.P., and Hawkesworth, C., 2001. Centennial-scale Holocene climate variability revealed by a highresolution speleothem 5180 record from SW Ireland. Science, 294, 1328–31.

McElhinny, M.W., 1973. Paleomagnetism and plate tectonics. Cambridge University Press, London, 358.

McMichael, A.J., 2012. Insights from past millennia into climatic impacts on human health and survival. Proceedings of the National Academy of Sciences, 109(13), 4730–4737.

Meeker, L.D., and Mayewski, P.A., 2002. A 1400-year high-resolution record of atmospheric circulation over the North Atlantic and Asia. Holocene, 12, 257–266.

Milankovitch, M., 1930. Mathematische klimalehre und astronomie theorie der klimaschwankungen. In: Ko¨ppen W and Geiger R (eds.) Handbuch der Klimatologie, vol. I(A), 1–176. Berlin: Gebru¨der Borntraeger.

Mu, Y., Qin, X., Zhang, L., Xu, B., 2016. Holocene climate change evidence from high-resolution loess/paleosol records and the linkage to fire–climate change–human activities in the Horqin dunefield in northern China. Journal of Asian Earth Sciences, 121, 1–8.

Muller, R.A., and MacDonald, G., 1997. Spectrum of the 100 kyr glacial cycle: Orbital inclination, not eccentricity. Proceedings of the National Academy of Sciences of the U.S.A., 94, 8329–8334.

Murakami, M., Hirose, K., Kawamura, K. Sato, N., Ohishi, Y., 2004. Post-perovskite phase transition in MgSiO3. Science 304, 855–858.

Nagata, T., Arai, Y., Momose, K., 1963. Secular variation of the geomagnetic total force during the last 5000 years. Journal of Geophysical Research, 68, 5277–5281.

Nakagawa, T. and Tackley, P.J., 2004. Effects of a perovskite-post perovskite phase change near core-mantle boundary in compressible mantle convection. Geophysical Research Letters, 31(16).

Nie, J., King, J., and Fang, X., 2008. Tibetan uplift intensifi ed the 400 k.y. signal in paleoclimate records at 4 Ma. Geological Society of America Bulletin, 120, 1338–1344.

Oganov, A.R. and Ono, S., 2004. Theoretical and experimental evidence for a post-perovskite phase of MgSiO3 in Earth's D" layer. Nature 430, 445–448.

Ogg, J.G., 2004. In A Geological Time Scale 2004. Gradstein, F.M., Ogg, J.G., and Smith, A.G., (Eds.), Cambridge Univ. Press, 307–339.

Oldfield, F., 1991. Environmental magnetism- a personal perspective. Quaternary Science Reviews, 10, 73–85.

Oldfield, F., Walden, J. and Smith, J., 1999. Environmental magnetism: a practical guide. Quaternary Research Association, no. 6.

Olson, P., 2003. Thermal interaction of the core and mantle. In: Jones, C.A., Soward, A.M., Zhang, K. (Eds.), Earth's Core and Lower Mantle. Taylor and Francis, London and New York, 218.

Olson, P.L., Coe, R.S., Driscoll, P.E., Glatzmaier, G.A. & Roberts, P.H., 2010. Geodynamo reversal frequency and heterogeneous core-mantle boundary heat flow. Phys. Earth Planet. Inter. 180, 66–79.

Olson, P., Deguen, R., Hinnov, L.A., and Zhong, S., 2013. Controls on geomagnetic reversals and core evolution by mantle convection in the Phanerozoic. Physics of the Earth and Planetary Interiors, 214, 87–103.

Oorschot, I.H.M.V., 2002. Chemical distinction between lithogenic and pedogenic iron oxides in environmental magnetism: a search for the perfect solution. Universiteit Utrecht.

Opdyke, N.D., and Channell, 1996. Magnetic stratigraphy. Academic Press, San Diego, California, 341.

Pan, B.T., Gao, H.S., Li, B.Y., Li, J.J., 2004. Step-like landforms and uplift of the Qinghai–Xizang Plateau [in Chinese]. Quaternary Sciences, 24, 50–57.

Pan, Y.S., 1999. Formation and uplifting of the Qinghai–Tibet Plateau [in Chinese]. Earth Science Frontiers, 6, 153–163.

Parés, J.M., PÉREZ-GONZÁLEZ, A., Arsuaga, J.L., Bermúdez de Castro, J.M., Carbonell, E. and Ortega, A.I., 2010. Characterizing the sedimentary history of cave deposits, using archaeomagnetism and rock magnetism, Atapuerca (Northern Spain). Archaeometry, 52(5), 882–898.

Paterson, G.A., 2011. A simple test for the presence of multidomain behavior during paleointensity experiments. J. Geophys. Res. (Solid Earth), 116, B10104.

Paterson, G.A., Tauxe, L., Biggin, A.J., Shaar, R., and Jonestrask, L.C., 2014. On improving the selection of paleointensity data. Geochem. Geophys. Geosyst., 15, 1180–1192.

Paulsen, D.E., Li, H.C., and Ku, T.L., 2003. Climate variability in central China over the last 1270 years revealed by high-resolution stalagmite records. Quaternary Sci. Rev., 22, 691–701.

Pavlov, V.E., Fluto, F., Veselovskii, R.V., Fetisova, A.M., and Latyshev, A.V., 2011. Secular Geomagnetic Variations and Volcanic Pulses in the Permian–Triassic Traps of the Norilsk and Maymecha–Kotui Provinces, Maymecha Izv. Phys. Solid Earth, 47(5), 402–417.

Pavlov, V.E, Fluteau, F., Veselovskiy, F., Fetisov, A., Latyshev, A., Elkins-Tanton, L.T., Sobolev, A., Krivolutskaya, N., 2015. Volcanic Pulses in the Siberian Traps as Inferred from Permo-Triassic Geomagnetic Secular Variations, In Volcanism and Global Environmental Change, Ed. A. Schmidt, K. Fristad, L. Elkins-Tanton, Cambridge University Press, United Kingdom, 63–78.

Pei, Y.P., Wu, N.Q., Li, F.J., 2004. Terrestrial mollusk evidence for the origin and sedimentary environment of the Late Tertiary red clay formation in the Loess Plateau, China. Chinese Science Bulletin, 49, 1072–1076.

Pick, T. and Tauxe, L., 1993. Geomagnetic palaeointensities during the Cretaceous normal superchron measured using submarine basaltic glass. Nature, 366, pp. 238–242.

Porter, S.C., and An, Z., 1995. Correlation between climate events in the North Atlantic and China during the last glaciation. Nature, 375, 305–308.

Prévot, M., El_Messaoud Derder, M., McWilliams, M., Thompson, J., 1990. Intensity of the Earth's magnetic field: evidence for a mesozoic dipole low. Earth Planet. Sci. Lett., 97, 129–139.

Prins, M.A., Vriend, M., Nugteren, G., Vandenberghe, J., Lu, H.Y., Zheng, H.B., Ao, H., Dong, J.B., Weltje, G.J., 2007. Late Quaternary Aeolian dust input variability on the Chinese Loess Plateau: inferences from unmixing of loess grain-size records. Quat. Sci. Rev., 26, 230–242.

Pye, K., 1984. Loess. Prog. Phys. Geogr., 8, 176–217.

Pye, K., 1987. Aeolian Dust and Dust Deposits. Academic Press, London.

Pye, K., and Zhou, L.P., 1989. Late Pleistocene and Holocene aeolian dust deposition in North China and the Northwest Pacific Ocean. Palaeogeography, Palaeoclimatology, Palaeoecology, 73, 11–23.

Qiang, X.K., Li, Z.X., Powell, C.M., Zheng, H.B., 2001. Magnetostratigraphic record of the late Miocene onset of the East Asian monsoon, and Pliocene uplift of northern Tibet. Earth and Planetary Science Letters, 187, 83–93.

Qiang, X., An, Z., Song, Y., Chang, H., Sun, Y., Liu, W., Ao, H., Dong, J.B., Fu, C.F., Wu, F., Lu, F.Y., Cai, Y.J., Zhou, W.J., Cao, J.J., Xu, X.W., Ai, L., 2011. New eolian red clay sequence on the western Chinese Loess Plateau linked to onset of Asian desertification about 25 Ma ago. Science China Earth Sciences, 54 (1), 136–144.

Rea, D. K., 1994. The paleoclimatic record provided by eolian deposition in the deep sea: The geologic history of wind, Rev. Geophys., 32, 159–195.

Rea, D.K., Snoeckx, H., Joseph, L.H., 1998. Late Cenozoic eolian deposition in the North Pacific: Asian drying, Tibetan uplift, and cooling of the northern hemisphere. Paleoceanography, 13, 215–224.

Reichow, M.K., Saunders, A.D., White, R.V., Pringle, M.S., Mukhamedov, A.I., Medvedev, A.I., Kirda, N.P., 2002. Ar-40/ Ar-39 dates from the West Siberian Basin: Siberian flood basalt province doubled. Science, 296, 1846-1849.

Reichow, M.K., Saunders, A.D., White, R.V., Almukhamedov, A.I., Medvedev, A.Ya., 2005. Geochemistry and petrogenesis of basalts from the West Siberian Basin: an extension of Permo-Triassic Siberian Traps, Russia. Lithos, 79, 425–452.

Reichow, M.K., Pringle, M.S., Al'Mukhamedov, A.I., Allen, M.B., Andreichev, V.L., Buslov, M.M., Davies, C.E., Fedoseer, G.S., Fitton, J.G., Inger, S., Medvedev, A.Ya., Mitchell, C., Puchkov, V.N., Safonava, I.Yu., Scoot, R.A., Saunders, A.D., 2009. The timing and the extent of the eruption of the Siberian traps large igneous province. Implications for the end-Permian environmental crisis. Earth Planet. Sci. Lett., 227, 9–20.

Renne, P.R., and Basu, A.R., 1991. Rapid eruption of the Siberian Traps Flood Basalts at the Permo-Triassic boundary. Science, 253, 176-179.

Renne, P.R., Zhang, Z.C., Richards, M.A., Black, M.T., Basu, A.R., 1995. Synchrony and causal relations between Permian-Triassic boundary crises and Siberian flood volcanism. Science, 269, 1413-1416.

Rial, J.A., 1999. Pacemaking the Ice Ages by frequency modulation of Earth’s orbital eccentricity. Science, 285, 564–568.

Ricci, J., Quidelleur, X., Pavlov, V., Orlov, S., Shatsillo, A., Courtillot, V., 2013. New 40Ar/39Ar and K–Ar ages of the Viluy traps (Eastern Siberia): Further evidence for a relationship with the Frasnian–Famennian mass extinction. Palaeogeog.Palaeoclim.Palaeoecol., 386, 531–540.

Riisager, P., and Riisager, J., 2001. Detecting multidomain magnetic grains in Thellier palaeointensity experiments. Phys. Earth Planet. Int., 125, 111–117.

Roberts, P.H., Jones, C.A., Calderwood, A., 2003. Energy fluxes and Ohmic dissipation in the Earth's core. In: Jones, C.A., Soward, A.M., Zhang, K. (Eds.), Earth's Core and Lower Mantle. Taylor and Francis, London and New York, 218.

Robinson, S.G., 1986. The late Pleistocene paleoclimatic record of North Atlantic deep-sea sediments revealed by mineral-magnetic measurements, Phys. Earth Planet. Inter., 42, 22–47.

Ruddiman, W.F., and Kutzbach, J.E., 1989. Forcing of late Cenozoic northern hemisphere climate by plateau uplift in southern Asia and the American West. Journal of Geophysical Research, 94, 18409–18427.

Rutter, N.W., 1992. Chinese loess and global change. Quat. Sci. Rev., 11, 275– 281.

Saunders, A.D., Englend, R.W., Reichow, M.K., White, R.W., 2005. A mantle plume origin for the Siberian traps: uplift and extension in the West Siberian Basin, Russia. Lithos, 79, 407–424.

Schwarzacher, W., and Fischer, A.G., 1982. Lime-stone-shale bedding and perturbations in the earth’s orbit. In Cyclic and Event Strat-ification, edited by G. Einsele, and A. Seilacher, pp. 72–95. Springer-Verlag, Berlin.

Selkin, P.A., and Tauxe, L., 2000. Long-term variations in palaeointensity. Philos. Trans. R. Soc. Lond. A, 358(1768), 1065–1088.

Shackleton, N.J., 1977. Carbon-13 in Uvigerina: tropical rainforest history and the equatorial Pacific carbonate dissolution cycles, in The Fate of Fossil Fuel CO2 in the Oceans, edited by Andersen, N.R., and Malahoff, A., pp. 401–427, Plenum Press, New York.

Shackleton, N.J., 2000. The 100,000-year ice-age cycle identified and found to lag temperature, carbon dioxide, and orbital eccentricity. Science, 289, 1897–1902.

Shackleton, N.J., Berger, A. Peltier, W.R., 1990. An alternative astronomical calibration of the Lower Pleistocene timescale based on ODP Site 677. Transactions of the Royal Society of Edinburgh Earth Sciences, 81, 251–261.

Shcherbakova, V.V., Shcherbakov, V.P., Vodovozov, V.V., Sycheva, N.K., 2005. Paleointensity at the Permian_Triassic boundary and in the late Permian. Izv. Acad. Sci. Phys. Solid Earth, 41 (11), 931–944.

Shcherbakova, V.V., Kovalenko, D.V., Shcherbakov, V.P., and Zhidkov, G.V., 2011. Paleointensity of the geomagnetic field in the Cretaceous (from Cretaceous rocks of Mongolia), Izv., Phys. Solid Earth, 47 (9), 775–791.

Shcherbakova, V.V., Bakhmutov, V.G., Shcherbakov, V.P., Zhidkov, G.V., Shpyra, V.V., 2012. Palaeointensity and palaeomagnetic study of Cretaceous and Palaeocene rocks from Western Antarctica. Geophys. J. Int., 189, 204–228.

Shcherbakova, V.V., Zhidkova, G.V., Latyshevb, A.V., Scherbakov V.P., 2013. Estimating the Variations in Paleointensity from the Siberian Traps of Maymecha–Kotui and Norilsk Regions. Izv. Phys. Solid Earth, 49(4), 488–504.

Shcherbakova, V.V., Zhidkov, G.V., Shcherbakov, V.P., Latyshev, A.V., Fetisova, A.M., 2015. Verifying the mesozoic dipole low hypothesis by the Siberian trap data. Izv. Phys. Solid Earth, 51 (3), 362–382.

Shen, J., 2013. Spatiotemporal variations of Chinese lakes and their driving mechanisms since the Last Glacial Maximum: a review and synthesis of lacustrine sediment archives. Chinese Science Bulletin, 58 (1), 17–31.

Shen, C.M., Liu, K.-B., Tang, L.Y., Overpeck, J.T., 2006. Quantitative relationships between modern pollen rain and climate in the Tibetan Plateau. Review of Palaeobotany and Palynology, 140, 61–77.

Shi, Y.F., Kong, Z.C. and Wang, S.M., 1992. Climatic variations and the major events in the Holocene Megathermal in China (in Chinese). Science in China, 12, 300–308.

Shi, Y.F., Li, J.J., Li, B.Y., Yao, T.D., Wang, S.M., Li, S.J., Cui, Z.J., Wang, F.B., Pan, B.T., Fang, X.M., Zhang, Q.S., 1999. Uplift of the Qinghai-Xizang (Tibetan) Plateau and East Asian environmental change during late Cenozoic [in Chinese]. Acta Geographica Sinica, 54, 9–20.

Shindell, D.T., Schmidt, G.A., Miller, R.L. and Mann, M.E., 2003. Volcanic and solar forcing of climate change during the preindustrial era. Journal of Climate, 16(24), 4094-4107.

Smirnov, A.V. and Tarduno, J.A., 2003. Magnetic hysteresis monitoring of Cretaceous submarine basaltic glass during Thellier paleointensity experiments: evidence for alteration and attendant low field bias, Earth Planet. Sci. Lett., 206(3–4), 571–585.

Smith, P. J., 1968. Estimates of the Devonian geomagnetic intensity in Scotland. US Geol. Surv. 575-D, 164–168.

Solodovnikov, G.M., 1996. Geomagnetic Intensity in the Early-Middle Devonian. Izvestiya Physics of the Solid Earth, 32(7), 615–621.

Song, Y.G., Fang, X.M., Li, J.J., An, Z.S., Miao, X.D., 2001. The Late Cenozoic uplift of the Liupan Shan, China. Science in China, Ser. D, 44, 176–184.

Song, Y.G., Fang, X.M., Torii, M., Ishikawa, N., Li, J., An, Z., 2007. Late Neogene rock magnetic record of climatic variation from Chinese eolian sediments related to the uplift of the Tibetan Plateau. Journal of Asian Earth Sciences, 30, 324–332.

Sroubek, P., Diehl, J.F., Kadlec, J. and Valoch, K., 2001. A Late Pleistocene palaeoclimate record based on mineral magnetic properties of the entrance facies sediments of Kulna Cave, Czech Republic. Geophysical Journal International, 147(2), 247–262.

Sroubek, P., Diehl, J.F. and Kadlec, J., 2007. Historical climatic record from flood sediments deposited in the interior of Spirálka Cave, Czech Republic. Palaeogeography, Palaeoclimatology, Palaeoecology, 251(3), 547–562.

Steig, E.J., 1999. Mid-Holocene climate change. Science, 286, 1485–87.

Sun, D.H., Liu, T.S., Cheng, M.Y., An, Z., Shaw, J., 1997. Magnetostratigraphy and paleoclimate of Red Clay sequences from the Chinese Loess Plateau. Sci. China, Ser., D 40, 337–343.

Sun, D.H., An, Z.S., Shaw, J., Bloemendal, J., Sun, Y.B., 1998. Magnetostratigraphy and paleoclimatic significance of Late Tertiary aeolian sequences in the Chinese Loess Plateau. Geophysical Journal International, 134, 207–212.

Sun, D.H., Shaw, J., An, Z.S., Chen, M.Y., Yue, L.P., 1998. Magnetostratigraphy and paleoclimatic interpretation of a continuous 7.2 Ma late Cenozoic eolian sediments from the Chinese Loess Plateau. Geophysical Research Letters, 25, 85–88.

Sun, J.M., 2000. Origin of eolian sand mobilization during the past 2300 years in the Mu Us Desert, China. Quaternary Research, 53, 73–88.

Sun, J.M., Ding, Z.L., Liu, T.S., Rokosh, D., Rutter, N.W., 1999. 580,000-year environmental reconstruction from aeolian deposits at the Mu Us desert margin, China. Quat. Sci. Rev., 18, 1351–1364.

Sun, J.M., Li, S. H., Han, P., Chen, Y., 2006. Holocene environmental changes in the central Inner Mongolia, based on single-aliquot-quartz optical dating and multi-proxy study of dune sands. Palaeogeography, Palaeoclimatology, Palaeoecology, 233, 51–62.

Sun, Q.L., Wang, S.M., Zhou, J., Shen, J., Cheng, P., Xie, X.P., Wu, F., 2009. Lake surface fluctuations since the late glaciation at Lake Daihai, North-central China: a direct indicator of hydrological process responses to East Asian monsoon climate. Quaternary International, 194, 45–54.

Sun, Y.B., Lu, H. and An, Z., 2006a. Grain size of loess, palaeosol and Red Clay deposits on the Chinese Loess Plateau: Significance for understanding pedogenic alteration and palaeomonsoon evolution. Palaeogeography, Palaeoclimatology, Palaeoecology, 241(1), 129–138.

Sun, Y.B., Clemens, S.C., An, Z.S., Yu, Z.W., 2006b. Astronomical timescale and palaeoclimatic implication of stacked 3.6-Myr monsoon records from the Chinese Loess Plateau. Quaternary Science Reviews, 25, 33–48.

Sun, Y.B., An, Z.S., Clemens, S.C., Bloemendal, J., Vandenberghe, J.F., 2010. Seven million years of wind and precipitation variability on the Chinese Loess Plateau. Earth and Planetary Science Letters, 297, 525–535.

Takafuji, N., Hirose, K., Mitome, M., Bando, Y., 2005. Solubilities of O and Si in liquid iron in equilibrium with (Mg,Fe)SiO3 perovskite and the light elements in the core. Geophysical Research Letters 32: L06313.

Takahashi, F., Matsushima, M., Honkura, Y., 2005. Simulations of a quasi-Taylor state geomagnetic field including polarity reversals on the Earth Simulator. Science 309, 459–461.

Tang, M.C., Dong, W.J., Wang, N.L., 2003. The research on the uplift process of Tibetan Plateau [In Chinese]. Advance in Natural Science, 13, 331–336.

Tarasov, P., Jin, G.Y., and Wagner, M., 2006. Mid-Holocene environmental and human dynamics in Northeastern China reconstructed from pollen and archaeological data. Palaeogeography Palaeoclimatology Palaeoecology, 241, 284–300.

Tarduno, J.A., Cottrell, R.D., Smirnov, A.V., 2006. The paleomagnetism of single silicate crystals: recording geomagnetic field strength during mixed polarity intervals, superchrons, and inner core growth. Rev. Geohys., 44, RG1002. doi:10.1029/ 2005RG000189.

Tauxe, L., 2002. Paleomagnetism Principles and Practice. Kluwer Academic Publishers, The Netherlands, 299.

Tauxe, L., and Staudigel, H., 2004. Strength of the geomagnetic field in the Cretaceous Normal Superchron: new data from submarine basaltic glass of the Troodos Ophiolite. Geochemistry Geophysics Geosystems, 5 (Art. No. Q02H06).

Tauxe, L., and Yamazaki, T., 2007. Paleointensities, in: Kono, M. (Ed.), Geomagnetism. Elsevier, Amsterdam, pp. 510-563.

Tauxe, L., Pick, T., Kok, Y., 1995. Relative paleointensity in sediments: a pseudo-Thellier approach. Geophys. Res. Lett., 22, 2885–2888.

Tauxe, L., Butler, R., Banerjee, S.K., van der Voo, R., 2008. Essentials of Rock and Paleomagnetism. University of California Press, USA, 509.

Tauxe, L., Gee, J.S., Steiner, M.B., & Staudigel, H., 2013. Paleointensity results from the Jurassic: New constraints from submarine basaltic glasses of ODP Site 801C. Geochemistry, Geophysics, Geosystems, 14(10), 4718-4733.

Tauxe, L, Banerjee, S.K., Butler, R.F. and van der Voo, R., 2014. Essentials of Paleomagnetism, 2nd Web Edition, University of California Press, USA.

Teilhard, D.C., Young, C.C., 1930. Some correlations between the geology of China proper and geology of Mongolia. Bulletin of the Geological Society of China, 9, 119–125.

Teilhard, D.C., Young, C.C., 1931. Fossils mammals from the Late Cenozoic of Northern China. Palaeontologia Sinica, Ser. C, 9, 1–67.

Thellier, E., 1941. Sur la vérification d'une method permattant de determiner l'intensité du champ terrestre dans le Passé. C.R. Hebd. Seances Acad. Sci., 212, 281–283.

Thellier, E., and Thellier, O., 1959. Sur l'intensité du champ magnétique terrestre dans le passé historique et géologique. Annales Geophysicae, 15, 285–376.

Thomas, D.N. and Biggin, A.J., 2003. Does the Mesozoic dipole low really exist? EOS, Trans. Am. Geophys. Union, 84, (11), 97–104.

Thompson, L.G., Mosley-Thompson, E., Davis, M.E., Bolzan, J.F., Dai, J., Yao, T., Gundestrup, N., Wu, X., Klein, Z. and Xie, Z., 1989. Holocene-Late Pleistocene climatic ice core records from Qinghai-Tibetan Plateau. Science, 246, 474–477.

Thompson, P., Schwarcz, H.P., Ford, D.C., 1974. Continental Pleistocene climatic variations from speleothem age and isotopic data. Science, 184, 893–894.

Thompson, R., Oldfield, F., 1986. Environmental Magnetism, Allen and Unwin, London.

Thompson, R., Bloemendal, J., Dearing, J.A., Oldfield, F., Rummery, T.A., Stober, J.C., and Turner, G.M., 1980. Environmental applications of Magnetic minerals. Science, 207, 481–485.

Tian, J., Wang, P.X., Chen, X.R., 2004a. Development of the East Asian monsoon and Northern Hemisphere glaciation: oxygen isotope records from the South China Sea. Quaternary Science Reviews, 23, 2007–2016.

Tian, J., Wang, P.X., Cheng, X.R, 2004b. Responses of foraminiferal isotopic variations at ODP Site 1143 in the southern South China Sea to orbital forcing. Science in China, Ser. D, 47, 943–953.

Tominaga, M., and Sager, W.W., 2010. Revised Pacific M-anomaly geomagnetic polarity timescale. Geophys. J. Int., 182, 203–232.

Torrence, C., Compo, G.P., 1998. A practical guide to wavelet analysis. Bulletin of the American Meteorological Society, 79, 61–78.

Tsuchiya, T., Tsuchiya, J., Umemoto, K. and Wentzcovitch, R.M., 2004. Phase transition in MgSiO3 perovskite in the Earth's lower mantle. Earth and Planetary Science Letters, 224(3), 241-248.

Usoskin, I.G., Solanki, S.K., Kovaltsov, G.A., 2007. Grand minima and maxima of solar activity: new observational constraints. Astronomy and Astrophysics, 471, 301–309.

Valet, J.P., 2003. Time variations in geomagnetic intensity. Reviews of Geophysics, 41(1), 4–44.

Valet, J.P., Brassart, J., Le Meur, I., Soler, V., Quidelleur, X., Tric, E., Gillot, P.Y., 1996. Absolute paleointensity and magnetomineralogical changes. J. Geophys. Res., 101(B11), 25029–25044, doi:10.1029/96JB02115.

Valet, J.P., Meynadier, L., Guyodo, Y., 2005. Geomagnetic dipole strength and reversal rate over the past two million years. Nature, 435, 802-805.

Van Huissteden, J., Nugteren, G., Vandenberghe, J., An, Z.S., 1997. Spectral analysis of a grain size record of the loess deposits in Central China, in Proceedings of the 30th International Geology Congress edited by Zhang, et al., vol. 2, pp. 313–325, VSP The Netherlands.

Vandenberghe, J., An, Z.S., Nugteren, G., Lu, H.Y., VanHuissteden, K., 1997. New absolute time scale for the Quaternary climate in the Chinese loess region by grain-size analysis. Geology, 25, 35–38.

Vandenberghe, J.F., Lu, H.Y., Sun, D.H., Van Huissteden, J., Konert, M., 2004. The late Miocene and Pliocene climate in East Asia as recorded by grain size and magnetic susceptibility of the Red Clay deposits (Chinese Loess Plateau). Palaeogeography, Palaeoclimatology, Palaeoecology, 204, 239–255.

Verosub, K.L. and Roberts, A.P., 1995. Environmental magnetism: Past, present, and future. Jour. Geophys. Res., 100, 2175–2192.

Vine, F.J. and Matthews, D.H., 1963. Magnetic anomalies over oceanic ridges. Nature, 199, 947–949.

Walton, D., Snape, S., Rolph, T.C., Shaw, J., Share, J., 1996. Application of ferromagnetic resonance heating to palaeointensity determinations. Physics of the Earth and Planetary Interiors, 94 (3–4), 183–186.

Wan, S., Li, A., Clift, P.D. and Jiang, H., 2006. Development of the East Asian summer monsoon: Evidence from the sediment record in the South China Sea since 8.5 Ma. Palaeogeography, Palaeoclimatology, Palaeoecology, 241(1), 139-159.

Wang, H., Chen, J., Zhang, X., & Chen, F., 2014. Palaeosol development in the Chinese Loess Plateau as an indicator of the strength of the East Asian summer monsoon: Evidence for a mid-Holocene maximum. Quaternary International, 334, 155–164.

Wang, L., Lu, H.Y., Wu, N.Q., Li, J., Pei, Y.P., Tong, G.B., Peng, S.Z., 2006. Palynological evidence for Late Miocene-Pliocene vegetation evolution recorded in the red clay sequence of the central Chinese Loess Plateau and implication for palaeoenvironmental change. Palaeogeography, Palaeoclimatology, Palaeoecology, 241, 118–128.

Wang, P., Clemens, S., Beaufort, L., Braconnot, P., Ganssen, G., Jian, Z., Kershaw, P., Sarnthein, M., 2005. Evolution and variability of the Asian monsoon system: state of the art and outstanding issues. Quaternary Science Reviews, 24, 595–629.

Wang, Y.J., Cheng, H., Edwards, R.L., An, Z.S., Wu, J.Y., Shen, C.C., Dorale, J.A., 2001. A high-resolution absolute-dated late Pleistocene monsoon record from Hulu Cave, China. Science, 294, 2345–2348.

Wanner, H., Solomina, O., Grosjean, M., Ritz, S. P., & Jetel, M., 2011. Structure and origin of Holocene cold events. Quaternary Science Reviews, 30(21), 3109–3123.

Weedon, G.P., 2003. Time-series Analysis and Cyclostratigraphy. P. 256, Cambridge University Press, Cambridge.

Wehausen, R., and Brumsack, H.J., 2002. Astronomical forcing of the East Asian monsoon mirrored by the composition of Pliocene South China Sea sediments. Earth and Planetary Science Letters, 201, 621–636.

Wen, R.L., Xiao, J.L., Chang, Z.G., Zhai, D.Y., Xu, Q.H., Li, Y.C., Itoh, S., 2010. Holocene precipitation and temperature variations in the East Asian monsoonal margin from pollen data from Hulun Lake in northeastern Inner Mongolia, China. Boreas, 39, 262–272.

Weng, H.Y., and Lau, K.M., 1994. Wavelets, period doubling, and timefrequency localization with application to organization of convection over the tropical western Pacific. Journal of Atmospheric Science, 51, 2523–2541.

White, W.B., 2007. Cave sediments and paleoclimate. Journal of Cave and Karst studies, 69(1), 76–93.

Wicht, J., and Olson, P., 2004. A detailed study of the polarity reversal mechanism in a numerical dynamo model. Geochem. Geophys. Geosys., 5.

Wilson, R.L., 1961. The Thermal Demagnetization of Natural Magnetic Moments in Rocks. Geophys. J. R. Astron. Soc., 5, (1), 45–58.

Witt, A., and Schumann, A.Y., 2005. Holocene climate variability on millennial scales recorded in Greenland ice cores. Nonlinear Processes in Geophysics, 12, 345–352.

Wurster, C.M., and Patterson, W.P., 2001. Late Holocene climate change for the eastern interior United States. evidence from highresolution 6180 value of marital otoliths. Palaeogeography Palaeoclimatology Palaeoecology, 170, 81–100.

Xiao, J.L., Porter, S.C., An, Z.S., Kumai, H., Yoshikawa, S., 1995. Grain size of quartz as an indicator of winter monsoon strength on the Loess Plateau of central China during the last 130,000 yr. Quaternary Research, 43, 22–29.

Xiao, J.L., Xu, Q.H., Nakamura, T., Yang, X.L., Liang, W.D., Inouchi, Y., 2004. Holocene vegetation variation in the Daihai Lake region of north-central China: a direct indication of the Asian monsoon climatic history. Quaternary Science Reviews, 23, 1669–1679.

Xu, T.C., and Liu, T.S., 1994. Implication of the magnetic susceptibility curve from the Chinese loess profile at Xifeng. Quaternary Science Reviews, 12, 249–254.

Xu, Y., Yue, L., Li, J., Sun, L., Sun, B., Zhang, J., Ma, J., Wang, J., 2009. An 11-Ma-old red clay sequence on the Eastern Chinese Loess Plateau. Palaeogeography, Palaeoclimatology, Palaeoecology, 284, 383-391.

Xu, Y., Yue, L., Li, J., Sun, L., Sun, B., Zhang, J., Ma, J., Wang, J., 2012. Red clay deposits on the Chinese Loess Plateau during 11.0–2.6 Ma and its implications for long-term evolution of East Asian monsoon. Environmental Earth Sciences, 66, 2021–2030.

Xue, X.X., and Zhao, J.B., 2003. Characteristic and significance of micromorphology of Neogene Red Clay of Xunyi Shanxi province [in Chinese with English abstract]. Acta Sedimentologica Sinica, 21, 448–481.

Yang, S.L., and Ding, Z.L., 2004. Comparison of particle size characteristics of the Tertiary 'red clay' and Pleistocene loess in the Chinese Loess Plateau: implications for origin and sources of the 'red clay'. Sedimentology, 51(1), 77–93.

Yang, X.P., Scuderi, L., Paillou, P., Liu, Z.T., Li, H.W., Ren, X.Z., 2011. Quaternary environmental changes in the drylands of China-a critical review. Quaternary Science Reviews, 30, 3219–3233.

Yu, L., and Oldfield, F., 1989. A multivariate mixing model for identifying sediment source from magnetic measurements, Quaternary Research, 32, 168–181.

Yu, Y., 2012. High-fidelity paleointensity determination from historic volcanoes in Japan, J. Geophys. Res. (Solid Earth), 117, B08101.

Yu, Y.J., and Tauxe, L., 2005. Testing the IZZI protocol of geomagnetic field intensity determination. Geochem Geophy Geosy., 6.

Zhang, X.Y., Arimoto, R., An, Z.S., 1999. Glacial and interglacial patterns for Asian dust transport. Quat. Sci. Rev., 18, 811–819.

Zhao, H., Chen, F.H., Li, S.H., Wintle, A.G., Fan, Y.X., Xia, D.S., 2007. A record of Holocene climate change in the Guanzhong Basin, China, based on optical dating of a loess-palaeosol sequence. The Holocene, 17(7), 1015–1022.

Zhao, Y., and Yu, Z., 2012. Vegetation response to Holocene climate change in East Asian monsoon-margin region. Earth-Science Reviews, 113(1), 1–10.

Zheng, H.B., Powell, C.M., An, Z.S., Zhou, J., Dong, G.R., 2000. Pliocene uplift of the northern Tibetan Plateau. Geology, 28, 715–718.

Zhou, L.P., Oldfield, F., Wintle, A.G., Robinson, S.G., and Wang, J.T., 1990. Partly pedogenic origin of magnetic variations in Chinese loess. Nature, 346, 737–739.

Zhou, S.Z., Chen, F.H., and Pan, B.T., 1991. Environmental changes during the Holocene in the Western China on millennial timescale. The Holocene, 1, 151–56.

Zhou, W.J., and An, Z.S., 1994. Stratigraphic divisions of the Holocene loess in China. Radiocarbon, 36, 37–45.

Zhou, W.J., Yu, S.Y., Georges, B., Kukla, G.J., Jull, A.J.T., Xian, F., Xiao, J.Y., Colman, S.M., Yu, H.G., Liu, Z., Kong, X.H., 2010. Postglacial changes in the Asian summer monsoon system: a pollen record from the eastern margin of the Tibetan Plateau. Boreas, 39, 528–539.

Zhu, Y.M., Zhou, L.P., Mo, D.W., Kaakinen, A., Zhang, Z.Q., Fortelius, M., 2008. A new magnetostratigraphic framework for late Neogene Hipparion Red Clay in the eastern Loess Plateau of China. Palaeogeography, Palaeoclimatology, Palaeoecology, 268, 47–57.

Zhu, Z.D., Liu, S., He, R.Z., 1982. Deserts evolution in the historic time, Physical Geography of China. Historic Geography, 6, 249–253.

Zijderveld, J.D.A., 1967. A.C. demagnetization of rocks, analysis of results. In: Methods in paleomagnetism, D.W. Collinson, K.M. Creer, and S.K. Runcorn, eds. Elsevier, Amsterdam, 254–286.

Zolotukhin, V.V., Al'mukhamedov, A.I., 1988. Traps of the Siberian platform. In: Macdougall, J.D. (Ed.), Continental Flood Basalts. Kluwer, Dordrecht, Netherlands, 273–310.

Zonenshain, L.P., Kuzmin, M.I., Natapov, L.M., 1991. Geology of the USSR: a Platetectonic Synthesis. American geophysical Union, Washington, 442.

Appendix A

Table A.1. Directions, intensities, breakdown of criteria fulfillment and Q_{PI} (Quality of Paleointensity) values determined from all the published paleointensity studies for the Permo-Triassic Siberian traps listed in the PINT database (http://earth.liv.ac.uk/pint/) along with this study (Chapter 4). QPI values are assigned based on the number of criteria (Biggin and Paterson, 2014) that the estimate passed. Here, '1' indicates that the given criterion has been met, while '0' indicates failure to do so.

Ref	Site	Region	Section	Lat°	Long°	Dec°	Inc°	Polarity	PI (μT)	Sd (mT)	VDM ($x10^{22}$ Am^2)	AGE	STAT	TRM	ALT	MD	ACN	TECH	LITH	QPI
2	DK	Maymecha-Kotuy	Maymecha	70.8	101.0	265.5	-64	Reversed	7.9	6.7	1.3	1	0	1	1	1	0	1	0	5
2	Flow 26	Maymecha-Kotuy	Maymecha	70.8	101.0	67.6	60.4	Normal	13.6	5.6	2.3	1	0	1	1	0	0	1	0	4
2	Flow 25	Maymecha-Kotuy	Maymecha	70.8	101.0	228.7	-55.1	Reversed	24.6		4.5	1	0	1	1	1	0	0	0	4
1,2	Flow 23	Maymecha-Kotuy	Maymecha	70.8	101.0	237	-39.7	Reversed	11.0	2.2	2.4	1	1	1	1	1	1	1	0	7
1	Flow 21	Maymecha-Kotuy	Maymecha						25.2	2.0	5.4	1	0	1	1	1	1	0	0	5
2	Flow 17	Maymecha-Kotuy	Maymecha	70.8	101.0				9.4	0.8	1.7	1	0	1	1	1	0	1	0	5
2	Flow 16	Maymecha-Kotuy	Maymecha	70.8	101.0	235.9	24.6	Normal	20.1	3.1	4.9	1	0	1	1	1	0	1	0	5
2	Flow 15	Maymecha-Kotuy	Maymecha	70.8	101.0				11.3		1.5	1	0	1	1	1	0	0	0	4
2	Flow 12	Maymecha-Kotuy	Maymecha	70.8	101.0	232.2	-80.8	Reversed	11.4	2.7	1.5	1	0	1	1	1	0	1	0	5
2	Flow 10	Maymecha-Kotuy	Maymecha	70.8	101.0	214.9	-82.7	Reversed	10.1	1.1	1.3	1	0	1	1	1	0	1	0	5
2	Flow 9	Maymecha-Kotuy	Maymecha	70.8	101.0	248.5	-81.6	Reversed	11.5	0.9	1.5	1	0	1	1	1	0	1	0	5
2	Flow 8	Maymecha-Kotuy	Maymecha	70.8	101.0	250.3	-83.3	Reversed	9.4	3.3	1.2	1	0	1	1	1	0	1	0	5
2	Flow 7	Maymecha-Kotuy	Maymecha	70.8	101.0	215.8	-63.5	Reversed	16.7	2.2	2.7	1	1	1	1	1	0	1	0	6
2	Flow 6	Maymecha-Kotuy	Maymecha	70.8	101.0	268.8	-82.3	Reversed	11.9	0.6	1.6	1	0	1	1	1	0	1	0	5
2	Flow 5	Maymecha-Kotuy	Maymecha	70.8	101.0	213.3	-72.9	Reversed	15.9	3.9	2.3	1	1	1	1	1	0	1	0	6
2	Flow 4	Maymecha-Kotuy	Maymecha	70.8	101.0	246.4	-70.1	Reversed	12.7	3.1	1.9	1	1	1	1	1	0	1	0	6
2	Flow 3	Maymecha-Kotuy	Maymecha	70.8	101.0	262.9	-81.2	Reversed	16.1	4.4	2.2	1	0	1	1	0	0	1	0	4

2	Flow 2	Maymecha-Kotuy	Maymecha	70.8	101.0	238.6	-77.9	Reversed	14.3	4.5	2.0	1	0	1	1	1	0	1	0	5
2	Flow 1	Maymecha-Kotuy	Maymecha	70.8	101.0	233.7	-70.7	Reversed	14.8	6.3	2.2	1	0	1	1	0	0	1	0	4
3	Flow 18	Maymecha-Kotuy	Truba	71.3	102.5	256.4	-73.4	Reversed	17.2	5.4	2.5	1	0	1	1	0	0	1	0	4
3	Flow 19	Maymecha-Kotuy	Truba	71.3	102.5	283.6	-71.5	Reversed	10.1	3.2	1.5	1	0	1	1	1	0	1	0	5
3	Flow 20	Maymecha-Kotuy	Truba	71.3	102.5	263.7	-74.8	Reversed	11.6	3.8	1.6	1	0	1	1	0	0	1	0	4
3	Flow 21	Maymecha-Kotuy	Truba	71.3	102.5	313.4	-79.1	Reversed	19	7.5	2.6	1	0	1	1	1	0	1	0	5
3	Flow 22	Maymecha-Kotuy	Truba	71.3	102.5	300.2	-79.3	Reversed	11.2	6.3	1.5	1	0	1	1	0	0	1	0	4
3	Flow 23	Maymecha-Kotuy	Truba	71.3	102.5	312.5	-77.2	Reversed	23.8	12.3	3.3	1	0	1	1	0	0	1	0	4
3	Flow 24	Maymecha-Kotuy	Truba	71.3	102.5	283.9	-72.4	Reversed	17.3	5.2	2.5	1	0	1	1	0	0	1	0	4
3	Flow 25	Maymecha-Kotuy	Truba	71.3	102.5	306.2	-76	Reversed	17.2	7.6	2.4	1	0	1	1	1	0	1	0	5
3	Flow 26	Maymecha-Kotuy	Truba	71.3	102.5	298.5	-71.8	Reversed	15.4	5	2.3	1	0	1	1	0	0	1	0	4
3	Flow 27	Maymecha-Kotuy	Truba	71.3	102.5	292.9	-68.1	Reversed	13.5	10.8	2.1	1	0	1	1	0	0	1	0	4
1,3	T (flow 28)	Maymecha-Kotuy	Truba	71.6	103.0	314.9	-72.2	Reversed	7.9	2.8	1.2	1	0	1	1	1	1	0	0	5
1,3	T (flow 29)	Maymecha-Kotuy	Truba	71.6	103.0	310.8	-73.4	Reversed	9.4	3.8	1.4	1	0	0	1	1	1	0	0	4
3	Flow 30	Maymecha-Kotuy	Truba	71.3	102.5	322.3	-73.3	Reversed	15.1	8.1	2.2	1	0	1	1	0	0	1	0	4
3	Flow 31	Maymecha-Kotuy	Truba	71.3	102.5	321.6	-68.4	Reversed	24.7	7.6	3.8	1	0	1	1	0	0	1	0	4
3	Flow 34	Maymecha-Kotuy	Truba	71.3	102.5	295.2	-69.8	Reversed	18.6	9.1	2.8	1	0	1	1	0	0	1	0	4
3	Flow 35	Maymecha-Kotuy	Truba	71.3	102.5	308.9	-70.9	Reversed	17.1	5.1	2.5	1	0	1	1	1	0	1	0	5
3	Flow 36	Maymecha-Kotuy	Truba	71.3	102.5	295.7	-68.6	Reversed	7.8	0.9	1.2	1	1	1	1	1	0	1	0	6
3	Flow 38	Maymecha-Kotuy	Truba	71.3	102.5	311.1	-69.6	Reversed	9.6	1.7	1.4	1	0	1	1	1	0	1	0	5
3	Flow 39	Maymecha-Kotuy	Truba	71.3	102.5	306.7	-70.2	Reversed	17	7	2.5	1	0	1	1	0	0	1	0	4
3	Flow 40	Maymecha-Kotuy	Truba	71.3	102.5	296.8	-68.6	Reversed	21.3	3.1	3.3	1	1	1	1	1	0	1	0	6
3	Flow 41	Maymecha-Kotuy	Truba	71.3	102.5	244.6	-51.3	Reversed	26.1	2.7	5	1	0	1	1	1	0	1	0	5
3	Flow 42	Maymecha-Kotuy	Truba	71.3	102.5	237.7	-46.1	Reversed	6.3	2.3	1.3	1	0	1	1	1	0	1	0	5
5	Bolshaya	Bolshaya Nirunda		62.0	95.0	265	-76	Reversed	13	3.2	1.8	1	1	0	1	0	0	0	0	3
5	Km	Norilisk		70.4	90.1	63.7	73.2	Normal	26.7	8	3.9	1	0	0	1	1	0	0	0	3
6	KMX4	Norilisk	Abagalakh	70.4	90.1	37	77	Normal	37.2	1.3	5.2	1	0	1	1	1	0	0	0	4
6	KMX3	Norilisk	Abagalakh	70.4	90.1	47	74	Normal	30.2	5.4	4.3	1	0	1	1	1	0	0	0	4
6	KMX2	Norilisk	Abagalakh	70.4	90.1	68	72	Normal	13.0	2.9	1.9	1	0	1	1	1	0	0	0	4

6	KMX1	Norilisk	Abagalakh	70.4	90.1	75	72	Normal	24.3	8.0	3.6	1	0	1	1	1	0	0	0	4
6	KM3	Norilisk	Abagalakh	70.4	90.1	75	73	Normal	12.1	1.8	1.7	1	0	1	1	1	0	0	0	4
6	KM1	Norilisk	Abagalakh	70.4	90.1	69	72	Normal	16.0	5.1	2.3	1	0	1	1	1	0	0	0	4
5	Hr	Norilisk		70.4	90.1	88	65.2	Normal	21.1	6.8	3.4	1	0	0	1	1	0	0	0	3
6	HR13	Norilisk	Abagalakh	70.4	90.1	59	81	Normal	14.7	2.5	2.0	1	0	1	1	1	0	0	0	4
6	HR11	Norilisk	Abagalakh	70.4	90.1	50	75	Normal	13.7	0.4	1.9	1	0	1	1	1	0	0	0	4
6	HR7	Norilisk	Abagalakh	70.4	90.1	96	73	Normal	30.2	3.0	4.4	1	0	1	1	1	0	0	0	4
6	HR6	Norilisk	Abagalakh	70.4	90.1	109	64	Normal	17.7	2.2	2.9	1	0	1	1	1	0	0	0	4
6	HR3	Norilisk	Abagalakh	70.4	90.1	85	53	Normal	19.6	4.0	3.7	1	0	1	1	1	0	0	0	4
6	HR2	Norilisk	Abagalakh	70.4	90.1	94	61	Normal	12.8	0.7	2.2	1	0	1	1	1	0	0	0	4
5	Mk	Norilisk		70.4	90.1	103.3	73.9	Normal	15.9	6.5	2.3	1	0	0	1	1	0	0	0	3
6	MK13	Norilisk	Abagalakh	70.4	90.1	95	71	Normal	15.7	4.1	2.3	1	0	1	1	1	0	0	0	4
6	MK12	Norilisk	Abagalakh	70.4	90.1	100	70	Normal	11.8		1.8	1	0	1	1	1	0	0	0	4
6	MK8	Norilisk	Abagalakh	70.4	90.1	106	79	Normal	20.2	1.9	2.8	1	0	1	1	1	0	0	0	4
6	MK7	Norilisk	Abagalakh	70.4	90.1	95	77	Normal	21.7		3.0	1	0	1	1	1	0	0	0	4
6	MK5	Norilisk	Abagalakh	70.4	90.1	123	82	Normal	16.4	0.0	2.2	1	0	1	1	1	0	0	0	4
6	MK4	Norilisk	Abagalakh	70.4	90.1	66	74	Normal	16.3	0.3	2.3	1	0	1	1	1	0	0	0	4
6	MK3	Norilisk	Abagalakh	70.4	90.1	84	72	Normal	10.6	1.3	1.6	1	0	1	1	1	0	0	0	4
6	MK2	Norilisk	Abagalakh	70.4	90.1	161	75	Normal	10.9	2.6	1.5	1	0	1	1	1	0	0	0	4
6	MK1	Norilisk	Abagalakh	70.4	90.1	141	78	Normal	35.9	8.9	4.9	1	0	1	1	1	0	0	0	4
6	MK0	Norilisk	Abagalakh	70.4	90.1	110	75	Normal	21.6	0.4	3.1	1	0	1	1	1	0	0	0	4
5	Mr	Norilisk		70.4	90.1	105.7	76.8	Normal	22	7.3	3	1	0	0	1	1	0	0	0	3
6	MR1	Norilisk	Abagalakh	70.4	90.1	117	77	Normal	15.2	3.4	2.1	1	0	1	1	1	0	0	0	4
6	MR2	Norilisk	Abagalakh	70.4	90.1	115	78	Normal	20.4		2.8	1	0	1	1	1	0	0	0	4
6	MR6	Norilisk	Icon	70.4	90.1	96	74	Normal	23.6	2.9	3.4	1	0	1	1	1	0	0	0	4
6	MR7	Norilisk	Icon	70.4	90.1	89	77	Normal	25.7	3.3	3.6	1	0	1	1	1	0	0	0	4
6	MR9	Norilisk	Icon	70.4	90.1	187	82	Normal	19.7	1.1	2.6	1	0	1	1	1	0	0	0	4
6	MR11	Norilisk	Icon	70.4	90.1	136	81	Normal	21.8	0.9	2.9	1	0	1	1	1	0	0	0	4
6	MR23	Norilisk	Icon	70.4	90.1	91	77	Normal	14.6		2.0	1	0	1	1	1	0	0	0	4
7	No. 1	Norilisk		69.5	91	291	-77	Reversed	26.0	5.8	3.6	1	1	0	0	1	0	0	1	4
7	No. 2	Norilisk		69.5	91	143	72	Normal	23.0	5.7	3.4	1	1	0	0	1	0	0	1	4

7	No. 3	Norilisk		69.5	91	136	70	Normal	23.0	4.9	3.5	1	1	0	0	1	0	0	1	4
7	No. 4	Norilisk		69.5	91	80	73	Normal	22.0	5.0	3.2	1	1	0	0	1	0	0	1	4
7	No. 5	Norilisk		69.5	91	84	72	Normal	22.0	4.8	3.2	1	1	0	0	1	0	0	0	3
7	No. 6	Norilisk		69.5	91	120	57	Normal	23.0	3.0	4.1	1	1	0	0	1	0	0	0	3
7	No. 7	Norilisk		69.5	91	100	76	Normal	35.0	7.1	4.9	1	1	0	0	0	0	0	0	2
7	No. 8	Norilisk		69.5	91	85	71	Normal	30.0	18.3	4.5	1	0	0	0	0	0	0	1	2
7	No. 9	Norilisk		69.5	91	91	75	Normal	28.0	8.1	4.0	1	0	0	0	1	0	0	1	3
7	No. 10	Norilisk		69.5	91	102	77	Normal	29.0	12.3	4.0	1	0	0	0	1	0	0	1	3
7	No. 11	Norilisk		69.5	91	101	68	Normal	25.0	8.7	3.9	1	0	0	0	1	0	0	1	3
7	No. 12	Norilisk		69.5	91	49	66	Normal	20.0	6.2	3.2	1	0	0	0	1	0	0	1	3
7	No. 13	Norilisk		69.5	91	80	74	Normal	21.0	2.6	3.0	1	1	0	0	1	0	0	0	3
7	No. 14	Norilisk		69.5	91	116	73	Normal	23.0	3.2	3.3	1	1	0	0	0	0	0	0	2
7	No. 15	Norilisk		69.5	91	111	57	Normal	22.0	4.1	3.9	1	1	0	0	0	0	0	1	3
7	No. 16	Norilisk		69.5	91	102	60	Normal	23.0	3.7	3.9	1	1	0	0	1	0	0	0	3
7	No. 17	Norilisk		69.5	91	83	75	Normal	22.0	3.2	3.1	1	1	0	0	1	0	0	0	3
7	No. 18	Norilisk		69.5	91	97	77	Normal	22.0	3.6	3.1	1	1	0	0	1	0	0	0	3
4	A1	Aikhal	Other	66.2	111.3	113.3	73.2	Normal	43.8	7.9	6.3	1	0	0	1	1	0	0	0	3
4	A2	Aikhal	Other	66.2	111.3	102.9	80.2	Normal	41.8	18.3	5.6	1	0	0	0	1	0	0	0	2
4	A3	Aikhal	Other	66.2	111.3	139.1	79	Normal	48.6	15.6	6.6	1	0	0	1	1	0	0	0	3
1,4	S1	Sytikanskaya	Other	66.1	111.8	280.6	-59.8	Reversed	18.6	2.8	3.2	1	1	1	1	0	1	1	0	6
1,4	S3	Sytikanskaya	Other	66.1	111.8	285.7	-66.8	Reversed	16.0	3.1	2.5	1	1	1	0	0	1	0	0	4
1,4	Y1	Yubileinaya	Other	66.0	111.7	97.4	81.2	Normal	48.5	7.3	6.4	1	1	1	1	1	1	1	0	7
4	Y2	Yubileinaya	Other	66.0	111.7	84	82.4	Normal	41.4	2.4	5.5	1	0	0	1	1	0	0	0	3
4	Y3	Yubileinaya	Other	66.0	111.7	100.2	81.4	Normal	49.0		6.5	1	0	0	0	1	0	0	0	2
4	Y4	Yubileinaya	Other	66.0	111.7	122.4	82.5	Normal	47.5	9.0	6.3	1	0	0	1	1	0	0	0	3

Ref: references, 1- this study (Chapter 4), 2- Scherbakova et al, 2015, 3- Scherbakova et al, 2013, 4- Blanco et al., 2012, 5- Scherbakova et al, 2005, 6- Heunemann et al, 2004, and 7- Solodovnikov, 1995. Lat: lattitude, Long: longitude, Dec:

declination, Inc: inclination, PI: paleointensity result, Sd: standard deviation, VDM: Virtual dipole moment. "AGE: a reliable age and palaeomagnetic behavior consistent with paleointensity derived from a primary component of remanence, STAT: a minimum of 5 individual sample estimates per unit with low dispersion (true SD/mean ≤25%), TRM: reasonable independent (e.g., microscopic) evidence that the component of remanence in the bulk of samples is likely a thermoremanent magnetization (TRM), ALT: reasonable evidence (e.g., pTRM checks or rock mag) that the final estimate was not significantly biased by alteration occurring during the experiment, MD: reasonable evidence (e.g., high f or pTRM tail checks) that the final estimate was not significantly biased by multidomain behavior during the experiment, ACN: reasonable evidence that the final estimate was not significantly biased by anisotropy of TRM, cooling rate effects, and non-linear TRM effects, TECH: estimate is an average of results from more than one palaeointensity technique, LITH: estimate is an average of results from more than one lithology or from samples from the same lithology showing significantly different unblocking behavior" (Biggin and Paterson, 2014).